Conical Nodes in Nonadiabatic Eigenfunctions

Peter W. Foster

B.S., Grove City College, 2013

A thesis submitted to the Faculty of the Graduate School of the University of Colorado in partial fulfillment of the requirements for the degree of

Doctor of Philosophy

Department of Chemistry

2019

This thesis entitled:
Conical Nodes in Nonadiabatic Eigenfunctions
written by Peter W. Foster
has been approved for the Department of Chemistry

_____
David M. Jonas

_____
Markus J. Pflaum

Date _____

The final copy of this thesis has been examined by the signatories, and we find that both the content and the form meet acceptable presentation standards of scholarly work in the above mentioned discipline.

Foster, Peter W. (Ph.D., Chemistry)

Conical Nodes in Nonadiabatic Eigenfunctions

Thesis directed by David M. Jonas

Where the Born-Oppenheimer Approximation breaks down, systems can best be understood using exact nonadiabatic eigenfunctions. Exact nonadiabatic eigenstates are calculated and factored using Hunter's exact factorization and it is found that when there are a finite number of coupled electronic states, nonadiabatic eigenfunctions can have nodes of zero probability density. These nodes create singularities in the electronic character where electronic character inverts through the node and where probability amplitude in the vicinity of the node forms a right elliptical cone (or a higher dimensional analog) with the node as its vertex. These nodes are in principle observable by measuring the vibrational probability density for systems with a finite number of coupled electronic states that contribute significantly.

Nonadiabatic eigenfunctions can have conical nodes in vibronically resonant systems, near conical intersections and even in tunneling regions where nonadiabaticity is minimal. Near circularly symmetric conical intersections, eigenfunctions with a psuedo-rotation quantum number of $j = 1/2$ will have probability amplitude on top of the conical intersection and eigenfunctions with a psuedo-rotation quantum number of $j \geq 3/2$ will have an essential conical or higher order node at the conical intersection. When that angular momentum symmetry is broken for an elliptical conical intersection, however, the nodes do not occur at the intersection and all eigenstates have probability amplitude at the conical intersection. Conical nodes are observable nonadiabatic features that highlight the importance of exact solutions of the Hamiltonian.

To my loving, understanding, and patient wife.
Without you, none of this would have been possible.

ACKNOWLEDGEMENTS

First, I would like to acknowledge my advisor, David Jonas. He has worked with me closely one-on-one for years, coaching me, encouraging me and helping me to be the best scientist I can be. I have learned incredible amounts from him, not just about physical chemistry, but about the mechanics of sound arguments, scientific writing, thorough research that thinks through every possibility. He has modelled the kind of scientist I hope to be, from his passionate love of the research to the care he shows for his graduate students and the commitment he has to his family. I have also learned a lot about baseball, whether it be Major League, Minor League or South Korean. Thank you.

I have also learned from my fellow lab mates, being coached by Vivek Tiwari and Austin Spencer, who made my research possible; having fascinating conversations with Dmitry Baranov and Callum Douglass, who made time in the lab more enjoyable; laughing at the wonderful stories of Sam Park; comparing notes about teaching with Anna Curtis; bouncing ideas back and forth with Alexa Carollo and Alina Mateo Tejada; and getting the pleasure to meet and briefly work with Sumit Singhal and Sarang Yeola. I also loved being able to go to class with and work through graduate school with my Physical Chemistry cohort of grad students, too many to name. Whether we playing fantasy football, watching Game of Thrones or attending each other's defense talks, it meant a lot to be part of this community.

I would like to thank my parents for their love and support throughout his process, as well as the love and support of my sister, my Yiayia and Papou and my entire family. My family means the world to me and it has been hard to be so far away, but they have supported and encouraged me in this process.

Friends, both local and distant have meant so much to me including (but certainly not limited to) the Sloan Family, Michael Royster, Frankie Naylor, Alex and Brynn Welch, David and Deborah Couch, Travis and Bianca Frazer, Jameson and Christine Reber, David and Kaitlyn Quigley, Dave and Abby Reens, Ryan and Janae Allsman, Kevin and Jewel Aagaard and Maddie and Ellis Mbeh. I have gained so much from my church family at Cornerstone Church of Boulder Valley, led by Gene Binder and Brian Carlucci, as well as Intervarsity Graduate Christian Fellowship, led by Emily Crider, Scott Filkin and Sarah Booth. Thank you to the God who has been with me and kept me going for this whole process.

Finally, thank you to my wife, Katie, who has worked with me and supported me through long hours and anxious evenings, through frustration, exaltation, confusion and exhaustion at the complicated world of nonadiabatic dynamics. Thank you. When I chose to come to Colorado, I was moving away across the country, but she stuck with me and followed me two years later. She has put up with my insecurities and my communication problems and helped guide me through difficult times, like the death of my grandparents and when I failed my Physical Chemistry Oral Exam. She agreed to marry me and has figured out life with me since, through easy times and hard times. Together we have built an exciting life, seeing the world together and living a constant adventure. Thank you for being my partner in everything and for coming with me as we boldly pave new adventures ahead. This dissertation is as much yours as it is mine.

CONTENTS

CHAPTER 1: INTRODUCTION **1**

1.1. The Adiabatic Factorization of the Wavefunction 2

1.2. The Limitations of the Adiabatic Approximation 6

1.3. The Appearance of Nodes 10

1.4. The Jahn-Teller Conical Intersection 14

1.5. The Elliptical Conical Intersection 29

1.6. Nonadiabatic Effects Far from a Conical Intersection 32

References **36**

CHAPTER 2: NONADIABTIC EIGENFUNCTIONS CAN HAVE CONICAL NODES **41**

2.1. Introduction 41

2.2. Model and Calculations 45

2.3. Results 49

2.4. Discussion 55

2.5. Conclusion 60

References **61**

CHAPTER 3: NONADIABATIC EIGENFUNCTIONS CAN HAVE AMPLITUDE, SIGNED CONICAL NODES, OR SIGNED HIGHER ORDER NODES AT A CONICAL INTERSECTION WITH CIRCULAR SYMMETRY 65

3.1. Introduction 66

3.2. Theory 70

3.3. Computational Methods 75

3.4. Results 78

3.5. Discussion 94

3.6. Conclusion 98

References 100

CHAPTER 4: NONADIABTIC CONICAL NODES ARE NEAR BUT NOT AT ELLIPTICAL CONICAL INTERSECTIONS **105**

4.1. Introduction 106

4.2. Theory 110

4.2.1. The Jahn-Teller Hamiltonian 110

4.2.2. Adiabatic Surfaces 112

4.2.3. The sign of the conical intersection 116

4.2.4. Exact nonadiabatic eigenstates 117

4.2.5. Colored exact factorization 119

4.2.6. The electronic index 120

4.3. Calculations 121

4.4. Results 122

4.4.1. Effects of unequal linear Jahn-Teller couplings 122

4.4.2. Nodes Near, but not at, Conical Intersections 126

4.4.3. Conical Node Creation and Annihilation via Tangential Nodes 136

4.4.4. The Role of Ellipticity 142

4.5. Discussion 145

4.6. Conclusion 147

References **149**

CHAPTER 5: NONADIABATIC EIGENFUNCTIONS CAN HAVE CONICAL NODES IN THE TUNNELING REGION **155**

5.1. Introduction 155

5.2. Theory 162

5.3. Calculations 166

5.4. Results 168

5.5. Discussion 194

5.6. Conclusion 196

References **198**

BIBLIOGRAPHY **201**

APPENDIX A **213**

References **215**

APPENDIX B: Chapter 3 Supporting Information **217**

References **229**

APPENDIX C: Chapter 4 Supplementary Material **231**

References **245**

APPENDIX D: Supporting Information for Chapter 5 **247**

LIST OF TABLES

TABLE 1.1: Numerical Energy Eigenvalues for Cylindrically Symmetric Jahn-Teller Hamiltonian 26

TABLE 1.2: Numerical Energy Eigenvalues for Elliptically Symmetric Jahn-Teller Hamiltonian 31

TABLE 3.1: The 6 Lowest Energy Eigenvalues for Small Jahn-Teller Stabilization Energies with $\omega = 200$ cm^{-1} 77

TABLE A.1: Analytical Comparison with Judd's Results 213

TABLE B.1: Eigenstate Correlation for 15 Lowest Energy Eigenstates 227

TABLE C.1: Energy Eigenvalues for 12 Lowest Energy Eigenstates from Figure C.8 242

TABLE C.2: Energy Eigenvalues for 12 Lowest Energy Eigenstates from Figure C.9 244

LIST OF FIGURES

FIGURE 1.1: One-Dimensional Cross-section of Total Probability Amplitude 10

FIGURE 1.2: Three-Dimensional Picture of Total Probability Amplitude Showing Conical Nodes 12

FIGURE 1.3: Adiabatic Potential Energy Surfaces for an Elliptical Conical Intersection 15

FIGURE 1.4: Adiabatic Energies as a Function of $(D\omega)/\omega$ for Three Values of the Pseudo-Rotation Quantum Number 18

FIGURE 1.5: Energy Eigenvalues of the Cylindrically Symmetric Jahn-Teller Hamiltonian as a Function of $(D\omega)/\omega$ 20

FIGURE 1.6: Colored Factorization of Three Lowest Energy Eigenstates for Three Values of $(D\omega)/\omega$ 22

FIGURE 1.7: Colored Factorization of Nonadiabatic Eigenfunction for Analytical Comparison with Judd's Results 28

FIGURE 1.8: Energy Eigenvalues of the Elliptically Symmetric Jahn-Teller Hamiltonian as a Function of d_2 30

FIGURE 2.1: Diabatic and Adiabatic Potential Energy Surfaces for a Nested Funnel Potential 47

FIGURE 2.2: Colored Factorization of Nine Lowest Energy Eigenstates for a Homodimer and a Heterodimer 50

FIGURE 2.3: Colored Factorization and Diabatic Projection of 559 cm^{-1} Eigenstates 52

FIGURE 2.4: Close-Up Colored Factorization Near a Conical Nodes 54

FIGURE 2.5: Colored Factorization of 559 cm^{-1} and 571 cm^{-1} Eigenstates for $\omega_A = 202\ cm^{-1}$ and $\omega_B = 198\ cm^{-1}$ 57

FIGURE 3.1: Adiabatic Potential Energy Surfaces for a Cylindrical Conical Intersection 72

FIGURE 3.2: Three Representations for the 12 Lowest Energy Nonadiabatic Eigenstates of a Cylindrical Jahn-Teller Hamiltonian 79

FIGURE 3.3: Colored Factorization and Diabatic Projection of Lowest Energy Eigenstate for Two Values of $(D\omega)/\omega$ 83

FIGURE 3.4: Diabatic Projections of Four Nonadiabatic Eigenfunctions Showing Different Orders of Essential Nodes 86

FIGURE 3.5: Close-up View of Colored Factorization and Diabatic Projections of Four Nonadiabatic Eigenfunctions Showing Different Orders of Essential Nodes 87

FIGURE 3.6: Adiabatic Potential Energy Surfaces for Jahn-Teller Hamiltonian with Reversed Displacement and Accompanying Colored Factorizations of Lowest Energy Nonadiabatic Eigenfunctions 92

FIGURE 3.7: Colored Factorization and Diabatic Projection of $(v=1,|j|=3/2)$ Eigenfunction for Four Values of $(D\omega)/\omega$ 97

FIGURE 4.1: Adiabatic Potential Energy Surfaces for an Elliptical Conical Intersection 114

FIGURE 4.2: Effects of varying Jahn-Teller displacement for the coupling coordinate 123

FIGURE 4.3: Accidental Conical Nodes are near but not at the Conical Intersection 128

FIGURE 4.4: Varying the coupling coordinate displacement 131

FIGURE 4.5: Splitting of Second Order Nodes 133

FIGURE 4.6: Effects of varying frequency for the coupling vibration 135

FIGURE 4.7: Creation and Annihilation of Conical Nodes through a Tangential Node 137

FIGURE 4.8: Generic structure around a tangential node 138

FIGURE 4.9: Node Movements that Change the Electronic Index Around a

Fixed Path 141

FIGURE 5.1: Diabatic and Adiabatic Projections of a Nonadiabatic Eigenfunction Showing Large Radius Nodes 161

FIGURE 5.2: Cross-Section of Projections of a Nonadiabatic Eigenfunction onto Adiabatic Surfaces with Inset 165

FIGURE 5.3: Cross-Section of Projections of a Nonadiabatic Eigenfunction onto Adiabatic Surfaces to Show Node in Tunneling Region 169

FIGURE 5.4: Six Lowest Energy $\sigma_v = +1$ Nonadiabatic Eigenfunctions and Their Adiabatic Projections 172

FIGURE 5.5: $(v = 1, |j| = 1/2)$ Nonadiabatic Eigenfunction and Its Adiabatic Projections for Six Values of $(D\omega)/\omega$ 177

FIGURE 5.6: Radius of Nodes on the Projections of the $(v = 1, |j| = 1/2)$ Nonadiabatic Eigenfunction onto the Upper and Lower Adiabatic States as a Function of Jahn-Teller Displacement 181

FIGURE 5.7: $(v = 1, |j| = 3/2)$ Nonadiabatic Eigenfunction and Its Adiabatic Projections for Six Values of $(D\omega)/\omega$ 183

FIGURE 5.8: $(v = 2, |j| = 3/2)$ Nonadiabatic Eigenfunction and Its Adiabatic Projections for Six Values of $(D\omega)/\omega$ 186

FIGURE 5.9: $(v = 2, |j| = 1/2)$ Nonadiabatic Eigenfunction and Its Adiabatic Projections for Six Values of $(D\omega)/\omega$ 189

FIGURE 5.10: Radial Function $\chi_j^m(R)$ for Five Values of $(D\omega)/\omega$ to Show the Creation of a Pair of Radial Nodes 192

FIGURE B.1: Three Representations for the $v = 3$ Nonadiabatic Eigenstates of a Cylindrically Symmetric Jahn-Teller Hamiltonian 220

FIGURE B.2: Three Representations for the $v = 4$ Nonadiabatic Eigenstates of a Cylindrically Symmetric Jahn-Teller Hamiltonian 221

FIGURE B.3: Three Representations for the 12 Lowest Energy Nonadiabatic Eigenstates of a Cylindrical Jahn-Teller Hamiltonian with Reversed Displacement 222

FIGURE B.4: Colored Factorization of 6 Lowest Energy $\sigma_v = +1$ Eigenfunctions for Five Values of $(D\omega)/\omega$ 224

FIGURE B.5: Colored Factorization of $v = 3$ Eigenfunctions for Five Values of $(D\omega)/\omega$ 225

FIGURE B.6: Colored Factorization of $v = 4$ Eigenfunctions for Five Values of $(D\omega)/\omega$ 226

FIGURE B.7: Colored Factorization of $v = 5$ and $v = 6$ Eigenfunctions Included in the 15 Lowest Energy Eigenvalues 228

FIGURE C.1: Colored Factorization of 6 Lowest Energy $\sigma_v = +1$ Eigenfunctions for Four Reflection Eigenvalues 233

FIGURE C.2: Colored Factorization of 6 Lowest Energy $\sigma_v = +1$ Eigenfunctions for Cases Surrounding the Accidental Born-Oppenheimer Case 234

FIGURE C.3: Colored Factorization of the 605 cm^{-1} Eigenfunction for Four Rotations of the Reflection Operator 236

FIGURE C.4: Colored Factorization of Six Eigenstates with Higher Order Nodes n = 0 through 5 237

FIGURE C.5: Probability Amplitude Cross-Sections Near a Tangential Node 238

FIGURE C.6: Close-up View of Node Formation Through a First Order Tangential Node 239

FIGURE C.7: Close-up Views of Six Large Radius Conical Nodes 240

FIGURE C.8: Adiabatic Potentials and Nonadiabatic Eigenfunctions when $\omega_1 d_1 = \omega_2 d_2$ 241

FIGURE C.9: Nonadiabatic Eigenfunctions with Unequal Frequencies and Equal Stabilization Energies 243

FIGURE D.1: Adiabatic Potential Energy Surfaces for $(D\omega)/\omega = 5$ 247

FIGURE D.2: Six Lowest Energy $\sigma_v = +1$ Nonadiabatic Eigenfunctions for Five Values of $(D\omega)/\omega$ 248

CHAPTER 1

INTRODUCTION

In chemistry, it is commonly assumed that electronic motion is much faster than nuclear motion, thus the two are separable and the wavefunction is understandable as a product of an electronic and a vibrational factor. This idea is encapsulated by the adiabatic approximation [1]. It has long been understood, however, that some molecular systems have regions of coordinate space where the adiabatic approximation breaks down and faster, nonadiabatic effects are dominant [2-7]. These regions are funnels between electronic states, often with a conical shape [2, 8]. In these cases, the system often behaves adiabatically at all regions of coordinate space other than the area in the vicinity of the conical intersection.

There are systems, however, where nonadiabatic behavior occurs throughout vibrational coordinate space and not just near a conical intersection. In 2013, Tiwari et. al. published a study suggesting that energy transfer in photosynthesis might occur via vibronic resonance and showing that all experimentally reported signatures of picosecond coherence in the 2D spectra of photosynthetic antenna were consistent with this hypothesis [9]. Energy was transferred through a "nested funnel" in which the donor harmonic oscillator potential lies within the acceptor harmonic oscillator potential along the tuning coordinate and the minimum energies were only separated by one vibrational quantum. In this system, nonadiabatic effects were prominent for all vibrational coordinates [9]. This motivated the present study into the limits of the adiabatic approximation and the effects that occur throughout vibrational coordinate space when it breaks down.

1.1. The Adiabatic Factorization of the Wavefunction

The vibrational-electronic energy of an eigenfunction of the Hamiltonian can be found using the Schrödinger Equation. Assuming a non-rotating molecule and approximating the center of mass as the center of nuclear mass to isolate vibrational-electronic effects, the Schrödinger Equation gives us

$$\hat{H}(\hat{r},\hat{q})\psi^{m}_{exact}(r,q) = E^{m}\psi^{m}_{exact}(r,q) \tag{1.1}$$

where $\hat{H}(\hat{r},\hat{q})$ is the vibrational-electronic Hamiltonian operator, E^{m} is the eigenvalue of the Hamiltonian for eigenstate m, and $\psi^{m}_{exact}(r,q)$ is the corresponding eigenfunction as a function of both electronic and vibrational coordinates (r and q, respectively).

Solving this differential equation is numerically difficult, so the most widely used approach is to adiabatically factor the wavefunction using a method [1] based on the work of Born and Oppenheimer [10]. This requires the vibrational-electronic Hamiltonian be split into an electronic Hamiltonian and a vibrational Hamiltonian that can be solved separately.

The vibrational-electronic Hamiltonian includes the kinetic energy of the electrons, the kinetic energy of the electrons, the Coulombic attraction of the electrons to the nuclei, the Coulombic repulsion between electrons and the Coulombic repulsion between nuclei as in

$$\hat{H}(\hat{r},\hat{q}) = \hat{T}_{elec} + \hat{T}_{vib} + V_{e-n}(\hat{r},\hat{q}) + V_{e-e}(\hat{r}) + V_{n-n}(\hat{q}) \tag{1.2}$$

The electronic Hamiltonian $\hat{H}_{elec}(q)$ includes all of the terms of the vibrational-electronic Hamiltonian that can be solved treating nuclear coordinate operators as parameters q, which excludes the vibrational kinetic energy. The electronic Hamiltonian is

$$\hat{H}_{elec}(q) \equiv \hat{H}(\hat{r}, q) - \hat{T}_{vib} \tag{1.3}$$

where the Hamiltonian is here a function of vibrational coordinate parameters q instead of operators $\hat{q}$ as in Eq. (1.2). The solutions of the electronic Schrödinger Equation are vibrational coordinate-dependent eigenvalues $E^n(q)$ [1]:

$$\hat{H}_{elec}(q)\psi^n_{elec}(r;q) = E^n(q)\psi^n_{elec}(r;q) \tag{1.4}$$

At each point in vibrational space, then, this yields a complete orthonormal set of adiabatic electronic eigenfunctions $\psi^n_{elec}(r;q)$. These normalized eigenfunctions are conditional probability amplitudes, given a fixed set of vibrational coordinates q. Each electronic eigenfunction has a corresponding vibrational coordinate-dependent eigenvalue $E^n(q)$, which can be used as a potential energy surface for the vibrations on electronic state n. The vibrational Hamiltonian is defined in reference to this potential energy surface with

$$\hat{H}_{vib} \equiv \hat{T}_{vib} + E^n(\hat{q}) \tag{1.5}$$

where $\hat{H}_{vib}$ contains the nuclear kinetic energy operator $\hat{T}_{vib}$ that was not included in the electronic Hamiltonian and the potential energy $E^n(\hat{q})$ from the electronic Hamiltonian eigenvalue. It should be noted that $\hat{q}$ is being used as an operator here instead of a parameter as in Eq. (1.4).

The vibrational Hamiltonian can be used to solve for the vibrational-electronic energy by

$$\hat{H}_{vib}\psi^{v;n}_{vib}(q) = E^{v;n}_{elec,vib}\psi^{v;n}_{vib}(q) \tag{1.6}$$

where the eigenvalue $E_{elec,vib}^{v;n}$ is the total vibrational-electronic energy of vibrational state v on electronic state n and $\psi_{vib}^{v;n}(q)$ is a marginal vibrational eigenfunction. [1, 11, 12] The set of these vibrational eigenfunctions $\psi_{vib}^{v;n}(q)$ form a complete real-valued orthonormal set.

This adiabatic approximation assumes the exact eigenfunction $\psi_{exact}^{m}(r,q)$ is a product of a conditional adiabatic electronic eigenfunctions $\psi_{elec}^{n}(r;q)$ of the electronic Hamiltonian and a marginal vibrational eigenfunction $\psi_{vib}^{v;n}(q)$ of the vibrational Hamiltonian,

$$\psi_{elec,vib}^{n,v}(r,q) = \psi_{elec}^{n}(r;q)\psi_{vib}^{v;n}(q) \tag{1.7}$$

where the conditional electronic eigenfunction $\psi_{elec}^{n}(r;q)$ is specified by an electronic quantum number n, is a function of electronic coordinates r, and is parametrically dependent on the vibrational coordinates q (parametric dependence is shown here by the semicolon) [1, 11, 12]. The marginal vibrational function $\psi_{vib}^{v;n}(q)$ is specified both by electronic quantum number n and vibrational quantum number v and is a function of vibrational coordinates q. $\left|\psi_{elec}^{n}(r;q)\right|^2$ is the conditional probability for a given set of vibrational coordinates q that the electrons will be found at electronic coordinate r when in the electronic eigenstate n. In a given electronic state n and vibrational state v at vibrational coordinates q, $\left|\psi_{vib}^{v;n}(q)\right|^2$ is the marginal probability density.

For given vibrational coordinates, the set of electronic eigenfunctions is a complete orthonormal set

$$\int \psi_{elec}^{n}(r;q)\psi_{elec}^{k}(r;q)^{*}\,dr = \delta_{nk}, \tag{1.8}$$

but the eigenfunctions at one point in vibrational space need not be orthonormal with respect to the eigenfunctions at another point in vibrational space. The most that can be said is

$$\left|\int \psi_{elec}^{n}(r;q)\psi_{elec}^{k}(r;q')^{*}\,dr\right| \le 1. \tag{1.9}$$

Analogously, each electronic eigenfunction has an accompanying infinite complete set of orthonormal vibrational eigenfunctions

$$\int \psi_{vib}^{v;n}(r;q)\psi_{vib}^{v';n}(r;q)^{*}\,dr = \delta_{vv'}, \tag{1.10}$$

but the eigenfunctions on one electronic state need not be orthonormal with respect to eigenfunctions on another electronic state. The most that can be said is

$$\left|\int \psi_{vib}^{v;n}(r;q)\psi_{vib}^{v';k}(r;q)^{*}\,dr\right| \le 1. \tag{1.11}$$

Within any set of eigenfunctions, the existence of nodes separating regions of positive and negative eigenfunction amplitude is required by orthogonality. Adiabatic electronic eigenfunctions and vibrational eigenfunctions will separately have nodes where the amplitude of the eigenfunction (and hence the probability density) is zero as the amplitude switches from positive to negative or vice versa. The dimensionality of the node is the dimensionality of the surface at the interface between the positive and negative regions, which will be one less than the dimensionality of the space. Therefore, a vibrational eigenfunction that is a function of M_v vibrational coordinates can have $M_v - 1$ dimensional nodal surface(s). This becomes important later when looking at the intersection of nodal surfaces.

1.2. The Limitations of the Adiabatic Approximation

Though useful, the adiabatic approximation is never exact. Even in diatomic hydrogen, the simplest molecular system, there are nonadiabatic effects [13]. An exact calculation of the interaction of two hydrogen atoms requires calculating interactions with excited electronic states using nonadiabatic theory [14, 15]. This error in adiabatic results arises from the approximation's neglect of two terms in the Hamiltonian [16]. Calculating the difference between the total Hamiltonian acting on the adiabatic vibrational-electronic wavefunction and the energy of the adiabatic approximation reveals two terms that are not included when vibrational coordinates are treated as parameters.

$$\begin{aligned}\hat{H}(\hat{r},\hat{q})\psi^{n,v}_{elec,vib}(r,q) - E^{n,v}_{elec,vib}\psi^{n,v}_{elec,vib}(r,q) \\ = -\frac{\hbar^2}{2M}\left(\frac{\partial^2\psi^{n}_{elec}(r;q)}{\partial q^2}\right)\psi^{v;n}_{vib}(q) - \frac{\hbar^2}{M}\left(\frac{\partial\psi^{n}_{elec}(r;q)}{\partial q}\right)\left(\frac{\partial\psi^{v;n}_{vib}(q)}{\partial q}\right)\end{aligned} \tag{1.12}$$

where M is a nuclear mass.

If the exact eigenstates of the Hamiltonian $\psi^{m}_{exact}(r,q)$ are assumed to be linear combinations of adiabatic vibrational-electronic states

$$\psi^{m}_{exact}(r,q) = \sum_{n,v} c_{m,n,v}\psi^{n,v}_{elec,vib}(r;q) \tag{1.13}$$

with $c_{m,n,v}$ being the coefficient of vibrational state v on electronic state n for exact nonadiabatic eigenfunction m, the nonadiabaticity can be calculated and added as a perturbation to the adiabatic calculation [17].

For polyatomic molecules, adiabatic eigenstates run into additional complications when two potential energy surfaces are degenerate at a point. There the adiabatic approximation

becomes non-single-valued [2, 3]. The potential energy surfaces around such a point typically have the form of an elliptical double cone and the vicinity of such a point is called a conical intersection. These intersections will be explored in depth later in this work. At these points, adiabatic factorization fails as the vibrational and electronic factors are not uniquely defined.

The adiabatic linear combination can be used to visualize a nonadiabatic eigenstate by plotting the vibrational projection on each participating adiabatic electronic state. For a nonadiabatic state, this requires comparing at least two vibrational projections. As will be shown later, however, there are difficulties with this approach in the vicinity of a conical intersection that have only recently been appreciated [18, 19], partially as a result of the work in this thesis [20]. Nevertheless, this approach is invaluable for measurements which probe one-electron processes, such as electronic spectroscopy [21].

It is also possible to approach studying the wavefunction without any factoring of electronic and vibrational states, instead using the exact eigenstates of the Hamiltonian $\psi^{m}_{exact}(r,q)$. To visualize these eigenstates, one can factor the wavefunction using Hunter's exact factorization, which, like the adiabatic approximation, separates each eigenfunction into a marginal vibrational probability amplitude and a conditional electronic factor [22, 23]. This approach has been useful for nonadiabatic problems [24-26] and has been extended to treat dynamics nonadiabatically [27, 28]. Hunter's factorization separates the total eigenfunction into a marginal vibrational factor $\text{þ}_{\text{m}}(q)$ and a conditional electronic factor $\text{K}_{\text{m}}(r;q)$. The term $\text{þ}_{\text{m}}(q)$ gives total amplitude over all electronic states as a function of nuclear coordinates by

$$\text{þ}_{\text{m}}(\text{q})=\sqrt{\int \psi^{m}_{exact}{}^{*}(r,q)\psi^{m}_{exact}(r,q)dr} \qquad (1.14)$$

The probability amplitude is the square root of the total probability density for vibronic state m at nuclear coordinates q integrated over all electronic coordinates r or, equivalently, summed over an orthonormal basis of electronic states. Each probability density is nonnegative, necessitating that $\text{þ}_{\text{m}}(q)$ is greater than or equal to zero. The eigenfunction is specified by only one index m instead of the two indices of n and v in the adiabatic factorization because the vibrational and electronic portions of the wavefunction are inseparable [22, 23].

The electronic character $\text{K}_{\text{m}}(r;q)$ specifies the linear combination of electronic states on which probability amplitude is located. It is the vibronic eigenfunction divided by its magnitude, making it analogous to a unit vector indicating the eigenfunction's direction in electronic space for a set of nuclear coordinates. It is defined by

$$\text{K}_{\text{m}}(r;q)=\psi^{m}_{exact}(r,q)/\text{þ}_{\text{m}}(q) \tag{1.15}$$

Each conditional electronic factor is square-normalized as a function of the electronic coordinates r for every set of vibrational coordinates q on which it depends parametrically. The electronic character depends on m, meaning that each eigenfunction has a different coordinate-dependent electronic character. The electronic character $\text{K}_{\text{m}}(r;q)$ contains all sign information, including sign changes arising from the vibrational eigenfunction in the adiabatic approximation. This factorization is useful for measurements in which the total vibrational probability density matters more than the state of an individual electron, as in diffraction-type imaging experiments [29].

There are disadvantages to this approach, however. Unlike the products of adiabatic factorization, neither the sets of the probability amplitude functions nor the sets of the electronic

character functions are mutually orthogonal and complete. Further, $\mathrm{K}_{\mathrm{m}}(r;q)$ becomes undefined when $\chi_{\mathrm{m}}(q)=0$ due to the definition in Eq. (1.14) [22, 23]. These points of no probability amplitude across all electronic states are called nodes and have interesting properties.

Wherever the electronic character $\mathrm{K}_{\mathrm{m}}(r;q)$ is defined, it can represent the nonadiabatic eigenfunction using any complete set of electronic basis states. The most convenient sets of basis states are the vibrational-electronic adiabatic states previously discussed and the vibrational-electronic diabatic basis states. Diabatic electronic states diagonalize the nuclear kinetic energy operator, but this requirement does not uniquely define them [7]. In the models studied here, the diabatic states are chosen to have harmonic potentials, which makes the harmonic oscillator eigenstates an especially suitable vibrational basis. The diabatic approach remains valid where the adiabatic factorization fails. This diabatic basis will be used extensively in this study.

These diabatic basis states are used to represent the electronic character using an electronic angle. This electronic angle $\Theta_{\mathrm{m}}(q)$ gives the direction for unit vector $\mathrm{K}_{\mathrm{m}}(r;q)$ in the electronic coordinate system specified by the electronic basis. With only two electronic basis states (x and y), the electronic factor at each point in the vibrational coordinate space can be fully specified (in character and phase) by the electronic angle

$$\begin{aligned}\Theta_{\mathrm{m}}(q) &\equiv \mathrm{atan2}(\langle y|\psi_m\rangle, \langle x|\psi_m\rangle) \\ &= \mathrm{atan2}(\langle y|\mathrm{K}_{\mathrm{m}}\rangle, \langle x|\mathrm{K}_{\mathrm{m}}\rangle)\end{aligned} \tag{1.16}$$

where atan2 returns angles over a 2π range [30]. Representing the positive vibrational factor by amplitude contours and the signed electronic factor by color (a colored exact factorization), real-valued nonadiabatic eigenfunctions can be completely visualized with a single map [30].

1.3. The Appearance of Nodes

Nodes with $\chi_m(q)=0$ require the exact eigenfunction have no probability density on any electronic basis state at vibrational coordinates q because total probability density is the sum of probability density on each basis state and probability density is always real and non-negative. While exploring diatomic molecules, such as the diatomic hydrogen case discussed earlier, Czub and Wolniewicz concluded that Hunter's factorization over one vibrational coordinate with an infinite set of coupled electronic states must produce a nodeless vibrational amplitude [31]. Such a nodeless eigenstate can be seen in Figure 1.1.

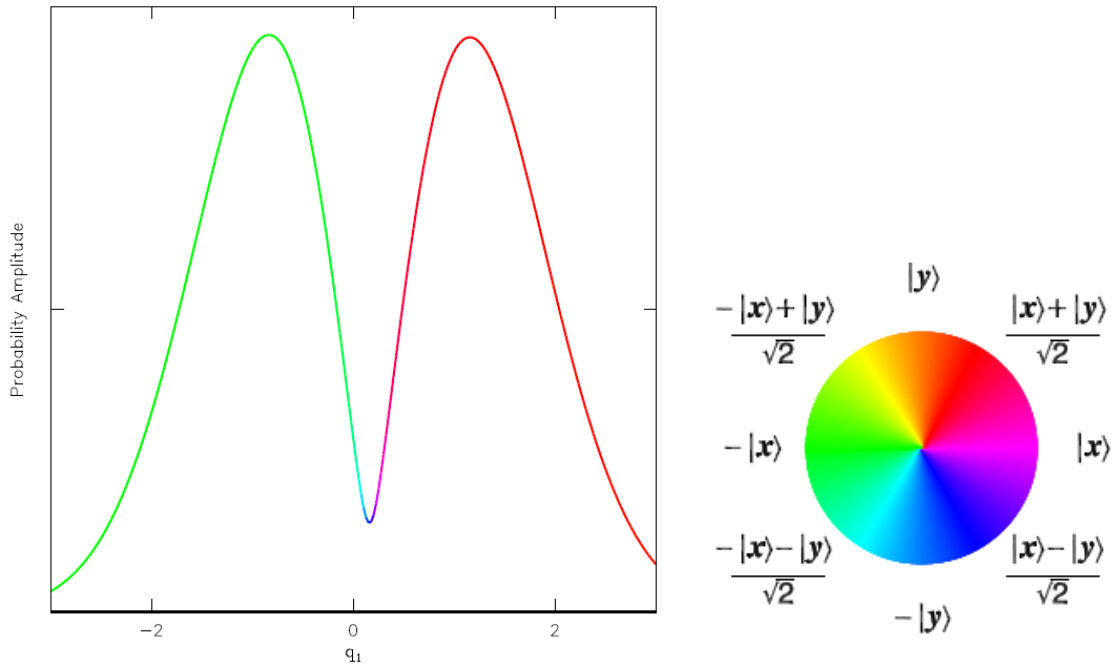

Figure 1.1: Left) The probability amplitude of a one-dimensional eigenstate which is dominated by the $v=1$ vibration on state $|x\rangle$, represented in green (negative amplitude) and red (positive amplitude), but is coupled to the $v=0$ vibration on state $|y\rangle$, represented in blue, which peaks through near where the amplitude on $|x\rangle$ is 0. Right) Color wheel used to indicate electronic eigenfunctions for adiabatic potential surfaces and the nonadiabatic factor K_m throughout the rest of this thesis. The 2π angular range is divided into 64 discrete colors for figures.

Figure 1.1 shows the vibrational probability amplitude for an eigenstate that is dominated by a $v=1$ vibration on one electronic basis state (represented with green for negative amplitude and red for positive amplitude) and where there is no vibrational amplitude from that electronic state near $q=0.1$ there is vibrational amplitude from another electronic basis state (represented in blue). This amplitude peaks through where the first electronic state has a minimum, meaning that there is no node unless all electronic states have the same node. In a higher number of vibrational dimensions with more normal mode vibrations, however, nodes can be observed [30].

While exploring photosynthetic energy transfer between chromophores in a dimer loosely modelled on the FMO antenna complex of green sulfur bacteria, the exact nonadiabatic eigenfunctions were mapped over two normal mode vibrations. The eigenfunction shown in Figure 1.2 suggests that the nonadiabatic eigenfunctions have zero-dimensional minima rather than the nodal curves found in the adiabatic approximation. It will be shown in Chapter 2 that these minima are point nodes. Two of these nodes can be observed in Figure 1.2 where the height of the plot represents $\þ_{\mathrm{m}}(q_A,q_B)$ and color represents electronic character as calculated using Eq. (1.16) and using a color wheel similar to that on the right of Figure 1.1.

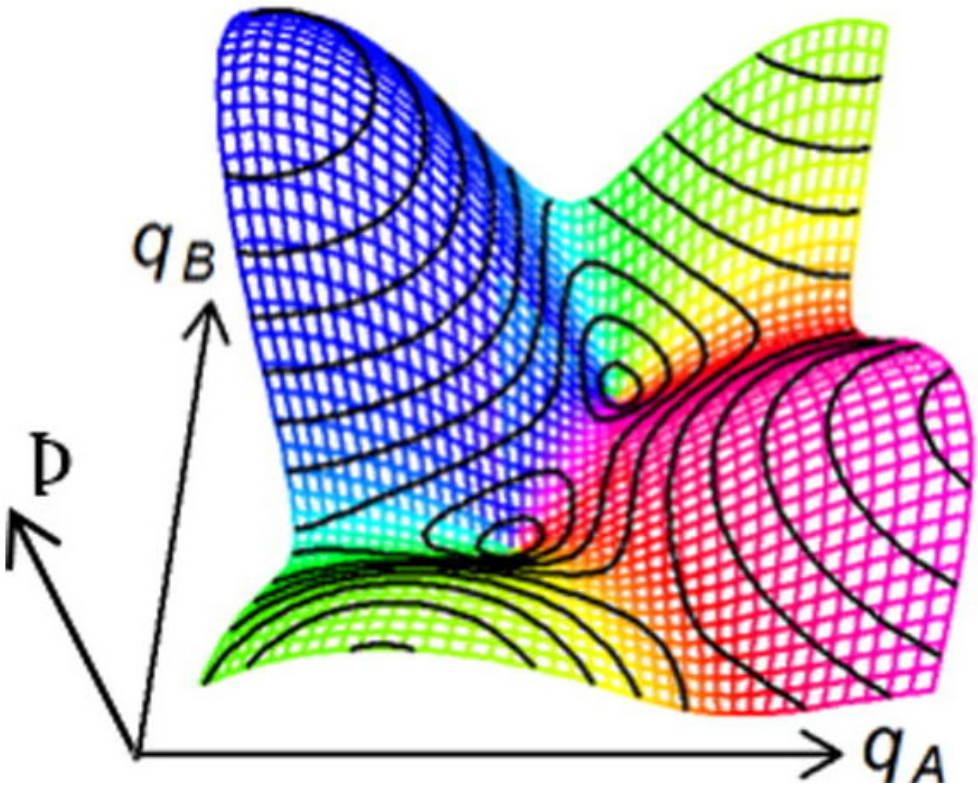

Figure 1.2: A three-dimensional picture of one eigenfunction of a dimer Hamiltonian over a selected coordinate range that includes two nodes. The height of the plot represents $\text{Þ}_{\text{m}}(q_A,q_B)$ and color represents $\text{K}_{\text{m}}(r;q_A,q_B)=0$ where color corresponds to the electronic angle $\Theta_m(q_A,q_B)$ using a color wheel similar to that on the right of Figure 1.1. The nodes are the points where $\text{Þ}_{\text{m}}(q_A,q_B)$ reaches a minimum.

These nodes were observable due to the relative number of electronic states and vibrational modes included. For each coupled electronic state with finite probability density, there is probability density at all vibrational coordinates except where regions of positive amplitude and negative amplitude interface. As discussed earlier with adiabatic electronic eigenfunctions, the dimensionality of the surface at the interface between the positive and negative regions will be one less than the dimensionality of the space. For instance, over two vibrational modes the vibrational amplitude on each electronic basis state will have one-

dimensional nodal curves between positive and negative regions. If there are two coupled electronic states, the maximum likely dimensionality of the overall node is the intersection of the two nodal curves from the two electronic states, which is a zero-dimensional point where the two nodal curves could cross. To generalize this, over M_v vibrational modes the vibrational amplitude on each electronic basis state will have $(M_v - 1)$-dimensional nodal hypersurfaces between positive and negative regions. If there are N_e coupled electronic states, the maximum likely dimensionality of the nodal surface is the intersection of the N_e nodal hypersurfaces from the N_e electronic states, which is $(M_v - N_e)$-dimensional [30]. When this nodal dimensionality is non-negative, nodes can occur by "accident". For adiabatic states, this reasoning reproduces the $M_v - 1$ dimensionality of the adiabatic vibrational nodes mentioned previously. The structure of this argument parallels the widely-used dimensional argument that conical intersections can occur by "accident" [2, 8, 32-35].

Given enough coupled electronic states, N_e will be greater than M_v and nodes are unlikely unless required by symmetry [30]. As a result, nodes in the dominant adiabatic wavefunction are avoided by a continuous change in electronic character in which a nonadiabatically coupled state "peeks through" at and around the node on the dominant state. In principle, the nodes in ref. [30] do not contradict this argument that true vibrational nodes are absent for an infinite number of coupled electronic states. In practice, it suggests observable weakly avoided vibrational zeroes of low dimensionality in the total vibrational probability density as may be seen in the interactions in refs. [23, 31].

1.4. The Jahn-Teller Conical Intersection

It is natural to wonder if these nodes that can occur for a finite number of coupled electronic basis states in areas with nonadiabatic dynamics would occur at locations with high symmetry and significant nonadiabatic effects, such as at conical intersections. These conical intersections between potential energy surfaces were noted by von Neumann and Wigner who examined the dimensionality of potential energy surfaces with an approach analogous to the preceding discussion of the dimensionality of nodal surfaces [2]. They saw that for polyatomic molecules, potential energy surfaces were likely to intersect, causing a breakdown of the adiabatic approximation. These intersections between surfaces will have the geometry of an elliptical cone or a higher dimensional analogue [2]. Jahn and Teller later proved that around high symmetry points, degenerate electronic states in many point groups would have a linear splitting of their orbital degeneracy [3]. This lowers their symmetry and forms a conical intersection around the high symmetry geometry. A Jahn-Teller conical intersection between two potential energy surfaces can be seen in Figure 1.3.

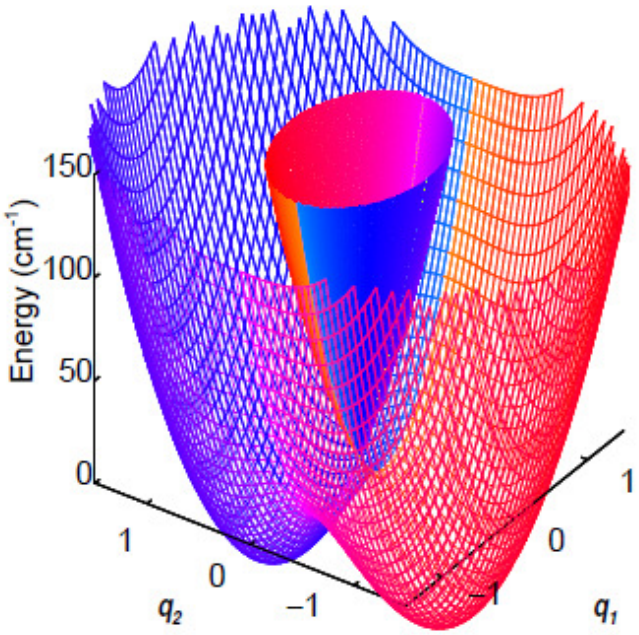

Figure 1.3: Adiabatic potential energy surfaces where they intersect at a Jahn-Teller conical intersection as a function of Jahn-Teller active normal coordinates (q_1, q_2) where the lower state is shown as a mesh and the upper state is shown as a solid surface. The shape of the intersection is a cone with the lower state reaching a peak where the upper reaches the bottom of the cone. The potential energy surfaces are continuous through the conical intersection. In this generic Jahn-Teller case, there is no circular symmetry and there are different minima along the different axes with the minima along q_1 occurring at $q_1 = \pm 0.4$ with energies of -16 cm^{-1} relative to the energy of the conical intersection and the minima along q_2 occurring at $q_2 = \pm 0.8$ with energies of -64 cm^{-1}. The cross-sections of the potential energy surfaces are exactly ellipses. The color of each potential surface at each coordinate indicates the adiabatic electronic character according to the color wheel on Figure 1.1. The geometric phase can be seen at the intersection of blue and orange along $q_2 = 0$ for $q_1 < 0$ on the upper state and along $q_2 = 0$ for $q_1 > 0$ on the lower state. The adiabatic potential surfaces have continuous coloring through the conical intersection and a sign-change discontinuity or cut (arbitrarily located along $q_2 = 0$) that is required by the geometric phase.

In Figure 1.3, there is a color discontinuity between orange ($+|y\rangle$ character) and blue ($-|y\rangle$ character) along the $q_2 = 0$ line. This geometric phase, first discovered by Longuet-

Higgins [6, 36] and further explored by Berry [37] and by Simon [38], is accumulated by circuiting the conical intersection once on an adiabatic eigenfunction, accounting for a sign change in the electronic character. Even in the adiabatic limit, where vibrational eigenfunctions do not approach the conical intersection, this generates half-odd integer "pseudo-rotation" quantum numbers for vibrations that circle the conical intersection [39, 40].

The potential energy surfaces in Figure 1.3 are continuous through the conical intersection, meaning that any path that approaches the conical intersection on one adiabatic state (lower or upper surface) and then continues through on the other adiabatic state will be continuous in energy and slope and will maintain its electronic character [36]. The geometric phase discontinuity at $q_2 = 0$, then, also continues through the conical intersection from positive q_1 on the upper state to negative q_1 on the lower state.

Using two diabatic states $\{|x\rangle, |y\rangle\}$ and dimensionless normal coordinates, the circularly symmetric Jahn-Teller conical intersection has the Hamiltonian (divided by $\hbar$)

$$\begin{aligned}\hat{\mathbf{H}} &= [(1/2)\omega(\hat{p}_1^2 + \hat{q}_1^2) + (1/2)\omega(\hat{p}_2^2 + \hat{q}_2^2)]\hat{\mathbf{I}} \\ &\quad + \omega d\hat{q}_1[|x\rangle\langle x| - |y\rangle\langle y|] + \omega d\hat{q}_2[|x\rangle\langle y| + |y\rangle\langle x|]\end{aligned} \tag{1.17}$$

where ω is the vibrational frequency, $\hat{q}_i$ and $\hat{p}_i$ are the dimensionless normal coordinate position and momentum operators (i = 1 or 2) for asymmetric vibrations, $\hat{\mathbf{I}} = |x\rangle\langle x| + |y\rangle\langle y|$ is the electronic identity operator, and d is the vibrational displacement, related to the Jahn-Teller stabilization energy by $(D\omega) = (1/2)\omega d^2$. The first line of the equation is an isotropic two-dimensional harmonic oscillator Hamiltonian and the second line contains the vibrational-

electronic couplings with q_1 being the tuning coordinate controlling the on-diagonal splitting and q_2 being the coupling coordinate controlling their off-diagonal coupling.

Moffit and Liehr studied Jahn-Teller conical intersections with circular symmetry and were intrigued by the limit of low barriers to the conical intersection where the electronic and vibrational effects are of similar magnitude, where they calculated coupling between nuclear modes and low-frequency electronic motions [41]. Later, Longuet-Higgins *et al.* analyzed the adiabatic limit for the same model [36], discovering a precursor to Berry's geometric phase [37, 38] by revealing the adiabatic sign discontinuity and the half-odd-integer quantum number (j here) for what is now called pseudo-rotation [40].

Studying the Jahn-Teller conical intersection for a variety of stabilization energies, Thompson, Mead and Truhlar showed that as stabilization energy varies, the nonadiabatic eigenfunctions switch between residing mainly on the lower "hat" adiabatic state and the upper "cone" adiabatic state as shown in Figure 1.4, which is a reproduction of Figure 8 in ref. [7].

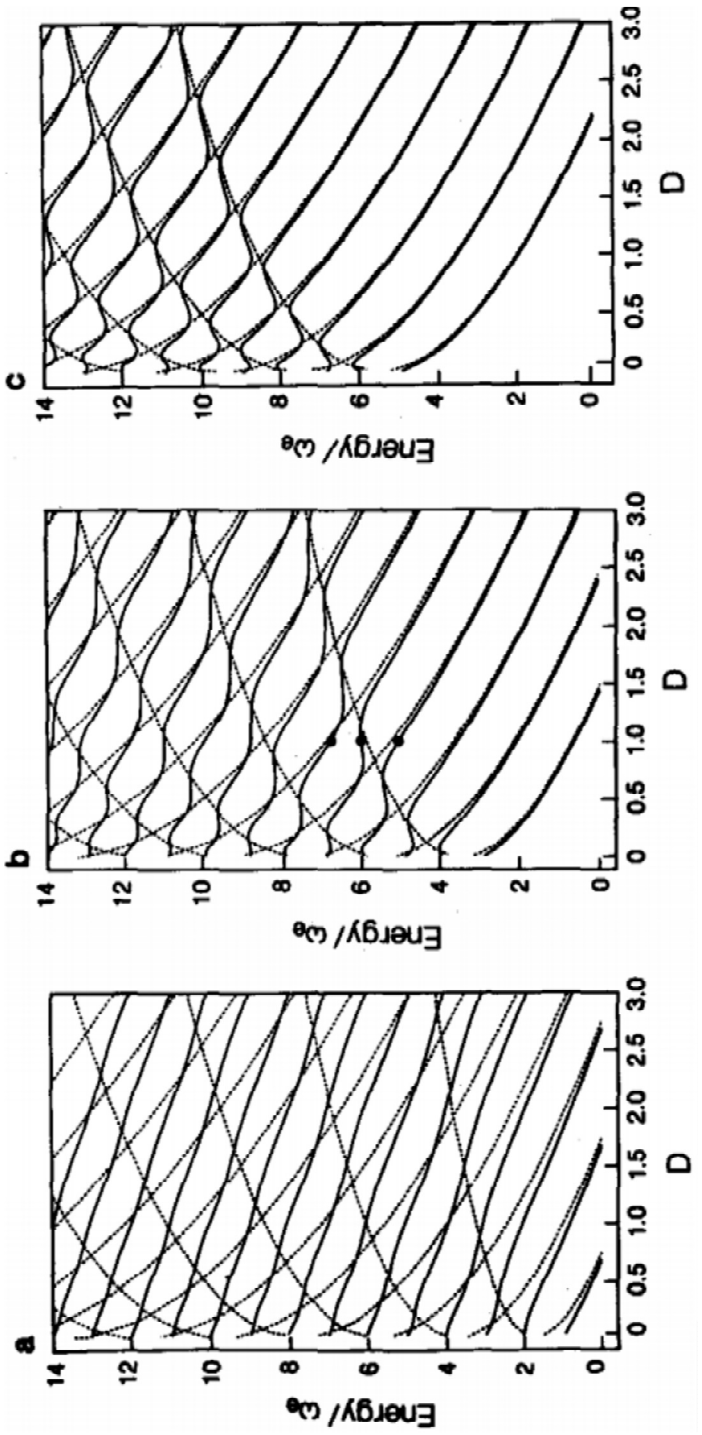

Figure 1.4: The energies of adiabatic states (shown with dashed curves) and nonadiabatic states (shown with solid curves) as a function of the Moffitt-Thorson parameter D, which is $(D\omega)/\omega$ as used here. The three panels show pseudo-rotation quantum numbers of (a) $j = 1/2$, (b) $j = 5/2$, and (c) $j = 9/2$. The three dots in part (b) identify states plotted in Figure 9 in ref. [7]. Reproduced with permission from J. Chem. Phys. 82, 2392 (1985). Copyright 1985, American Institute of Physics.

As can be observed in panel (c) of Figure 1.4, the energy of each nonadiabatic state alternates between following a downward sloping curve, representing the energy of a vibrational state on the lower energy adiabatic state (the "hat"), and following an upward sloping curve, representing the energy of a vibrational state on the higher energy adiabatic state (the "cone"). Each nonadiabatic state eventually settles onto the lower adiabatic state for large enough stabilization energy. As the nonadiabatic eigenstate energies approach each intersection between the energies of vibrational states on the two adiabatic states, Figure 1.4(c) reveals that the energies of the nonadiabatic states deviate from the adiabatic states to avoid the intersection and remain non-crossing. In Figure 1.4(b) the intersections are more strongly avoided so they barely alternate between adiabatic states and in Figure 1.4(a) the intersections are so strongly avoided that avoided crossings are not apparent.

Figure 1.5 compares the energies of all eigenstates up to $v = 4$ over a small range of Jahn-Teller stabilization energies. The different colored points represent different values of the pseudo-rotation quantum number j. These colors highlight that, while there are strongly avoided crossings between states with the same value of their pseudo-rotation quantum number, states with different j-values cross one another. All states start on the left in the small stabilization energy limit and, by the time they reach the right, the lower states have energies that trend downward, indicating they have started to converge to their adiabatic energies. It should be noted that while several of these crossings happen at similar values of $(D\omega)$, a closer look reveals that no two crossings happen for the exact same value of the stabilization energy. Thorson and Moffitt reported a similar pattern for an octahedral symmetry three-dimensional Jahn-Teller conical intersection [42].

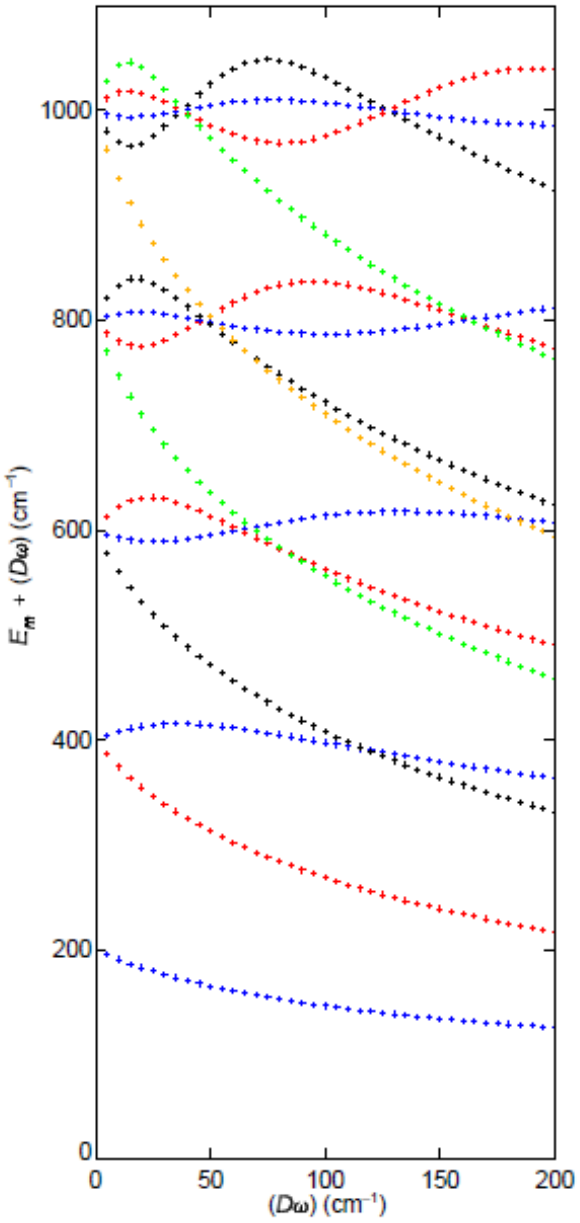

Figure 1.5: The shifted energies $E_m + (D\omega)$ of eigenstates with a small Jahn-Teller stabilization energy vibrational quantum number $v = 0$, 1, 2, 3, or 4 as a function of Jahn-Teller stabilization energy $(D\omega)$ from 0 cm^{-1} to 200 cm^{-1} where $\omega = 200$ cm^{-1}. Eigenstates with different j quantum numbers cross starting between 25 cm^{-1} and 100 cm^{-1}, changing the energetic ordering of the quantum numbers. The marker color indicates the pseudo-rotation quantum number with $j = 1/2$, $3/2$, $5/2$, $7/2$, and $9/2$ being represented as blue, red, black, green, and orange respectively. This figure is consistent with Fig. 8 of ref. [7] as shown in Fig. 1.4, but shows results for more pseudo-rotation quantum numbers over a smaller range of energies and stabilization energies.

The eigenfunctions can be plotted as well and, using Hunter's factorization, the real-valued nonadiabatic eigenfunctions can be completely visualized with a single map [30]. This is shown by representing the positive vibrational factor $\wp_m(q)$ by amplitude contours and the signed electronic factor using color (a colored exact factorization) where color corresponds to the electronic angle $\Theta_m(q)$ as shown in Figure 1.1. This colored exact factorization is used to create Figure 1.6.

The eigenfunctions for a D_{4h} symmetry Jahn-Teller conical intersection such as is shown in Figure 1.3 are doubly degenerate, however, and thus require a greater level of specification to make them uniquely defined. This consideration also applies to the circularly symmetric conical intersection given by Eq. (1.17) which is a special case of D_{4h} symmetry. This degeneracy arises from the Hamiltonian separately commuting with two mutually non-commuting reflection operators σ_v and σ_d [43]. Eigenstates can be chosen so that they are simultaneously eigenstates of the Hamiltonian and of either reflection operator, so for Figure 1.6, σ_v will be arbitrarily chosen to be +1.

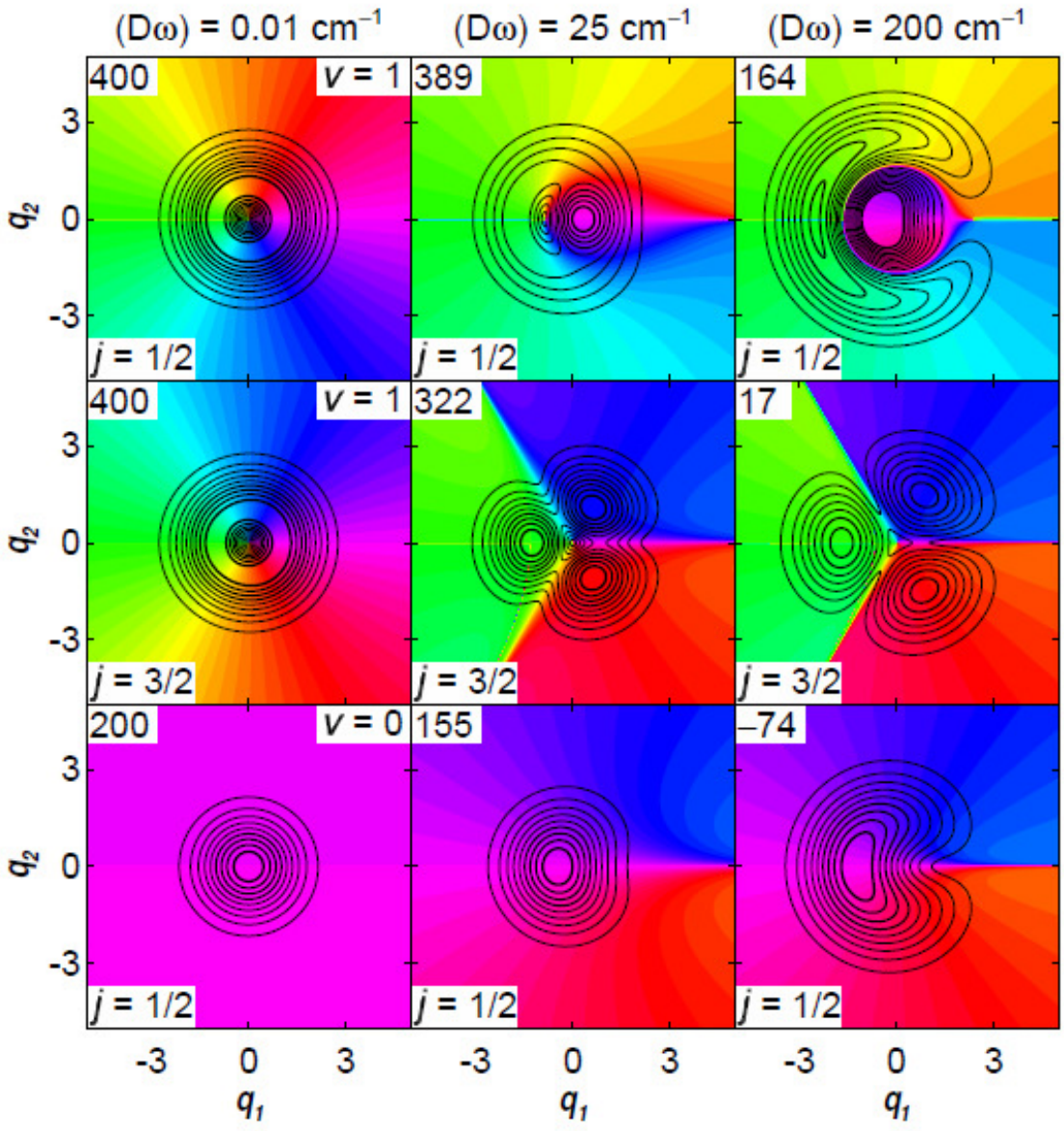

Figure 1.6: The $\sigma_v = +1$ eigenfunctions correlating to the three lowest energy eigenvalues for the limit of small displacement. The left column shows $(D\omega) = 0.01$ cm^{-1} with energies (upper left) and quantum numbers (pseudo-rotation at lower left and vibrational at upper right) labelled. The next two columns show the eigenfunctions to which they correlate for $(D\omega) = 25$ cm^{-1} and $(D\omega) = 200$ cm^{-1}, also labelled with their energies (upper left) and pseudo-rotation quantum numbers (lower left). For each eigenstate, the contour lines show 10% intervals of its maximum probability amplitude and color shows electronic character from the color wheel in Fig. 1.1. For $(D\omega) = 200$ cm^{-1}, the zero point level is energetically below the conical intersection at $E = 0$.

In Figure 1.6, there are electronic singularities where all the colors appear to converge to a single point. For instance, both 400 cm^{-1} states in the left column have such a singularity near the origin. As the stabilization energy increases from left to right, the singularity in the $j = 3/2$ eigenstate remains at the origin while the singularity in the $j = 1/2$ eigenstate moves to the left. These electronic singularities are nodes. They have amplitude beneath the lowest contour of ρ_m and when the point is crossed electronic character changes sign and therefore color changes. The tremendous difference in the coordinate-dependent electronic characters between eigenstates is also a nonadiabatic effect.

Stabilization energy increases in Figure 1.6 from near the limit of low stabilization energy to an energy that starts to approach the adiabatic regime. The eigenfunctions of the circularly symmetric Jahn-Teller conical intersections can be understood through three parameter regimes with simple expressions for the energy eigenvalues [36]. The half-odd integral pseudo-rotation quantum number *j* is rigorously conserved across all three parameter regimes. For small Jahn-Teller displacements, as in the left column of Figure 1.6, the 2D harmonic oscillator vibrational quantum number *v* is good and the energy levels are well approximated by perturbation theory [30, 36]. The perturbation theory expression involves three quantum numbers: the 2D harmonic oscillator vibrational quantum number v and vibrational angular momentum l, plus an electronic angular momentum $\lambda = \pm 1$ that couples with l to give the pseudo-rotation quantum number $j = l + \lambda/2$. The energy eigenvalues are given by [30]

$$E = \omega(v+1) - 2(D\omega)[l\lambda + 1] \tag{1.18}$$

As *d* increases, all three electronic and vibrational quantum numbers (v, l, λ) break down through $j-$ conserving avoiding crossings [7, 42]. Before a level undergoes its first avoided crossing (as

shown in Figure 1.5), the small Jahn-Teller displacement quantum numbers (v,$|j|$) remain good. For larger displacements, the lower eigenvalues approximate those of a radial potential $V(r) = (1/2)\omega(r-d)^2$ with half-odd integral pseudo-rotation quantum numbers. In this regime, the eigenvalues are

$$E = \omega(p+1/2) - (D\omega) + \omega j^2 / 2d^2 \tag{1.19}$$

where the radial vibrational quantum number p is a nonnegative integer (Eq. (6.16) of ref. [36] defines p differently). Since radial curve crossing between the lower and upper adiabatic potentials is unhindered at the origin in this model, it has diabatic aspects. At very large displacements, the low energy eigenstates become vibrational eigenstates of the lower adiabatic potential (the hat) and the $\omega j^2 / 2d^2$ term in the energy tends to zero. [36]

For any given vibrational eigenstate of the hat, increasing $(D\omega)$ involves a finite number of avoided crossings. After a level's last avoided crossing, its adiabatic quantum numbers $(p,|j|)$ become good. Since the vibronic eigenstates of the upper adiabatic potential (the cone) are embedded among the higher energy vibrational eigenstates of the hat, an endless series of avoided crossings prevents convergence to adiabatic behavior as the Jahn-Teller displacement increases [7]. Nonetheless, for specific Jahn-Teller displacements, some eigenstates are predominantly on the cone as can be seen in Figure 1.4. For instance, in panel (c) when D=0.7 the fifth, seventh and ninth lowest energy eigenstates are on the upper adiabatic state [7].

The eigenvalues shown in Figure 1.5 match these perturbation theory results closely for small Frank-Condon displacement, but, partially as a result of the avoided crossings, the eigenvalues deviate significantly before the displacement nears the first avoided crossing at

about $(D\omega) = 20\ \text{cm}^{-1}$. This can be seen in Table 1.1 where the energy eigenvalues can be seen for different stabilization energies and significant deviations from perturbation theory start appearing at $(D\omega) = 20\ \text{cm}^{-1}$.

quantum numbers		($D\omega$)									
v	*j*	0.01	0.1	1	5	10	20	25	100	200	
0	1/2	199.9800010	199.8000999	198.0098688	190.2345894	180.8852197	163.1910822	154.7574362	46.6061807	-73.7859940	
1	3/2	399.9600060	399.6005980	396.0580798	381.2923974	364.5731170	335.0305057	321.6418171	168.7828555	17.2671417	
1	1/2	399.9999980	399.9998001	399.9801320	399.5159235	398.1230803	392.9417455	389.3133507	297.5589610	163.7523481	
2	5/2	599.9400150	599.4014921	594.1424975	572.9944266	550.1009057	511.2955166	494.1690670	307.9879554	131.6875166	
2	1/2	599.9800030	599.8002996	598.0296077	590.7043291	582.6614783	569.6008450	564.2879215	513.8908239	406.9487443	
2	3/2	600.0199910	600.1991016	601.9115212	607.9087655	612.0584631	610.7046816	606.0653107	463.0188545	290.3043903	
3	7/2	799.9200280	799.2027797	792.2611778	765.2184782	736.9566285	690.3782006	670.1563969	456.2648409	258.7277687	
3	3/2	799.9600120	799.6011968	796.1169656	782.6851919	769.9113345	755.1222116	751.9287670	736.6262814	573.1944144	
3	1/2	799.9999960	799.9996005	799.9605281	799.0637526	796.4920997	787.7072007	782.0368055	686.9145459	611.7052511	
3	5/2	800.0399800	800.3980066	803.8061504	815.5789753	823.4707357	819.5245466	810.4516741	621.8937900	423.5380654	
4	9/2	999.9000450	999.0044585	990.4123444	957.8767217	924.8294054	871.4593970	848.5476785	610.4334811	394.0125835	
4	5/2	999.9400250	999.4024894	994.2401772	975.3227891	959.3707684	948.4111889	950.2219848	931.1953281	724.0902474	
4	1/2	999.9800050	999.8004991	998.0490837	991.1427385	984.1984686	974.2497094	970.5318674	907.1866038	785.8979899	
4	3/2	1000.0199850	1000.1985032	1001.8530587	1006.5811274	1007.3603971	996.8391462	987.9611519	875.6301918	838.9537022	
4	7/2	1000.0599650	1000.5965175	1005.6659411	1022.6321968	1032.6236953	1020.7371170	1006.0433060	781.8296853	562.8087185	

Table 1.1 (caption on next page)

Table 1.1 (on previous page)**:** Energy eigenvalues E_m for the nonadiabatic Hamiltonian in Eq. (1.17) with the quantum numbers in the left-hand column for nine Jahn-Teller stabilization energies with $\omega = 200$ cm^{-1}. All energies reported here are converged for all decimal places reported. For $(D\omega) = 100$ cm^{-1} and $(D\omega) = 200$ cm^{-1}, the eigenvalues are not ordered energetically and are not the fifteen lowest eigenvalues.

The overall accuracy of the calculated eigenvalues can be shown through a comparison with the results of Judd's 1979 paper in which he found *isolated* analytic eigenvalues of Jahn-Teller conical intersections for *particular* values of the stabilization energy [44]. The eigenvalues in these cases were calculated numerically and quantitatively compared with the analytical results [45]. Table A.1 in Appendix A shows the quantitative comparison for the eigenvalues while the exact factorization of the corresponding eigenfunctions is seen in Figure 1.7.

This comparison confirms 14-digit numerical accuracy in the eigenvalues with error only occurring in the final numerical digit on the order of 10^{-12} cm^{-1} for eigenvalues of order 10^{2} cm^{-1}. It should be noted that all of the states in Figure 1.7 reside primarily on the lower adiabatic potential. This is evidenced by the color of the eigenfunctions indicating that they either have the same or sign-inverted electronic character of the lower adiabatic surface.

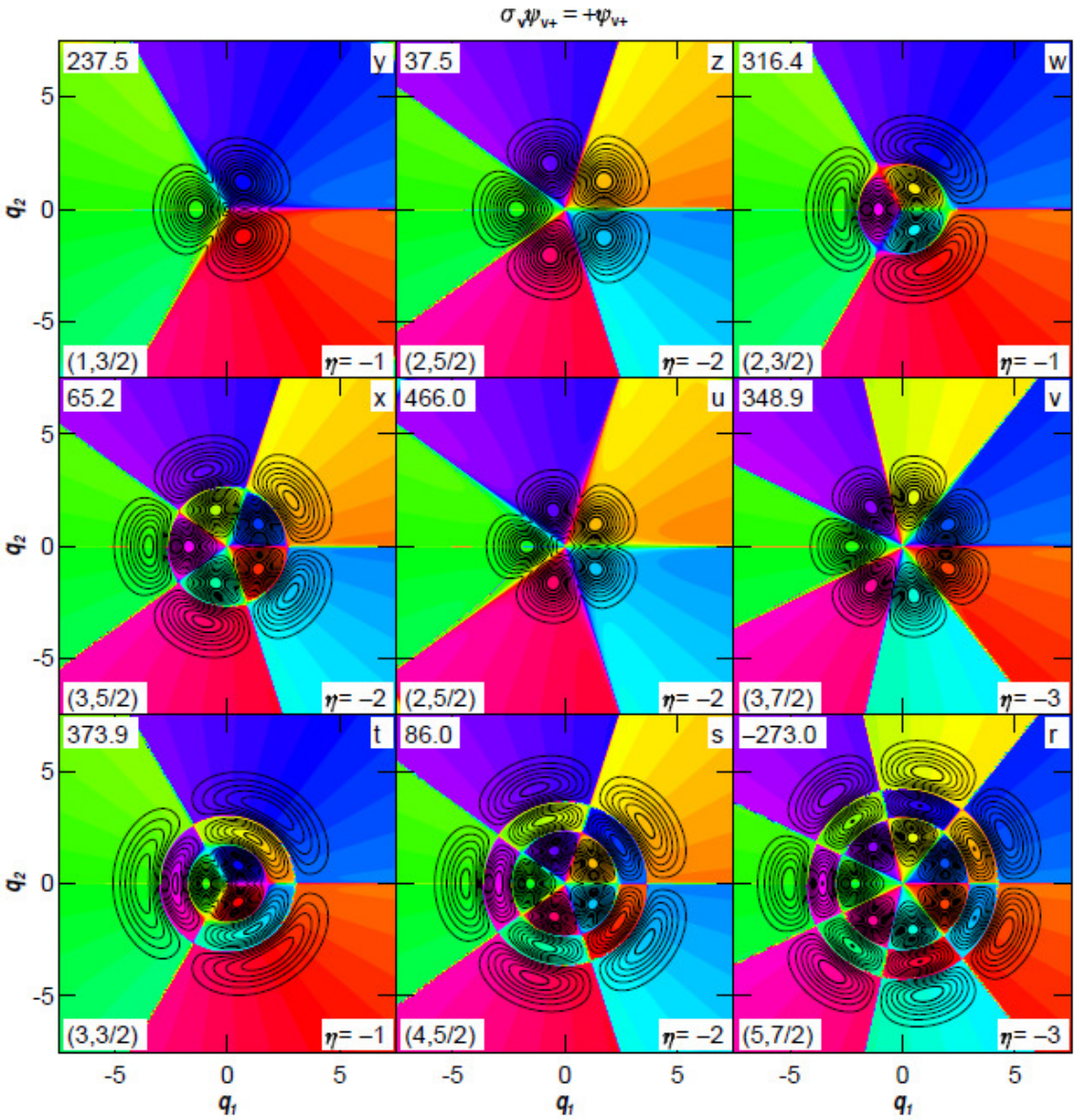

Figure 1.7: The nine panels here show the nonadiabatic eigenfunctions for the $\sigma_v = +1$ eigenstates with exact eigenvalues in Table A.1. For each eigenfunction, the energy eigenvalue (in cm^{-1}) is given at upper left, Judd's label at upper right, the small Jahn-Teller displacement circular quantum numbers (v, $|j|$) from Table A.1 at lower left, and the electronic index around the perimeter at lower right. The v quantum number is assigned based on eigenfunction appearance so that $v - (|j| - 1/2)$ gives the number of radial nodes (such assignments jump through avoided crossings). In each panel, the contour interval is 10% of the maximum probability amplitude for that state, with thicker contour lines for higher amplitude. The color wheel in Figure 1.1 is used to represent electronic character. Note that each eigenfunction in this figure arises from a different Hamiltonian, which is specified in Table A.1 according to the label at upper right. Comparing the angular dependence of the eigenstate colors to those for the lower adiabatic electronic state in Figure 1 of ref. [30] indicates that all of these eigenstates are predominantly on the lower adiabatic potential surface (the hat state).

1.5. The Elliptical Conical Intersection

The analysis of Jahn-Teller conical intersections up until this point have been for circularly symmetric conical intersections. A key result is that eigenstates with $|j| \geq 3/2$ have nodes at the origin, where the conical intersection is located [20]. This can be seen for the $j = 3/2$ state in Figure 1.6. Which aspects of these results arise from the symmetry and which aspects are true for all Jahn-Teller conical intersections? To assess this, it is necessary to study a more general case: the elliptical conical intersection.

An elliptical Jahn-Teller conical intersection is pictured in Figure 1.3. It does not have circular symmetry as the minima along the q_1 axis are at a different distance from the origin than the minima along the q_2 axis. When the circular symmetry is broken as pictured in Figure 1.3, there is no angular momentum symmetry and therefore no pseudo-rotation quantum number. In fact, for stabilization energies far from the adiabatic limit, the lower adiabatic potential has two wells separated by two saddle points and there are no good quantum numbers at all.

One way to break angular momentum symmetry is by making the Frank-Condon displacements along the two normal mode vibrations unequal. The energy eigenvalues of such an elliptical conical intersection are shown in Figure 1.8. Avoided crossings can be observed between all states regardless of the pseudo-rotation quantum number at circular symmetry. These results are also tabulated in Table 1.2 where eigenvalues are shown for Jahn-Teller conical intersections with one stabilization energy fixed and the other varying.

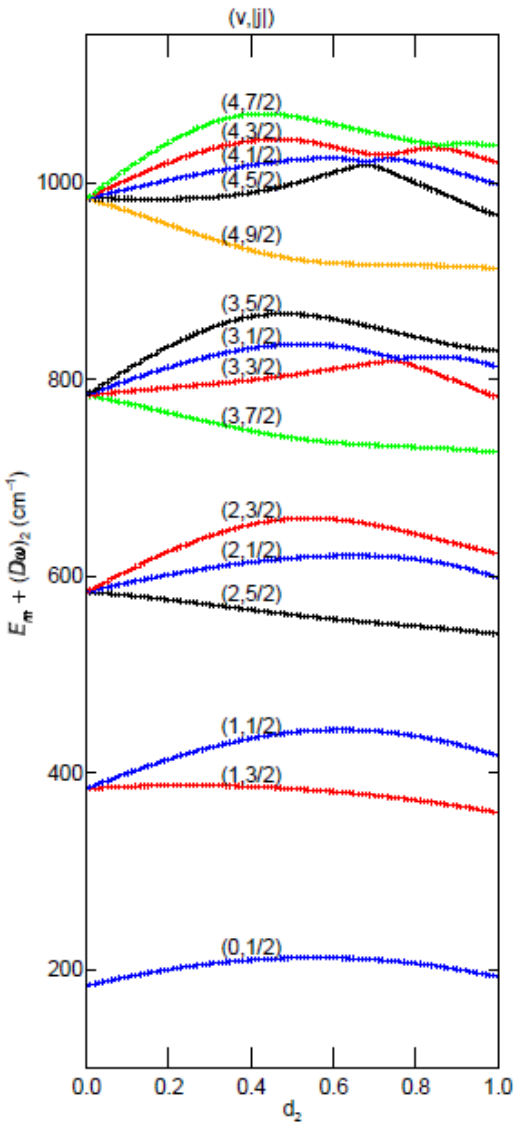

Figure 1.8: The energy eigenvalues for the 15 lowest pairs of eigenstates are shown for the Jahn-Teller Hamiltonian with $\omega_1 = \omega_2 = 200$ cm^{-1} and $d_1 = 0.4$ as a function of d_2 from 0 to 1 (step size is 0.01). To show relative trends more clearly, the vertical axis is the sum of the eigenstate energy E_m and the Jahn-Teller stabilization energy $(D\omega)_2 = (1/2)\omega_2 d_2^{\,2}$. The quantum numbers v and $|j|$ for the eigenstates are specified at $d_2 = 0.4$ where the conical intersection has circular symmetry and the pseudo-rotation quantum number j is rigorous. The marker color indicates the correlation to $|j|$ at circular symmetry: blue for $|j| = 1/2$, red for $|j| = 3/2$, black for $|j| = 5/2$, green for $|j| = 7/2$, and orange for $|j| = 9/2$. Several avoided crossings can be seen, including weakly avoided crossings between eigenvalues labelled (4,5/2) and (4,1/2); (4,1/2) and (4,3/2); (4,3/2) and (4,7/2); (3,3/2) and (3,1/2); crossing between (3,1/2) and (3,5/2) appears to be more strongly avoided. The quantum numbers characteristic of each eigenfunction can be determined by pretending each weakly avoided crossing is an actual crossing, so the quantum numbers do not necessarily correlate with marker color beyond $d_2 = 0.6$.

Quantum Numbers in Circular Symmetry		Numerical Energy Eigenvalues (cm^{-1}) for $\omega_1 = \omega_2 = 200\ cm^{-1}$, $d_1 = 0.4$ and d_2 specified					
v	j	$d_2 = 0$	$d_2 = 10^{-10}$	$d_2 = 0.2$	$d_2 = 0.4$	$d_2 = 0.6$	$d_2 = 0.8$
0	1/2	184.000000000000	184.000000000000	180.565095246248	170.125283738329	152.320722683800	126.694700417582
0	1/2	184.000000000000	184.000000000002	180.565095246250	170.125283738333	152.320722683800	126.694700417582
1	3/2	383.999999999999	383.999999993183	367.541999592926	346.342118067196	321.269765036856	292.594240084540
1	3/2	384.000000000000	383.999999993183	367.541999592927	346.342118067199	321.269765036857	292.594240084542
1	1/2	384.000000000000	384.000000006818	394.141673298400	395.369313113912	384.064650690666	357.740380346399
1	1/2	384.000000000000	384.000000006819	394.141673298404	395.369313113912	384.064650690668	357.740380346402
2	5/2	583.999999999999	583.999999987410	556.252387494798	525.963160943148	496.590888122214	469.426835580456
2	5/2	584.000000000000	583.999999987410	556.252387494799	525.963160943152	496.590888122215	469.426835580458
2	1/2	584.000000000000	583.999999999997	581.692342934045	574.396095014677	560.788974834820	537.599367538494
2	1/2	584.000000000002	584.000000000000	581.692342934046	574.396095014679	560.788974834823	537.599367538495
2	3/2	584.000000000004	584.000000012592	604.984709138495	612.654738041824	598.069711514026	563.101895663671
2	3/2	584.000000000005	584.000000012593	604.984709138498	612.654738041825	598.069711514027	563.101895663671
3	7/2	783.999999999999	783.999999982460	746.286233909557	707.839312281093	676.047227088426	651.312249855972
3	7/2	784.000000000000	783.999999982461	746.286233909559	707.839312281098	676.047227088432	651.312249855975
3	3/2	784.000000000000	783.999999994458	771.634718813502	759.517876813196	750.750781167499	742.279607372564
3	3/2	784.000000000000	783.999999994459	771.634718813502	759.517876813199	750.750781167500	742.279607372565
3	1/2	784.000000000001	784.000000005540	792.356753806846	791.702492762055	774.365833853301	733.608848747555
3	1/2	784.000000000001	784.000000005541	792.356753806848	791.702492762055	774.365833853303	733.608848747557
3	5/2	784.000000000003	784.000000017538	813.756121342917	823.878877562159	801.595570372299	763.231620902958
3	5/2	784.000000000005	784.000000017539	813.756121342918	823.878877562160	801.595570372300	763.231620902963

Table 1.2 (caption on next page)

Table 1.2 (on previous page)**:** Numerical eigenvalues for the twenty lowest energy eigenstates of Jahn-Teller Hamiltonians with $\omega_1 = \omega_2 = 200$ cm^{-1}, $d_1 = 0.4$ and displacements d_2 tabulated above each column. These eigenvalues include all eigenstates of a circularly-symmetric conical intersection shown in this dissertation. Quantum numbers are assigned to eigenvalues based on eigenfunction appearance, which agrees with assignment based on continuous energy eigenvalue correlation except for $(v = 3, |j| = 3/2)$ and $(v = 3, |j| = 1/2)$ at $d_2 = 0.8$. Symmetry required degeneracies are maintained to 15 digits. The numerical eigenvalues for $d_2 = 0$ (accidental Born-Oppenheimer case) exhibit 15 digit accuracy vs. the analytic formula $E(v,v) = \omega(v + 1/2) + \omega(v + 1/2) - (D\omega)$ where $(D\omega) = (1/2)\omega d^2 = 16$ cm^{-1}. Numerical eigenvalues for $d = 10^{-10}$ match degenerate first order perturbation theory expressions for the v = 0, 1, and 2 energies to 15 digit accuracy.

While eigenfunctions with pseudo-rotation quantum number $|j| \geq 3/2$ have nodes at the origin for all stabilization energies when angular momentum symmetry is present due to circular symmetry [20], these nodes do not occur at the origin for an elliptical conical intersection [45]. This happens because these nodes at the origin result from angular momentum symmetry, so in systems without it, such as the elliptical conical intersection, no nodes are forced to occur at the origin and there will always be probability amplitude on the conical intersection [45]. This causes extremely awkward discontinuities in the projections onto adiabatic electronic states [18, 19].

1.6. Nonadiabatic Effects Far from a Conical Intersection

Nonadiabatic effects are not constrained to the vicinity of a conical intersection, however. As mentioned at the beginning of the chapter, while it is traditionally understood that nonadiabatic effects dominate near conical funnels and adiabatic effects dominate at all other regions of coordinate space, nonadiabatic effects can occur anywhere in vibrational space. A

precise calculation of the wavefunctions far from a Jahn-Teller conical intersection indicates that nonadiabatic effects may be more ubiquitous than previously imagined.

Both adiabatic potential energies become very large far from a Jahn-Teller conical intersection, so having probability density on low energy eigenstates at large radius is classically forbidden [11]. Any probability amplitude in this region is due to tunneling [46] and a one-dimensional analysis of adiabatic tunneling predicts that amplitude should be monotonically decreasing to zero with increasing radius [11]. A multi-dimensional analysis reveals a much more complicated picture with amplitude varying angularly as well as radially [47-49]. Prior work on multidimensional tunneling for a single adiabatic potential anticipates that angular nodes extend from the origin to infinite radius in the tunneling region where the potential energy is greater than the energy of the eigenstate. Recent work on nonadiabatic tunneling [50-53] has focused on the effects of the adiabatic sign change around the conical intersection.

A precise calculation with two vibrational dimensions helps extend our understanding by revealing that some eigenstates have zero-dimensional nonadiabatic nodes in the tunneling region where the projections of the nonadiabatic eigenfunction onto both adiabatic electronic basis states change sign. For these eigenstates, the projection of the eigenfunction onto the lower adiabatic electronic state features angular nodes extending to infinite radius and the projection of the eigenfunction onto the upper adiabatic electronic state features radial nodes in the tunneling region, which intersect to form nonadiabatic conical nodes. This observation of nonadiabatic nodes in the tunneling region conflicts with the adiabatic intuition that there should be no radial nodes perpendicular to the steepest ascent vector beyond the classical turning point.

These nodes in the tunneling region arise from conical intersections where $(D\omega)$ and ω are similar in magnitude. This is the region between the limits of $(D\omega) \ll \omega$ and $(D\omega) \gg \omega$ which can separately be well-understood. In the limit of $(D\omega) \ll \omega$, the $p = 0$ or $v = |j| - 1/2$ nonadiabatic eigenfunctions (lowest energy eigenstate for a given j) will not have any nodes except at the conical intersection because the projection onto the upper state and the projection onto the lower state will only have angular nodes. Except at the origin, the nodal curves in the projections cannot intersect to form nodes in the nonadiabatic eigenfunctions. In the limit of $(D\omega) \gg \omega$, the lowest energy eigenfunctions can be understood adiabatically. These adiabatic eigenfunctions have angular nodes and radial nodes and reside entirely on the lower adiabatic potential [18, 19, 54], but when $(D\omega)/\omega$ is finite there is still tunneling amplitude on the upper adiabatic state and this amplitude is continuous through the conical intersection with the amplitude on the lower adiabatic potential [24].

In the adiabatic limit, there are features in $p \geq 1$ nonadiabatic eigenfunctions that resemble avoided radial nodal curves. These occur because the projections onto both adiabatic electronic states have radial nodes at nearly the same radius. As stabilization energy decreases and the dynamics become more nonadiabatic, the radial nodes in the projection onto the upper adiabatic electronic state have been observed to move out to large radius, causing conical nodes deep in the classically forbidden region. Such nodes are accompanied by extrema in the radial projections. The annihilation of pairs of radial nodes has also been observed in projections onto the upper adiabatic electronic state. These behaviors do not occur in the Adiabatic Approximation. For electronically nonadiabatic systems, conical nodes in the vibrational

tunneling region are an indication of dynamics that could affect chemical reactions in which tunneling is important.

The adiabatic approximation makes the study of electronic and vibrational chemistry much easier and is essential for measurements in spectroscopy and other fields of study [21]. There are systems in which the approximation fails, however. Near areas of vibronic resonance or conical intersections, nonadiabatic effects are prominent [9, 20, 24, 30, 32]. Even in a tunneling region with minimal probability amplitude far from a conical intersection, nonadiabatic effects can be responsible for the creation of nodes. Using exact nonadiabatic calculations reveals interesting new features that would not otherwise be observed and which merit further study.

References

1. Born, M. and K. Huang, *Dynamical Theory of Crystal Lattices*. 1962, Oxford: Clarendon Press.

2. von Neumann, J. and E. Wigner, *Uber Das Verhalten Von Eigenwerten Bei Adiabatischen Prozessen.* Physik. Z., 1929. **30**(15): p. 467-470.

3. Jahn, H.A. and E. Teller, *Stability of Polyatomic Molecules in Degenerate Electronic States. I. Orbital Degeneracy.* Proc. R. Soc. of Lond. A, 1937. **161**(905): p. 220.

4. Landau, L.D., *Zur Theorie der Energieubertragung. II.* Physikalische Zeitschrift der Sowjetunion, 1932. **2**: p. 46-51.

5. Zener, C., *Non-Adiabatic Crossing of Energy Levels.* Proc. R. Soc. Lond. A, 1932. **137**(6): p. 696-702.

6. Longuet-Higgins, H.C., *The intersection of potential energy surfaces in polyatomic molecules.* Proc. R. Soc. Lond. A, 1975. **344**: p. 147-156.

7. Thompson, T.C., D.G. Truhlar, and C.A. Mead, *On the form of the adiabatic and diabatic representation and the validity of the adiabatic approximation for X3 Jahn-Teller systems.* 82, 1985. **5**: p. 2392-2407.

8. Klessinger, M. and J. Michl, *Excited States and Photochemistry of Organic Molecules*. 1995, New York: VCH Publishers.

9. Tiwari, V., W.K. Peters, and D.M. Jonas, *Electronic resonance with anticorrelated pigment vibrations drives photosynthetic energy transfer outside the adiabatic framework.* Proc. Natl. Acad. Sci. USA, 2013. **110**(4): p. 1203-1208.

10. Born, M. and R. Oppenheimer, *Zur Quantentheorie Der Molekeln.* Ann. Phys. (Berlin), 1927. **389**(20): p. 457-470.

11. Atkins, P.W. and R.S. Friedman, *Molecular Quantum Mechanics*. 3rd ed. 1997, New York: Oxford University Press.

12. Tully, J.C., *Nonadiabatic Processes in Molecular Collisions*, in *Dynamics of Molecular Collisions Part B*, W.H. Miller, Editor. 1976, Plenum Press: New York. p. 217-267.

13. Dunham, J.L., *The Wentzel-Brillouin-Kramers Method os Solving the Wave Equation.* Phys. Rev., 1932. **41**: p. 713.

14. Bunker, P.R., *The Effect of the Breakdown of the Born-Oppenheimer Approximation on the Determination of Be and we for a Diatomic Molecule.* J. Mol. Spectrosc., 1970. **35**: p. 306-313.

15. Bunker, P.R., *Errata of "The Effect of the Breakdown of the Born-Oppenheimer Approximation on the Determination of Be and we for a Diatomic Molecule".* J. Mol. Spectrosc., 1971. **38**(1): p. 197.

16. Renner, R., *Zur Theorie der Wechselwirkung zwischen Elektronen- und Kernbewegung bei dreiatomigen, stabförmigen Molekülen.* Z. Phys., 1934. **92**(3-4): p. 172-193.

17. Strickler, S.J., *Spectroscopic Effects of a Breakdown of the Born-Oppenheimer Approximation.* J. Phys. Chem., 1976. **80**(20): p. 2149-2154.

18. Yarkony, D.R., et al., *Diabatic and adiabatic representations: Electronic structure caveats.* Comput. Theor. Chem., 2019. **1152**: p. 41-52.

19. Fedorov, D.A. and B.G. Levine, *A discontinuous basis enables numerically exact solution of the Schrödinger equation around conical intersections in the adiabatic representation.* J. Chem. Phys., 2019. **150**: p. 054102.

20. Foster, P.W. and D.M. Jonas, *Nonadiabatic Eigenfunctions Can Have Amplitude, Signed Conical Nodes, or Signed Higher Order Nodes at Conical Intersection with Circular Symmetry.* J. Phys. Chem. A., 2017. **121**(39): p. 7401-7413.

21. Field, R.W. and H. Lefebvre-Brion, *The Spectra and Dynamics of Diatomic Molecules*. 2004: Elsevier Academic Press.

22. Hunter, G., *Conditional Probability Amplitudes in Wave Mechanics.* Int. J. Quantum Chem., 1975. **9**(2): p. 237-242.

23. Hunter, G., *Nodeless Wave-Functions and Spiky Potentials.* Int. J. Quantum Chem., 1981. **19**(5): p. 755-761.

24. Meek, G.A. and B.G. Levine, *Wave Function Continuity and the Diagonal Born-Oppenheimer Correction at Conical Intersections.* J. Chem. Phys., 2016. **144**(18): p. 184109.

25. Cederbaum, L.S., *The exact molecular wavefunction as a product of an electronic and a nuclear wavefunction.* J. Chem. Phys., 2013. **138**(22).

26. Jecko, T., B.T. Sutcliffe, and R.G. Woolley, *On factorization of molecular wavefunctions.* J. Phys. A: Math. Theor., 2015. **48**: p. 445201.

27. Abedi, A., N.T. Maitra, and E.K.U. Gross, *Exact Factorization of the Time-Dependent Electron-Nuclear Wave Function.* Phys. Rev. Lett., 2010. **105**: p. 123002.

28. Gidopoulos, N.I. and E.K.U. Gross, *Electronic non-adiabatic states: towards a density functional theory beyond the Born-Oppenheimer approximation.* Phil. Trans. R. Soc. A, 2014. **372**(2011): p. 20130059.

29. Fechner, P.C. and H. Helm, *Imaging of spatial many-body wave functions via linear momentum measurements.* Phys. Chem. Chem. Phys., 2014. **16**(2): p. 453-457.

30. Foster, P.W., W.K. Peters, and D.M. Jonas, *Nonadiabatic Eigenfunctions Can Have Conical Nodes.* Chem. Phys. Lett., 2017. **683**: p. 268-275.

31. Czub, J. and L. Wolniewicz, *On the Non-Adiabatic Potentials in Diatomic-Molecules.* Mol. Phys., 1978. **36**(5): p. 1301-1308.

32. Yarkony, D.R., *Nuclear Dynamics near Conical Intersections in the Adiabatic Representation: I. The Effects of Local Topography on Interstate Transitions.* J. Chem. Phys., 2001. **114**(6): p. 2601-2613.

33. Bernardi, F., M. Olivucci, and M.A. Robb, *Potential Energy Surface Crossings in Organic Photochemistry.* Chem. Soc. Rev., 1996. **25**(5): p. 321-328.

34. Truhlar, D.G. and C.A. Mead, *Relative likelihood of encountering conical intersections and avoided intersections on the potential energy surfaces of polyatomic molecules.* Phys. Rev. A, 2003. **68**(3): p. 032501.

35. Matsika, S. and D.R. Yarkony, *Intersecting Conical Intersection Seams: Their Location, Representation, and Effect on Local Topography.* J. Phys. Chem. A., 2002. **106**(11): p. 2580-2591.

36. Longuet-Higgins, H.C., et al., *Studies of the Jahn-Teller Effect II. The Dynamical Problem.* Proc. R. Soc. Lond. A, 1958. **244**(1236): p. 1-16.

37. Berry, M.V., *Quantal Phase Factors Accompanying Adiabatic Changes.* Proc. R. Soc. Lond. A, 1984. **392**: p. 45-57.

38. Simon, B., *Holonomy, the Quantum Adiabatic Theorem, and Berry's Phase.* Phys. Rev. Lett., 1983. **51**(24): p. 2167-2170.

39. Mead, C.A. and D.G. Truhlar, *On the Determination of Born–Oppenheimer Nuclear Motion Wave Functions Including Complications Due to Conical Intersections and Identical Nuclei.* J. Chem. Phys., 1979. **70**(5): p. 2284-2296.

40. Longuet-Higgins, H.C., *The Geometric Phase Effect.* Adv. Spectrosc., 1961. **2**: p. 429.

41. Moffitt, W. and A.D. Liehr, *Configurational Instability of Degenerate Electronic States.* Phys. Rev., 1957. **106**(4): p. 1195-1200.

42. Thorson, W. and W. Moffitt, *Some Calculations on the Jahn-Teller Effect in Octahedral Systems.* Phys. Rev., 1968. **168**(2): p. 362-369.

43. Landau, L.D. and E.M. Lifschitz, *Quantum Mechanics*. 3rd ed. ed. 1977, New York: Pergamon Press.

44. Judd, B.R., *Exact Solutions to a Class of Jahn-Teller Systems.* J. Phys. C: Solid State Phys., 1979. **12**: p. 1685-1692.

45. Foster, P.W. and D.M. Jonas, *Nonadiabatic conical nodes are near but not at an elliptical conical intersection.* Chem. Phys., 2019. **520**: p. 108-121.

46. McQuarrie, D.A., *Quantum Chemistry*. 2008, Sausalito, CA: University Science Books.

47. Kapur, P.L. and R. Peierls, *Penetration into Potential Barriers in Several Dimensions.* Proc. R. Soc. Lond. A, 1937. **163**: p. 606-610.

48. Caldeira, A.O. and A.J. Leggett, *Quantum Tunneling in a Dissipative System.* Ann. Phys., 1983. **149**: p. 374-456.

49. Peierls, R., *More Surprises in Theoretical Physics*. Princeton Series in Physics, ed. P.W. Anderson, A.S. Wightman, and S.B. Tremain. 1991, Princeton, NJ: Princeton University Press.

50. Xie, C., et al., *Constructive and Destructive Interference in Nonadiabatic Tunneling via Conical Intersections.* J. Chem. Theory Comput., 2017. **13**(5): p. 1902-1910.

51. Xie, C., et al., *Nonadiabatic Tunneling in Photodissociation of Phenol.* J. Am. Chem. Soc., 2016. **138**(25): p. 7828-7831.

52. Xie, C., D.R. Yarkony, and H. Guo, *Nonadiabatic tunneling via conical intersections and the role of the geometric phase.* Phys. Rev. A, 2017. **95**: p. 022104.

53. Ryabinkin, I.G., L. Joubert-Doriol, and A.F. Izmaylov, *Geometric Phase Effects in Nonadiabatic Dynamics near Conical Intersections.* Acc. Chem. Res., 2017. **50**(7): p. 1785-1793.

54. Xie, C., et al., *Up to a Sign. The Insidious Effects of Energetically Inaccessible Conical Intersections on Unimolecular Reactions.* Acc. Chem. Res., 2019. **52**(2): p. 501-509.

CHAPTER 2

NONADIABTIC EIGENFUNCTIONS CAN HAVE CONICAL NODES

It has been argued the total vibrational probability amplitude for a molecular nonadiabatic eigenfunction should not have nodes unless required by symmetry. For a model with two nonadiabatically coupled electronic states, exact factorization of nonadiabatic eigenfunctions into a total vibrational probability amplitude and a normalized electronic factor reveals zero-dimensional nodes in nonadiabatic eigenfunctions over a two-dimensional vibrational space. These conical nodes have the shape of a right elliptical cone with the node at the vertex. Low dimensionality nodes are likely when the number of nonadiabatically coupled electronic states is less than or equal to the dimensionality of the vibrational space.

The contents of this chapter have been adapted from the paper titled "Nonadiabatic Eigenfunctions Can Have Conical Nodes", which was published in May 2017 in *Chemical Physics Letters*.

2.1. Introduction

The adiabatic approximation separates eigenfunctions into electronic and vibrational factors based on fast, light electrons and slow, heavy nuclei.[1-3] In the adiabatic approximation, the electronic eigenvalues for fixed nuclei generate potential energy surfaces on which the nuclei vibrate. In the one-dimensional vibrational space of a diatomic molecule, potential curves of the same symmetry obey a non-crossing rule.[4] Von Neumann and Wigner[5] recognized that potential energy surfaces were likely to intersect in polyatomic molecules. Their reasoning was dimensional: two or more vibrational coordinates could

simultaneously adjust both the energy gap and the off-diagonal coupling to zero. They further showed that, in the vicinity of the intersection, if each coordinate has a linear effect on the coupling and on the gap, the generic shape of the intersection will be an elliptical cone. This dimensional argument showed that conical intersections may occur "by accident". Later, Jahn and Teller[6] showed that conical intersections must occur at high symmetry geometries in degenerate electronic states. Controversy about accidental conical intersections in photochemistry[7-9] was settled after the development of Berry's geometric phase[10] as a diagnostic.[11, 12] Accidental conical intersections between adiabatic potential energy surfaces are ubiquitous and important.[13-15] Dimensional arguments are useful in predicting typical behavior in higher dimensional vibrational spaces with more electronic potential energy surfaces,[16] such as intersections of conical seams.[17, 18]

For adiabatically separable states, the eigenfunctions may be written as products $\psi^{n,v}_{elec,vib}(r,q) = \psi^{n}_{elec}(r;q)\psi^{v;n}_{vib}(q)$.[2, 3, 19] With this separation, each adiabatic electronic eigenfunction is specified by a set of electronic quantum numbers *n*, is a function of the electronic coordinates *r*, and depends parametrically upon the vibrational coordinates *q* (as indicated by the semicolon); the complete set of adiabatic electronic eigenstates is orthonormal at every vibrational coordinate. Each adiabatic electronic eigenstate has a complete orthonormal set of adiabatic vibrational eigenfunctions with quantum numbers *v*; this set depends parametrically upon the electronic quantum numbers *n*. The diabatic approximation leads to a similar separable factorization.[3, 20] Under such separable approximations, a general theorem about eigenfunctions[21] proves that all excited vibrational eigenstates must have nodes where the eigenfunctions are zero. These nodes are $(M_v - 1)$-dimensional hypersurfaces in an M_v-

dimensional vibrational space (points in 1D, curves in 2D, etc.). The familiar vibrational quantum numbers are eigenfunction node counts.

Nonadiabatic interactions mix vibrational and electronic character so that the eigenstates are not separable.[3, 22-24] Eigenstates with strong nonadiabatic interactions form a complete orthonormal set but cannot be factorized with one electronic eigenfunction for a complete orthonormal set of vibrational eigenstates. Each nonadiabatic eigenstate can be expressed as a linear combination of adiabatic (or diabatic) product states. Hunter showed that each nonadiabatic vibrational-electronic eigenstate could be uniquely separated into an electronic-vibrational product. [25] For nonadiabatic eigenstate *m*, the vibrational factor is the square root of the total vibrational probability density, integrated over all electronic coordinates,

$$\Phi_m(q) = \left[\int \psi_m^*(r,q)\psi_m(r,q)dr \right]^{1/2}. \qquad (2.1)$$

In a one-dimensional vibrational space, the nonadiabatic vibrational factors should not have nodes because it is improbable that the different vibrational-electronic basis states that contribute to one non-adiabatic eigenstate all have their nodes at the same vibrational coordinates.[26] For a "nearly adiabatic" nonadiabatic eigenfunction of one vibrational coordinate, the eigenfunction quickly passes through some nonadiabatically mixed electronic character as the dominant adiabatic character changes sign through each vibrational node. Because the zeroes are avoided, one can obtain the electronic factor by division,[26, 27]

$$\Chi_m(r;q) = \psi_m(r,q) / \Phi_n(q). \qquad (2.2)$$

This resembles the adiabatic factorization in that each electronic amplitude factor is a normalized function of the electronic coordinates at every vibrational coordinate and each vibrational amplitude factor is normalized as a function of the vibrational coordinates. However, at a given *q*, the electronic factor may be different for every state *m*.[25, 26] This nonadiabatic vibrational

factor has sometimes been called a “nodeless wavefunction”.[27, 28] By a very general theorem,[21] the excited nonadiabatic eigenfunctions must have nodes in the total vibrational-electronic space. Integrating the vibrational probability density over electronic coordinates (or summing it over electronic states) can hide this underlying nodal structure.[27]

Recent work has explored and extended Hunter’s exact factorization.[28-34] We have found Hunter’s factorization useful for visualizing nonadiabatic eigenfunctions.[35] This letter uses that visualization to find “accidental” nonadiabatic wavefunction nodes which are somewhat analogous to accidental conical intersections in a toy model of a heterodimer with one vibration on each monomer. Investigating their origin, the argument that the vibrational factor is nodeless depends, like the possibility for intersections between potential surfaces, on the dimensionality of the vibrational space and the number of nonadiabatically coupled electronic states. Since the number of coupled electronic states is infinite, the nodeless argument holds in principle.[26, 27] However, at low energy, the most important nonadiabatic couplings often involve only a few states, so dimensional arguments become relevant, in practice, to the question of whether nonadiabatic eigenfunctions can have nodes in the vibrational space.

2.2. Model and calculations

The toy model studied here has a coupled heterodimer Hamiltonian in which each monomer has one vibration that is harmonic in the absence of coupling.[36-39] The Hamiltonian is

$$\mathbf{H}/\hbar = \left[\frac{\omega_A}{2}\left(\hat{p}_A^2+\hat{q}_A^2\right)+\frac{\omega_B}{2}\left(\hat{p}_B^2+\hat{q}_B^2\right)\right]\mathbf{I} + \begin{bmatrix} E_0-\frac{\delta}{2}-\omega_A d_A \hat{q}_A & J \\ J & E_0+\frac{\delta}{2}-\omega_B d_B \hat{q}_B \end{bmatrix} \tag{2.3}$$

The first line contains the sum of the two harmonic oscillator Hamiltonians, which depend on the vibrational operators of dimensionless coordinates and momenta, $\hat{q}$ and $\hat{p}$. As indicated by the electronic identity operator **I**, this sum contributes to the Hamiltonian for every electronic state. It is the only term in the Hamiltonian for the ground electronic state (neither monomer excited) and contributes to the Hamiltonian for the two electronically excited states in which either monomer *A* or monomer *B* is electronically excited. The additional terms for these excited states are given in matrix form on the second line, in the diabatic electronic basis $\{|A\rangle,|B\rangle\}$ of the uncoupled monomers. The $\omega d\hat{q}$ terms on the diagonals cause a Franck-Condon displacement of the equilibrium vibrational coordinate from $(q_A^{eq},q_B^{eq})=(0,0)$ on the ground electronic state to $(d_A,0)$ on $|A\rangle$ and $(0,d_B)$ on $|B\rangle$. These displacements are accompanied by a reduction in energy (Marcus reorganization energy) of $\lambda_A=(1/2)\omega_A d_A^2$ upon excitation of $|A\rangle$ and $\lambda_B=(1/2)\omega_B d_B^2$ upon excitation of $|B\rangle$. With these displacements, the off-diagonal electronic coupling *J* generates nonadiabatic dynamics, but a constant coupling *J* does not allow a conical

intersection.[40] The ground electronic state is only used as a reference point and a convenient vibrational basis.

In this letter, the diagonal splitting between uncoupled states with one monomer excited is $\delta = 150$ cm^{-1} (*A* below *B*) the off-diagonal coupling between these excited states is $J = 66.14$ cm^{-1}, and each monomer has displacement d such that $\lambda = 5$ cm^{-1}. For $\omega = 200$ cm^{-1}, this sets $d = 0.22$ so the displacements are smaller than the range of zero point vibration ($-1 \le q \le +1$). Two cases are illustrated here: equal vibrational frequencies for uncoupled monomers of $\omega_A = \omega_B = 200$ cm^{-1}; and unequal vibrational frequencies of $\omega_A = 210$ cm^{-1} and $\omega_B = 190$ cm^{-1}. The equal frequency case corresponds to the heterodimer treated in ref. [40], and the electronic character is shown as a function of both the correlated and anticorrelated vibrational coordinates as a reference point for the unequal frequency case. The equal frequency case has equal displacements ($d_A = d_B$) and a monomer exchange symmetry that completely decouples the correlated vibrational coordinate from the nonadiabatic dynamics.[40] Maintaining the same reorganization energies for both monomers ($\lambda_A = \lambda_B = 5$ cm^{-1}) requires unequal displacements for unequal vibrational frequencies. In both cases, the zero of energy is taken as the uncoupled diabatic electronic potential energy of monomer *A* at the origin of coordinates $(q_A, q_B) = (0,0)$ [setting $E_0 = (\delta / 2) = 75$ cm^{-1} in Eq. (2.3)]. Crossing diabatic potential energy surfaces for the uncoupled monomers with unequal vibrational frequencies are shown in Figure 2.1a. The nested adiabatic potential energy surfaces are shown in Figure 2.1b; these surfaces show the change in electronic character around the avoided crossing as a color variation. In the diabatic and adiabatic approximations, every vibronic eigenfunction will have the coordinate dependent electronic character indicated by the color of its potential surface at that point.

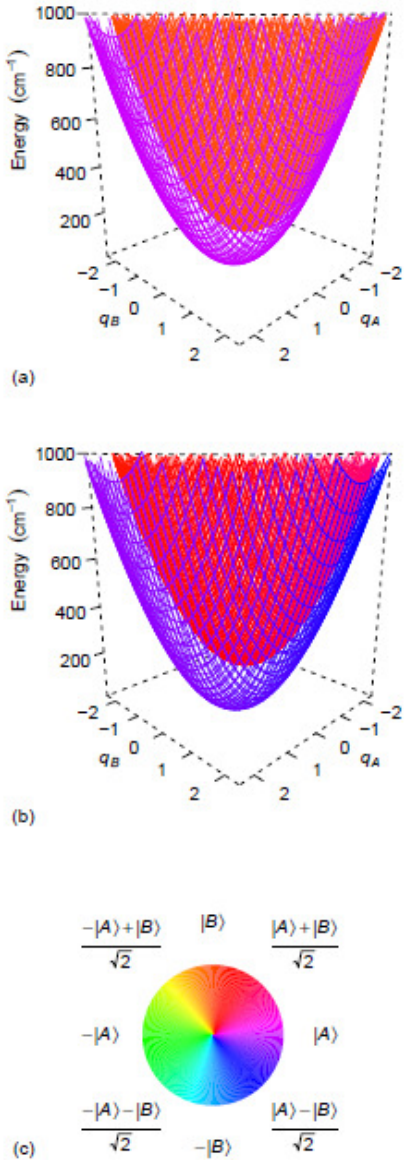

Figure 2.1: Potential energy surfaces for the unequal frequency heterodimer and color wheel for visualization of electronic character (bottom). The top panel shows the coordinate-dependent potential energy surfaces for the uncoupled diabatic states localized on each monomer. The purple lower paraboloid is the potential energy surface of *A* and the orange upper paraboloid is the potential energy surface of *B*. The point of view lies above the correlated coordinate axis, and shows the two surfaces, which have their lowest energy crossing at $(q_A, q_B) =$ (-1.53, 1.84) with energy 640 cm^{-1} above the minimum of *A*. The middle panel shows the potential energy surfaces for the coupled adiabatic states, which become delocalized in the vicinity of the avoided crossing. The lower adiabatic potential energy surface is purple (localized $|A\rangle$ electronic character) on the left and becomes blue [delocalized $(|A\rangle - |B\rangle)/\sqrt{2}$ electronic character] on the right. Similarly, the upper adiabatic potential energy surface is orange (localized $|B\rangle$ electronic character) on the left and becomes red [delocalized $(|A\rangle + |B\rangle)/\sqrt{2}$ electronic character] on the right.

Numerical calculation of the exact nonadiabatic states is carried out in the (diabatic) uncoupled monomer electronic basis using harmonic oscillator eigenstates of the undisplaced electronic ground state as vibrational basis states. In dimensionless normal coordinates, all matrix elements of the Hamiltonian can be calculated analytically from the expressions in ref. [41]. This phase convention makes the Hamiltonian matrix real-valued and symmetric. A truncated Hamiltonian matrix is diagonalized using the DEVCSF routine from the IMSL library, which calculates all eigenvectors and eigenvalues using an implicit rational QR algorithm. For the parameters stated above, increasing the number of harmonic oscillator basis states for each coordinate on each electronic state from 13 to 25 (from a total of 338 to 1250 vibronic basis states) indicates the nine lowest eigenvalues are all converged to within 10^{-12} cm^{-1} and all of their 338 common normalized basis state coefficients are converged to within 6×10^{-14}. Using a basis of 25 normalized harmonic oscillator eigenfunctions for each coordinate on a discrete 2D coordinate grid with spacing 0.01 over the domain [-9,9], the nine lowest two-dimensional eigenfunctions are orthonormal to within 2×10^{-12}. The basis state approach allows the nonadiabatic eigenfunctions to be examined with high local resolution in the vibrational coordinates, an aspect critical for this study.

Exploiting Hunter's exact factorization, the complete nonadiabatic eigenfunction is visualized here by simultaneously plotting probability amplitude contours of the positive vibrational factor $\text{Þ}_m(q_a, q_b)$ and colors for the normalized electronic factor

$$\Theta_m(q_a, q_b) = \text{atan2}\left(\left\langle B \middle| \mathrm{K}_m; q_a, q_b \right\rangle, \left\langle A \middle| \mathrm{K}_m; q_a, q_b \right\rangle\right) \tag{2.4}$$

in the uncoupled monomer basis. In. Eq. (2.4), atan2 is an arctangent function with two arguments that recovers the phase angle over a 2π range. [Eq. (2.4) can be written with the complete nonadiabatic eigenfunction in place of Hunter's nonadiabatic electronic factor.] The

electronic factor contains the sign of the nonadiabatic wavefunction, which is shown in the color map. Although the vibrational factor can have a derivative discontinuity, figures showing both factors display the complete nonadiabatic eigenfunction, which is an allowed wavefunction with continuous derivatives.

2.3. Results

Figure 2.2 shows the 9 lowest nonadiabatic eigenstates for each case. For equal vibrational frequencies, the nonadiabatic interaction uniquely defines the correlated coordinate $(q_A + q_B)/\sqrt{2}$ with slope = +1 and the anti-correlated coordinate $(q_A - q_B)/\sqrt{2}$ with slope = -1 as the normal modes of vibration.[38-40, 42] The two vibrations are separable in the contours and in the electronic character. The non-adiabatic eigenstates have adiabatic nodal lines perpendicular to the correlated coordinate that are evident in abrupt color changes such as the green $-|A\rangle$ to purple $+|A\rangle$ transition between the lowest contours for the 371 cm^{-1} eigenstate. The eigenstates also have nonadiabatic avoided nodes perpendicular to the anti-correlated coordinate, such as the yellow to pink transition through orange $|B\rangle$ electronic character near the local probability density minimum for the 356 cm^{-1} eigenstate. The resonant nonadiabatic interaction leads to strongly avoided nodes, similar to one avoided node in Fig. 1b of ref. [33]. Because correlated vibrations affect only the sign of the electronic character, the correlated quantum numbers can be assigned by inspection. The eigenstates at 171, 371, and 571 cm^{-1} are $|A\rangle|v_+ = 0\rangle$, $|v_+ = 1\rangle$, and $|v_+ = 2\rangle$, respectively (all with anti-correlated vibrational state $|v_- = 0\rangle$), and all closely resemble the corresponding states obtained in the adiabatic approximation. The states at 356 and 385 cm^{-1} are delocalized nonadiabatic mixtures of $|A\rangle|v_- = 1\rangle$ and $|B\rangle|v_- = 0\rangle$

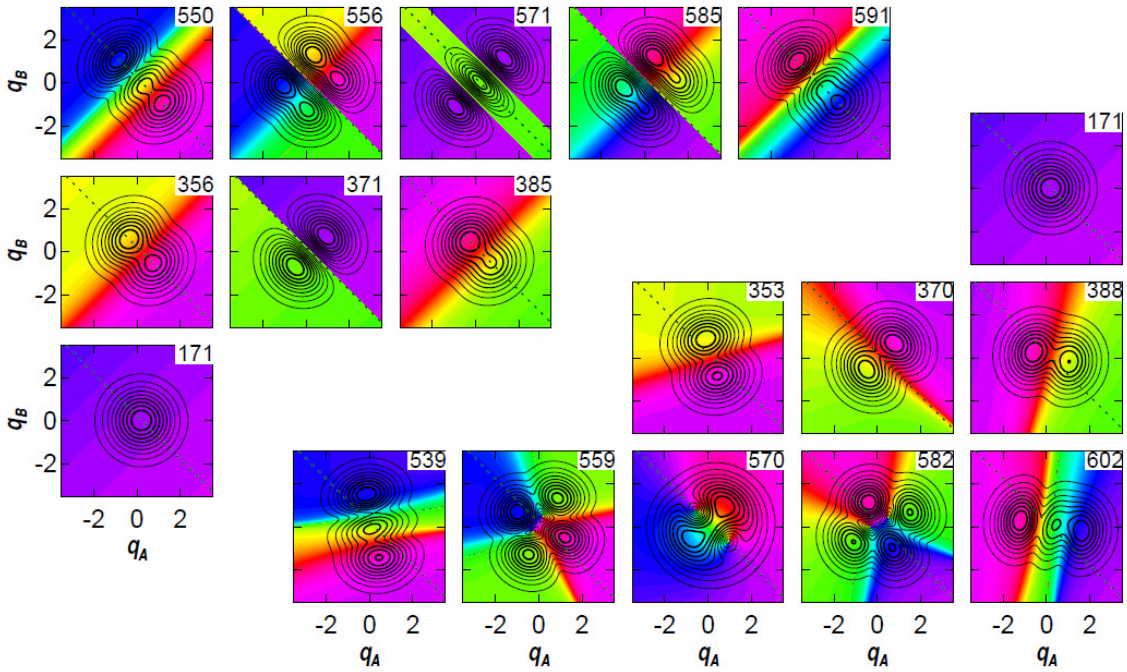

Figure 2.2: The lowest 9 eigenstates of the equal vibrational frequency (upper left) and unequal vibrational frequency (lower right) nonadiabatic heterodimer Hamiltonians. Each numerically exact nonadiabatic eigenstate's amplitude and electronic character are shown as a function of the monomer vibrational coordinates and each eigenstate's energy is given at the top right of its map. Total vibrational amplitude is indicated with black contours at 10% intervals (higher contours are thicker). Colors from the wheel in Figure 2.1 show the coordinate dependent electronic character. The dotted line is $q_A + q_B = d$, along which the correlated coordinate is at equilibrium for equal frequencies. The upper left portion of this figure shows the 9 lowest eigenstates for equal vibrational frequencies. The lowest energy eigenstate is on the bottom left, with energy increasing upward and toward the right. The lower right portion of this figure shows 9 eigenstates for unequal vibrational frequencies. The lowest energy eigenstate is at top right, with energy increasing downward and toward the right. The unequal vibrational frequency eigenstates with energies of 559, 570, and 582 cm^{-1} each have two valleys where contour levels decrease.

(both with correlated vibrational quantum state $|v_+ = 0\rangle$). Adding one quantum of vibration in the correlated coordinate to these two eigenstates gives the eigenstates at 556 and 585 cm^{-1}. The states at 550 and 591 cm^{-1} are delocalized nonadiabatic mixtures of $|A\rangle|v_- = 2\rangle$ and $|B\rangle|v_- = 1\rangle$ (both with $|v_+ = 0\rangle$).

The adiabatic separability of the correlated coordinate does not extend to the unequal vibrational frequency case. Based on electronic character and vibrational probability density, every eigenstate for unequal vibrational frequencies has an obvious correspondence to the closest energy eigenstate for equal vibrational frequencies. By and large, the sharp color changes at nodal lines have been replaced by gradual color changes at strongly avoided nodes, which are tilted away from the correlated and anti-correlated coordinates. However, the 6th, 7th, and 8th eigenstates (at 559, 570, and 582 cm^{-1}) each appear to have two points that resemble the center of the color wheel in Figure 2.1, where all colors meet. This observation illustrates the value of showing the complete nonadiabatic eigenfunction using color. Each such point is reminiscent of the electronic singularity at a conical intersection between adiabatic potential surfaces and raises fundamental questions: Do these nonadiabatic eigenfunctions have electronic singularities (points where the electronic factor becomes undefined) and, if so, how do they arise?

The 6th, 7th, and 8th unequal vibrational frequency eigenstates each correspond to equal vibrational frequency eigenstates in which the two nodal curves or avoided nodal curves include at least one nodal curve for the correlated vibration. This suggests looking at the vibrational nodal structure by projecting the nonadiabatic eigenstates onto separable electronic basis states. Figure 2.3 compares the 6th nonadiabatic eigenstate with the diabatic projections. With this higher resolution, the nonadiabatic eigenstate appears to show two electronic singularities in the vicinity of the origin. The electronic character (as represented by color) changes sign across each singularity in every direction. The electronic singularities are in valleys with probability density below the 10% contour. The projection onto $|A\rangle$ has two non-intersecting nodal curves and the projection onto $|B\rangle$ has two non-intersecting nodal curves. The points of intersection between one nodal curve in the projection onto $|B\rangle$ and the two nodal curves in the projection onto $|A\rangle$

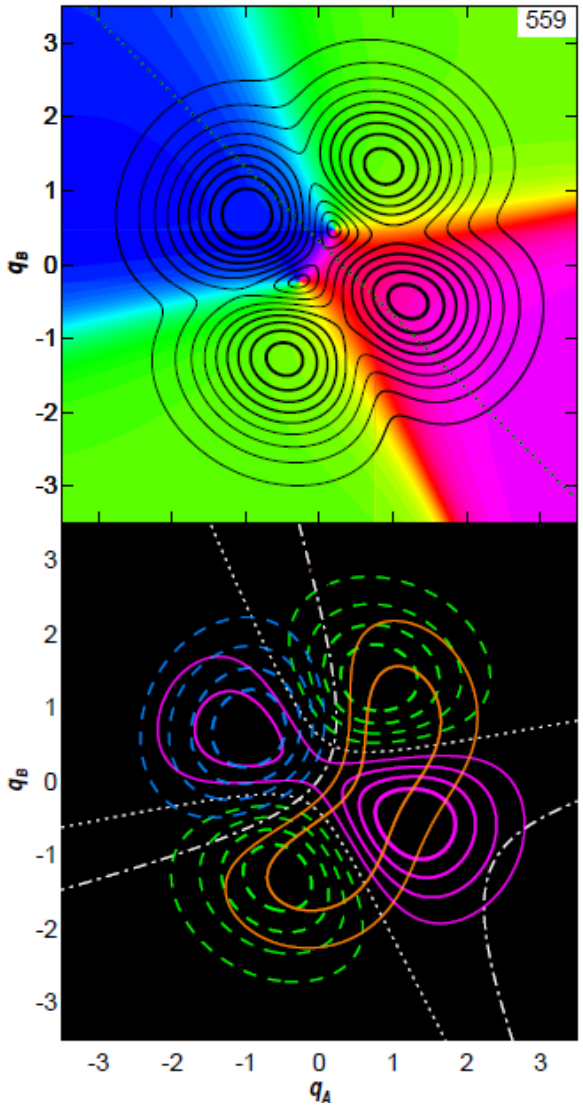

Figure 2.3: Two representations of the 6th non-adiabatic eigenstate for unequal vibrational frequencies from Figure 2.2. In both, the electronic character is again shown using the color wheel in Figure 2.1. The upper panel shows the coordinate dependent electronic character and total vibrational amplitude with black contour levels at 10% intervals as in Figure 2.2 (contours with larger absolute value are thicker). There are two electronic singularities, at (q_A, q_B) = (-0.23, -0.27) and (0.20, 0.48). Each singularity lies in a valley beneath the lowest probability density contour. The lower panel shows non-adiabatic eigenfunction contours projected onto the diabatic states $|A\rangle$ (positive contours in solid pink and negative contours in dashed green with the zero contour nodal curves shown as dotted white lines) and $|B\rangle$ (positive contours in solid orange and negative contours in dashed blue with the zero contour nodal curves shown as dot-dashed white lines). One nodal curve on $|B\rangle$ crosses the two nodal curves on $|A\rangle$ at oblique angles to generate two nodal points in the overall non-adiabatic eigenfunction. These two points of intersection between nodal curves coincide with the two electronic singularities in the upper panel.

must each have zero probability density. The coordinates of the two nodal curve intersections coincide with the coordinates of the two singularities in electronic character. Nodes are avoided everywhere else because either one or the other projection does not have a node there; as Hunter explained in 1D, the probability densities with different electronic character add to fill in the nodes in each projection. The 2D case is different because 1D nodal curves can intersect. In Figure 2.3, the nodes for different electronic characters intersect at oblique angles. Such curved nodal lines allow the possibility that nodal curves will not intersect, as for the other nodal curve on $|B\rangle$ and the eigenstates with 539 and 602 cm^{-1} energy in Figure 2.2. Qualitatively, the nodal curves underlying the two electronic singularities in the 582 cm^{-1} state are similar to those in Figure 2.3. The 570 cm^{-1} state has a closed nodal ellipse in the projection onto $|A\rangle$ that has two points of intersection with a nodal curve that runs more or less along the dashed line in the projection onto $|B\rangle$. These examples also illustrate how the nodal curves of projections onto the diabatic states can be somewhat irregular in a vibronically coupled system.

There is a simple argument that such projections must have nodal curves in a two-dimensional vibrational space. Excited eigenfunctions must have nodal curves in two dimensions,[21] though the nodes can be rather irregular in a strongly coupled system.[43] In a two-dimensional vibrational space, for any finite number of electronic states, the orthogonality of eigenfunctions requires that the higher real-valued nonadiabatic eigenstates have vibrational nodal curves when projected onto a set of separable electronic basis states. Without vibrational nodal curves, the number of orthogonal states could not exceed the finite number of separable electronic basis states. Both diabatic and adiabatic electronic basis states are separable, because they have only a parametric dependence on the vibrational coordinates, and no dependence on the vibrational state. In contrast, because the nonadiabatic eigenstates are not separable, the

above line of argument does not require that their projections have nodes in the vibrational space. Thus, the nodal properties of the vibrational wavefunctions obtained by projecting the nonadiabatic eigenfunctions onto a set of separable electronic basis states can be used to determine the nodal properties of the nonadiabatic eigenfunctions.

Figure 2.4 shows a close-up view of the non-adiabatic eigenfunction in the vicinity of the node. The contours are nearly concentric ellipses. At each angle, the integer multiple contour levels of eigenfunction amplitude are nearly equidistant from the node. This suggests that the non-adiabatic eigenfunction locally has the shape of a cone with its vertex at the node, its axis perpendicular to the vibrational coordinate plane and an elliptical base (i.e. a right elliptical cone).

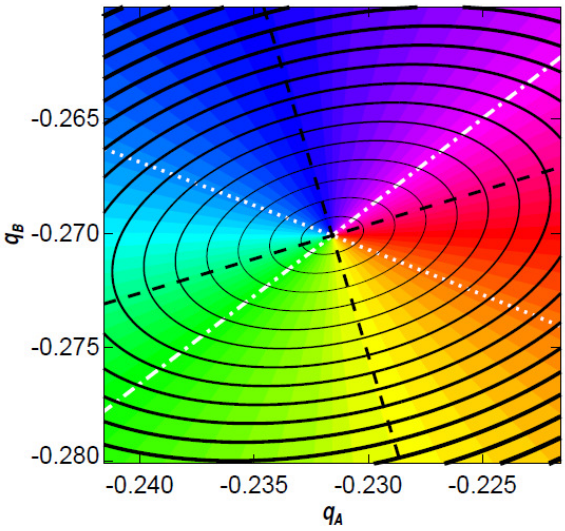

Figure 2.4: A close look at the 6th non-adiabatic eigenfunction in the vicinity of the leftmost node in Figure 2.3. Color again indicates the signed electronic character through the wheel shown in Figure 2.1. Here, solid black contour lines show the positive non-adiabatic eigenfunction amplitude at integer multiples of $0.005\times P_{max}$. The dotted and dot-dashed white lines show the nodes in the projections onto $|A\rangle$ and $|B\rangle$, respectively. The major and minor elliptical axes are shown with dashed black lines, which are asymmetrically angled with respect to these nodal lines. With 0.001 grid spacing, the electronic character appears to uniformly change sign upon rotation by π around the node. The integer multiple contour lines appear to be equidistant concentric ellipses around the node. These local aspects of the non-adiabatic eigenfunction are consistent with a right elliptic cone that has its vertex at the node. The corresponding total vibrational probability density is an elliptic paraboloid with a minimum of zero.

Locally, such nodes of non-adiabatic eigenfunctions are vertices of right elliptic cones. The proof is suggested by the intersecting nodal curves in Figures 2.3 and 2.4. Taking the node as the origin, the nodal curves may be written locally as lines $y = m_A x$ and $y = m_B x$, where the slopes are not equal (except by coincidence or symmetry). Locally, the real-valued vibrational eigenfunction factors on the two electronic basis states may be approximated by first-order Taylor series expansions as $\psi_A = c_A(y - m_A x)$ and $\psi_B = c_B(y - m_B x)$, which leads to $\psi_{NA}^2 = c_A^2(y - m_A x)^2 + c_B^2(y - m_B x)^2$. An orthogonal transformation of this positive and symmetric quadratic form gives the equation of a right elliptic cone, $(\psi_{NA}/c)^2 = (x'/a)^2 + (y'/b)^2$. (Conical intersections[44] and symmetry[21] may generate different local behavior around a zero, allowing other shapes.) Nonadiabatic eigenfunctions commonly have "conical nodes".

2.4. Discussion

Although non-adiabatic eigenfunctions in a one-dimensional vibrational space do not have nodes generically, they can have nodes "coincidentally". For example, with equal frequencies (hence separable coordinates), a node can be created at one anti-correlated coordinate in the 5th eigenstate (550 cm^{-1}) by adjusting the displacement d, but this node exists for only one point within a continuum and is thus a "coincidental node". In a probabilistic sense, a coincidental node has an *a priori* probability of zero unless the coincidence is a consequence of symmetry. Likewise, in a two-dimensional vibrational space, a nodal curve in a non-adiabatic eigenfunction can either occur by coincidence or symmetry. Such a coincidence requires *a priori* improbable coincident vibrational nodal curves in the electronic projections. The nodal line in the 371 cm^{-1} eigenstate arises from the symmetry of equal vibrational frequencies. The conical nodes found here are neither coincidental nor required by symmetry; they occur for a

broad range of model parameters and move as the parameters are adjusted. These conical nodes can also disappear from an eigenstate for some parameter ranges; in particular, the accidental conical nodes found here do not appear for small departures from monomer exchange symmetry (see Fig. 2.5), but appear for sufficiently large frequency differences. In a probabilistic sense, conical nodes sometimes occur because it is *a priori* likely that 2 one-dimensional nodal curves will intersect at a point in a two-dimensional vibrational space. Von Neumann and Wigner[5] used similar dimensional arguments to deduce that conical intersections between potential energy surfaces are likely to occur by "accident" (even when not required by symmetry)[12, 13, 16, 17, 45] in vibrational spaces with dimension greater than or equal to two. In this sense, the conical nodes found here are both "accidental" and "likely".

There is a theoretical sense in which the conical nodes found here do not violate Hunter's argument that non-adiabatic eigenfunctions do not have vibrational nodes. If non-adiabatic interactions with a third electronic state are considered, it is *a priori* improbable that 3 one-dimensional nodal curves will intersect at a single point in a two-dimensional vibrational space, so conical nodes should be avoided or at least "weakly avoided" unless required by symmetry. We call a node weakly avoided if there is a near-zero in the probability density, effectively defining a weakly avoided node by limits on measuring the probability density in a given study. The interactions in ref. [26-28] lead to avoided nodes that are weak in comparison to the vibronically resonant interactions in Fig. 2.2. In this practical sense, the vicinity of a weakly avoided zero-dimensional conical node will be a small "dot" of near zero vibrational probability density in the nonadiabatic eigenstate. This near-zero "dot" contrasts with the small "wire" of near zero vibrational probability density around a one-dimensional nodal curve for an adiabatic

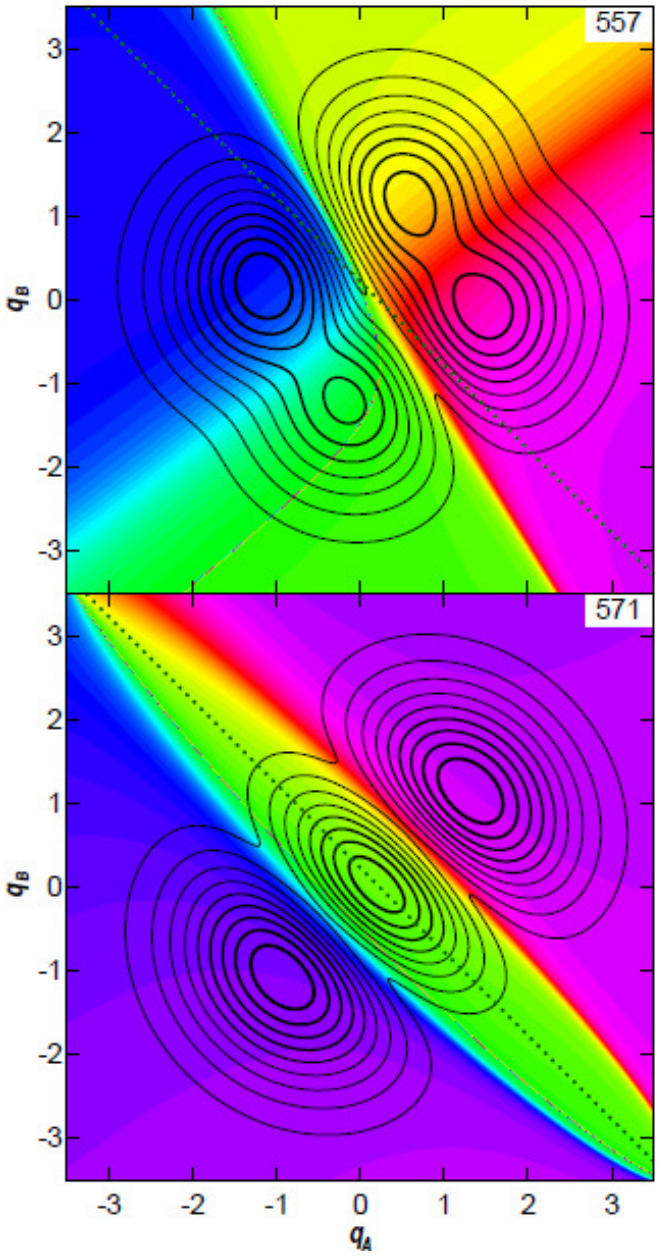

Figure 2.5: Exact factorization views of the 6th (top) and 7th (bottom) nonadiabatic eigenstates for unequal vibrational frequencies with ω_A=202 cm^{-1} and ω_B=198 cm^{-1}. The coordinate dependent electronic character and sign are shown in color. The total vibrational amplitude is shown with black contour levels at 10% intervals (contours with larger absolute value are thicker). This 4 cm^{-1} frequency difference is closer to the separable equal frequency limit in the upper left panels of Figure 2.2 than to the 20 cm^{-1} frequency difference in the lower right panels of Figure 2.2. Here, the 6th and 7th eigenstates have weakly avoided nodal lines with rapid changes in electronic character. The 7th eigenstate hints at two conical nodes moving in from infinity, but accidental conical nodes have not yet appeared for the 6th eigenstate. For the model studied here, accidental conical nodes arise from larger frequency differences with larger departures from exact separability.

eigenstate in a two-dimensional vibrational space. As discussed below, this lower dimensionality of apparent nodes may be a detectable aspect of nonadiabatic eigenfunctions.

The dimensionality of the nodes changes with the number of electronic states N_e and vibrations M_v involved in the nonadiabatic interactions. In the M_v-dimensional space of vibrational projections onto electronic states, the vibrational node hypersurfaces have dimension $(M_v - 1)$. Barring an improbable coincidence (or symmetry), the intersection between N_e nodal hypersurfaces of dimension $(M_v - 1)$ is likely to generate a node with dimension $D_{node} = (M_v - N_e)$. Nodal dimensions of $D_{node} = 0$, 1, 2 and so on correspond to nodal points, curves, surfaces, and hypersurfaces, while nodal dimensions below zero indicate that nodes are improbable. The shapes of these higher dimensional nodal hypersurfaces generalize the right elliptical cone; for example, non-adiabatic interaction between two electronic states over a three-dimensional vibrational space containing two-dimensional nodal surfaces leads to their likely intersection along one-dimensional nodal curves. Extending the local arguments used to establish the 0D right elliptical cone shape shows such 1D nodes lie at the bottom of V-shaped valleys. For complex-valued wavefunctions (e.g., solutions of the time-dependent Schrodinger equation), the number of electronic states can be effectively doubled because the squares of the real and imaginary parts of each vibrational projection add independently.

The total vibrational probability density is a quantum mechanical observable, so the dimensionality of nodes in the total vibrational amplitude could be probed experimentally. The nonadiabatic eigenfunctions can either be expanded in a separable electronic-vibrational basis or individually and uniquely factored into a vibrational amplitude and a coordinate dependent electronic factor. The separable expansion has proven widely useful and is very naturally connected to electronic spectroscopies that can selectively probe one facet of the system's

electronic character through a one-electron operator sum, such as the transition dipole moment. On the other hand, Hunter's exact factorization and the total vibrational probability density may be more closely connected to experiments that effectively trace over electronic degrees of freedom to probe internuclear distances and their correlations. Considering recent advances in imaging the nodal structure of vibrational wavefunctions, the conical nodes described here may become experimentally observable as 0D dots of zero vibrational probability density rather than the 1D wires expected for adiabatic eigenfunctions in a 2D vibrational space. Particularly interesting are Coulomb-explosion imaging experiments, in which complete dissociation of a multiply-charged ion is driven by Coulomb repulsion between fragments.[46] Related techniques that detect neutral fragments have shown remarkable power in imaging the vibrational wavefunctions of the H_2^+ molecular ion,[47] and have been extended to image the nodal structure of low-lying excited states of the D_3 and H_3 molecules.[48] As an alternative to structural techniques, vibronic coupling has been exploited to infer vibrational probability density from a measurement of electronic probability density in a scanning tunneling microscopy (STM) experiment on Jahn-Teller distorted metalloporphyrins.[49] This strategy relies on a model Hamiltonian, making it less general than Coulomb explosion, but has the attractive feature of supplying the vibrational probability density in symmetry coordinates rather than Cartesian coordinates. Since the actual measurement is a spatial electron probability density, the analysis used for the STM experiment might be generalizable to pump-probe X-ray diffraction experiments,[50] which provide a Fourier transform of the electron density. Such observation would require that the conical nodes found here for a toy model, and shown to be likely for dimensional reasons, do occur in a weakly avoided way in an actual molecule.

2.5. Conclusion

For a simple model of two nonadiabatically coupled electronic states, we have shown that exact factorization of nonadiabatic eigenfunctions into a total vibrational probability amplitude and a normalized electronic factor reveals zero-dimensional nodes in the nonadiabatic eigenfunctions over a two-dimensional vibrational space. In contrast, adiabatic eigenfunctions have one-dimensional nodal curves. Considering the infinite number of electronic states that can have a nonzero nonadiabatic coupling, such nodes should be weakly avoided in principle, so that this observation does not contradict prior statements that the nonadiabatic total vibrational probability density has no zeros. In practice, low dimensionality nodes are likely, but not required, whenever the number of nonadiabatically coupled electronic states is less than or equal to the dimensionality of the vibrational space. In two-dimensions, the nonadiabatic eigenfunctions locally have the shape of a right elliptical cone with its vertex at the node. Accounting for the change in sign of the electronic factor across the node, there is no discontinuity in the total nonadiabatic eigenfunction or its derivatives; conclusions based on the total nonadiabatic eigenfunction are independent of the exact factorization. The observable consequence for a nonadiabatic eigenfunction in a two-dimensional vibrational space would be a vibrational probability density having the local shape of a two-dimensional elliptic paraboloid around an isolated minimum point with zero probability density. More generally, nonadiabatic eigenfunctions can have weakly avoided accidental low dimensionality zeroes in the total vibrational probability density.

References

1. Born, M. and R. Oppenheimer, *Zur Quantentheorie der Molekeln.* Annalen der Physik, 1927. **389**(20): p. 457-484.

2. Born, M. and K. Huang, *Dynamical Theory of Crystal Lattices*. 1962, Oxford: Clarendon Press.

3. Tully, J.C., *Nonadiabatic Processes in Molecular Collisions*, in *Dynamics of Molecular Collisions Part B*, W.H. Miller, Editor. 1976, Plenum Press: New York. p. 217-267.

4. Landau, L.D. and E.M. Lifschitz, *Quantum Mechanics*. 3rd ed. 1977, New York: Pergamon Press.

5. von Neumann, J. and E. Wigner, *Uber das Verhalten von Eigenwerten bei adiabatischen Prozessen.* Physikalische Zeitschrift, 1929. **30**(15): p. 467-470.

6. Jahn, H.A. and E. Teller, *Stability of Polyatomic Molecules in Degenerate Electronic States I - Orbital Degeneracy.* Proceedings of the Royal Society of London. Series A, Mathematical and Physical Sciences (1934-1990), 1937. **161**(905): p. 220-235.

7. Teller, E., *Internal Conversion in Polyatomic Molecules.* Israel Journal of Chemistry, 1969. **7**(2): p. 227-235.

8. Michl, J., *Photochemical Reactions of Large Molecules. I. A Simple Physical Model of Photochemical Reactivity.* Mol. Photochem., 1972. **4**: p. 243-257.

9. Zimmerman, H.E., *MO Following: the Molecular Orbital Counterpart of Electron Pushing.* Accounts of Chemical Research, 1972. **5**(12): p. 393-401.

10. Berry, M.V., *Quantal phase factors accompanying adiabatic changes.* Proc. R. Soc. Lond. A, 1984. **392**(1802): p. 45-57.

11. Yarkony, D.R., *Diabolical conical intersections.* Reviews of Modern Physics, 1996. **68**(4): p. 985-1013.

12. Bernardi, F., M. Olivucci, and M.A. Robb, *Potential Energy Surface Crossings in Organic Photochemistry.* Chem. Soc. Rev., 1996. **25**(5): p. 321-328.

13. Klessinger, M. and J. Michl, *Excited States and Photochemistry of Organic Molecules*. 1995, New York: VCH Publishers.

14. Robb, M.A. and M. Olivucci, *Photochemical processes: potential energy surface topology and rationalization using VB arguments.* J. Photochem. Photobiol. A, 2001. **144**(2-3): p. 237-243.

15. Corrales, M.E., et al., *Structural dynamics effects on the ultrafast chemical bond cleavage of a photodissociation reaction.* Phys. Chem. Chem. Phys., 2014. **16**(19): p. 8812-8818.

16. Truhlar, D.G. and C.A. Mead, *Relative likelihood of encountering conical intersections and avoided intersections on the potential energy surfaces of polyatomic molecules.* Physical Review A, 2003. **68**(3): p. 032501.

17. Matsika, S. and D.R. Yarkony, *Intersecting Conical Intersection Seams: Their Location, Representation, and Effect on Local Topography.* The Journal of Physical Chemistry A, 2002. **106**(11): p. 2580-2591.

18. Ben-Nun, M., et al., *The role of intersection topography in bond selectivity of cis-trans photoisomerization.* Proceedings of the National Academy of Sciences of the United States of America, 2002. **99**(4): p. 1769-1773.

19. Atkins, P.W. and R.S. Friedman, *Molecular Quantum Mechanics*. 3rd (with corrections ed. 1997, New York: Oxford University Press. 545.

20. Mead, C.A. and D.G. Truhlar, *Conditions for the definition of a strictly diabatic electronic basis for molecular systems.* J. Chem. Phys., 1982. **77**(12): p. 6090-6096.

21. Courant, R. and D. Hilbert, *Methods of Mathematical Physics*. First English ed. Vol. I. 1953: Wiley-Interscience. 560.

22. Herzberg, G.H., *Electronic Spectra of Polyatomic Molecules*. Molecular Spectra and Molecular Structure. Vol. III. 1991, Malabar, FL: Krieger.

23. Koppel, H., W. Domcke, and L.S. Cederbaum, *Multimode Molecular-Dynamics Beyond the Born-Oppenheimer Approximation.* Advances in Chemical Physics, 1984. **57**: p. 59-246.

24. Worth, G.A. and L.S. Cederbaum, *Beyond Born-Oppenheimer: Molecular Dynamics Through a Conical Intersection.* Annual Review of Physical Chemistry, 2004. **55**: p. 127-58.

25. Hunter, G., *Conditional Probability Amplitudes in Wave Mechanics.* International Journal of Quantum Chemistry, 1975. **9**(2): p. 237-242.

26. Czub, J. and L. Wolniewicz, *On the Non-Adiabatic Potentials in Diatomic-Molecules.* Molecular Physics, 1978. **36**(5): p. 1301-1308.

27. Hunter, G., *Nodeless Wave-Functions and Spiky Potentials.* International Journal of Quantum Chemistry, 1981. **19**(5): p. 755-761.

28. Chiang, Y.-C., et al., *The exact wavefunction factorization of a vibronic coupling system.* Journal of Chemical Physics, 2014. **140**(5): p. 054104.

29. Abedi, A., N.T. Maitra, and E.K.U. Gross, *Exact Factorization of the Time-Dependent Electron-Nuclear Wave Function.* Physical Review Letters, 2010. **105**(12): p. 123002.

30. Abedi, A., N.T. Maitra, and E.K.U. Gross, *Correlated electron-nuclear dynamics: Exact factorization of the molecular wavefunction.* Journal of Chemical Physics, 2012. **137**(22): p. 22A530.

31. Cederbaum, L.S., *The exact molecular wavefunction as a product of an electronic and a nuclear wavefunction.* Journal of Chemical Physics, 2013. **138**(22): p. 224110.

32. Gidopoulos, N.I. and E.K.U. Gross, *Electronic non-adiabatic states: towards a density functional theory beyond the Born-Oppenheimer approximation.* Philosophical

Transactions of the Royal Society a-Mathematical Physical and Engineering Sciences, 2014. **372**(2011): p. 20130059.

33. Lefebvre, R., *Perturbations in vibrational diatomic spectra: Factorization of the molecular wave function.* Journal of Chemical Physics, 2015. **142**(7): p. 074106.

34. Eich, F.G. and F. Agostini, *The adiabatic limit of the exact factorization of the electron-nuclear wave function.* J. Chem. Phys., 2016. **145**(5): p. 054110.

35. Peters, W.K., *Carrier Dynamics in Nanocrystalline Lead Salts and Non-Adiabatic Dynamics in Near-Degenerate States of Molecules*, in *Chemistry*. 2013, University of Colorado: Boulder.

36. Witkowski, A. and W. Moffitt, *Electronic Spectra of Dimers: Derivation of the Fundamental Vibronic Equation.* Journal of Chemical Physics, 1960. **33**(3): p. 872-875.

37. Fulton, R.L. and M. Gouterman, *Vibronic Coupling. I. Mathematical Treatment for 2 Electronic States.* Journal of Chemical Physics, 1961. **35**(3): p. 1059-1071.

38. Fulton, R.L. and M. Gouterman, *Vibronic Coupling. II. Spectra of Dimers.* Journal of Chemical Physics, 1964. **41**(8): p. 2280-2286.

39. Friesner, R. and R. Silbey, *Exciton-phonon coupling in a dimer: An analytical approximation for eigenvalues and eigenvectors.* J. Chem. Phys., 1981. **74**(2): p. 1166-1174.

40. Tiwari, V., W.K. Peters, and D.M. Jonas, *Electronic resonance with anticorrelated pigment vibrations drives photosynthetic energy transfer outside the adiabatic framework.* Proc. Nat. Acad. Sci. USA, 2013. **110**(4): p. 1203-1208.

41. Papousek, D. and M.R. Aliev, *Molecular Vibrational-Rotational Spectra*. 1982, New York: Elsevier Scientific.

42. Förster, T., *Delocalized excitation and excitation transfer*, in *Modern Quantum Chemistry*, O. Sinanoglu, Editor. 1965, Academic Press, Inc.: New York. p. 93-137.

43. Gutzwiler, M.C., *Chaos in Classical and Quantum Mechanics*. 1991, New York: Springer.

44. Yarkony, D.R., *Nuclear dynamics near conical intersections in the adiabatic representation: I. The effects of local topography on interstate transitions.* Journal of Chemical Physics, 2001. **114**(6): p. 2601-2613.

45. Yarkony, D.R., *Conical intersections: The new conventional wisdom.* Journal of Physical Chemistry A, 2001. **105**(26): p. 6277-6293.

46. Vager, Z., R. Naaman, and E.P. Kanter, *Coulomb Explosion Imaging of Small Molecules.* Science, 1989. **244**(4903): p. 426-431.

47. Schmidt, L.P.H., et al., *Spatial Imaging of the H_2^+ Vibrational Wave Function at the Quantum Limit.* Phys. Rev. Lett., 2012. **108**(7): p. 073202.

48. Fechner, P.C. and H. Helm, *Imaging of spatial many-body wave functions via linear momentum measurements.* Phys. Chem. Chem. Phys., 2014. **16**(2): p. 453-457.

49. Lee, J., et al., *Orbiting Orbitals: Visualization of Vibronic Motion at a Conical Intersection.* J. Phys. Chem. A, 2013. **117**(46): p. 11655-11664.

50. Kupper, J., et al., *X-Ray Diffraction from Isolated and Strongly Aligned Gas-Phase Molecules with a Free-Electron Laser.* Phys. Rev. Lett., 2014. **112**(8): p. 083002.

CHAPTER 3

NONADIABATIC EIGENFUNCTIONS CAN HAVE AMPLITUDE, SIGNED CONICAL NODES, OR SIGNED HIGHER ORDER NODES AT A CONICAL INTERSECTION WITH CIRCULAR SYMMETRY

Numerically exact nonadiabatic eigenfunctions are computed for a two-dimensional conical intersection with circular symmetry, for which a pseudo-rotation quantum number is conserved and all eigenstates are doubly degenerate. In the calculations reported here, the conical intersection is submerged, with energy below the zero point level. The complete real-valued vibrational-electronic eigenfunctions are visualized using Hunter's exact factorization for the total vibrational amplitude factor and color for the electronic factor [*Chem. Phys. Lett.* **2017**, *683*, 268-275]. The zero-point levels have nonzero amplitude at the conical intersection. Nodes in the degenerate nonadiabatic eigenfunctions are classified as accidental if they can be moved or removed by a change in degenerate basis, and as essential if they cannot. An integer electronic index defines the order of the nodes for nonadiabatic eigenfunctions by simple closed counterclockwise line integrals. Higher eigenstates can have accidental conical nodes around the conical intersection and essential nodes of varying circular orders at the conical intersection. The signs of the essential nodes are all opposite the sign of the conical intersection and the signed node orders obey sum rules. Even for submerged conical intersections, the appearance of the exact eigenstates motivates use of signed, half-odd-integral, pseudo-rotation quantum numbers j. Essential nodes of absolute order $(|j|-1/2)$ are located on the conical intersection for $|j|$ greater than or equal to 3/2. The eigenfunctions around essential first order nodes are right circular cones with their vertex at the conical intersection.

The contents of this chapter have been adapted from the paper titled "Nonadiabatic Eigenfunctions Can Have Amplitude, Signed Conical Nodes or Signed Higher Order Nodes at a Conical Intersection with Circular Symmetry", which was published in September 2017 in the *Journal of Physical Chemistry A*. The supporting information has been adapted into an appendix.

3.1. Introduction

Soon after Born and Oppenheimer published their fundamental paper on the separation of electronic and vibrational motions,[1] von Neumann and Wigner established that potential energy surfaces in polyatomic molecules are likely to intersect, which can cause a breakdown of the Born-Oppenheimer approximation.[2] The intersections between surfaces have the geometry of an elliptical cone. Later, Jahn and Teller proved that degenerate electronic states in many point groups would split their degeneracy by lowering their symmetry away from a conical intersection at the high symmetry geometry.[3] Moffit and Liehr treated a conical intersection with circular symmetry in the nonadiabatic limit where the vibrational-electronic coupling and vibrational forces are comparable.[4] Later, Longuet-Higgins *et al.* analyzed the adiabatic limit for the same model,[5] finding two vibrational periods per electronic period (a precursor of Berry's geometric phase[6, 7]) and a half-odd-integer quantum number for what is now called pseudo-rotation.[8] Thompson, Truhlar, and Mead calculated eigenfunctions of the Hamiltonian at the conical intersection using both a diabatic Hamiltonian and the adiabatic approximation with half-odd integer pseudo-rotation quantum numbers.[9] Conical intersections and their higher dimensional analogs are now appreciated as widely important for photochemistry.[10-14] Because of their symmetry, Jahn-Teller conical intersections are the simplest type.[15-18]

For nonadiabatic systems, Hunter developed a factorization that parallels the Born-Oppenheimer factorization in many ways. In Hunter's exact factorization,[19, 20] each normalized eigenfunction $\psi_m(\mathbf{r},\mathbf{q})$ is written as a product of a marginal vibrational factor,

$$Þ_m(\mathbf{q}) = \sqrt{\int \psi_m^*(\mathbf{r},\mathbf{q})\psi_m(\mathbf{r},\mathbf{q})\mathrm{d}\mathbf{r}} \tag{3.1}$$

and a conditional electronic factor

$$\mathrm{K}_m(\mathbf{r};\mathbf{q}) = \psi_m(\mathbf{r},\mathbf{q}) / Þ_m(\mathbf{q}) . \tag{3.2}$$

Each vibrational factor is square-normalized with respect to integration over all vibrational coordinates. Each conditional electronic factor is square-normalized, as a function of the electronic coordinates **r**, for every set of vibrational coordinates **q** on which it depends parametrically. This factorization has been useful for nonadiabatic problems[21, 22] and extended to treat nonadiabatic dynamics.[23, 24] Ref. [25] exploited the fact that, if only two electronic states (*x* and *y*) are involved, the electronic factor at each point in the vibrational coordinate space can be fully specified (in character and phase) by the electronic angle

$$\begin{aligned}\Theta_m(\mathbf{q}) &\equiv \mathrm{atan2}(\langle y|\psi_m\rangle, \langle x|\psi_m\rangle) \\ &= \mathrm{atan2}(\langle y|\mathrm{K}_m\rangle, \langle x|\mathrm{K}_m\rangle)\end{aligned} \tag{3.3}$$

where atan2 returns angles over a 2π range. $\Theta_m(\mathbf{q})$ does not depend on the division in Eq. (3.2). Representing the positive vibrational factor by amplitude contours and the signed electronic factor by color (a colored exact factorization) allows complete visualization of real-valued nonadiabatic eigenfunctions with a single map.[25]

Although the structure of marginal vibrational and conditional electronic factors parallels the Born-Oppenheimer factorization, Hunter's exact factorization differs from the Born-Oppenheimer factorization in two key ways: first, nonadiabatic electronic factors can be different

for each vibrational-electronic eigenstate; second, nonadiabatic vibrational factors need not have nodes. The Born-Oppenheimer approximation requires a sum of vibrational-electronic products for such nonadiabatic states. In both factorizations, the separate factors may not be allowed wavefunctions – the exact factors may not have continuous derivatives in the adiabatic limit and the Born-Oppenheimer factors may not be single-valued around a conical intersection (Berry phase). The Born-Oppenheimer factorization is quite naturally connected to spectroscopy measurements that depend on one-electron operators (which can image one electronic factor in a sum), while Hunter's exact factorization is natural for diffraction and imaging measurements that probe the total vibrational probability density.[25]

For diatomics, the division used to define the electronic factor is made possible by the absence of nodes in the vibrational factor Φ_m.[26] This occurs because Φ_m is the square root of the total vibrational probability density obtained by tracing over the electronic states and because the vibrational amplitudes on different electronic states are unlikely to all have a zero at exactly the same place unless required by symmetry.[27] As a result, nodes in the dominant adiabatic wavefunction are avoided by a continuous change in electronic character in which a nonadiabatically coupled state "peeks through" at and around the dominant node. This nodeless property is exploited in use of the exact factorization for nonadiabatic dynamics.[23, 24] Recently, it has been shown that accidental nodes can occur if the dimensionality of the vibrational coordinate space exceeds the number of coupled electronic states.[25] Such nodes have the shape of a right elliptical cone with the node at the vertex (conical nodes). In principle, this result does not contradict the absence of true vibrational nodes for an infinite number of coupled electronic states. In practice, it suggests observable weakly avoided vibrational zeroes of low dimensionality in the total vibrational probability density.[25]

This paper uses the colored exact factorization to examine the nodes of exact nonadiabatic eigenfunctions at a conical intersection with circular symmetry. The conical intersections studied here are submerged below the zero point energy. This high symmetry model is identical to that studied by Moffit and Liehr,[4] by Longuet-Higgins *et al*.,[5] and by Judd.[28] It is also a higher symmetry version of the submerged conical intersection used to model experiments that measured loss of electronic alignment on a ~100 fs timescale[29, 30] and slower loss of electronic coherence[31] in a doubly degenerate electronic state of a silicon naphthalocyanine.

Recent work has discussed the adiabatic effects required to generate nonadiabatic wavefunction amplitude at a conical intersection in terms of compensating divergent nonadiabatic corrections[32] or compensating discontinuities in the adiabatic factors.[22] The amplitude and phase behavior around a conical intersection are critical for nonadiabatic tunneling.[33, 34] The nonadiabatic eigenfunctions obtained here are consistent with conjectures about nonzero amplitude at a conical intersection.[22, 32] At the conical intersection studied here, essential nodes in the nonadiabatic eigenfunctions can be required by symmetry. It will be shown that these conical nodes and higher order nodes have lowest radial exponents determined by the pseudo-rotation quantum number.

3.2. Theory

Using the diabatic electronic basis $\{|x\rangle, |y\rangle\}$ and dimensionless normal coordinates, the circularly symmetric Jahn-Teller Hamiltonian[35] is (divided by $\hbar$)

$$\begin{aligned}\hat{\mathbf{H}} = &[(1/2)\omega(\hat{p}_1^2 + \hat{q}_1^2) + (1/2)\omega(\hat{p}_2^2 + \hat{q}_2^2)]\hat{\mathbf{I}} \\ &+\omega d\hat{q}_1[|x\rangle\langle x| - |y\rangle\langle y|] + \omega d\hat{q}_2[|x\rangle\langle y| + |y\rangle\langle x|]\end{aligned} \tag{3.4}$$

where ω is the vibrational frequency, $\hat{q}_i$ and $\hat{p}_i$ are the dimensionless normal coordinate position and momentum operators (i = 1 or 2) for asymmetric vibrations, $\hat{\mathbf{I}} = |x\rangle\langle x| + |y\rangle\langle y|$ is the electronic identity operator, and d is the vibrational displacement. The first line is an isotropic two-dimensional harmonic oscillator Hamiltonian. The second line contains vibrational-electronic couplings. This Hamiltonian separately commutes with two mutually non-commuting reflection operators σ_v and σ_d, and thus all energy eigenvalues are doubly degenerate.[36] These reflection operators have the following effects[31] on the asymmetric coordinates and the electronic basis states:

$$\sigma_v q_1 = +q_1, \ \sigma_v q_2 = -q_2, \tag{3.5a}$$

$$\sigma_v |x\rangle = +|x\rangle, \ \sigma_v |y\rangle = -|y\rangle, \tag{3.5b}$$

and

$$\sigma_d q_1 = -q_1, \ \sigma_d q_2 = +q_2, \tag{3.5c}$$

$$\sigma_d |x\rangle = +|y\rangle, \ \sigma_d |y\rangle = +|x\rangle \tag{3.5d}$$

Eigenstates can be chosen so that they are simultaneously eigenstates of the Hamiltonian and of either reflection operator.

Figure 3.1 shows the two adiabatic potential energy surfaces obtained by neglecting the momentum operators and diagonalizing the resulting electronic Hamiltonian at each coordinate.

Color indicates the coordinate-dependent electronic character and phase for each surface, which have been chosen for maximum continuity. The two adiabatic potential surfaces have circular symmetry, a Jahn-Teller conical intersection at the origin, and a lower surface minimum below it at $V_{\min} = -(1/2)\omega d^2 = -(D\omega)$. $(D\omega)$ is known as the Jahn-Teller stabilization energy,[37-39] and its definition exactly parallels that of the Marcus reorganization energy[40] for a totally symmetric coordinate. In Fig. 3.1, the zero point energy is marked by black rings on the potential energy surfaces. In some sense, only about half of the zero point energy is available to each of the two coordinates. Even so, the conical intersection is submerged below the zero point energy. The light blue to orange color discontinuities indicate π phase shifts along $q_2 = 0$ after one circuit around the conical intersection. The location of this discontinuity is arbitrary, but the necessity for such a "cut" was first noted by Mead and Truhlar,[41] and it can be regarded as a consequence of Berry's geometric phase.[6]

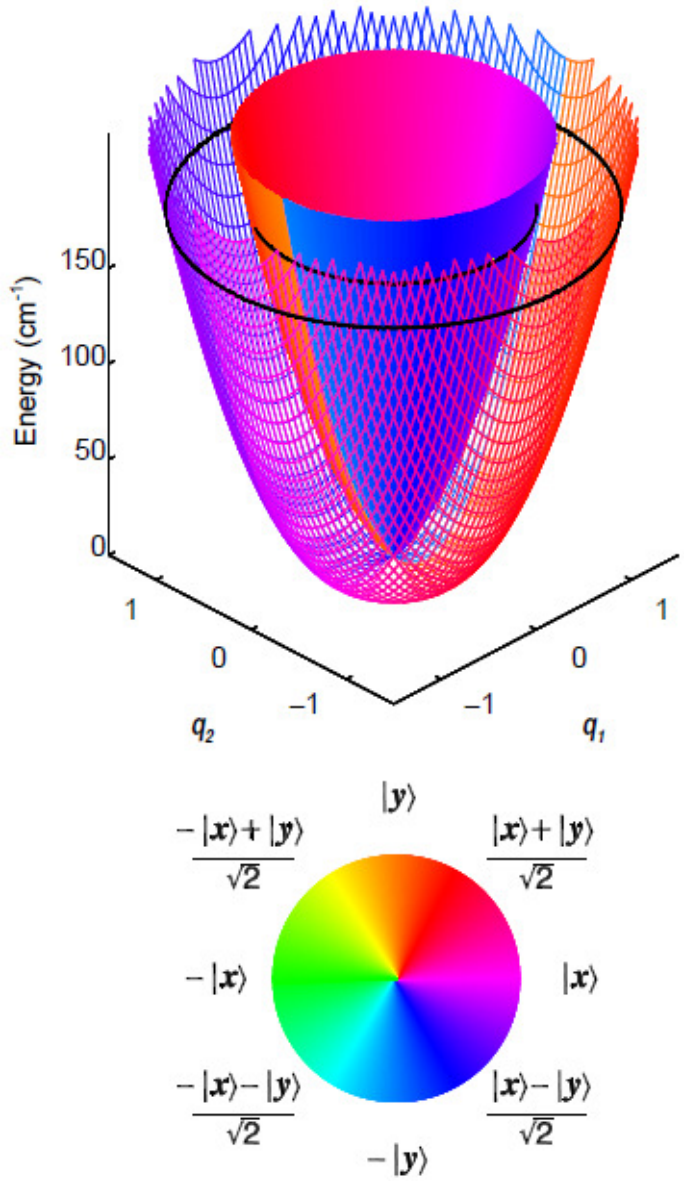

Figure 3.1: The adiabatic potential energy surfaces and coordinate dependent electronic character for the model Hamiltonian. The vibrational frequency is ω=200 cm^{-1} and the Jahn-Teller stabilization energy is $(D\omega)$=10 cm^{-1}. Color represents adiabatic electronic character $|\psi_{elec}(q_1,q_2)\rangle$ according to the color wheel at the bottom. The conical intersection at $q_1 = q_2 = 0$ and $E = 0$ is submerged below the zero-point energy of E_{zp} = 181 cm^{-1} (black curve). The lower adiabatic potential surface descends from the conical intersection to its minimum at $E_{\min} = -(D\omega)$ around the circle $(q_1^2 + q_2^2)^{1/2} = d$. An adiabatic phase discontinuity in electronic character must occur for both the inner (solid) and outer (mesh) surfaces, is arbitrarily placed along $q_2 = 0$, and is visible as an angular color discontinuity from orange $|B\rangle$ to light blue $-|B\rangle$. Starting and stopping at the discontinuity, a counterclockwise path around either adiabatic surface rotates halfway around the color wheel in a counterclockwise direction.

Longuet-Higgins *et al.* discovered that the circularly symmetric Jahn-Teller Hamiltonian can be extended to reveal a rigorously conserved quantum number[5] for what is now called pseudo-rotation.[8] Subsequent work by Hougen[35] and Oka[42] has emphasized that the form of this quantum number depends on the phase convention (it is not the total angular momentum as stated in ref. [4] and [5]). In order to use the current standard phase conventions, we extend the Hamiltonian by regarding the electronic states $|x\rangle$ and $|y\rangle$ as $-\cos\theta$ and $-\sin\theta$ [these choices most resemble the standard doubly-degenerate 2D particle in a square box states (n_x,n_y) = (2,1) and (1,2), respectively]. These two electronic states span $\lambda = \pm 1$ within a complete set of electronic states of the form $\exp(i\lambda\theta)$, where θ is a continuous electronic rotation angle and λ is the electronic angular momentum projection quantum number, which may take on any integer value. Within this extended basis set, the electronic operators $|x\rangle\langle x| - |y\rangle\langle y|$ and $|x\rangle\langle y| + |y\rangle\langle x|$ in the Hamiltonian on the second line of Eq. (3.4) may be regarded as restrictions of $2\cos(2\theta)$ and $-2\sin(2\theta)$, respectively. Taking $q_1 = \rho\cos\phi$ and $q_2 = \rho\sin\phi$, where ρ and ϕ are the standard coordinates for an isotropic two-dimensional harmonic oscillator,[43] Longuet-Higgins extended Hamiltonian thus has a vibrational-electronic interaction [second line of Eq. (3.4)] given by

$$\hat{\mathbf{H}}_{ev} = 2\omega d\,\hat{\rho}\cos(2\hat{\theta} - \hat{\phi}). \tag{3.6}$$

Taking q_1 and q_2 as the standard b_{1g} and b_{2g} normal modes for a square symmetric molecule,[35] a positive displacement d in Eq. (3.4) gives the Jahn-Teller effect on a particle in a square 2D box[44-46] expected from the Hellmann-Feynman theorem.[47]

The extended Hamiltonian does not depend on the pseudo-rotation angle $\phi + (\theta/2)$ orthogonal to $2\theta - \phi$. The cyclic coordinate[48, 49] $\phi + (\theta/2)$ thus gives rise to a conserved

pseudo-rotation quantum number $j = \ell + (\lambda / 2)$ where ℓ is the quantum number for the vibrational angular momentum conjugate to ϕ (any multiple of *j* is conserved). Since ℓ and λ are both integers, this pseudo-rotation quantum number *j* has been chosen half-odd-integral, a choice motivated by the appearance of the eigenfunctions below. *j* is a signed quantum number with complex-valued eigenstates - all energy levels are doubly degenerate with respect to the sign of *j*.

For the computations presented in this paper, we use a direct product of one-dimensional harmonic oscillator vibrational basis states in the dimensionless normal coordinates q_1 and q_2. The 1D harmonic oscillator matrix elements are also chosen to follow the phase convention in ref. [43], which assumes that the rightmost lobe at positive *q* always has positive amplitude. With this phase convention, the complex-valued isotropic two-dimensional harmonic oscillator basis states obey $\sigma_v \left| v, \ell \right\rangle = \left| v, -\ell \right\rangle$.[50] This is consistent with the phase convention of Condon and Shortley and electronic angular momentum projection basis states that obey $\sigma_v \left| \lambda \right\rangle = \left| -\lambda \right\rangle$.[51] (This phase convention differs from those of Moffitt and Liehr[4] and of Oka.[42]) Together, these establish that degenerate energy eigenstates of the pseudo-rotation quantum number may be found from the corresponding pair of degenerate σ_v eigenstates as $\left| m, \pm j \right\rangle = (\left| m, + \right\rangle \pm i \left| m, - \right\rangle) / 2^{1/2}$. Such complex-valued eigenstates exhibit the circular symmetry of the Hamiltonian.

For Jahn-Teller stabilization energies that are small relative to the vibrational frequency, second-order perturbation theory[42] leads to the following expression for the energies

$$E_{v,j}^{(2)} = \omega(v+1) - 2(D\omega)[\ell\lambda + 1]. \tag{3.7}$$

In Eq. (3.7), the vibrational quantum number v and the pseudo-rotation quantum number *j* on the left combine to unambiguously determine the relative signs of the vibrational (ℓ) and electronic (λ) angular momentum quantum numbers on the right. Since $\ell = \mathrm{v}, (\mathrm{v}-2) \ldots -\mathrm{v}$ and $\lambda = \pm 1$, a given $j = \ell + (\lambda / 2)$ can only arise in one way for each v. Eq. (3.7) contains an isotropic 2D harmonic oscillator energy $\omega(\mathrm{v}+1)$, Jahn-Teller stabilization along both coordinates $[-2(D\omega)]$, and a typical internal angular momentum coupling[52] contribution to the energy $[-2(D\omega)\ell\lambda]$. Eq. (3.7) shows that the energy depends on the relative sign of ℓ and λ, not their individual signs. The form of this last term can be expected based on the analogy to vibrational-vibrational angular momentum coupling discussed by Oka.[42]

3.3. Computational Methods

Computations use a basis state approach to enable high local resolution in the vibrational coordinates for study of the nodes. States are calculated using a truncated vibronic Hamiltonian matrix that includes *n* one-dimensional harmonic oscillator basis states for each coordinate, so that there are n^2 vibrational basis states on each of the two diabatic electronic basis states. Diagonalizing this Hamiltonian matrix yields $2n^2$ nonadiabatic eigenstates. The harmonic oscillator basis states are all centered at the origin. Off-diagonal matrix elements in dimensionless normal coordinates are calculated analytically.[43] The truncated Hamiltonian is numerically diagonalized using the DEVCSF routine from the IMSL library,[53] which calculates eigenvectors and eigenvalues using an implicit QR algorithm[54] (which does not respect other symmetries in the Hamiltonian). 4 steps are taken to generate unique eigenstate symmetries and phases. First, a numerically stable basis set rotation for σ_d symmetry[31] is applied to each pair of degenerate eigenvectors before sorting into σ_d eigenvalues of +1 and -1.

Second, each pair of degenerate states is then basis-set-rotated by $\pi/4$ to generate σ_v symmetry states,[31] which are sorted into states with eigenvalues of +1 and -1. Third, for each σ_v eigenstate, the overall sign is then changed, if necessary, to make the basis state coefficient with the largest magnitude positive [so states have dominant $+|x\rangle$ or $+|y\rangle$ electronic character]. Fourth, for each σ_d eigenstate, the overall sign is changed, if necessary, to make the largest magnitude basis state coefficient on *x* positive [so states have dominant $(|x\rangle+|y\rangle)/2^{1/2}$ or $(|x\rangle-|y\rangle)/2^{1/2}$ electronic character]. In cases where these rules decide the sign based on finite numerical precision, sign adjustments are made for consistency between figures.

For a vibrational frequency of 200 cm^{-1} and a reorganization energy of 10 cm^{-1}, increasing the number of harmonic oscillator basis states for each vibration from 13 to 25 (from a total of 338 to a total of 1250 vibronic states) indicates that the twelve lowest eigenvalues are all converged to within 2×10^{-12} cm^{-1} and that all of their 338 common normalized basis state coefficients are converged to within 4.3×10^{-10}. Higher energy states or larger stabilization energies can require a larger basis to establish convergence (see SI). The lowest 12 eigenvalue pairs are degenerate beyond the 14th digit (to within 2×10^{-12} cm^{-1}). With the basis states used, eigenstates of σ_v have a systematic pattern of zeros in their coefficients;[31] all coefficients that should be zero by symmetry have magnitudes of less than 2×10^{-14}. Using a basis of 25 normalized harmonic oscillator eigenfunctions for each coordinate on a discrete 2D grid with 0.01 spacing over the domain [-9,9], the twelve lowest two-dimensional eigenfunctions are orthogonal to within 4.8×10^{-14} and normalized to within 2.2×10^{-12}. The normalized eigenfunctions are converged at all grid points to within 10^{-14}.

For several Jahn-Teller stabilization energies, Table 3.1 gives the quantum numbers and numerical energy eigenvalues for the six lowest energy levels. Each energy level is doubly degenerate, so these levels correspond to the 12 lowest eigenstates.

Table 3.1: The 6 Lowest Energy Eigenvalues for Small Jahn-Teller Stabilization Energies with $\omega = 200$ cm^{-1}

					$(D\omega)$ [cm^{-1}]			
v	$\|j\|$	ℓ	λ	$E^{(2)}$	0.01	0.1	1	5
0	1/2	0	±1	$\omega - 2(D\omega)$	199.980	199.800	198.010	190.235
1	3/2	±1	±1	$2\omega - 4(D\omega)$	399.960	399.601	396.058	381.292
1	1/2	±1	∓1	2ω	400.000	400.000	399.980	399.516
2	5/2	±2	±1	$3\omega - 6(D\omega)$	599.940	599.401	594.143	572.999
2	1/2	0	±1	$3\omega - 2(D\omega)$	599.980	599.800	598.030	590.718
2	3/2	±2	∓1	$3\omega + 2(D\omega)$	600.020	600.199	601.912	607.918

Dominant basis state quantum numbers and second order perturbation theory expressions for the energies from Eq. (3.7) are in the columns at left.

The nonadiabatic energies in Table 3.1 demonstrate that perturbation theory is quantitatively accurate for small Jahn-Teller stabilization energies [$(D\omega) \ll \omega$], smaller vibrational quantum numbers v, and smaller magnitude pseudo-rotation quantum numbers $|j|$. The supporting information (Appendix B) contains a more extensive table with more states, a larger range of Jahn-Teller stabilization energies, and more accurate energies. The energies there quantitatively reproduce those reported by Longuet-Higgins *et al.*[5] for pseudo-rotation quantum numbers j =1/2 and 3/2, all of which involve larger displacements than in Table 3.1.

3.4. Results

Figure 3.2 provides a complete characterization of the 12 lowest nonadiabatic eigenfunctions for a "submerged" conical intersection that is well below the zero point energy. These 12 eigenfunctions occur in degenerate pairs for the 6 lowest energy levels in Table 3.1. The exact factorization is used to show a positive amplitude and color is used to show the electronic character, including all phase/sign information. At each point in the vibrational coordinate space, the electronic character and phase are displayed as an electronic angle using Eq. (3.3).

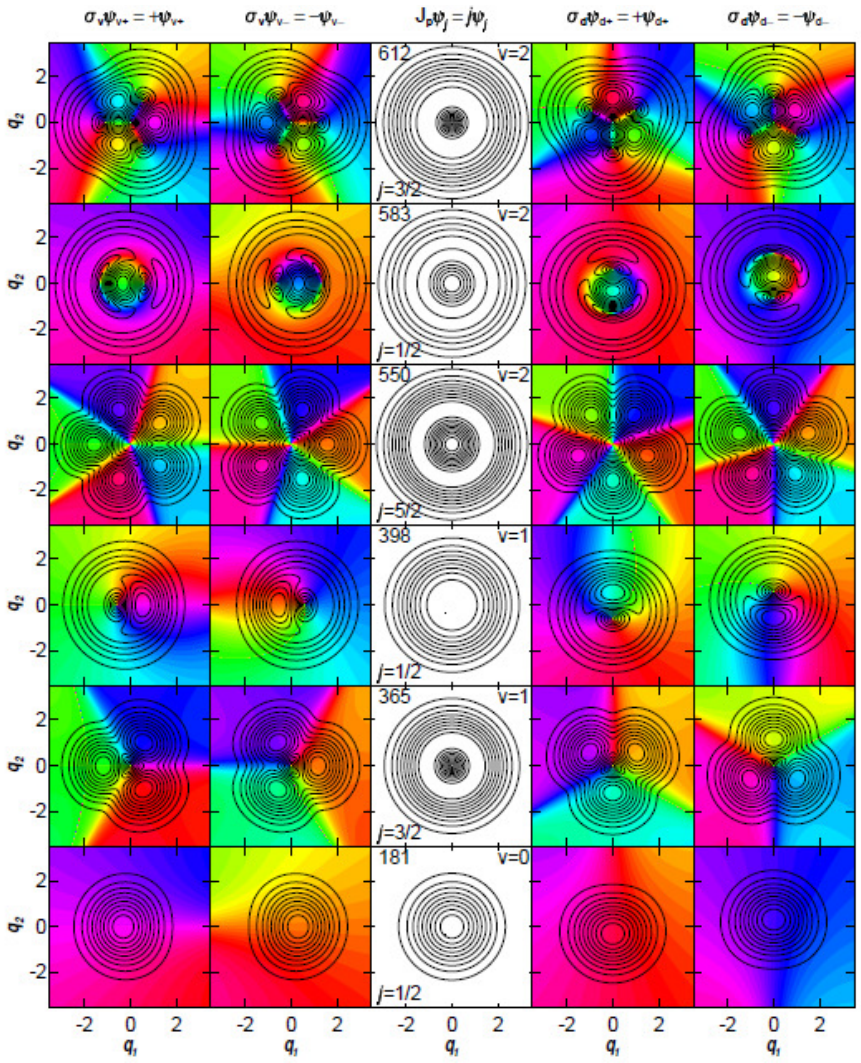

Figure 3.2: Three representations of the lowest 12 nonadiabatic eigenstates of the Hamiltonian with Jahn-Teller stabilization energy $(D\omega)$ = 10 cm^{-1} and vibrational frequency $\omega = 200$ cm^{-1}. The contours indicate the nonadiabatic amplitude factor $\beta_m(q_1,q_2)$ and the colors (in columns 1, 2, 4 and 5) indicate the nonadiabatic electronic character $\left|K_m(q_1,q_2)\right\rangle$ using the color wheel in Figure 3.1. Together, these factors fully characterize real-valued nonadiabatic eigenfunctions. For each eigenstate, the contours are at multiples of 10% of the maximum amplitude, with higher contour lines being thicker. Due to the pairwise exact degeneracy, these states have been further specified using three non-commuting operators that each commute with the Hamiltonian. The first two columns show real-valued eigenstates of the σ_v operator with eigenvalues of +1 and -1, respectively. These two columns contain the complete set of the lowest 12 eigenstates. The middle column shows the circularly symmetric amplitude factor for complex-valued eigenstates with a signed pseudo-rotation quantum number *j*. In this column, each panel also gives the vibrational quantum number v and the energy in wavenumbers (cm^{-1}) for its row. The fourth and fifth columns show the same complete set of the 12 lowest eigenstates as real-valued eigenstates of σ_d, with eigenvalues of +1 and -1, respectively.

As in ref. [25], isolated point nodes in the amplitude factor are always accompanied by singularities in the electronic factor. The total nonadiabatic eigenfunctions are single-valued and continuously differentiable - *apparent* derivative discontinuities in the vibrational amplitude on crossing through a vibrational node are compensated by an electronic sign change at the electronic singularity. The leftmost two columns show real-valued degenerate eigenstates of σ_v, the rightmost two columns show the real-valued linear combinations of these same two states that are eigenfunctions of σ_d, and the middle column shows the magnitude for either complex-valued linear combination of these same two states with a signed pseudo-rotation quantum number. The circular symmetry of the conical intersection is reflected in the circularly symmetric magnitudes of the complex-valued eigenstates with signed pseudo-rotation quantum numbers. With respect to the sign of *j*, these eigenfunctions occur in degenerate pairs, but the real and positive amplitude factor is independent of the sign of *j* and the complex-valued electronic character is not shown (it would require a different color wheel), so a single column suffices. Precursors of half-odd-integral adiabatic pseudorotation are already visible in the threefold and fivefold symmetric vibrational amplitude factors Φ_m for the real-valued eigenfunctions with |*j*|=3/2 and |*j*|=5/2, respectively.

At the same time, the adiabatic electronic sign change (Berry phase of $\pm\pi$) required for a path circling the conical intersection (see Fig. 3.1) does not appear for the exact total eigenfunctions in Fig. 3.2. As noted by Longuet-Higgins et al.,[5] an adiabatic sign change in the electronic factor must be compensated by a sign change in the nuclear factor so that their product is an overall single-valued total wavefunction. The single-valued total eigenfunctions in Fig. 3.2 are not confined to a single adiabatic surface and are far from the adiabatic limit.

Around the conical intersection, each nonadiabatic eigenfunction makes an integer number of circuits around the electronic color wheel.

The v=0, j=1/2 zero point eigenstates and higher j =1/2 states in Fig. 3.2 all have nonzero amplitude at the origin, where the conical intersection is located. The higher $|j|$ =1/2 states have "accidental" conical nodes in different locations for σ_v and σ_d eigenstates. These disappear for circularly symmetric pseudo-rotation eigenstates. For example, in Fig. 3.2, v=1, $|j|$ =1/2 and v=2, $|j|$=1/2 have 1 and 2 accidental conical nodes, respectively. These "accidental" conical nodes arise in the same way as the "accidental" conical nodes in ref. [25].

All $|j|$=3/2 states have threefold symmetry in the amplitude factor $\Phi_m(q_1,q_2)$ and "essential" conical nodes at the conical intersection. We call these nodes essential because they occur at the same location for eigenstates of all three non-commuting operators. For all essential nodes, the absolute numerical eigenfunction amplitudes at the origin are less than 2×10^{-14}. In addition to the essential conical node, the higher $|j|$ =3/2 states have accidental conical nodes away from the origin; v=2, $|j|$ =3/2 in Fig. 3.2 has three accidental conical nodes. Circling each conical node by itself, the electronic character makes one circuit around the color wheel.

The essential node at the origin of the five-fold symmetric amplitude $\Phi_m(q_1,q_2)$ for v=2, $|j|$=5/2 is not conical, as can be seen from the contour spacings. For this single node, the electronic character makes two circuits around the color wheel. These properties are connected, and will be explored below after investigating the $|j|$ = 1/2 levels.

For the zero point level and all states with pseudo-rotation quantum number $|j|$=1/2, Fig. 3.2 shows nonzero probability amplitude on top of the conical intersection at the origin. Furthermore, the maximum probability amplitude is off-center for the real-valued eigenfunctions. Table 3.1 shows that the perturbation theory errors in energy are small for the

zero point level. Therefore, perturbation theory should be useful for understanding the off-center maximum in the zero point probability density indicated by Fig. 3.2. Figure 3.3 shows the zero-point level's exact factorization and its projections onto diabatic basis states for two different Jahn-Teller stabilization energies.

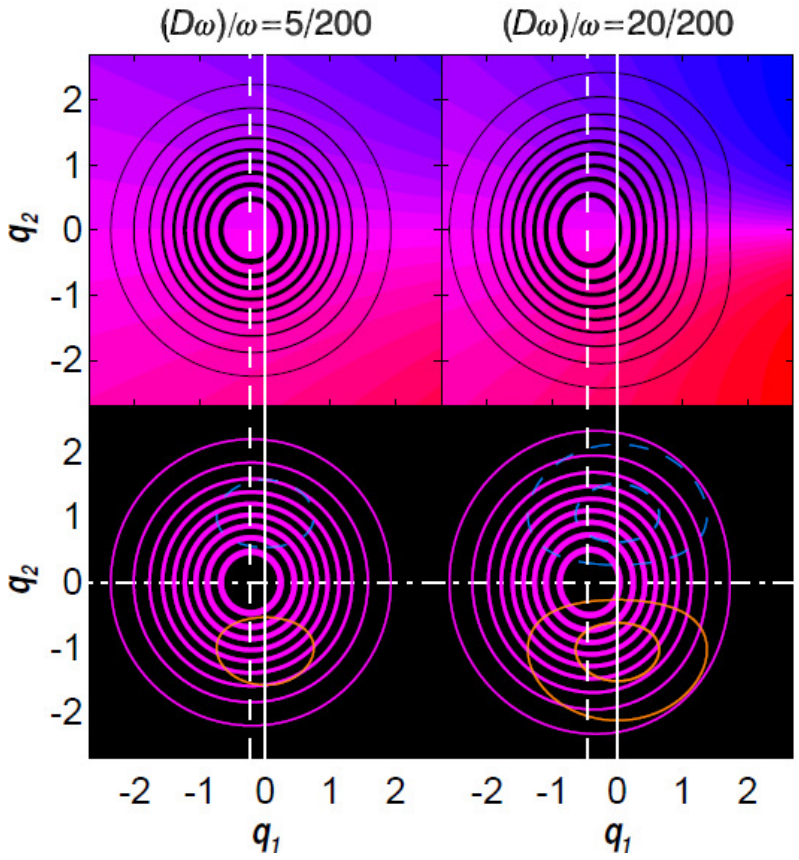

Figure 3.3: Exact factorization (top row) and coordinate-dependent projections of zero-point eigenstates with $\sigma_v = +1$ onto the diabatic electronic basis states (bottom row) for two different Jahn-Teller stabilization energies $(D\omega)$ with vibrational frequency $\omega = 200$ cm^{-1}. The factorization is plotted as in Figure 3.2. Both diabatic projections are overlaid using the color wheel in Figure 3.1. Positive projections $\langle q_1, q_2 | \langle x | \psi_0 \rangle$ have solid magenta contours at 10% of $\rho_{\max}$. Projections $\langle q_1, q_2 | \langle y | \psi_m \rangle$ have solid orange 10% contours when positive, dashed blue 10% contours when negative, and a dot-dashed white line marking the node. The solid white vertical lines mark $q_1 = 0$. The dashed white vertical lines mark $q_1 = -d$, the equilibrium vibrational displacement of $|x\rangle$. Left column) $(D\omega) = 5$ cm^{-1} [$d = (1/20)^{1/2} \approx 0.2236$]. Right column) $(D\omega) = 20$ cm^{-1} [$d = \sqrt{1/5} \approx 0.4472$].

Figure 3.3 shows the zero point eigenstate's exact factorization and its projections onto the diabatic basis states for $(D\omega) = 5$ cm^{-1} and $(D\omega) = 20$ cm^{-1}. In first-order perturbation theory, the zero-point basis state with $\sigma_v = +1$ becomes

$$\begin{aligned}\left|\psi^{(1)}_{0,0,x}\right\rangle = &\left|\mathrm{v}_1 = 0, \mathrm{v}_2 = 0\right\rangle\left|x\right\rangle \\ &-(d/2^{1/2})\left|\mathrm{v}_1 = 1, \mathrm{v}_2 = 0\right\rangle\left|x\right\rangle \\ &-(d/2^{1/2})\left|\mathrm{v}_1 = 0, \mathrm{v}_2 = 1\right\rangle\left|y\right\rangle.\end{aligned} \tag{3.8}$$

In Eq. (3.8), all one-dimensional harmonic oscillator basis states are centered on the origin. For $(D\omega) = 5$ cm^{-1}, normalizing this approximation yields projections that are visually indistinguishable from the exact projections at the scale shown. The crucial insight from Fig. 3.3 is that the off-center maximum occurs at $(q_1, q_2) = (-d, 0)$ for the $\sigma_v = +1$ eigenstate. Quantitatively, the maxima in Fig. 3.3 occur at -0.220 (for d = 0.224) and -0.425 (for d = 0.447); the position of the maximum approaches $-d$ quantitatively as d decreases, exceeding three digit accuracy for d = 0.1. Perturbation theory also correctly indicates that the off-center maximum occurs at $(+d, 0)$ for the $\sigma_v = -1$ zero point eigenstate, $(0, -d)$ for $\sigma_d = +1$, and $(0, +d)$ for $\sigma_d = -1$. The real-valued zero point eigenstates are driven off-center by the Jahn-Teller stabilization energy and have their maximum probability density near the equilibrium displacement of their dominant electronic basis state (so long as that displacement is small).

For this high symmetry model, the location and number of the "accidental" conical nodes are not truly accidental. For example, the accidental nodes for j = 3/2 states occur in sets of 3 at a common radius and have predictable angles for each reflection symmetry. Similarly, the higher j =1/2 states with vibrational quantum number v have v accidental conical nodes. These nodes occur along the q_1 axis for σ_v eigenstates and along the q_2 axis for σ_d eigenstates. Using

the reflection symmetry dependent equilibrium displacements found in the discussion of the zero point states above, the locations approximate the zeroes of displaced one-dimensional harmonic oscillator eigenfunctions with $v_1 = v$ (for σ_v eigenstates) and $v_2 = v$ (for σ_d eigenstates). The higher states (see SI) reveal more systematic patterns. The number of accidental axial and radial node distances is $(v - |j| + 1/2)$, and each radial node distance has $2|j|$ nodes, so that the total number of accidental nodes is $2|j|(v - |j| + 1/2)$. (This result has limited generality because the isotropic 2D harmonic oscillator quantum number v goes bad in the adiabatic limit.) For the same reasons stated in ref. [25], these accidental nodes have the shape of right elliptical cones with the node at the vertex. For every state examined, their principal axes are observed to be radial and angular, with the minor axis in the radial direction. In short, the "accidental" conical nodes are consequences of the circular symmetry of the model.

Figure 3.4 shows the projections of 4 nonadiabatic eigenfunctions onto the diabatic electronic basis states. Nodes in each projection are shown as dotted and dot-dashed white lines. When two white lines from different projections cross, the amplitude on both basis states must be zero so that the nonadiabatic eigenfunction must have a node; this occurs only at the origin for these states. Figure 3.4 illuminates how half-odd-integer avoided angular nodes arise from integer angular nodes in the underlying projections. The lowest states with $j = 3/2$, 5/2, and 7/2 have 1, 2, and 3 angular nodes through the origin in each projection, respectively giving a total of 4, 8, and 12 angular half nodes over both projections. In each case, half of an angular node along the negative q_1 axis disappears under a negative minimum in the x projection. This leaves 3 angular half nodes for $j = 3/2$, which all become avoided half nodes. For $j = 5/2$ and 7/2, angular node halves curve close together in 2 and 4 pairs, respectively, to reduce the number of angular avoided half nodes to 5 and 7. Figure 3.5 zooms in to reveal the nodal behavior near the origin.

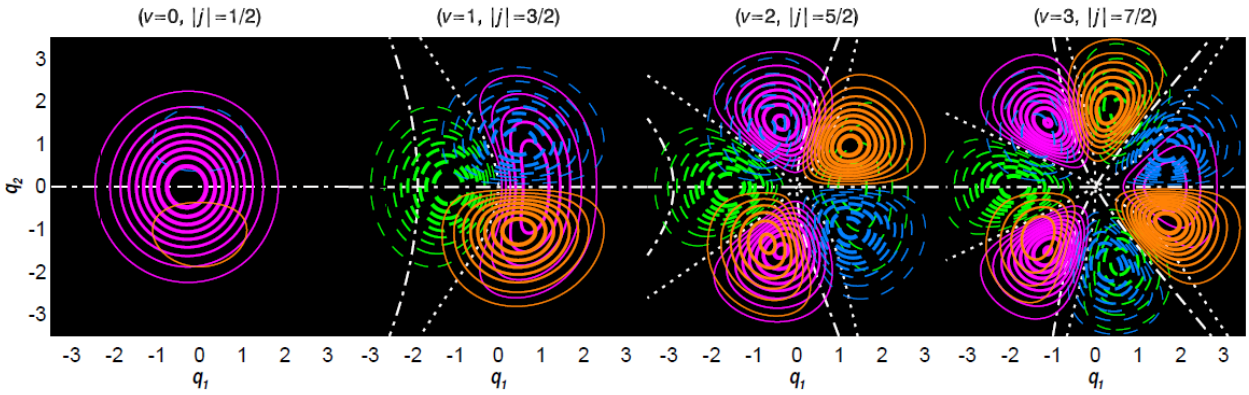

Figure 3.4: Coordinate dependent projections of 4 nonadiabatic eigenstates onto the diabatic electronic basis states, all shown as eigenstates of σ_v with eigenvalue +1. Using the color wheel in Figure 3.1, projections $\langle q_1, q_2 | \langle x | \psi_m \rangle$ have solid magenta contours when positive and dashed green contours when negative, with white dotted lines marking zero. Each projection is overlaid with the corresponding projection $\langle q_1, q_2 | \langle y | \psi_m \rangle$ which is solid orange when positive, dashed blue when negative, and dot-dashed white when zero.

Figure 3.5 shows how, for increasing values of the pseudo-rotation quantum number, the essential nodes at the origin have an increasing order. In the exact factorization (top panels), this order can be easily characterized by the number of rotations around the electronic color wheel. The order can also be characterized by the radial spacing of the contours, which are evenly spaced in amplitude for each panel. From left to right: v = 0, j = 1/2 has no node and the electronic character does not circle the color wheel – (0^{th} order); v = 1, j = 3/2 has a right circular conical node with its vertex at the origin – the even spacing of contours with radius indicates a linear amplitude proportional to ρ and the electronic factor makes one circuit around the electronic color wheel, so this is a 1^{st} order node; for v = 2, j = 5/2, the growth in contour spacing with radius quantitatively indicates a quadratic amplitude proportional to ρ^2 and the electronic factor makes two circuits around the color wheel, so this is a 2^{nd} order node; for (v = 3, j = 7/2), the contours have a cubic amplitude growing as ρ^3 for small ρ and the electronic factor makes three circuits around the color wheel, so this is a 3^{rd} order node.

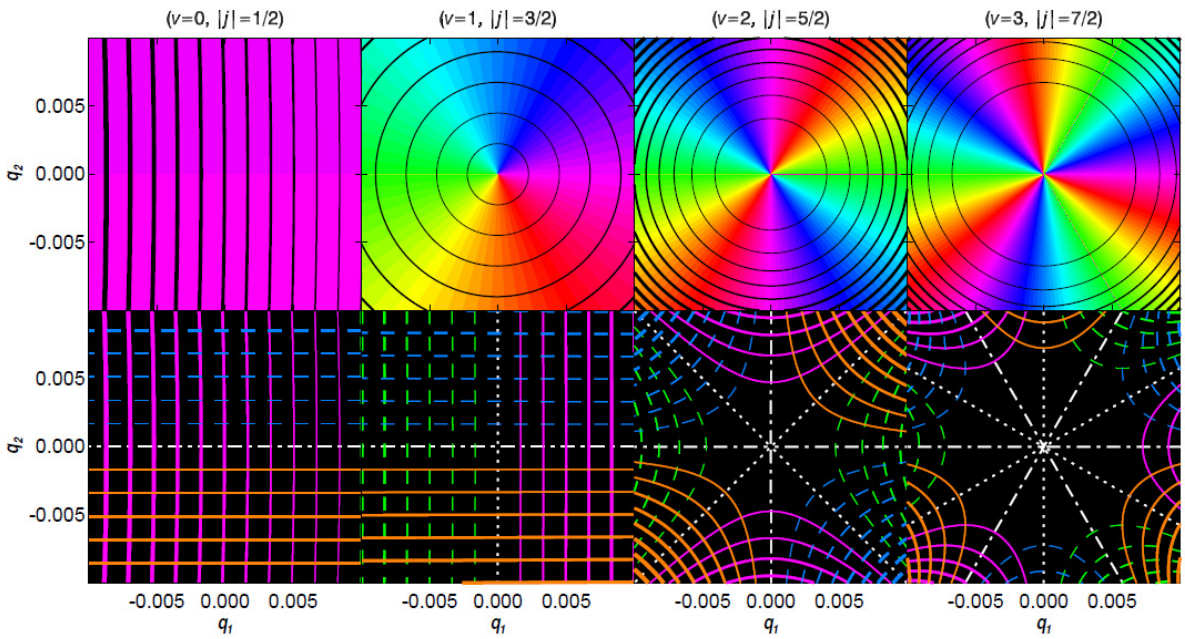

Figure 3.5: Close up view around the origin for the $\sigma_v = +1$ eigenstates in Figure 3.4. Top row) exact factorization with positive contours for the amplitude factor $\wp_m(q_1,q_2)$ and color for the electronic character $\left|\mathrm{K}_m(q_1,q_2)\right\rangle$ using the color wheel in Figure 3.1. Bottom row) overlaid coordinate dependent projections onto the electronic basis states $\langle q_1,q_2|\langle x|\psi_m\rangle$ (using solid magenta contours for positive amplitude, dashed green contours for negative amplitude, and dotted white curves for zero) and $\langle q_1,q_2|\langle y|\psi_m\rangle$ (using solid orange contours for positive amplitude, dashed blue contours for negative amplitude, and dot-dashed white curves for zero). The contour levels change from panel to panel. (v=0,|*j*|=1/2) in the leftmost column has no node, and the exact factorization contours are at 0.05% intervals from 95.15% to 95.65%, the *x*-projection contours are at 0.05% intervals from 95.15% to 95.65% of $\wp_{max}$, and the *y*-projection contours are at 0.05% intervals of $\wp_{max}$ around 0. (v=1, |*j*|=3/2) has a conical node, and the exact factorization contour interval is 0.2% of $\wp_{max}$ and the projection contour intervals are at 0.2% of $\wp_{max}$. (v=2, |*j*|=5/2) has a quadratic node, the exact factorization contour intervals are $10^{-5}\times\wp_{max}$, and the projection contour intervals are $2\times10^{-5}\times\wp_{max}$. (v=3, |*j*|=7/2) in the rightmost column has a cubic node, the exact factorization contour interval is $10^{-7}\times\wp_{max}$, and the projection contour intervals are $2\times10^{-7}\times\wp_{max}$.

The coordinate dependent projections of the eigenstates onto diabatic basis states in the bottom panels provide insight into these orders. Except for the *j* = 1/2 state, the number of

angular nodes in each projection matches the order. At the conical node in (v=1, j = 3/2), one nodal line on $|x\rangle$ intersects one nodal line on $|y\rangle$. At the quadratic node in (v=2, j =5/2), two nodal lines on $|x\rangle$ and two nodal lines on $|y\rangle$ all intersect. For the cubic node in (v=3, j = 7/2), there are three nodal lines on each state that all converge on the origin. The essential nodes at the conical intersection are consequences of circular symmetry, for which higher vibrational angular momentum requires higher radial powers in the amplitude.

In Fig. 3.5, higher order nodes at the conical intersection exhibit a link between the radial exponent for the vibrational amplitude factor and the number of circuits around the electronic color wheel at small ρ – both are given by |j| - 1/2, where j is the pseudorotation quantum number. This linkage can be proven based on a conserved pseudorotation quantum number. With a conserved pseudo-rotation quantum number and electronic angular momentum projection quantum numbers of $\lambda = \pm 1$, an eigenstate with a given signed $j = \ell + (\lambda / 2)$ can have contributions from basis states with only two signed vibrational angular momentum quantum numbers, $\ell = j \pm (1/2)$. Thus, $|\ell|_{\min} = |j| - (1/2)$. Around the origin, the local behavior of the eigenstates for the isotropic two-dimensional harmonic oscillator is given by the power series term of lowest order, which is proportional to $\rho^{|\ell|} \exp(i\ell\phi)$. The two degenerate eigenstates have lowest order terms proportional to

$$\psi_{v,j}(\rho,\phi) \sim \rho^{|\ell|_{\min}} \exp(\pm i\,|\,\ell\,|_{\min}\,\phi)[|x\rangle \pm i|y\rangle]. \tag{3.9}$$

In Eq. (3.9), the symbol ~ means leading order equality in the limit as $\rho \to 0$. Eq. (3.9) proves that essential nodes have true zeros in eigenfunction amplitude at the conical intersection. Linear

combinations can give real-valued eigenfunctions with a local behavior of

$$\begin{aligned}\psi_{\mathrm{v},|j|}(\rho,\phi) \sim\ & \rho^{|\ell|_{\min}} \cos(|\ell|_{\min}\,\phi-\alpha)\big|x\big\rangle \\ & -\rho^{|\ell|_{\min}} \sin(|\ell|_{\min}\,\phi-\alpha)\big|y\big\rangle\end{aligned} \tag{3.10a}$$

and

$$\begin{aligned}\psi_{\mathrm{v},|j|}(\rho,\phi) \sim\ & \rho^{|\ell|_{\min}} \sin(|\ell|_{\min}\,\phi-\alpha)\big|x\big\rangle \\ & +\rho^{|\ell|_{\min}} \cos(|\ell|_{\min}\,\phi-\alpha)\big|y\big\rangle\end{aligned}, \tag{3.10b}$$

where α is an arbitrary reflection symmetry plane angle. The σ_v eigenstates have $\alpha=0$, and the σ_d eigenstates have $\alpha=\pi/4$. The $\sigma_v=+1$ [$\sigma_v=-1$] eigenfunctions in Fig. 3.5 follow Eq. (3.10)a [Eq. (3.10)b] with $\alpha=0$ and $|\ell|_{\min}=|j|-1/2$. Inserting Eq. (3.10) into Eq. (3.1) - (3.3) gives

$$\Phi_{\mathrm{v},|j|}(\rho,\phi) \sim \rho^{|\ell|_{\min}} \tag{3.11}$$

and

$$\Theta_{\mathrm{v},|j|}(\rho,\phi) \sim -(|\ell|_{\min}\,\phi-\alpha) \tag{3.12a}$$

for the $\sigma_v=+1$ eigenfunctions in Eq. (3.10)a, or

$$\Theta_{\mathrm{v},|j|}(\rho,\phi) \sim -(|\ell|_{\min}\,\phi-\alpha)-\pi/2 \tag{3.12b}$$

for the $\sigma_v=-1$ eigenfunctions in Eq. (3.10)b.

We now define the "electronic index" $\eta(C)$ through a line integral around any simple closed counterclockwise path *C* that does not pass through a node,

$$\eta(C)=\frac{1}{2\pi}\oint_C d\Theta_m(q_1,q_2)\,. \tag{3.13}$$

In pictorial terms, the electronic index is equal to the number of counterclockwise spins around the color wheel on the path of integration. With this definition, the electronic index is independent of the arbitrary overall sign of the eigenfunction [by the definition of Θ_m in Eq. (3.3)] and the arbitrary phase α, but does depend on the phase convention for the electronic basis states $|x\rangle$ and $|y\rangle$. In other words, electronic indices are significant relative to each other, even for different eigenstates. Since the nonadiabatic eigenfunctions are real-valued, continuous, and differentiable, they form a differentiable vector field (see ref. [55]) of electronic state vectors over the vibrational coordinates (this is why Θ_m is defined in terms of ψ_m). The electronic index is the index of this vector field over the oriented planar surface of vibrational coordinates. This has two consequences: first, the electronic index is an integer; second, the electronic index depends only on the number, order, and sign of the nonadiabatic nodes enclosed by the path. The electronic indices for paths that circle only the essential node at the conical intersection can be obtained from Eq. (3.12) and (3.13) using a path at small constant radius so that $d\Theta_{v,|j|}(\rho,\phi) = -|\ell|_{\min}\, d\phi$ and $\eta(C) = -|\ell|_{\min}$ or by visual inspection of Fig. 3.2. The electronic indices around the conical intersection are $\eta(C) = 0$ for (v=0, |*j*|= 1/2), $\eta(C) = -1$ for (v=1, |*j*|= 3/2), $\eta(C) = 0$ for (v=1, |*j*|=1/2), $\eta(C) = -2$ for (v = 2, |*j*|=5/2) , $\eta(C) = 0$ for (v = 2, |*j*|=1/2), and $\eta(C) = -1$ for (v=2, |*j*|= 3/2).

Locally, the vibrational radial exponent and the electronic index have precisely the same magnitude and define the order of the essential node as $|\ell|_{\min} = |j| - 1/2$. Furthermore, the sign of the electronic index for a sufficiently small loop around the origin is the same for all essential nodes. Remarkably, the essential node signs are all opposite the sign of the conical intersection, which is defined by the sign of the counterclockwise line integral around the conical intersection:

$$\gamma(C) = \frac{1}{2\pi}\int_C d\Theta^a(q_1, q_2). \tag{3.14}$$

In Eq. (3.14), Θ^a is the adiabatic electronic mixing angle. The line integral can either start and stop at the discontinuity for a single-valued Θ^a or be closed for a double-valued Θ^a (half-integer line integrals are possible because the adiabatic electronic eigenfunctions do not form a *differentiable* vector field over an oriented surface, only a vector bundle[7]). The sign of a conical intersection, sgn(γ), has the same dependence on the phase convention for the electronic basis set as the electronic index (and no dependence on arbitrary adiabatic eigenfunction sign or phase). The line integral around the conical intersection in Fig. 3.1 is $\gamma(C) = +1/2$, so the sign of the conical intersection is positive; it is independent of which adiabatic surface (upper or lower) is used to evaluate it. As a result, the sign of a conical intersection is meaningful relative to the electronic indices for all nodes. The sign of the conical intersection can be reversed by reversing the sign of the Jahn-Teller displacement *d* in either the diagonal or off-diagonal Jahn-Teller coupling term in the Hamiltonian. Figure 3.6 shows the adiabatic surfaces and the lowest energy 6 nonadiabatic eigenstates of σ_v for a conical intersection with a negative sign generated by reversing the sign of the diagonal coupling. All of the equilibrium displacements along q_1 are reversed with respect to Fig. 3.2, and all of the conical node signs are reversed.

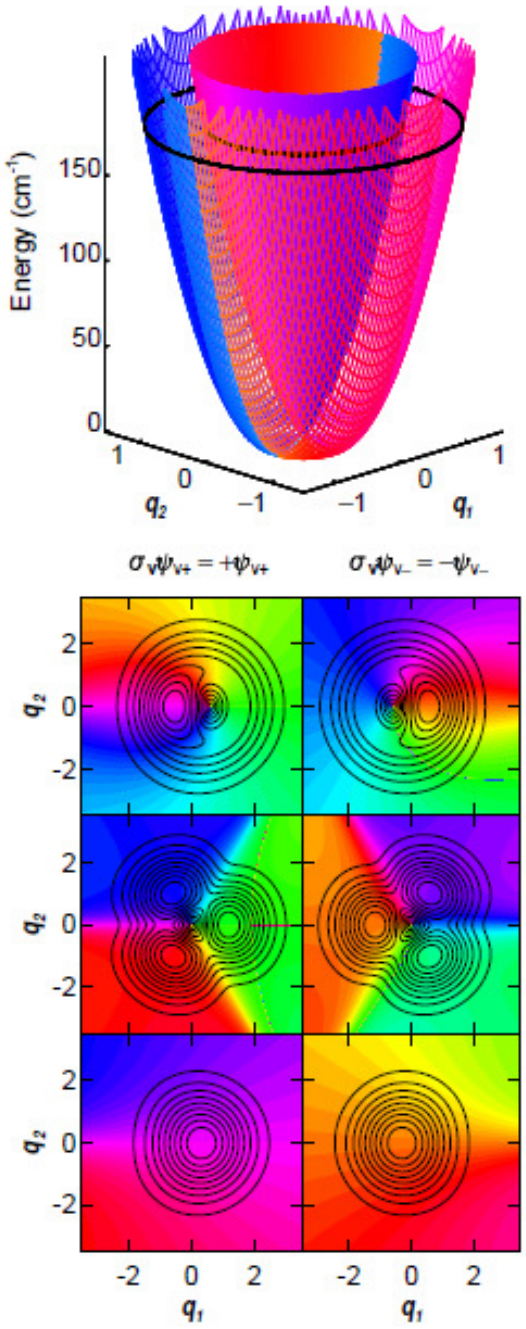

Figure 3.6: Top) The adiabatic potential energy surfaces and coordinate dependent electronic character for a model Hamiltonian in which sign of the Jahn-Teller displacement along q_1 has been reversed compared to Fig. 3.1. All other parameters are the same as in Fig. 3.1. In contrast to Fig. 3.1, a counterclockwise path around either adiabatic surface now rotates halfway around the color wheel in a clockwise direction. Bottom) The 6 lowest energy real-valued eigenstates of σ_v with reversed displacement along q_1. All other parameters are the same as in Fig. 3.2. For

each eigenstate, the sense of rotation around the color wheel is reversed in comparison to the corresponding eigenstate in Fig. 3.2.

In contrast to a submerged conical intersection, a high energy conical intersection will push amplitude away from the origin on the lower surface. In the isotropic 2D harmonic oscillator basis, this involves cancellation of the lowest order radial powers between basis states with the same vibrational angular momentum ℓ but different vibrational quantum numbers v [for example, cancellation of the constant radial term between $(v = 0, \ell = 0)$ and $(v = 2, \ell = 0)$]. Thus, $|j|$-1/2 is a *lower bound* on the radial power law exponent for the vibrational amplitude near the origin. For adiabatic eigenfunctions confined to the lower surface, which require a high conical intersection, various models indicate that the lowest radial power law exponent must exceed $\sqrt{1/2}$ (ref. [56]), $1/2+\sqrt{1/2}$ (ref. [57]), or $\sqrt{5/2}$ (ref. [58]).

This proves that, near the origin, all eigenstates of the circular symmetry conical intersection have a vibrational amplitude factor with a radial power law exponent of *at least* $|j|$-1/2 and an electronic factor that circles the electronic color wheel *exactly* $|\eta(C)| = |j| - 1/2$ times. This allows states with $|j|=1/2$ to have nonzero amplitude at the conical intersection, proves that states with $|j|=3/2$ can have conical nodes with the form of a right circular cone at the conical intersection, and establishes the linked vibrational-electronic form of the higher order nodes at the conical intersection. Circular symmetry was assumed for the above proof; the results may not apply for lower symmetry conical intersections.

It was proven above that the essential nodes at the conical intersection all have the same sign for the local electronic index. The accidental conical nodes do not. For example, the (v = 2, $|j| = 1/2$) states in Fig. 3.2 have two oppositely signed nodes, such that the electronic index is zero for any path that encompasses them both. All of the conical nodes in ref. [25] occur in such oppositely signed pairs. However, any counterclockwise circuit that encompasses all 4 conical

nodes in (v=2, |j| = 3/2) has an electronic index of $|\eta(C)| = +2$. This is precisely analogous to the results for the 4 conical intersections in the linear plus quadratic $E \otimes e$ C_{3v} Jahn-Teller coupling treated by Zwanziger and Grant.[17] Here, it arises because the conical node at the origin has an electronic index of -1 while the three accidental conical nodes have electronic indices of +1, so that the sum of the enclosed electronic indices is +2. Note that this eigenstate has $\ell = \pm 2$ and $\lambda = \mp 1$, so that $\lambda\ell = -2$. For every state examined (all states through v = 4), the signed electronic index around the perimeter shown in the figures here is equal in magnitude and opposite in sign to $\lambda\ell\,\mathrm{sgn}(\gamma)$, where $\mathrm{sgn}(\gamma)$ is the sign of the conical intersection [$\mathrm{sgn}(\gamma)$ = +1 in Fig. 3.1]; this is proportional to the electronic-vibrational angular momentum coupling term in the second-order perturbation theory eigenstate energies of Eq. (3.7). Effects detailed in Chapter 5 change the electronic index when the perimeter is expanded.

3.5. Discussion

The results obtained here directly address questions about wavefunction amplitude around conical intersections. Mead has shown that single-surface eigenfunctions must approach zero at a conical intersection in two-dimensions.[56] Varandas and Xu have provided analytic support for this result in X_3 molecules.[58] For a pure conical intersection potential, Yarkony found that the eigenfunctions approach zero at the conical intersection.[57] The above treatments do not directly address systems for which the conical intersection is weak or submerged. In such circumstances, nonadiabatic eigenfunctions can span more than one adiabatic surface, as in the pioneering study by Moffitt and Liehr.[4] Although a different basis and phase convention are used, the perturbation theory results of Moffitt and Liehr [their Eq. (36) and (38)] match Eq. (3.8). For the zero point level, these expressions place large amplitude

at the conical intersection, and this amplitude is continuously present with the same sign as the Jahn-Teller displacement *d* is tuned through 0 (where the zero point eigenfunction becomes the zero point level for an isotropic two-dimensional harmonic oscillator, which guarantees nonzero amplitude on the conical intersection). This example (which is 60 years old) thus concretely illustrates nonzero nonadiabatic eigenfunction amplitude at a conical intersection, a phenomenon discussed in ref. [32] and [22]. In 1985, Thompson, Truhlar, and Mead calculated eigenfunctions with probability density at the conical intersection, though they did not comment on this phenomenon [9]. As the analysis of Fig. 3.3 shows, the zero-point state's maximum amplitude follows the Jahn-Teller displacement away from the conical intersection. This suggests nonzero amplitude at the lower symmetry conical intersection for the silicon naphthalocyanine studied in ref. [29-31]. These nonadiabatic results are apparently heading towards agreement with the adiabatic results for a conical intersection with sufficiently high energy to confine low energy eigenstates onto the lower adiabatic surface. To form a complete basis, some eigenstates with sufficiently high energy must have eigenfunction amplitude in an arbitrarily small region around the conical intersection.

Figure 3.7 shows how the nonadiabatic eigenfunctions for v=1, $|j| = 3/2$ begin approaching the limit of adiabatic pseudo-rotation. For small Jahn-Teller stabilization energy, there is a conical node at the origin and three strongly avoided angular half nodes. These nonadiabatic eigenfunctions are everywhere single-valued and continuous, with continuous derivatives – the apparent derivative discontinuities in the amplitude crossing through the origin are compensated by the electronic sign change. Their 2π angular periodicity corresponds to the adiabatic product of compensating electronic and vibrational factors with half-odd-integral angular momenta,[5, 41] so the geometric Berry phase is hidden. As the height of the conical

intersection increases, the conical node at the origin starts to connect three weakly avoided angular half nodes that will become the three angular half nodes in the adiabatic limit. In the projections onto the diabatic states, the incipient formation of adiabatic nodes is associated with the dotted nodal curve on $|x\rangle$ that is moving in from the right. Forming true angular half-nodes for the adiabatic limit will require that this nodal curve on $|x\rangle$ precisely coincide with the nodal curve on $|y\rangle$ (dot-dashed). Until this additional node coincides exactly, the derivation showing how conical nodes arise from crossing between nodes in the two separable electronic projections[25] applies at sufficiently short range. These observations for the lowest eigenstates suggest that, relative to the vibronic energy, the conical intersection energy is crucial for limiting nonadiabatic eigenfunction amplitude there (at least from a diabatic perspective). An understanding of the submerged conical intersection limit with lower symmetry may be useful for investigating questions about adiabatic eigenfunction behavior when there is nonadiabatic amplitude at a conical intersection[22] and the transition from adiabatic to nonadiabatic tunneling.[33]

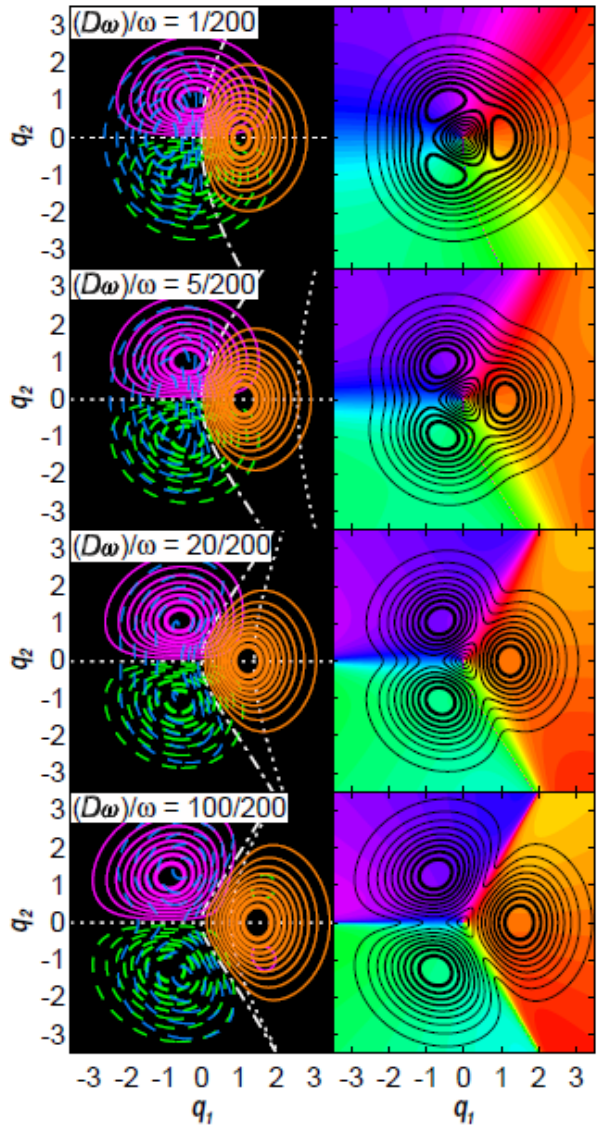

Figure 3.7: Coordinate dependent electronic projections (left column) and exact factorization (right column) for the (v=1, |*j*|=3/2) eigenstate with $\sigma_v = -1$ as a function of the Jahn-Teller stabilization energy $(D\omega)$ at a constant vibrational frequency of $\omega = 200$ cm^{-1}. The contour interval is 10% of ρ_{max} for all panels and larger magnitude contours are thicker. Positive *x*-projection contours are solid magenta, negative *x*-projections are dashed green, *x*-projection nodes are dotted white, positive *y*-projections are solid orange, negative *y*-projections are dashed blue, and *y*-projection nodes are dot-dashed white. For exact factorization, colors indicate the electronic character according to the wheel in Figure 3.1. Rows from top to bottom show $(D\omega) = 1$ cm^{-1} ($E_{zp} = 198$ cm^{-1}, $E_{v=1,j=3/2} = 396$ cm^{-1}); $(D\omega) = 5$ cm^{-1} ($E_{zp} = 190$ cm^{-1}, $E_{v=1,j=3/2} = 381$ cm^{-1}); $(D\omega) = 20$ cm^{-1} ($E_{zp} = 163$ cm^{-1}, $E_{v=1,j=3/2} = 335$ cm^{-1}); and $(D\omega) = 100$ cm^{-1} ($E_{zp} = 47$ cm^{-1}, $E_{v=1,j=3/2} = 169$ cm^{-1}). The conical intersection is at $E = 0$ in all cases.

The above observations about the signs of nonadiabatic nodes deserve some comment. Examples above show a closed path that encircles two conical nodes can give an electronic index of -2, 0, or 2. The sum rule suggests that two overlapping conical nodes of the same sign might merge into a second order node, that second order nodes might split into two conical nodes of the same sign, and that oppositely signed conical nodes can be created or annihilated as model parameters are varied. Zwanziger and Grant showed that a path enclosing 4 conical intersections with a net sign of 2 gives rise to a Renner-Teller effect.[17] This suggests that, just as conical nodes are in many ways analogous to conical intersections,[25] second order nonadiabatic nodes may be analogous to Renner-Teller intersections between electronic states.

Analogies between the dimensionality dependence of conical intersections and the dimensionality dependence of conical nodes[25] both suggest the above results may depend on the dimensionality of the Jahn-Teller conical intersection. We have not yet investigated their dimensionality dependence.

3.6. Conclusions

The conical intersection with circular symmetry investigated here is submerged below the zero point level so that eigenfunctions are not confined to a single surface. The nonadiabatic eigenfunctions can have nonzero amplitude at a conical intersection. The zero point levels have their maximum amplitude near the Jahn-Teller displacement, approaching it more accurately as the Jahn-Teller displacement goes to zero. Around the conical intersection, the lowest order essential node in the nonadiabatic eigenfunctions has the form of a right circular cone, and its vertex is a node at the conical intersection. For nonadiabatic eigenfunctions, electronic indices have been defined through line integrals around simple closed counterclockwise paths and

proven to be integers. Circular conical nodes and higher order nodes at the conical intersection occur with a lowest radial power law exponent equal to the absolute value of the electronic index for a sufficiently small path around the conical intersection. For the path tracing the perimeter of the plots shown or any circular path shown enclosing the outermost 10% contour, the total number of additional nodes surrounding the conical intersection is found to be $2|j|(v - |j| + 1/2)$ so long as the 2D harmonic oscillator vibrational quantum number v is good. Nonadiabatic nodes have a sign manifested in their electronic index, and the sign of the nonadiabatic nodes at the conical intersection is always opposite the sign of the conical intersection. The electronic index is equal to the sum of the electronic indices for all nodes inside the simple closed path. So long as the 2D harmonic oscillator vibrational angular momentum quantum number ℓ remains good, the electronic index at a radius sufficient to enclose all of the nodes enumerated above is $\eta(C) = -\lambda\ell\,\mathrm{sgn}(\gamma)$, where $\lambda\ell$ governs the perturbative energy from vibrational-electronic interaction and sgn(γ) is the sign of the conical intersection (It will be shown in Chapter 5 that additional conical nodes can exist deep into the tunneling region). The results about nonzero amplitude at a conical intersection, the signs and electronic indices of nonadiabatic nodes, and the sum rule for the electronic indices are independent of the circular symmetry and submerged nature of the conical intersection studied here.

References

1. Born, M. and R. Oppenheimer, *Zur Quantentheorie der Molekeln.* Annalen der Physik, 1927. **389**(20): p. 457-484.

2. von Neumann, J. and E. Wigner, *Uber das Verhalten von Eigenwerten bei adiabatischen Prozessen.* Physikalische Zeitschrift, 1929. **30**(15): p. 467-470.

3. Jahn, H.A. and E. Teller, *Stability of Polyatomic Molecules in Degenerate Electronic States. I. Orbital Degeneracy.* Proceedings of the Royal Society of London. Series A, Mathematical and Physical Sciences (1934-1990), 1937. **161**(905): p. 220.

4. Moffitt, W. and A.D. Liehr, *Configurational Instability of Degenerate Electronic States.* Phys. Rev., 1957. **106**(4): p. 1195-1200.

5. Longuet-Higgins, H.C., et al., *Studies of the Jahn-Teller effect II. The dynamical problem.* Proc. R. Soc. Lond. A, 1958. **244**(1236): p. 1-16.

6. Berry, M.V., *Quantal phase factors accompanying adiabatic changes.* Proc. R. Soc. Lond. A, 1984. **392**: p. 45-57.

7. Simon, B., *Holonomy, the Quantum Adiabatic Theorem, and Berry's Phase.* Phys. Rev. Lett., 1983. **51**(24): p. 2167-2170.

8. Hagelberg, F., *Electron Dynamics in Molecular Interactions*. 2014, London: Imperial College Press.

9. Thompson, T.C., D.G. Truhlar, and C.A. Mead, *On the form of the adiabatic and diabatic representation and the validity of the adiabatic approximation for X3 Jahn-Teller systems.* 82, 1985. **5**: p. 2392-2407.

10. Atchity, G.J., S.S. Xantheas, and K. Ruedenberg, *Potential energy surfaces near intersections.* Journal of Chemical Physics, 1991. **95**(3): p. 1862-1876.

11. Bernardi, F., M. Olivucci, and M.A. Robb, *Potential Energy Surface Crossings in Organic Photochemistry.* Chem. Soc. Rev., 1996. **25**(5): p. 321-328.

12. Levine, B.G. and T.J. Martinez, *Isomerization Through Conical Intersections.* Annu. Rev. Phys. Chem., 2007. **58**: p. 613-634.

13. Matsika, S. and P. Krause, *Nonadiabatic Events and Conical Intersections.* Annual Review of Physical Chemistry, 2011. **62**: p. 621-643.

14. Yarkony, D.R., *Nonadiabatic Quantum Chemistry—Past, Present, and Future.* Chem. Rev., 2012. **112**(1): p. 481-498.

15. Englman, R., *The Jahn-Teller Effect in Molecules and Crystals*. 1972, London: Wiley-Interscience.

16. Koppel, H., W. Domcke, and L.S. Cederbaum, *Multimode Molecular-Dynamics Beyond the Born-Oppenheimer Approximation.* Advances in Chemical Physics, 1984. **57**: p. 59-246.

17. Zwanziger, J.W. and E.R. Grant, *Topological phase in molecular bound states: Application to the Exe system.* J. Chem. Phys., 1987. **87**(5): p. 2954-2964.

18. Applegate, B.E., T.A. Barckholtz, and T.A. Miller, *Explorations of Conical Intersections and Their Ramifications for Chemistry Through the Jahn-Teller Effect.* Chemical Society Reviews, 2003. **32**: p. 38-49.

19. Hunter, G., *Conditional Probability Amplitudes in Wave Mechanics.* International Journal of Quantum Chemistry, 1975. **9**(2): p. 237-242.

20. Hunter, G., *Nodeless Wave-Functions and Spiky Potentials.* International Journal of Quantum Chemistry, 1981. **19**(5): p. 755-761.

21. Cederbaum, L.S., *The exact molecular wavefunction as a product of an electronic and a nuclear wavefunction.* Journal of Chemical Physics, 2013. **138**(22): p. 224110.

22. Meek, G.A. and B.G. Levine, *Wave function continuity and the diagonal Born-Oppenheimer correction at conical intersections.* J. Chem. Phys., 2016. **144**(18): p. 184109.

23. Abedi, A., N.T. Maitra, and E.K.U. Gross, *Exact Factorization of the Time-Dependent Electron-Nuclear Wave Function.* Physical Review Letters, 2010. **105**(12): p. 123002.

24. Gidopoulos, N.I. and E.K.U. Gross, *Electronic non-adiabatic states: towards a density functional theory beyond the Born-Oppenheimer approximation.* Philosophical Transactions of the Royal Society a-Mathematical Physical and Engineering Sciences, 2014. **372**(2011): p. 20130059.

25. Foster, P.W., W.K. Peters, and D.M. Jonas, *Nonadiabatic eigenfunctions can have conical nodes.* Chem. Phys. Lett., 2017. **683**(September 1): p. 268-275.

26. Czub, J. and L. Wolniewicz, *On the Non-Adiabatic Potentials in Diatomic-Molecules.* Molecular Physics, 1978. **36**(5): p. 1301-1308.

27. Peters, W.K., V. Tiwari, and D.M. Jonas, *Nodeless vibrational amplitudes and quantum nonadiabatic dynamics in the nested funnel for a pseudo Jahn-Teller molecule or homodimer.* J. Chem. Phys., submitted.

28. Judd, B.R., *Exact solutions to a class of Jahn-Teller systems.* J. Phys. C: Solid State Phys., 1979. **12**: p. 1685-1692.

29. Farrow, D.A., et al., *Polarized Pump-Probe Measurements of Electronic Motion via a Conical Intersection.* J. Chem. Phys., 2008. **128**(7): p. 144510.

30. Farrow, D.A., et al., *The polarization anisotropy of vibrational quantum beats in resonant pump-probe experiments: Diagrammatic calculations for square symmetric molecules.* Journal of Chemical Physics, 2008. **129**(17): p. 174509.

31. Kitney-Hayes, K.A., et al., *Two-Dimensional Fourier Transform Electronic Spectroscopy at a Conical Intersection.* J. Chem. Phys., 2014. **140**: p. 124312

32. Ryabinkin, I., L. Joubert-Doriol, and A.F. Izmaylov, *When do we need to account for the gemoetric phase in excited state dynamics?* J. Chem. Phys., 2014. **140**(21): p. 214116.

33. Xie, C., et al., *Constructive and Destructive Interference in Nonadiabatic Tunneling via Conical Intersections.* Journal of Chemical Theory and Computation, 2017. **13**(5): p. 1902-1910.

34. Xie, C., D.R. Yarkony, and H. Guo, *Nonadiabatic tunneling via conical intersections and the role of the geometric phase.* Phys. Rev. A, 2017. **95**(2): p. 022104.

35. Hougen, J.T., *Vibronic Interactions in Molecules with a Fourfold Symmetry Axis.* Journal of Molecular Spectroscopy, 1964. **13**: p. 149-167.

36. Landau, L.D. and E.M. Lifschitz, *Quantum Mechanics*. 3rd ed. 1977, New York: Pergamon Press.

37. Child, M.S. and H.C. Longuet-Higgins, *Studies of the Jahn-Teller effect III. The rotational and vibrational spectra of symmetric top molecules in electronically degenerate states.* Philosophical Transactions of the Royal Society A, 1961. **254**(1041): p. 259-294.

38. Child, M.S., *Studies of the Jahn-Teller effect IV. The vibrational spectra of spin-degenerate molecules.* Philosophical Transactions of the Royal Society A, 1962. **255**(1050): p. 31-53.

39. Child, M.S., *Anomalous spectrocopic properties accompanying a weak dynamic Jahn-Teller effect.* Journal of Molecular Spectroscopy, 1963. **10**: p. 357-365.

40. Marcus, R.A., *Electron Transfer Reactions in Chemistry: Theory and Experiment (Nobel Lecture).* Angewandte Chemie, 1993. **32**(8): p. 1111-1121.

41. Mead, C.A. and D.G. Truhlar, *On the determination of Born–Oppenheimer nuclear motion wave functions including complications due to conical intersections and identical nuclei.* J. Chem. Phys., 1979. **70**(5): p. 2284-2296.

42. Oka, T., *Vibration—Rotation Interaction in Symmetric-Top Molecules and the Splitting between A_1 and A_2 Levels.* J. Chem. Phys., 1967. **47**(12): p. 5410-5426.

43. Papousek, D. and M.R. Aliev, *Molecular Vibrational-Rotational Spectra*. 1982, New York: Elsevier Scientific.

44. Smith, E.R., D.A. Farrow, and D.M. Jonas, *Response functions for dimers and square symmetric molecules in four-wave-mixing experiments with polarized light.* J. Chem. Phys., 2005. **123**(4): p. 044102.

45. Smith, E.R., D.A. Farrow, and D.M. Jonas, *Publisher's Note: "Response functions for dimers and square symmetric molecules in four-wave-mixing experiments with polarized light" [J. Chem. Phys. **123,** 044102 (2005)]*. J. Chem. Phys., 2005. **123**: p. 179902.

46. Smith, E.R., D.A. Farrow, and D.M. Jonas, *Erratum: "Response functions for dimers and square symmetric molecules in four-wave-mixing experiments with polarized light" [J. Chem. Phys. **123,** 044102 (2005)]*. J. Chem. Phys., 2008. **128**: p. 109902.

47. Clinton, W.L. and B. Rice, *Reformulation of the Jahn-Teller Theorem.* J. Chem. Phys., 1959. **30**(2): p. 542-546.

48. Landau, L.D. and E.M. Lifschitz, *Mechanics*. 3rd ed. 1976, New York: Pergamon Press.

49. Arnold, V.I., *Mathematical Methods of Classical Mechanics*. 1st ed. 1978, New York: Springer.

50. DiLauro, C. and I.M. Mills, *Coriolis Interactions about X-Y axes in Symmetric Tops.* J. Mol. Spectrosc., 1966. **21**(1-4): p. 386-413.

51. Hougen, J.T., *The Calculation of Rotational Energy Levels and Rotational Line Intensities in Diatomic Molecules (National Bureau of Standards Monograph 115)*. 1970, Washington, DC: US Government Printing Office. (52 pages).

52. Herzberg, G.H., *Infrared and Raman Spectra of Polyatomic Molecules*. Molecular Spectra and Molecular Structure. Vol. II. 1991, Malabar, FL: Krieger.

53. *Visual Numerics IMSL numerical libraries*. Rogue Wave Software: Boulder, CO.

54. Parlett, B.N., *The Symmetric Eigenvalue Problem*. 1980, Englewood Cliffs, NJ: Prentice-Hall.

55. do Carmo, M.P., *Differential Geometry of Curves and Surfaces*. 1976, Englewood Cliffs, NJ: Prentice-Hall.

56. Mead, C.A., *Electronic Hamiltonian, wave functions, and energies, and derivative coupling between Born-Oppenheimer states in the vicinity of a conical intersection.* J. Chem. Phys., 1983. **78**(2): p. 807-814.

57. Yarkony, D.R., *Nuclear dynamics near conical intersections in the adiabatic representation: I. The effects of local topography on interstate transitions.* Journal of Chemical Physics, 2001. **114**(6): p. 2601-2613.

58. Varandas, A.J.C. and Z.R. Xu, *On the behavior of single surface nuclear wavefunctions in the vicinity of the conical intersection for an X_3 system.* Chem. Phys. Lett., 2000. **316**: p. 248-256.

CHAPTER 4

NONADIABTIC CONICAL NODES ARE NEAR BUT NOT AT ELLIPTICAL CONICAL INTERSECTIONS

Numerical nonadiabatic eigenfunctions are calculated for 2D Jahn-Teller conical intersections with the elliptical shape found in square-symmetric molecules. Hunter's exact factorization is used to visualize the complete real-valued vibronic eigenfunctions. Point nodes are observed in the vibrational factor and the nodal structures are compared with those for circularly symmetric conical intersections. Without pseudo-rotation symmetry, essential n^{th} order nodes at circular conical intersections split into n accidental conical nodes that are near but not at the elliptical conical intersection. For each eigenfunction, the integer electronic index that measures electronic state vector rotation around a closed vibrational path is locally stable to perturbations. Pairs of oppositely signed conical nodes can be generated or annihilated as Hamiltonian parameters are continuously varied. At annihilation, a tangential node with an electronic index of zero is created. For elliptical conical intersections, all eigenfunctions examined generate nonzero total vibrational probability density at the conical intersection.

The contents of this chapter have been adapted from the paper titled "Nonadiabatic Eigenfunctions are Near, but not at Elliptical Conical Intersections", which was published in January 2019 in *Chemical Physics*. The supporting information has been adapted into an appendix.

4.1. Introduction

Nonadiabatic dynamics are important in many photochemical reactions and often proceed through conical intersections between adiabatic potential surfaces.[1-10] The adiabatic perspective faces interesting challenges when a conical intersection is submerged so that its energy lies below the zero point energy or is otherwise accessible. In these circumstances, the eigenfunctions can be delocalized over both adiabatic potential surfaces and their behavior at and around the conical intersection is of interest.[11, 12] In spectroscopy, submerged conical intersections are readily accessible as an extreme limit of the dynamical Jahn-Teller effect[13-15] and can generate femtosecond nonadiabatic dynamics.[10, 16, 17] This paper is concerned with the eigenfunctions of low symmetry Jahn-Teller conical intersections, which occur in square-symmetric molecules such as porphyrins and phthalocyanines.[18, 19] In such molecules, non-degenerate asymmetric vibrations lower the molecular symmetry to lift the electronic degeneracy between adiabatic potential energy surfaces.

For nonadiabatic systems, Hunter[20] developed an exact factorization[21, 22] that closely parallels the Born-Oppenheimer factorization in many ways but also has fundamental differences. This factorization completely characterizes the exact eigenfunctions and is used to visualize nonadiabatic eigenfunctions here.[23-25] Each normalized eigenfunction is written as a product of a marginal vibrational factor and a conditional electronic factor. Like the Born-Oppenheimer factorization, each marginal vibrational factor is square-normalized for integration over all vibrational coordinates and, for every set of vibrational coordinates, each conditional electronic factor is square-normalized over the electronic coordinates. Unlike the Born-Oppenheimer factorization, the vibrational-coordinate dependent electronic factors vary from vibronic state to vibronic state and the vibrational factors are not orthogonal, which are both

heavy prices. However, since the square of the vibrational factor gives the total vibrational probability density,[24] Hunter's exact factorization is more natural for visualizing diffraction and imaging measurements[26, 27] that probe the total vibrational probability density.

If only two electronic states are involved, the electronic factor, which depends on the vibrational coordinates, can be fully specified by one electronic angle. As a result, as shown in ref. [23-25], a colored exact factorization with amplitude contours for the positive vibrational factor and color for the signed electronic factor provides complete visualization of real-valued nonadiabatic eigenfunctions with a single map.[24] This colored factorization led to the discovery of low dimensionality nodes in the exact factorization of nonadiabatic eigenfunctions[24] for an energy transfer Hamiltonian. These are in principle observable as isolated zeroes in the vibrational probability density. The dimensional considerations that govern the appearance of these nodes are similar to those for conical intersections between adiabatic potential energy surfaces; for two electronic dimensions over two vibrational dimensions, one obtains point nodes. Since the surrounding vibrational amplitude has the shape of an elliptical cone with the node at the vertex, these are called conical nodes.[24] These results do not contradict the idea that, with an infinite number of coupled electronic states, nonadiabatic couplings will always fill in nodes in the vibrational factor to some extent.[22, 28-30] In practice, they suggest observable weakly avoided vibrational zeroes of low dimensionality in the total vibrational probability density.[24]

Further exploration of a circularly symmetric Jahn-Teller Hamiltonian with a conical intersection that is submerged below the zero point level found that some eigenfunctions had vibrational amplitude at the conical intersection and some had essential nodes there.[25] These essential nodes are required by the circular symmetry when pseudo-rotation is excited and have

integer orders given by the electronic index, which arises from variation of the electronic state vector around an encircling path.[25] For an essential node, the electronic index also gives the local radial dependence of the vibrational probability amplitude factor. With circular symmetry, essential first order nodes are circular conical nodes. Nonadiabatic wavefunction amplitude at a conical intersection is consistent with conjectures about nonzero amplitude at a conical intersection[11, 12] and is critical for nonadiabatic tunneling.[31-33]

Here we examine the relationship between conical intersections and nonadiabatic nodes for a lower symmetry Jahn-Teller Hamiltonian[15] which occurs for square-symmetric molecules. Square-symmetric molecules have either D_{4h} symmetry (the point group symmetry of a square) or C_{4v} symmetry (the point group symmetry of a square with different colors on the two faces). In molecules belonging to these point groups (and also molecules belonging to the D_4 and D_{2d} point groups isomorphic to C_{4v}), the Jahn-Teller effect is driven by non-degenerate vibrations of two different symmetries, giving the conical intersection an elliptical shape,[34] which has no tilt along its major or minor axes. All vibrational-electronic eigenfunctions remain doubly degenerate. Square-planar D_{4h} porphyrins have 4 non-planar distortions: doming, propellering, and saddling/ruffling;[35] these give distorted equilibrium geometries with C_{4v}, D_4, and D_{2d} point group symmetry, respectively. As a result, any single non-planar distortion does not alter the form of the linear Jahn-Teller coupling Hamiltonian. In a silicon naphthalocyanine molecule with D_{4h} molecular symmetry, a submerged conical intersection with Jahn-Teller stabilization energies of ~1 meV drives electronic dynamics on ~100 fs timescales.[17, 36, 37]

In this paper, it will be shown that the lower symmetry around conical intersections in square-symmetric molecules has multiple consequences. Numerically exact calculations do not find nodes at the conical intersection. We found this numerical result surprising because the

conical intersection has no tilt or asymmetry to drive nodes to one side over the other, so analytic perturbation theory is then used to demonstrate this result. A numerical example shows that first order nodes move continuously as the equilibrium Jahn-Teller displacement of the coupling coordinate is varied. Another numerical example shows that n^{th} order nodes, when not required by symmetry, split into n first order nodes that locally conserve the electronic index. Numerical examples in which the frequency of the coupling coordinate is varied exhibit node creation and annihilation phenomena. Numerically, these creation (annihilation) events generate (destroy) two nodes which have equal and opposite electronic indices. It is found numerically and shown analytically that node creation and annihilation proceeds through a nonadiabatic point node with a non-conical structure and an electronic index of zero; these are called tangential nodes. These node creation and annihilation phenomena also conserve the electronic index locally, so long as no node crosses the closed path along which the electronic index is calculated. To address the question of whether the electronic index has a globally conserved character, we report numerical results demonstrating that conical nodes can move in towards the conical intersection from large radius. These results, along with avoided crossings between eigenstates with different electronic indices around the perimeter examined here, suggest a globally conserved large radius electronic index either does not exist or is not easily accessible in numerical studies. To justify the title, it is shown that square-symmetric Jahn-Teller Hamiltonians can have global elliptical symmetry. Although the ellipticity in the shape of the adiabatic conical intersection can be transformed away, it is demonstrated that ellipticity cannot be transformed away from the nonadiabatic Hamiltonian. Ellipticity generates amplitude at an energetically accessible conical intersection for all eigenstates examined here. Finally, we discuss how probability amplitude at conical intersections might be experimentally observed.

4.2. Theory

This section begins with a brief presentation of the standard linear Jahn-Teller coupling Hamiltonian for square-symmetric point groups in a diabatic basis.[18] From there, globally valid vibrational coordinate dependent adiabatic potential energy surfaces and adiabatic electronic eigenstates with maximum continuity through the conical intersection are developed. A colored representation of the adiabatic electronic eigenstates clearly shows the phase discontinuity or cut radiating out from the conical intersection on each surface. Conical intersections have a sign which specifies the direction of electronic phase evolution for any path encircling the conical intersection.[3] This sign impacts the non-adiabatic eigenfunctions and is defined by a line integral following ref. [25]. The doubly degenerate non-adiabatic eigenfunctions are uniquely chosen to be eigenstates of one reflection operator that follow a standard phase convention. This allows straightforward comparisons between eigenfunctions as Hamiltonian parameters are varied. After defining the colored exact factorization used for visualization of the complete nonadiabatic eigenfunctions, the integer electronic index developed in ref. [25] to quantify the electronic circulation[38] around a nonadiabatic node is defined and its key properties are briefly summarized.

4.2.1. *The Jahn-Teller Hamiltonian*

The Hamiltonian will be written down assuming the highest symmetry square-symmetric point group, D_{4h}, because symmetry species in the lower symmetry square-symmetric point groups can then be obtained through correlation tables.[34] Doubly degenerate electronic states subject to Jahn-Teller distortion have E_g or E_u symmetry at square-symmetric geometries. The (n_x, n_y) = (2,1) and (1,2) states for a particle in a 2D square box provide an example of an E_u

symmetry electronic state. Diabatic electronic basis states x and y for the *E* state are assumed to be independent of the vibrational coordinates. Dimensionless normal coordinates and their canonically conjugate momenta can be obtained from internal vibrational coordinates[39] by a canonical scale transformation[40] of the normal coordinates that necessarily scales their generalized or conjugate momenta. Using the $\{|x\rangle, |y\rangle\}$ basis and dimensionless normal coordinates, the square-symmetric linear Jahn-Teller coupling Hamiltonian[18] (divided by $\hbar$) is

$$\begin{aligned}\hat{\mathbf{H}} = &[(1/2)\omega_1(\hat{p}_1^2 + \hat{q}_1^2) + (1/2)\omega_2(\hat{p}_2^2 + \hat{q}_2^2)]\hat{\mathbf{I}} \\ &+\omega_1 d_1 \hat{q}_1[|x\rangle\langle x| - |y\rangle\langle y|] + \omega_2 d_2 \hat{q}_2[|x\rangle\langle y| + |y\rangle\langle x|]\end{aligned} \tag{4.1}$$

where ω_i are the Jahn-Teller active vibrational frequencies (*i* = 1 or 2), $\hat{q}_i$ and $\hat{p}_i$ are the dimensionless normal coordinate position and momentum operators, d_i are the equilibrium Jahn-Teller displacements for those vibrations in dimensionless normal coordinates, and $\hat{\mathbf{I}} = |x\rangle\langle x| + |y\rangle\langle y|$ is the electronic identity operator for the Jahn-Teller degenerate states. The first line is a harmonic oscillator Hamiltonian for two vibrations. The second line contains linear vibrational-electronic couplings, which are specified by the equilibrium Jahn-Teller displacement of the lower adiabatic potential energy surface. All vibrations without a linear Jahn-Teller coupling have been omitted. In this paper, all vibrational frequencies and energy eigenvalues will be given in wavenumbers (which must be multiplied by $2\pi c$ to convert into angular frequencies).

In the D_{4h} point group, the Jahn-Teller active asymmetric vibrations q_1 and q_2 have b_{1g} and b_{2g} symmetry, respectively (correlating to b_1 and b_2, respectively, in the 3 isomorphic lower symmetry groups). Using the terminology for more general conical intersections,[41] q_1 is the

tuning coordinate (*g*) and q_2 is the coupling coordinate (*h*). For a particle in a square 2D box, rectangular and diamond symmetry lowering deformations of the square box would have b_{1g} and b_{2g} symmetry.[37, 42-44] There are equal numbers of b_{1g} and b_{2g} vibrations in any D_{4h} symmetry molecule, but these Jahn-Teller active vibrations are non-degenerate (unlike other *n*-fold point group symmetries with Jahn-Teller distortions)[34]. Low frequency vibrations sometimes occur in b_{1g}/b_{2g} pairs with similar frequencies and Jahn-Teller displacements.[45] With equal frequencies ($\omega_1 = \omega_2$) and displacements ($d_1 = d_2$), this Hamiltonian generates[18] a circularly symmetric conical intersection.[13, 46]

4.2.2. *Adiabatic Surfaces*

The adiabatic electronic Hamiltonian is obtained by neglecting the kinetic energy operators and regarding the vibrational coordinates as parameters:

$$\begin{aligned}\hat{\mathbf{H}}_{elec}(q_1,q_2) = &[(1/2)\omega_1 q_1^2 + (1/2)\omega_2 q_2^2]\hat{\mathbf{I}} \\ &+\omega_1 d_1 q_1[|x\rangle\langle x| - |y\rangle\langle y|] + \omega_2 d_2 q_2[|x\rangle\langle y| + |y\rangle\langle x|].\end{aligned} \tag{4.2}$$

The adiabatic potential energy surfaces are obtained by diagonalizing the electronic Hamiltonian at each coordinate (q_1, q_2):

$$\hat{\mathbf{H}}_{elec}(q_1,q_2)\,|\pm; q_1, q_2\rangle = U_{\pm}(q_1,q_2)\,|\pm; q_1, q_2\rangle. \tag{4.3}$$

The adiabatic potential surfaces are the electronic energy eigenvalues,[47]

$$\begin{aligned}U_{\pm}(q_1,q_2) = &[(1/2)\omega_1 q_1^2 + (1/2)\omega_2 q_2^2] \\ &\pm\sqrt{(\omega_1 d_1 q_1)^2 + (\omega_2 d_2 q_2)^2}.\end{aligned} \tag{4.4}$$

As shown in Fig. 4.1, the two surfaces intersect at the origin (the square-symmetric geometry) and together form an elliptical double cone in its immediate neighborhood. Along the q_1-axis ($q_2 = 0$), slices through the pair of potential surfaces give parabolas with positive curvature that intersect at the origin and have their minima displaced to $q_1 = \pm d_1$, the equilibrium Jahn-Teller displacement parameter used here to specify the linear vibrational-electronic coupling. Both minima are lower than the conical intersection by the Jahn-Teller stabilization energy $(D\omega)_1 = (1/2)\omega_1 d_1^2$. Similar statements hold for the slice along the q_2-axis. In 2D, the minima for slices along the coordinate axis with the smaller stabilization energy become saddle points separating true minima along the coordinate axis with the larger stabilization energy. The lower surface has two symmetry related minima separated by two symmetry related saddle points and a local maximum that touches the bottom of the upper cone at its minimum.[18, 34] The point of contact between upper cone and lower surface is the conical intersection, and the two surfaces locally form an elliptical double cone around it. Moving from one adiabatic surface onto the other on passing through the conical intersection makes the pair of potential energy surfaces have continuous derivatives with respect to vibrational coordinates. For this reason, Longuet-Higgins et al. referred to the two adiabatic electronic eigenvalue surfaces as continuations of each other.[13]

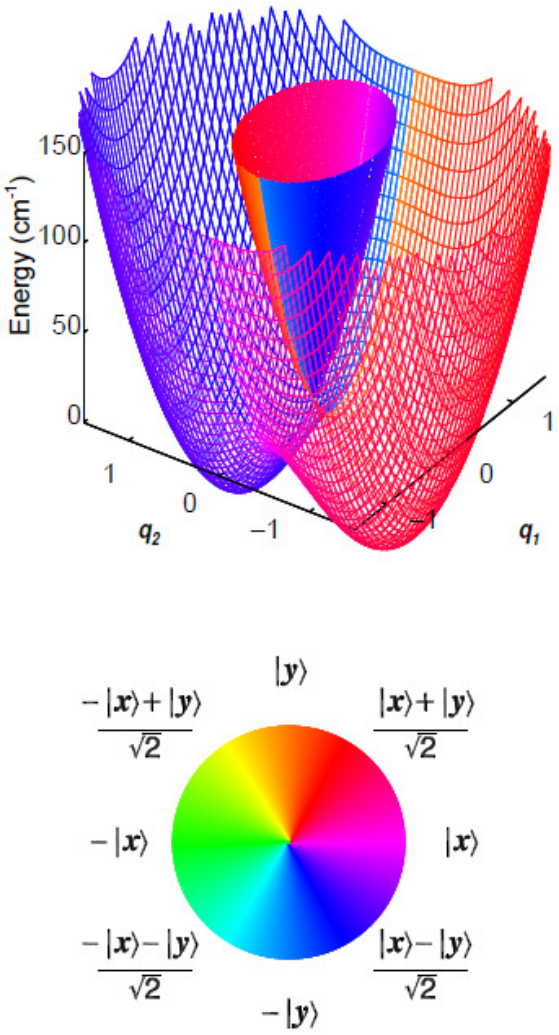

Figure 4.1: Potential Surfaces around the Conical Intersection for a Square-Symmetric Molecule

Top) The adiabatic potential energy surfaces for a doubly degenerate *E* symmetry electronic state as a function of Jahn-Teller active normal coordinates (q_1, q_2) with b_{1g} and b_{2g} symmetry. The Hamiltonian parameters in Eq. (4.1) have accidentally equal vibrational frequencies $\omega_1 = \omega_2 =$ 200 cm^{-1} with unequal displacements $d_1 = 0.4$ and $d_2 = 0.8$ along q_1 and q_2, respectively. The lower surface has minima [front right and back left] at $(0, \pm d_2)$ that are stabilized by $(D\omega)_2 = 64$ cm^{-1} below the conical intersection. The two saddle points [front left and back right] at $(\pm d_1, 0)$ are stabilized by $(D\omega)_1 = 16$ cm^{-1}. The upper cone has elliptical cross sections with major axes along q_1. The color of each potential surface at each coordinate indicates the adiabatic electronic eigenfunction according to the color wheel. Bottom) Color wheel used to indicate electronic eigenfunctions for the adiabatic potential surfaces above and for nonadiabatic eigenfunctions throughout the rest of the paper. The 2π angular range is divided into 64 discrete colors. The adiabatic potential surfaces have continuous coloring through the conical intersection and a sign-change discontinuity or cut (arbitrarily located along $q_2 = 0$) that is required by the geometric phase.

The real-valued adiabatic electronic energy eigenstates depend only on the adiabatic mixing angle

$$\phi(q_1, q_2) = \text{atan2}(\omega_2 d_2 q_2, \omega_1 d_1 q_1), \tag{4.5}$$

where atan2(y, x) extends arctangent(y/x) over a 2π range. Square-symmetry dictates the adiabatic electronic character up to a sign on the $q_1 = 0$ and $q_2 = 0$ lines, but does not dictate the quantitative electronic variation with angle in the (q_1, q_2) plane, which depends on the coupling parameters through Eq. (4.5). [In contrast, for circularly symmetric conical intersections, which have $\omega_1 d_1 = \omega_2 d_2$, the adiabatic mixing angle ϕ becomes equal to the polar coordinate in the (q_1, q_2) plane.] For real-valued eigenfunctions, Longuet-Higgins showed the adiabatic electronic eigenfunctions must encounter a sign change discontinuity for any closed curve encircling the conical intersection.[48] This sign change discontinuity or cut radiates out from the conical intersection point, but its location is arbitrary.[49] The adiabatic electronic eigenstates are chosen for maximum continuity as:

$$|-;\phi\rangle = \text{ssqw}(\phi/2)\{\sin(\phi/2)|x\rangle - \cos(\phi/2)|y\rangle\} \tag{4.6a}$$

for the lower adiabatic state and

$$|+;\phi\rangle = \text{csqw}(\phi/2)\{\cos(\phi/2)|x\rangle + \sin(\phi/2)|y\rangle\} \tag{4.6b}$$

for the upper adiabatic state. Eq. (4.6) has been simplified by defining a sinusoidal square wave function

$$\text{ssqw}(\vartheta) = \text{signum}[\sin(\vartheta)] \tag{4.7a}$$

and a cosinusoidal square wave function

$$\mathrm{csqw}(\vartheta) = \mathrm{signum}[\cos(\vartheta)] \qquad (4.7)\text{b}$$

by means of the standard[50] signum function

$$\mathrm{signum}(\xi) = \begin{cases} +1 & (\xi > 0) \\ 0 & (\xi = 0) \\ -1 & (\xi < 0) \end{cases} \qquad (4.8)$$

With this form of Eq. (4.6), the adiabatic mixing angle ϕ can take on any real value. The trigonometric square wave functions specify the locations of cuts (see Figure 4.1). Here, the cuts on the two surfaces have been arranged into a maximally continuous single cut along $q_2 = 0$ such that the lower surface cut for $q_2 < 0$ connects to the upper surface cut for $q_2 > 0$ and separates $\pm|y\rangle$ on both surfaces. Eq. (4.6) shows that $|+;\phi+\pi\rangle = |-;\phi\rangle$ everywhere except at the conical intersection point, where both are undefined. As can be seen from the surface colors in Fig. 4.1, moving from one adiabatic surface to the other on passing through the conical intersection makes the pair of adiabatic electronic eigenstates continuous across the conical intersection (except for the undefined electronic character of the separate surfaces at the conical intersection point). For this reason, Longuet-Higgins et al. also referred to the two adiabatic electronic eigenstates as continuations of each other.[13]

4.2.3 *The sign of the conical intersection*

Conical intersections have a sign[3] which can be defined by the sign of any counterclockwise line integral around the conical intersection:[25]

$$\gamma(C) = \frac{1}{2\pi}\int_C d\Theta^a(q_1, q_2). \qquad (4.9)$$

where $\Theta^a_{\pm}(q_1,q_2) \equiv \arctan\left[\left\langle y\middle|\pm;\phi\right\rangle / \left\langle x\middle|\pm;\phi\right\rangle\right]$ are diabatic to adiabatic transformation angles. From Eq. (4.6), the transformation angles are $\Theta^a_{-}(q_1,q_2) = (\phi - \pi)/2$ over the domain $\phi = (0, 2\pi)$ and $\Theta^a_{+}(q_1,q_2) = \phi/2$ over the domain $\phi = (-\pi, \pi)$; each becomes undefined at its cut. The line integral starts and stops at the cut for the single-valued Θ^a used here. For real-valued electronic states, the phase angle $2\pi\gamma(C)$ is an integer multiple of π and gives the adiabatic electronic sign discontinuity found by Longuet-Higgins[13, 48, 51, 52] for closed paths around a conical intersection (an example of a geometric phase [53]). The sign of a conical intersection, signum(γ), depends on the phase convention for the diabatic electronic basis set but not on arbitrary adiabatic eigenfunction sign or phase. Any line integral around the conical intersection is $\gamma(C) = +1/2$ for *either* surface in Fig. 4.1, so the sign of this conical intersection is positive.

4.2.4. *Exact nonadiabatic eigenstates*

The nonadiabatic eigenfunctions solve the full time-independent Schrodinger equation

$$\hat{\mathbf{H}}\psi_m(\mathbf{r}, q_1, q_2) = E_m\psi_m(\mathbf{r}, q_1, q_2) \tag{4.10}$$

and depend on both electronic (**r**) and vibrational coordinates. Although the degeneracy of the adiabatic potential energy surfaces is lifted everywhere but at the conical intersection, the nonadiabatic vibrational-electronic eigenstates of the square-symmetric Jahn-Teller Hamiltonian all remain doubly degenerate. The degeneracy arises because the total Hamiltonian in Eq. (4.1) has a molecular symmetry group[54] that remains isomorphic to the square-symmetric point group even when Jahn-Teller distortions lower the equilibrium point group symmetry.[18] The square-symmetric Hamiltonian separately commutes with two mutually non-commuting reflection operators σ_{v} and σ_{d}; this requires degeneracy[55] and imposes symmetries on the

eigenstates beyond those required by four-fold rotational symmetry. Under these reflection operators, the asymmetric coordinates and diabatic electronic basis states transform as:[37]

$$\sigma_{\mathrm{v}} q_1 = +q_1,\ \sigma_{\mathrm{v}} q_2 = -q_2, \tag{4.11a}$$

$$\sigma_{\mathrm{v}} |x\rangle = +|x\rangle,\ \sigma_{\mathrm{v}} |y\rangle = -|y\rangle, \tag{4.11b}$$

and

$$\sigma_{d} q_1 = -q_1,\ \sigma_{d} q_2 = +q_2, \tag{4.11c}$$

$$\sigma_{\mathrm{d}} |x\rangle = +|y\rangle,\ \sigma_{d} |y\rangle = +|x\rangle \tag{4.11d}$$

Pairs of doubly degenerate eigenstates can be chosen as simultaneous eigenstates of the Hamiltonian and either reflection operator.

When the conical intersection parameters generate circular symmetry, the eigenfunctions have an additional rigorous pseudo-rotation quantum number *j* and an approximate vibrational quantum number *v*. Vibrational quantum numbers characterize such eigenfunctions well in the limits of small *d* (circular 2D harmonic oscillator quantum numbers) and large *d* (separable adiabatic radial vibration on the lower surface).[13, 56] Circular 2D harmonic oscillator quantum numbers are used here to describe elliptical conical intersection eigenstates by correlation to eigenstates of a circular conical intersection with reasonably small Jahn-Teller displacement *d*. These quantum numbers are not "good" for elliptical conical intersections, just convenient correlation labels that provide an energetic point of reference.

4.2.5. *Colored exact factorization*

To simultaneously visualize a complete nonadiabatic eigenfunction, we use Hunter's exact factorization.[20, 29] Each normalized eigenfunction $\psi_m(\mathbf{r}, q_1, q_2)$ is written as a product of an everywhere positive marginal vibrational factor,

$$Þ_m(q_1, q_2) = \sqrt{\int \psi_m^*(\mathbf{r}, q_1, q_2)\psi_m(\mathbf{r}, q_1, q_2)\mathrm{d}\mathbf{r}}\,, \tag{4.12}$$

and a signed conditional electronic factor

$$\mathrm{K}_m(\mathbf{r}; q_1, q_2) = \psi_m(\mathbf{r}, q_1, q_2) / Þ_m(q_1, q_2)\,. \tag{4.13}$$

Like Born-Oppenheimer factors, each exact vibrational factor is square-normalized over the vibrational coordinate space and each conditional electronic factor is square-normalized over the electronic space (**r**) at each vibrational coordinate (q_1, q_2). The conditional electronic factor is a unit vector in the electronic state space. If the vibrational factor has a node, the exact factors are not separately acceptable wavefunctions, motivating the use of the Icelandic letter thorn to emphasize that the vibrational factor is the square root of the diagonal element of the reduced vibrational density operator obtained by tracing over electronic states. The exact vibrational factor for a real-valued nonadiabatic eigenfunction may have integer-order essential nodes if they are required by symmetry and accidental first order conical nodes, which become likely when the vibrational dimensionality exceeds the electronic dimensionality. When only two electronic states (*x* and *y*) are involved, the exact electronic factor at each set of vibrational coordinates can be fully specified (in character and phase) for each nonadiabatic state *m* by the electronic angle

$$\begin{aligned}\Theta_m(q_1, q_2) &\equiv \mathrm{atan2}(\langle y|\psi_m\rangle, \langle x|\psi_m\rangle) \\ &= \mathrm{atan2}(\langle y|\mathrm{K}_m\rangle, \langle x|\mathrm{K}_m\rangle),\end{aligned} \tag{4.14}$$

which becomes undefined if the vibrational factor is zero. Representing the positive vibrational factor by amplitude contours and the signed electronic factor by color (referencing the color wheel in Figure 4.1) allows a single map to completely specify a real-valued nonadiabatic eigenfunction.[24] A price paid for using this colored exact factorization is that visualization of linear combination states requires thinking about how the mixing of colors represents the addition of vibrational amplitude weighted electronic factors.

4.2.6. *The electronic index*

A key property of the nonadiabatic eigenfunctions is the electronic index $\eta(C)$ for line integrals around any simple closed counterclockwise path *C* in the vibrational coordinate space that does not pass through a node,[25]

$$\eta(C) = \frac{1}{2\pi} \oint_C d\Theta_m(q_1, q_2) \,. \tag{4.15}$$

Visually, the electronic index equals the integer number of net counterclockwise turns around the color wheel on the path *C*. Like the sign of a conical intersection, the electronic index depends on the phase convention for the diabatic electronic basis states $|x\rangle$ and $|y\rangle$, but is independent of the arbitrary overall sign of the eigenfunction. As a result, electronic indices for different eigenstates are significant relative to each other. For a two-dimensional electronic state space over a two dimensional vibrational space, ref. [25] proved that the integer electronic index depends only on the number, order, and sign of the nonadiabatic nodes enclosed by the path.

4.3. Calculations

The diabatic basis set Hamiltonian diagonalization computations are similar to those in ref. [25]. For high spatial resolution, harmonic oscillator basis state coefficients are found and used to construct eigenfunctions. All harmonic oscillator basis states are centered at the origin. Harmonic oscillator matrix elements are obtained analytically.[36, 39] Calculations use a truncated vibronic Hamiltonian matrix that includes all vibrational states with $v_1 + v_2 \leq N$ (roughly, this includes all 2D harmonic oscillator basis states up to a certain energy, which provides faster convergence compared to the separate maxima for v_1 and v_2 used in ref. [25]). The number of vibrational basis states on each diabatic electronic state is $(N+1)(N+2)/2$, so each calculation includes a total of $(N+1)(N+2)$ diabatic vibronic basis states. The Hamiltonian is diagonalized using the DEVCSF routine from the IMSL library which uses an implicit QR algorithm[57] to evaluate eigenvalues and eigenvectors. All results shown are for N=39. In addition to the convergence checks in ref. [25], the eigenvalues were checked for accuracy against Judd's exact results,[58] which provide some analytic eigenvalues for specific circular symmetry conical intersection parameters (see Table A.1 in Appendix A and Figure 1.7 in Chapter 1). This check indicates 14-digit numerical accuracy for the eigenvalues. Table 1.2 and Figure 1.8 (also in Chapter 1) show eigenvalues for a square-symmetric Hamiltonian.

A numerically stable basis set rotation is applied to each pair of degenerate eigenstates to find states with σ_d symmetry.[37] The basis set is then rotated by $\pi/4$ to find states with σ_v symmetry. These states are then separated into states with eigenvalues of $+1$ and -1 with respect to the σ_v operator. Finally, overall eigenfunctions signs are chosen to match perturbation theory results for small d_2. All of the nonadiabatic eigenfunctions shown in the main body of

this paper have a σ_v eigenvalue of +1 so that $\sigma_v |\psi_m\rangle = +|\psi_m\rangle$. Pairs of degenerate eigenstates of σ_v and the alternative representation of each pair as eigenstates of σ_d are shown together in Appendix C Fig. C.1.

4.4. Results

4.4.1. *Effects of unequal linear Jahn-Teller couplings*

Fig. 4.2 shows the colored exact factorization of the lowest eigenstates for several Jahn-Teller Hamiltonians with different equilibrium displacements for the coupling coordinate. (Fig. 1.8 shows that the energy eigenvalues undergo avoided crossings[59] as a function of the linear Jahn-Teller coupling parameter d_2.) In the rightmost column of Fig. 4.2, both Jahn-Teller displacements are $d_1 = d_2 = 0.4$, generating a circularly symmetric conical intersection. This circularly-symmetric case is not general, and differences between d_1 and d_2 are expected for square-symmetric molecules. The eigenstates in the rightmost column are similar to those in column 1 of Fig. 4.2 from ref. [25] where $d_1 = d_2 = 0.316$. However, some arbitrary overall eigenfunction signs are different here in order to more simply connect with results from perturbation theory starting from Hougen's accidental Born-Oppenheimer[18] case. For $d_2 = 0$, the phases have been chosen to agree with the phase convention of Papousek and Aliev[39] as in ref. [25].

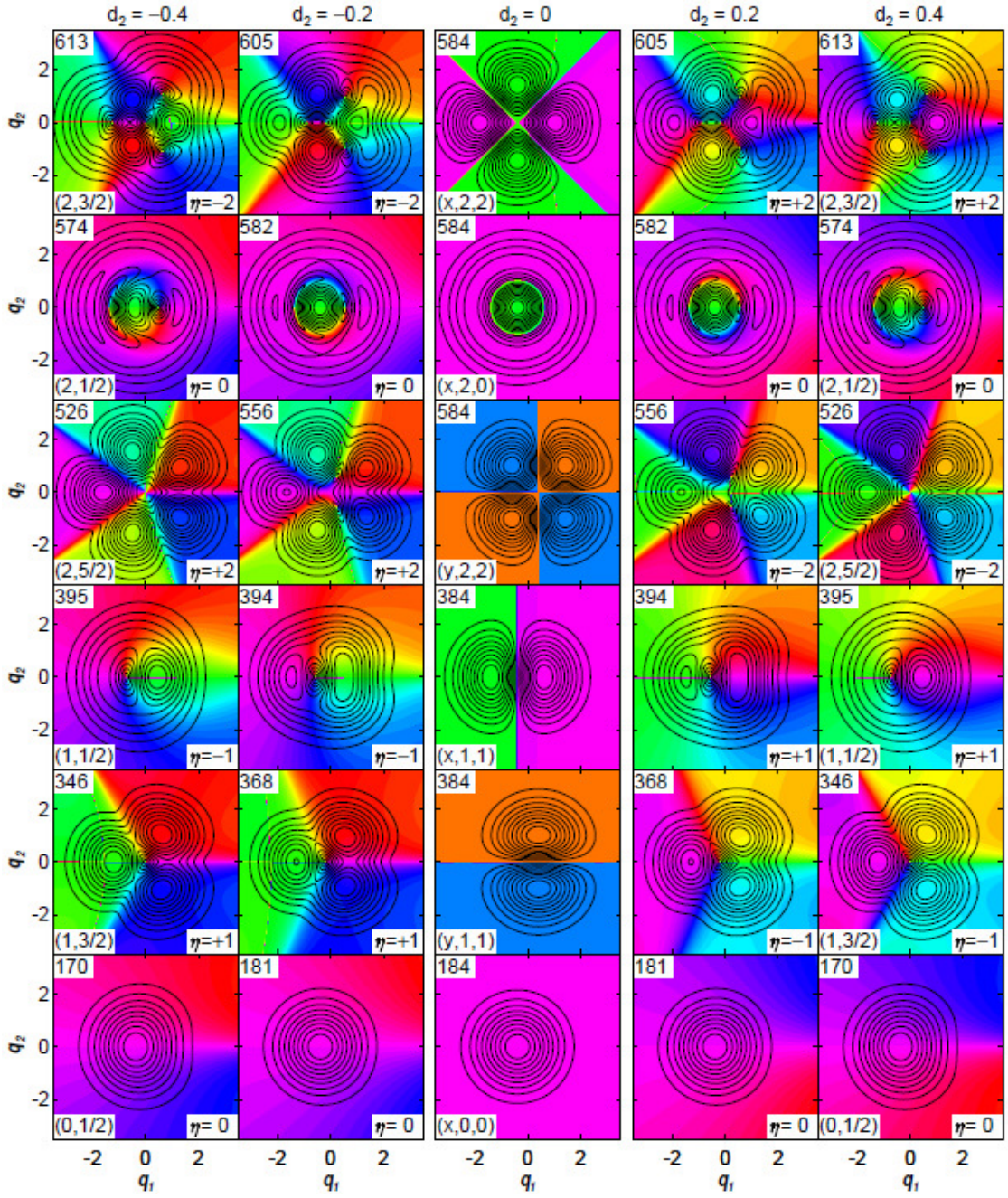

Figure 4.2: Effects of varying Jahn-Teller displacement for the coupling coordinate

The five columns each have showing the probability amplitude and electronic character of the six lowest energy eigenstates with $\sigma_v = +1$ for the Jahn-Teller Hamiltonian with vibrational frequencies $\omega_1 = \omega_2 = 200$ cm^{-1} and Jahn-Teller displacement $d_1 = 0.4$ for the tuning coordinate. The five columns systematically vary the Jahn-Teller displacements d_2 for the coupling coordinate. In each panel, the contour interval is 10% of the maximum probability amplitude for that state, with thicker contour lines for higher amplitude. The color wheel in Figure 4.1 is used

to represent electronic character. In each column, the lowest energy state is on the bottom and energy increases upward. In each panel, the label at upper left gives the eigenstate energy in wavenumbers and the label at lower right specifies the electronic index η for paths around the perimeter. The leftmost and rightmost columns have circular symmetry conical intersections with opposite signs. These eigenstates have a good vibrational quantum number v and a rigorous absolute value of the half-odd integral pseudo-rotation quantum number $|j|$ given at lower left $(v,|j|)$. In each column, three have essential nodes of order $(|j|-1/2)$ at the conical intersection (346, 526, and 613), and three have accidental conical nodes elsewhere (395, 574, and 613). The second and fourth columns have nonadiabatic Hamiltonians with elliptical conical intersections, which break pseudo-rotation symmetry. The eigenstates do not have rigorous quantum numbers beyond σ_v and have only accidental conical nodes. None of the accidental nodes occur at the conical intersection at the origin. The middle column is an accidental Born-Oppenheimer case with adiabatic nodal lines or curves indicated by abrupt color changes. In the middle column, degenerate states are chosen so each has a definite adiabatic electronic state (x or y), vibrational quantum number v, and absolute value of the vibrational angular momentum $|\ell|$ about the equilibrium geometry on its adiabatic potential surface given at lower left $(x/y,v,|\ell|)$.

In all five columns of Fig. 4.2, every $\sigma_v = +1$ eigenstate shown is degenerate with an eigenstate having $\sigma_v = -1$ and any linear combination of the degenerate eigenstates is also an energy eigenstate. Linear combinations of the doubly degenerate eigenstates with $\sigma_v = \pm 1$, $\sigma_d = \pm 1$, and signed pseudo-rotation quantum numbers $\pm j$ are shown for a circularly symmetric conical intersection in Fig. 3.2 (Fig. 2 from ref. [25]) and the transformations between them are discussed there. Fig. C.1 shows the set of $\sigma_v = \pm 1$ and $\sigma_d = \pm 1$ eigenfunctions for the elliptical conical intersection in the fourth column of Fig. 4.2.

Important differences between the states studied here and those studied in ref. [25] arise because circular symmetry generates a conserved pseudo-rotation quantum number j. In Fig. 4.2, some circular symmetry eigenstates have higher order essential nodes that do not occur without pseudo-rotation symmetry. Essential nodes occur because j takes on half-odd integral

values ($-v - 1/2, \ldots -3/2, -1/2, +1/2, +3/2 \ldots v + 1/2$) and requires radial amplitude power law exponents of at least $\Phi_{v,j}(\rho,\phi) \propto \rho^{|j|-(1/2)}$ in the vibrational amplitude.[25] Further, these essential nodes have an electronic index with a magnitude of exactly $|j|-(1/2)$ for simple closed counterclockwise paths that encircle the essential node but do not encircle any other node. This index is negative (clockwise around the color wheel for a counterclockwise path) for all three essential nodes in the rightmost column of Fig. 4.2 and positive (counter-clockwise around the color wheel for a counterclockwise path) for the three essential nodes in the leftmost column of Fig. 4.2. This change in sign of the index is accompanied by a change in sign of the conical intersection. The leftmost column in Fig. 4.2 here differs from Fig. 3.6 (Fig. 6 of of ref. [25]) in reversing the sign of the conical intersection by changing the sign of d_2 instead of d_1. Examination of the Hamiltonian in Eq. (4.1) shows that changing the sign of the equilibrium Jahn-Teller displacement d_i is equivalent to changing the sign of the coordinate q_i. While both the electronic index of a node and the sign of a conical intersection depend on the phase convention for the electronic basis states, their physically meaningful ratio does not. As proven in ref. [25], the electronic index for a simple closed path that encircles several nodes is the sum of the electronic indices for the enclosed nodes. Such summed electronic indices are stable with respect to the symmetry lowering perturbations in the second and fourth columns of Fig. 4.2. However, as the displacement d_2 is varied over a wider domain from 0 to 1 for this family of square-symmetric Jahn-Teller Hamiltonians (in which all other parameters remain fixed), Fig. 1.8 shows avoided crossings between states with different summed electronic indices; these avoided crossings indicate that the summed electronic indices are not globally conserved over the vibrational coordinate region shown in Fig. 4.2.

The changes in coupling coordinate displacement from left to right in Fig. 4.2 lower the symmetry of and then annihilate a negative conical intersection at an accidental adiabatic point before creating a positive conical intersection and restoring circular symmetry. Two level crossings occur as the conical intersection is annihilated: eigenstates correlating to $(v=1,|j|=3/2)$ and $(v=1,|j|=1/2)$ on the left cross at $d_2=0$ to correlate with $(v=1,|j|=1/2)$ and $(v=1,|j|=3/2)$, respectively, on the right; similarly, $(v=2,|j|=5/2)$ and $(v=2,|j|=3/2)$ on the left cross to become $(v=2,|j|=3/2)$ and $(v=2,|j|=5/2)$, respectively, on the right; $(v=2,|j|=1/2)$ passes through this higher energy level crossing. (The level crossings at $d_2=0$ are examined closely in Fig. C.2 in Appendix C.) For each eigenstate, the electronic index for paths around the perimeter is conserved through these crossings over the range of equilibrium Jahn-Teller displacements shown in Fig. 4.2.

4.4.2. *Nodes Near, but not at, Conical Intersections*

In square-symmetric molecules, Hamiltonians with circular symmetry and their eigenstates with essential nodes are improbable (zero probability) because they require two exact equalities between continuously variable parameters. Similarly, the adiabatic case with nodal lines and curves in the middle column is improbable (zero probability) because it requires that one parameter be exactly zero. The eigenfunctions shown in the second and fourth columns of Figure 4.2 also require a one parameter equality (equal frequencies) for square-symmetric molecules. For these nonadiabatic eigenfunctions, the only nodes are accidental conical nodes, each with an elliptical shape. So long as no node crosses the enclosing path as the Hamiltonian symmetry is lowered, the electronic index for the square-symmetric case is equal to the electronic index for the circularly symmetric case. For 5 of the 6 states in Fig. 4.2, conical nodes

simply change their position continuously as a function of coupling coordinate displacement until they disappear along with the conical intersection at $d_2 = 0$. For the 6th state $(v = 2, |j| = 5/2)$, the essential second order node splits into two first order conical nodes with the same sign as the symmetry is lowered. This splitting preserves the total electronic index for small radius paths that enclose the origin and both split nodes.

Conical nodes need not occur at the conical intersection for elliptical conical intersections in square-symmetric molecules. Close inspection of columns 2 and 4 in Fig. 4.2 indicates that conical nodes occur near the conical intersection, but not at the conical intersection. This result can be understood based on the nonadiabatic eigenstates shown in Fig. 4.3, which can be accurately obtained from first order degenerate perturbation theory starting from a basis of eigenstates for $d_2 = 0$.

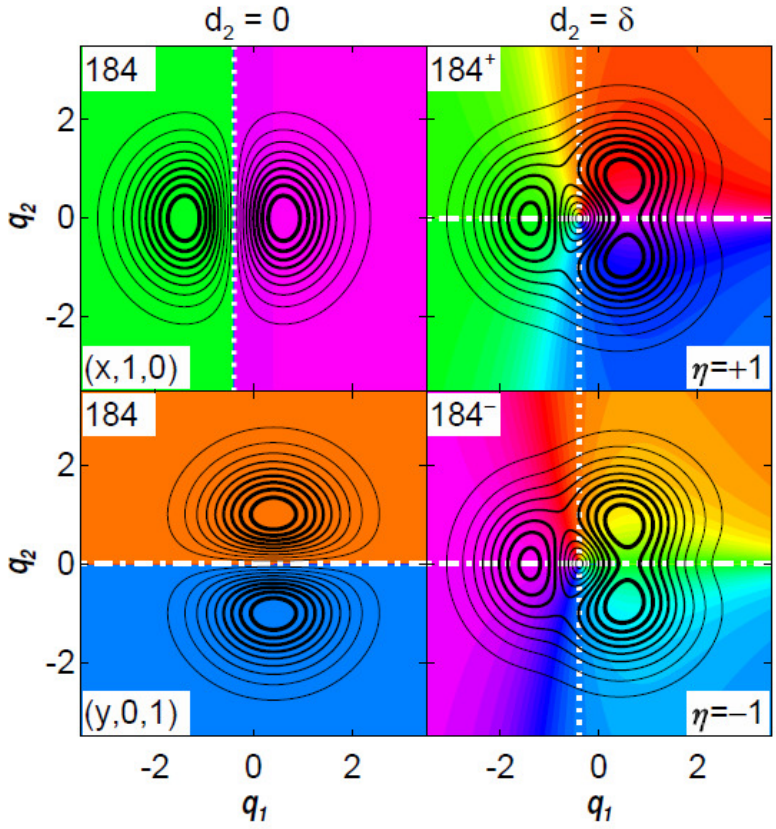

Figure 4.3: Accidental Conical Nodes are near but not at the Conical Intersection

Left Column) Probability amplitude and electronic character for eigenfunctions with $\sigma_v = +1$ and one quantum of vibration for an accidental Born-Oppenheimer Hamiltonian with parameters $\omega_1 = \omega_2 =$ 200 cm^{-1}, $d_1 = 0.4$, and $d_2 = 0$. Contour intervals are 10% of each state's maximum probability amplitude, and are thicker for higher amplitude. The top eigenfunction has quantum numbers $(x, v_1 = 1, v_2 = 0)$ and has a vertical nodal line (dotted white) through the equilibrium geometry of adiabatic electronic state x, $(q_1 = -d_1, q_2 = 0)$. The bottom eigenfunction has quantum numbers $(y, v_1 = 0, v_2 = 1)$ and has a horizontal nodal line (dot-dashed white) through the equilibrium geometry of adiabatic electronic state y, $(q_1 = +d_1, q_2 = 0)$. Both energy eigenvalues are exactly 184 cm^{-1}. Right Column) Probability amplitude and electronic character for eigenfunctions with $\sigma_v = +1$ and one quantum of vibration for a nonadiabatic Hamiltonian with parameters $\omega_1 = \omega_2 =$ 200 cm^{-1}, $d_1 = 0.4$, and $d_2 = \delta$, where $\delta = 10^{-10}$. The nonadiabatic energy eigenvalues are nondegenerate, with shifts of ±6.818×10^{-9} cm^{-1} to 184$^+$ (top) and 184$^-$ (bottom). For both nonadiabatic eigenfunctions, the dot-dashed and dashed nodal lines of the projections onto adiabatic basis states intersect at the conical node, which occurs at $(q_1 = -d_1, q_2 = 0)$ in the limit as δ tends to zero.

In square-symmetric molecules, the equilibrium Jahn-Teller displacements along any pair of Jahn-Teller active modes are independent of each other. When either displacement d_i is zero, the Jahn-Teller Hamiltonian accidentally becomes an adiabatic Hamiltonian with analytic solutions.[18] The adiabatic electronic eigenstates become $|x\rangle$ and $|y\rangle$, which are allowed to cross because they have different symmetries. The vibrational coordinates q_1 and q_2 become separable, with harmonic oscillator quantum numbers v_1 and v_2 (this basis is useful even when the vibrational frequencies are different). With $d_2 = \delta$, the degenerate adiabatic states $|x\rangle|v_1 = 1\rangle|v_2 = 0\rangle$ and $|y\rangle|v_1 = 0\rangle|v_2 = 1\rangle$ both have $\sigma_v = +1$ and are directly coupled by the off-diagonal tuning coordinate perturbation operator

$$\hat{H}_1 = \omega_2 \delta \hat{q}_2 [|x\rangle\langle y| + |y\rangle\langle x|]. \tag{4.16}$$

The direct matrix element coupling these two states is given by

$$\begin{aligned} H_{y01,x10} &= \langle v_2^y = 1|\langle v_1^y = 0|\langle y|\hat{H}_1|x\rangle|v_1^x = 1\rangle|v_2^x = 0\rangle \\ &= \omega_2 \delta \langle v_1^y = 0|v_1^x = 1\rangle\langle v_2^y = 1|q_2|v_2^x = 0\rangle \\ &= \omega_2 \delta\, [\sqrt{2} d_1 \exp(-d_1^2)][1/\sqrt{2}] \end{aligned} \tag{4.17}$$

On the last line, the first factor in brackets is the Franck-Condon overlap integral for mode 1 (relative to each other, the electronic states x and y are displaced by $2d_1$), and the second factor in brackets is the harmonic oscillator matrix element for mode 2. For the parameters used in Fig. 4.3, $H_{y01,x10} \approx 6.817\times10^{-9}$ cm^{-1}. Degenerate first-order perturbation theory[55] yields the eigenstates

$$|\psi_+\rangle = (1/\sqrt{2})[|y\rangle|v_1 = 0\rangle|v_2 = 1\rangle + |x\rangle|v_1 = 1\rangle|v_2 = 0\rangle] \tag{4.18}$$

and $$|\psi_-\rangle = (1/\sqrt{2})[|y\rangle|v_1 = 0\rangle|v_2 = 1\rangle - |x\rangle|v_1 = 1\rangle|v_2 = 0\rangle] \quad (4.19)$$

with eigenvalues

$$E_{\pm}^{(1)} = E^{(0)} \pm H_{y01,x10}\,. \quad (4.20)$$

Since δ is positive, the lower eigenstate is the antisymmetric linear combination and the upper eigenstate is the symmetric linear combination. For this pair of states, all other couplings are of second order. Since the contributing adiabatic basis states have nodal lines that cross, their crossing point locates the conical node at $(q_1 = -d_1, q_2 = 0)$.

A slightly more complicated analysis can be performed for states with 2 quanta of vibration (see the discussion of perturbation theory for two-quanta states in the Supplementary Material). In this analysis, vibrational eigenstates of the 2D harmonic oscillator having definite absolute values of the vibrational angular momentum $|\ell|$ form a natural basis when the Jahn-Teller displacement for mode 1 also approaches zero. The eigenstates with 2 quanta in Fig. 4.2 still bear a resemblance to linear combinations of these natural basis states, which are shown for $d_2 = 0$. These analyses can also be generalized to unequal vibrational frequencies. Thus, perturbation theory shows that conical nodes can occur off the elliptical conical intersection for square-symmetric molecules.

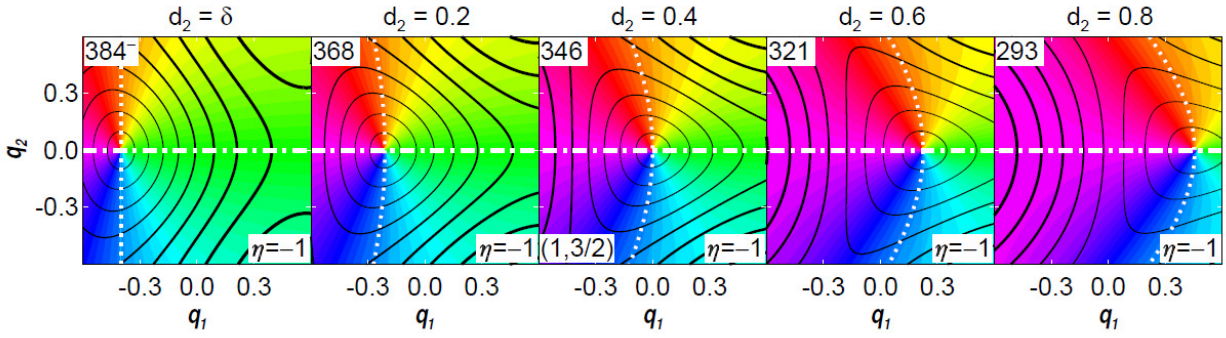

Figure 4.4: Varying the coupling coordinate displacement

The five panels show how variation of d_2 affects the conical node in the second lowest energy $\sigma_v = +1$ eigenstate of the Jahn-Teller Hamiltonian with vibrational frequencies $\omega_1 = \omega_2 = 200$ cm^{-1} and $d_1 = 0.4$. Panels are labeled at upper left by the eigenstate energy in cm^{-1}. Each panel overlays the nodal curves in the eigenfunction projections onto adiabatic electronic states x (dotted white curve) and y (dot-dashed white line). Contour intervals are 10% of maximum amplitude. From left to right: $d_2 = \delta$) here $\delta = 10^{-10}$ and the conical node is located at $q_1 = -d_1 = -0.4$. This is a close-up of the lower right panel in Fig. 4.3.; $d_2 = 0.2$) the conical node is located at about $q_1 \approx -0.210$. This is a close-up of the eigenfunction in the second row and fourth column of Fig. 4.2.; $d_2 = 0.4$) here, $d_1 = d_2$ and the node lies exactly on the circular conical intersection at the origin. This is a close-up of the eigenfunction $(v = 1, |j| = 3/2)$ in the fifth column of Fig. 4.2; $d_2 = 0.6$) the node has continued shifting further to the right and lies at about $q_1 \approx 0.225$; $d_2 = 0.8$) the node has continued shifting further to the right and lies at $q_1 \approx 0.455$. The Hamiltonian parameters in this rightmost panel match those for the adiabatic potential energy surfaces in Fig. 4.1.

Fig. 4.4 shows that the locations of nodes in nonadiabatic eigenstates vary continuously as a function of the Jahn-Teller displacement for the coupling mode. The conical intersection lies at the origin for all d_2. As d_2 increases, the vertically elongated elliptical conical node gradually approaches the origin for $d_2 = d_1$ (where it becomes circular), and then moves beyond it and becomes horizontally elongated.

For elliptical conical intersections in square-symmetric molecules, all of the energy levels are doubly degenerate, which raises the question: Are the conical nodes "accidental" in the sense

that they can be removed by a change in degenerate basis? A perturbation theory analysis of the $\sigma_v = -1$ eigenstates with one vibrational quantum exactly parallels the one above and shows that their conical nodes occur at $(q_1 = +d_1, q_2 = 0)$. Taking complex-valued linear combinations of degenerate states with $\sigma_v = \pm 1$ thus proves that the conical nodes in Fig. 4.3 are accidental. The doubly degenerate sets of $\sigma_v = \pm 1$ and $\sigma_d = \pm 1$ eigenstates in Fig. C.1 all have conical nodes, but the nodes are on opposite sides of the conical intersection for the two eigenstates in each degenerate pair. This shows that the conical nodes for elliptical conical intersections in Fig. 4.2 are all accidental. The results are not particular to the symmetries chosen: Fig. C.3 in Appendix C shows many basis-set rotations of a degenerate eigenstate pair and all have the same number of conical nodes with node coordinates in one related to the node coordinates in the other by inversion through the conical intersection. These relationships between nodal coordinates within each degenerate pair are relevant for measurement of point zeroes in the total vibrational probability density (see discussion).

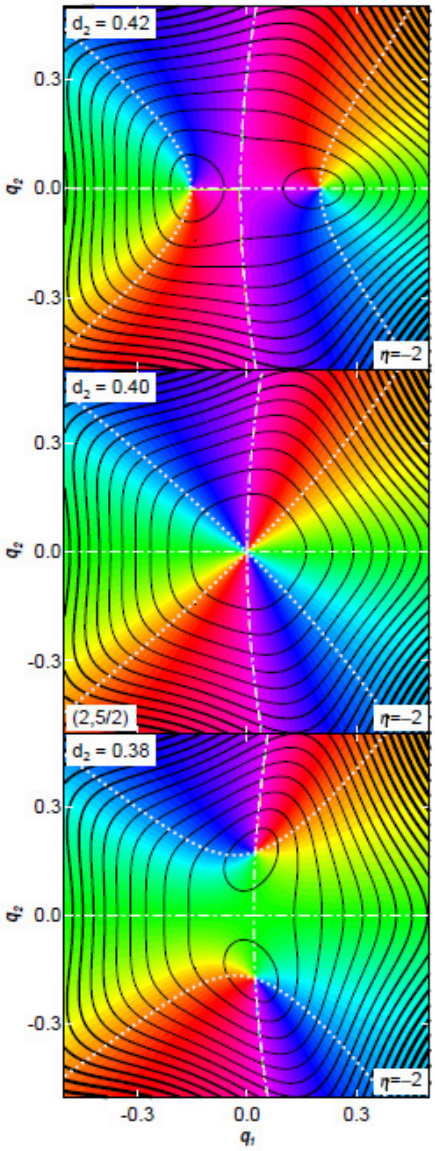

Figure 4.5: Splitting of Second Order Nodes

All panels show the $\sigma_v = +1$ eigenstate correlating to $(v = 2, |j| = 5/2)$ for parameters $\omega_1 = \omega_2 = 200$ cm^{-1} and $d_1 = d_2 =$ 0.4, as the coupling coordinate displacement d_2 changes from panel to panel. Each panel overlays the nodal curves in the eigenfunction projections onto adiabatic electronic states *x* (dotted white curve) and *y* (dot-dashed white line). The contour interval is 2% of each state's maximum amplitude, with thicker contours for higher amplitudes. Top) $d_2 = 0.42$ gives rise to two conical nodes with index -1 to the left and right of the origin. Middle) $d_2 = 0.4 (= d_1)$ shows the second order node with an electronic index of -2. This second order node arises from the intersection of four nodal lines at the origin, Bottom) $d_2 = 0.38$ generates two conical nodes with electronic index -1 above and below the origin.

When $\omega_1 = \omega_2 = 200$ cm^{-1} and $d_1 = d_2 =$ 0.4, Fig. 4.2 shows that the $(v = 2, |\, j \,| = 5/2)$ eigenstate has a second order node. The middle panel of Fig. 4.5 shows that this second order node arises from the simultaneous intersection of two nodal curves in the projection onto adiabatic electronic state *x* with two nodal curves in the projection onto *y*. In each projection, these nodal curves intersect at a 90° angle at the origin because of the circular symmetry of the conical intersection. When this circular symmetry is broken, however, the nodal curves in each adiabatic projection need not pass through the conical intersection at the origin and need not intersect (ref. [60] discusses non-intersecting nodal curves). As shown in the top and bottom panels of Fig. 4.5, the second order node separates into two first order nodes with the same sign. The splitting preserves the total electronic index for any simple closed path that encircles both conical nodes and the origin in all three cases. Fig. C.4 in Appendix C shows, for states with n = 1-5, that n^{th} order nodes at the circularly symmetric conical intersection split into n conical nodes for slightly unequal frequencies. The first order conical nodes have the generic elliptical shape. The sum of the electronic indices for the first order nodes arising from the split equals the electronic index of the higher order parent node.

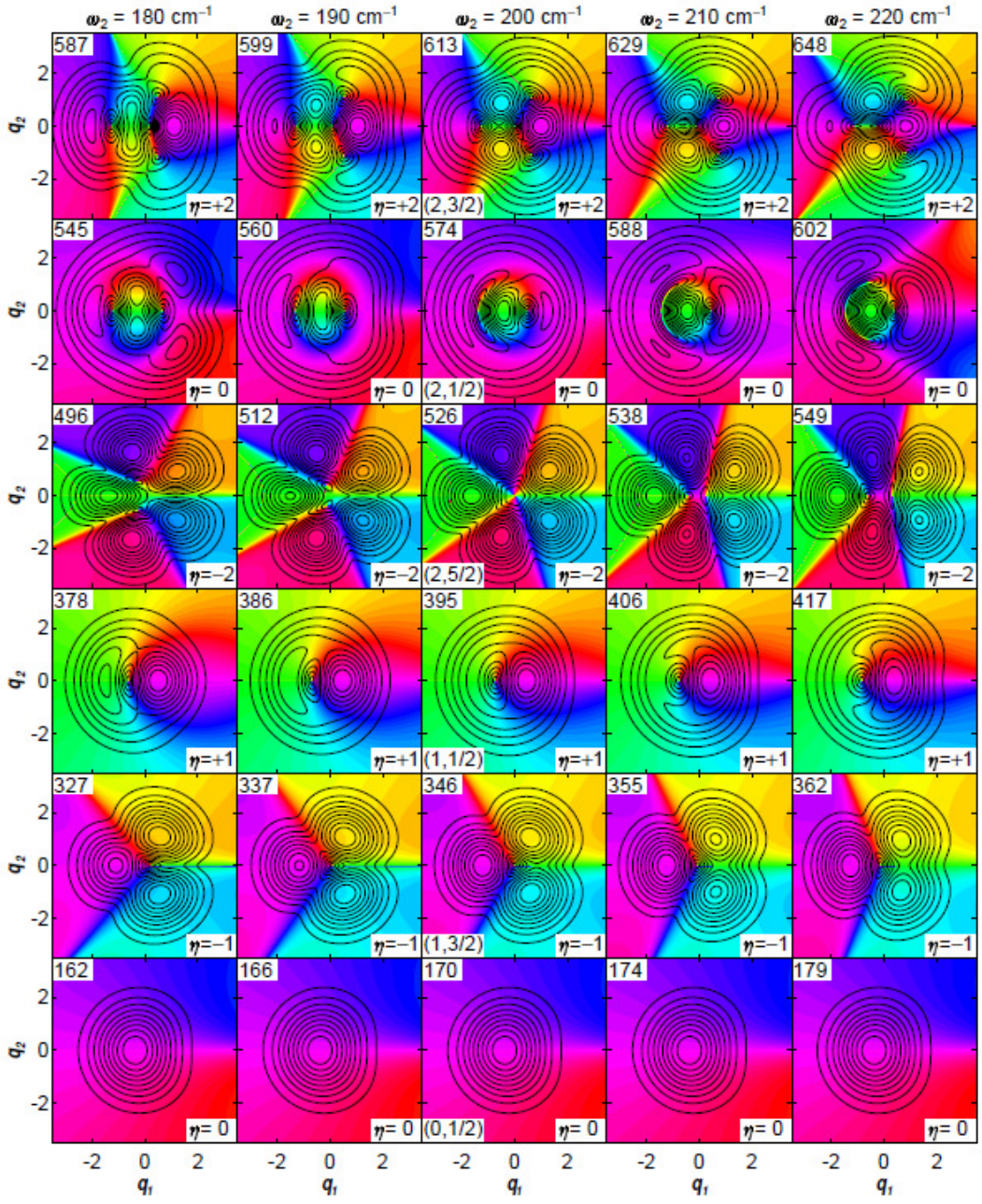

Figure 4.6: Effects of varying frequency for the coupling vibration

The probability amplitude and electronic character for the six lowest energy $\sigma_v = +1$ eigenstates of the Jahn-Teller Hamiltonian are shown for vibrational frequency $\omega_1 = 200$ cm^{-1} and $d_1 = d_2 =$ 0.4. Each column has a different coupling vibration frequency ω_2 given at the top. The contour interval is 10% of the maximum probability amplitude for each state, with thicker contours for higher amplitude. Color represents electronic character as shown in the color wheel in Figure 4.1. Energy eigenvalues are given in cm^{-1} at the upper left of each panel. The eigenfunctions in the center column match the rightmost column of Fig. 4.2 and have quantum numbers $(v,|\,j\,|)$ in the lower left of each panel.

4.4.3. *Conical Node Creation and Annihilation via Tangential Nodes*

Fig. 4.6 shows the eigenfunctions as the coupling vibration frequency is changed while the tuning vibration frequency remains fixed and the Jahn-Teller displacements remain equal. When the frequencies are equal (center column), the Hamiltonian and conical intersection are circular. Since the Jahn-Teller stabilization energy for the coupling vibration is given by $(D\omega)_2 = (1/2)\omega_2 d_2^{\,2}$, an increase (decrease) in frequency ω_2 destroys the circular symmetry of the adiabatic potential surfaces by creating minima (maxima) at $q_2 = \pm d_2$. By stretching the adiabatic potential surfaces vertically, these distortions generate elliptical conical intersections for the other four columns of Fig. 4.6. For the nonadiabatic Hamiltonian, unequal vibrational frequencies introduce an asymmetry in the kinetic energy operator that does not occur for unequal displacements alone. Comparing the states correlated to $(v = 2, |\, j \,| = 1/2)$ in row 5, columns 3-5 of Fig. 4.6 shows a node creation phenomenon not seen in Fig. 4.2, but the electronic index around the perimeter of each panel is stable.

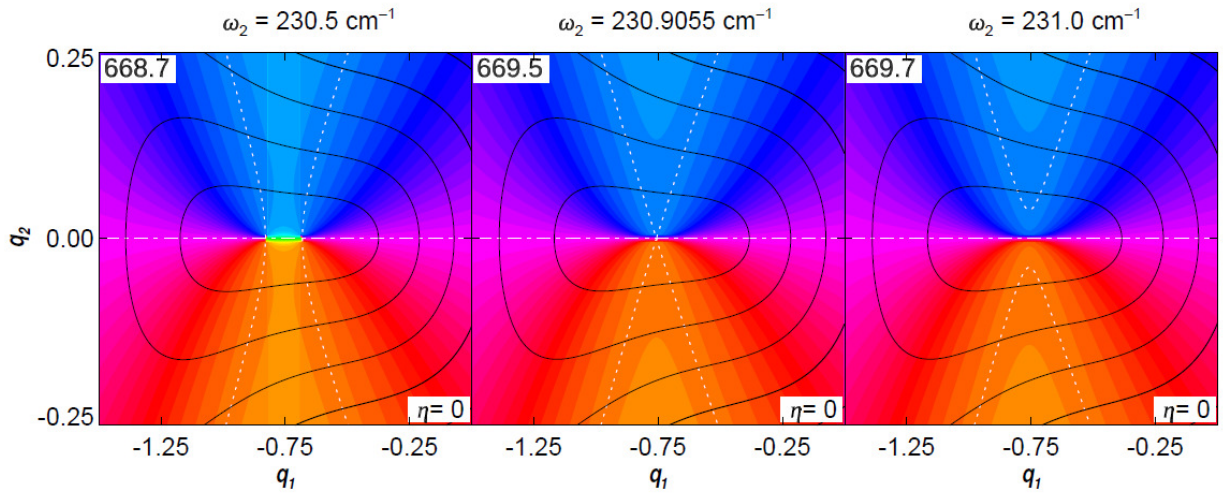

Figure 4.7: Creation and Annihilation of Conical Nodes through a Tangential Node

Close-up view of the nonadiabatic eigenfunctions correlated to $(v = 2, |\, j \,| = 3/2)$ for fixed Jahn-Teller Hamiltonian parameters of $\omega_1 = 200$ cm^{-1} and $d_1 = d_2 = 0.4$ as ω_2 is increased beyond the range shown in Fig. 4.6. Each panel overlays the nodal curves in the eigenfunction projections onto adiabatic electronic states *x* (dotted white curve) and *y* (dot-dashed white line). For each state, the contour interval is 10% of its maximum amplitude, with thicker contours for higher amplitude. Axis ranges are in a 3:1 ratio. Left) Two conical nodes still remain where nodal curves on *x* intersect the horizontal nodal line on *y*. The left and right conical nodes have electronic indices of -1 and +1, respectively. Middle) The two oppositely signed nodes combine to annihilate one another when the nodal curves on *x* cross each other at $\omega_2 \approx 230.9055$ cm^{-1}. Right) Having crossed, the two nodal curves on *x* swap connections to avoid each other and do not cross the nodal line on *y*, so there are no nodes.

As the vibrational frequency is changed, pairs of oppositely signed nodes can be created or annihilated. Fig. 4.7 shows an instance of this by extending the frequency difference beyond the domain shown in the top row of Figure 4.6. At the frequency for which two conical nodes annihilate, there appears to be a point node where three nodal curves in the two adiabatic electronic projections cross. Around this point, the electronic character reverses sign along q_2 while remaining locally constant along q_1, so this is not a conical node. The overall electronic index for simple closed paths around this region remains 0 in all panels of Fig. 4.7.

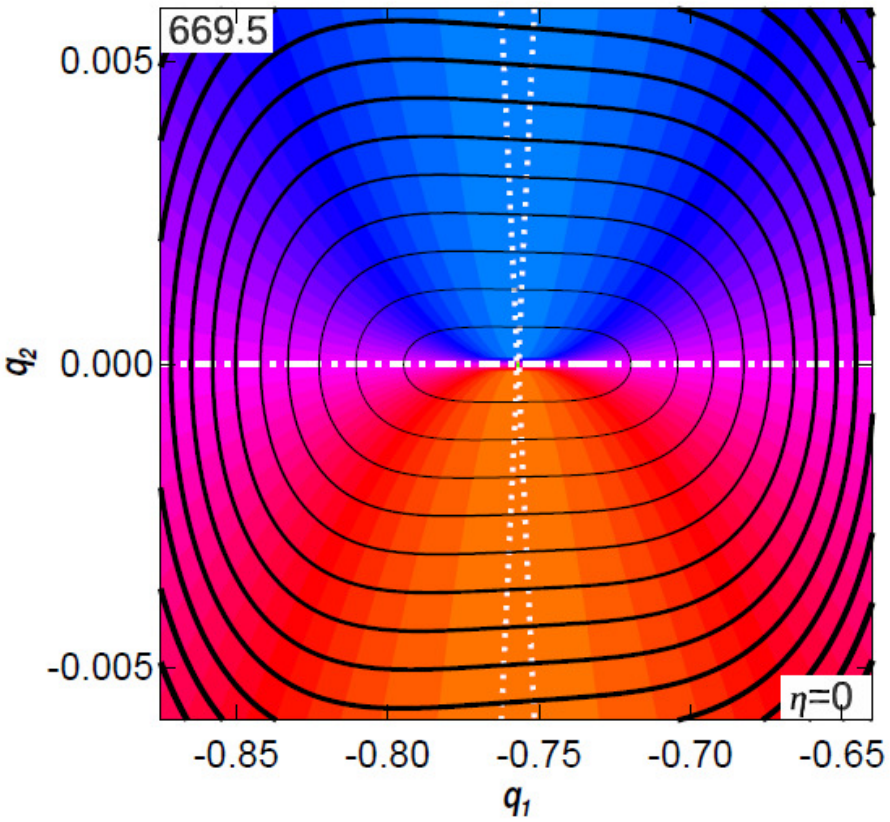

Figure 4.8: Generic structure around a tangential node

A closer view of the tangential node shown in the middle panel of Fig. 4.7, portraying the sixth lowest eigenstate of $\sigma_v = +1$ symmetry for the Jahn-Teller Hamiltonian with $\omega_1 = 200$ cm^{-1}, $\omega_2 = 230.9055$ cm^{-1}, and $d_1 = d_2 =$ 0.4. The contour interval is 0.1% of the maximum probability amplitude, with thicker contours for higher amplitude. Color shows electronic character using the color wheel in Figure 4.1. The nodal curve in the eigenfunction projection onto electronic state *x* is dotted white while *y* is dot-dashed white. Axis ranges are in a $20:1$ ratio to show the different amplitude variation along the tangential (q_1) and perpendicular (q_2) axes. The energy (cm^{-1}) is shown at upper left and the electronic index η is shown at lower right.

This node at the point of annihilation is here referred to as a tangential node. Fig. 4.8 zooms into the region around this node for a frequency numerically close to annihilation. Although the intersection of three diabatic nodal curves at a single point arises by varying a parameter in the presence of symmetry, the shape of this node may be typical. Along q_2, the

electronic character changes sign from $+|y\rangle$ below the node to $-|y\rangle$ above the node. The even contour spacing shows that amplitude grows linearly along q_2, like a conical node. Along q_1, the electronic character is $+|x\rangle$ for all points except the node itself, where electronic character is undefined. The uneven contour spacing indicates an amplitude that grows quadratically along q_1, like a second-order node. The electronic index η is zero for any simple closed path around just this node.

The simplest generic creation/annihilation event for two oppositely signed nodes involves shifting two adiabatic vibrational nodal curves that intersect twice so that their intersections coalesce to a single point and then disappear. The two nodal curves generically become tangent at the point where they coalesce and annihilate the two conical nodes, suggesting the name tangential node. Tangential nodes are "accidental" because a parameter must be precisely tuned to the creation/annihilation event. Fig. C.5 from Appendix C shows slices through the amplitude along the tangential direction as two conical nodes annihilate. Without loss of generality in determining nodal shape, we may choose perpendicular coordinates (w,z) with the point of coalescence as the origin and the tangent line along axis *w*. Locally, the nonadiabatic eigenfunction can be written in terms of two orthogonal electronic basis states as

$$|\psi;w,z\rangle = (az-\alpha w^2)|A\rangle + (bz-\beta w^2)|B\rangle, \tag{4.21}$$

This has a vibrational amplitude factor

$$\text{Þ}(w,z) = \sqrt{(az-\alpha w^2)^2 + (bz-\beta w^2)^2} \tag{4.22}$$

that gives the generic shape for a tangential node. The electronic factor is locally constant along the tangent line,

$$\left|\mathrm{K};\, w, z=0\right\rangle = (-\alpha\left|A\right\rangle - \beta\left|B\right\rangle) / \sqrt{(\alpha)^2 + (\beta)^2}\ , \tag{4.23a}$$

but abruptly changes sign along the perpendicular to the tangent through the origin,

$$\left|\mathrm{K};\, w=0, z\right\rangle = \mathrm{signum}(z)(a\left|A\right\rangle + b\left|B\right\rangle) / \sqrt{(a)^2 + (b)^2}\ . \tag{4.23b}$$

Note that the electronic factors along the tangent line and its perpendicular through the origin are not generically orthogonal – their orthogonality requires $a\alpha + b\beta = 0$, which is a consequence of symmetry in Fig. 4.8 (with $w = q_1 - c$, $z = q_2$, $\left|A\right\rangle = \left|x\right\rangle$ and $\left|B\right\rangle = \left|y\right\rangle$, Eq. (4.11) requires $a = 0$ and $\beta = 0$ for $\sigma_v = +1$ states). Eq. (4.21) can be used to show that, in the absence of symmetry, the electronic index around a generic tangential node is zero.

Figure C.6 from Appendix C shows that conical nodes can also be created or annihilated in a different fashion as the Hamiltonian parameters change in the presence of symmetry. This creation event for the eigenstate correlated to $(v = 2, |j| = 1/2)$ occurs near $\omega_2 = 210.2$ cm^{-1} (within the range shown in Fig. 4.6). The intersection of three nodal curves at a single point creates two new conical nodes with the same sign as the original node and reverses the sign of the original node. As a result, the overall electronic index for simple closed paths around the region of node creation remains constant, indicating a first order singularity in the electronic factor. Even at the convergence limit of these calculations, the vibrational amplitude around the node lies between that around an adiabatic nodal curve and that around a tangential node (a hypothetical accidental first order tangential node in the presence of symmetry would not conflict with either generic accidental zeroth order tangential nodes in the absence of symmetry or symmetry-required first-order conical nodes).

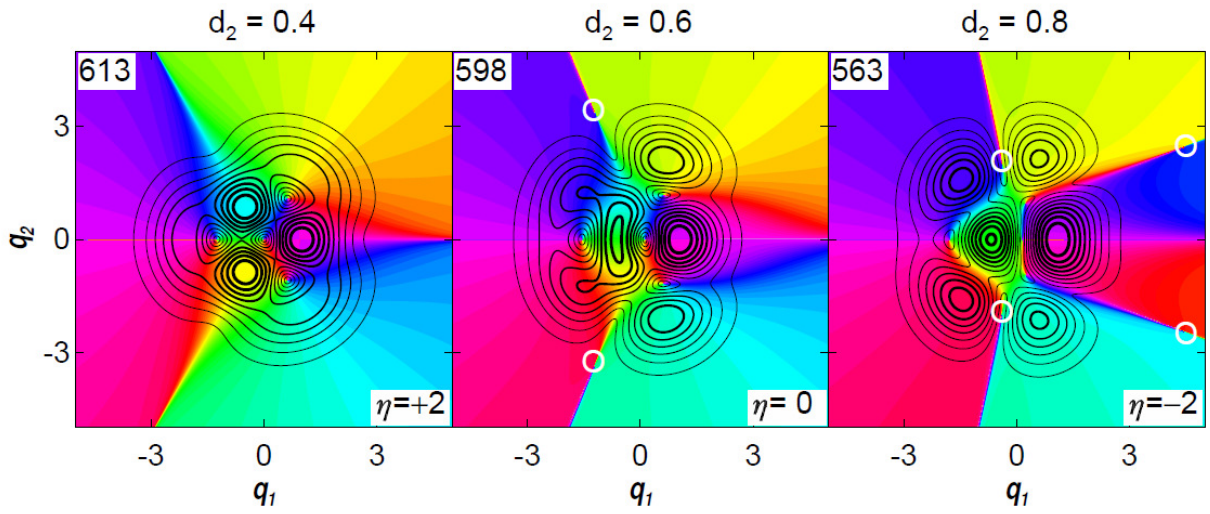

Figure 4.9: Node Movements that Change the Electronic Index Around a Fixed Path

The three panels show the probability amplitude and electronic character for the sixth lowest energy $\sigma_v = +1$ eigenstate of the Jahn-Teller Hamiltonian for $\omega_1 = \omega_2 = 200$ cm^{-1}, $d_1 = 0.4$ and d_2 as specified above each panel. Contours represent 10% of the maximum probability amplitude for each state, with thicker contour lines for higher amplitude. Color represents electronic character as shown at the bottom of the color wheel in Figure 4.1. The energy (cm^{-1}) for each eigenstate is shown at upper left and the electronic index around the perimeter of the area shown is at lower right. Moving from left to right, nodes enclosed in white circles have moved into the area shown and changed the electronic index around its perimeter.

Up to this point, every figure has shown a constant electronic index around the perimeter of the coordinate region plotted for each eigenstate. Fig. 4.9 shows how the (v = 2, |j| = 3/2) eigenstate of the circularly symmetric conical intersection changes as d_2 increases. In the circularly symmetric case (left panel), the electronic index for a path around the perimeter is $\eta = +2$. Compared to Fig. 4.2, the wider coordinate range reveals that the three radial lines at ϕ = 0, 2π/3 and 4π/3 approximate nodal lines at the perimeter. All four conical nodes from the left panel can be correlated throughout the three panels. For $d_2 = 0.6$, two conical nodes (circled) have moved into the range shown. Both conical nodes have an electronic index of $\eta = -1$ (see Fig. C.7 in Appendix C for close-ups), so that the electronic index around the

perimeter is $\eta = 0$. For $d_2 = 0.8$, two more conical nodes with electronic index $\eta = -1$ have appeared, each along a new approximate nodal line. With 4 nodes that do not appear in the leftmost panel (node close-ups again in Fig. C.7), the electronic index around the perimeter is $\eta = -2$. This shows that conical nodes can move in from (or out to) large distances from the conical intersection. These changes do not involve an obvious weakly avoided level crossing in Fig. 1.8 (in Chapter 1), but the energy eigenvalue's curvature with d_2 suggests strong level mixing in this range.

Although nodal curves should not typically appear in nonadiabatic eigenfunctions, 7 out of the 8 conical nodes in the right panel of Fig. 4.9 can be connected by curves along which the amplitude never rises above 20% of the maximum amplitude. These low amplitude regions may be developing nodal curves, which suggests that conical nodes commonly occur in the weakly avoided nodal curves of eigenfunctions that are nearly adiabatic.

4.4.4. *The Role of Ellipticity*

Although all of the adiabatic potential surfaces considered so far have elliptical conical intersections, the symmetry equivalent minima and saddle points are obvious deformations from a simple scale transformation for one coordinate of a circular conical intersection. This raises questions about whether the amplitude at the origin is caused by the local elliptical shape of the conical intersection, global departures from an elliptical potential, or an elliptical form of the kinetic energy operator. The following considerations justify the title of this paper.

Locally circular conical intersections can be obtained by requiring that both Jahn-Teller active vibrations have the same linear coupling; $\omega_1 d_1 = \omega_2 d_2$. This still allows the Jahn-Teller stabilization energies to differ, so the adiabatic potential surfaces have minima and saddle points

at the equilibrium Jahn-Teller displacements. For one Hamiltonian of this type (see Fig. C.8 in Appendix C), all of the nonadiabatic eigenfunctions examined have nonzero amplitude at the conical intersection. A locally circular conical intersection is not sufficient to keep nonadiabatic eigenfunction amplitude off the conical intersection.

Purely elliptical Jahn-Teller Hamiltonians can be found by requiring that both Jahn-Teller active vibrations have the same stabilization energy; $(1/2)\omega_1 d_1^{\,2} = (1/2)\omega_2 d_2^{\,2} = (D\omega)$. In this case, a little algebra shows that the adiabatic potential surfaces in Eq. (4.4) simplify to

$$U_{\pm}(q_1, q_2) = [(1/2)\omega_1 q_1^2 + (1/2)\omega_2 q_2^2] \pm 2\sqrt{(D\omega)}\sqrt{[(1/2)\omega_1 q_1^2 + (1/2)\omega_2 q_2^2]}. \tag{4.24}$$

Since the level contours of $f = [(1/2)\omega_1 q_1^{\,2} + (1/2)\omega_2 q_2^{\,2}]$ are ellipses, each elliptical contour of constant f gives one elliptical contour of constant adiabatic potential energy on each adiabatic surface: $U_{\pm} = f \pm 2\sqrt{(D\omega)}\sqrt{f}$. As a result, all contours of constant adiabatic potential energy are similar ellipses with a common center at the origin and the same eccentricity [$e = \sqrt{1-(\omega_{\min}/\omega_{\max})}$ where $\omega_{\min} = \min(\omega_1, \omega_2)$ and $\omega_{\max} = \max(\omega_1, \omega_2)$]. Since the kinetic energy operator in the nonadiabatic Hamiltonian has the same eccentricity, equal stabilization energies create an elliptically symmetric nonadiabatic Hamiltonian. For a numerical example of a purely elliptical Jahn-Teller Hamiltonian, every nonadiabatic eigenfunction examined has nonzero amplitude at the conical intersection (see Fig. C.9 in Appendix C).

For adiabatic potential surfaces, one can transform any untilted elliptical 2D conical intersection into a circular 2D conical intersection by a scale transformation of one vibrational coordinate.[61] However, for non-adiabatic dynamics, ellipticity in the shape of the conical

intersection cannot be transformed away because any canonical scale transformation[40] that expands a coordinate by a factor of α necessarily contracts its canonically conjugate momentum by a factor of $1/\alpha$ (this appears as an effective mass scaling in Eq. (12) of ref. [61]). In particular, the canonical transformation $q_2' = (\omega_2 / \omega_1)^{1/2} q_2$, $p_2' = (\omega_1 / \omega_2)^{1/2} p_2$ transforms the above purely elliptical adiabatic potential surfaces into circular ones, but gives the nonadiabatic Hamiltonian an elliptic kinetic energy perturbation of $(1/2)[(\omega_2^2 - \omega_1^2)/\omega_1]\hat{p}_2^2$. Similarly, transforming the purely elliptical nonadiabatic Hamiltonian to make the kinetic energy operator have the circular form $(1/2)\omega_1[\hat{p}_1^2 + (\hat{p}_2')^2]$ leaves the potential surfaces elliptical. Ellipticity in *either* the potential or the kinetic energy operator makes the nonadiabatic states fundamentally different from those of a circularly symmetric nonadiabatic Hamiltonian. One could diabolically construct an apparently elliptical Hamiltonian by transformation of a circular Hamiltonian so that both the potential surfaces and the kinetic energy operator would have compensating ellipticities, but such truly circular Hamiltonians lie within an improbable lower-dimensionality sub-space in the space of purely elliptical Hamiltonians, which are themselves improbable in the higher-dimensionality space of square-symmetric Hamiltonians. Such dimensional arguments rationalize why, throughout this study, every eigenfunction calculated without global circular symmetry had nonzero amplitude at the conical intersection.

4.5. Discussion

Conical node points in nonadiabatic eigenfunctions have a lower dimensionality than the nodal curves in adiabatic eigenfunctions.[24] In principle, these nodes of the exact eigenfunction are observable by imaging the vibrational probability density for an eigenstate. Techniques for such imaging are discussed in ref. [26, 27]. This contrasts with conical intersections, which are a feature of the adiabatic approximation and, as such, cannot be directly observed but are calculated or inferred from their consequences. In square-symmetric molecules, the vibrational-electronic eigenstates occur in degenerate pairs and have only accidental conical nodes. Since accidental conical nodes have different vibrational coordinates for the two members of a degenerate pair, their observation in the molecular frame would require selective preparation of one eigenstate out of a degenerate pair. The vibrational imaging techniques of ref. [27] and [62] involve laboratory frame measurements. Symmetry prevents a distinction between equivalent molecular frame $\hat{x}$ and $\hat{y}$ axes. Fortunately, although linearly polarized excitation from the zero point vibrational level of a totally symmetric electronic state generates $\sigma_v = +1$ states for $\hat{x}$ polarization and $\sigma_v = -1$ for $\hat{y}$ polarization, the opposite placement of accidental conical nodes with respect to the $q_1 = 0$ plane in Fig. C.1 in Appendix C gives these degenerate state pairs the same laboratory frame vibrational probability density as each other. Similarly, the $\sigma_d = \pm 1$ states excited for $(\hat{x} \pm \hat{y})/2^{1/2}$ polarization have the same laboratory frame vibrational probability density as each other (but different from that for $\hat{x}$ or $\hat{y}$ polarization). For square-symmetric molecules with 4 equivalent atoms such as the tetra-chalcogen dications[63-65] and their iso-electronic anions,[66] (which require counter-ion stabilization), gas-phase laboratory frame coordinates might be appropriately mapped using a 4-particle Dalitz plot[67, 68] analogous to

the 3-particle Dalitz plots used by ref. [27] for H_3. The larger number of atoms in typical square planar molecules might eventually become accessible by improving on the spatial and temporal resolution of the surface technique used by Apkarian and co-workers.[62] Both appear to be more challenging prospects than observing essential nodes at higher symmetry conical intersections. Alternatively, conical nodes near and vibrational probability density at a conical intersection might be measurable in lower symmetry molecules such as the the radicals formed from three dissimilar alkali atoms treated by Longuet-Higgins.[48]

For the elliptical conical intersections without tilt studied here, every eigenstate examined has vibrational amplitude at the conical intersection. It is well known that single-surface adiabatic eigenfunctions do not have amplitude at a conical intersection.[61, 69, 70] Fundamentally, this amplitude arises because the conical intersection is energetically accessible in the Hamiltonians studied here and there is no conserved pseudo-rotation angular momentum to generate a centrifugal barrier when pseudo-rotation is excited. For the circularly symmetric Jahn-Teller Hamiltonian, only eigenfunctions without a centrifugal barrier can have amplitude at the conical intersection,[25] but every eigenfunction of the square-symmetric Jahn-Teller Hamiltonian can have amplitude there. The pair of studies thus leaves open questions about whether some eigenstates cannot have amplitude at the conical intersection for intermediate symmetry Hamiltonians (e.g. groups with three-fold, five-fold, or six-fold rotations, octahedral symmetry, etc.). In the absence of such high global symmetry, the present study suggests that almost every nonadiabatic eigenstate will have amplitude on top of any energetically accessible conical intersection. Thus, conjectures by Izmaylov and co-workers[11] and by Meek and Levine[12] that nonadiabatic wavefunctions can have amplitude at a conical intersection appear to be the typical case for energetically accessible conical intersections. Such extreme examples

of the dynamical Jahn-Teller effect can still generate femtosecond conical intersection dynamics in square-symmetric molecules,[10, 17, 37] and this investigation sheds light on the eigenfunctions involved.

4.6. Conclusions

Elliptical conical intersections have nonadiabatic eigenstates that behave similarly to those for circular conical intersections with a few notable differences. Perturbing one frequency or one displacement from circular symmetry lowers the symmetry to D_{4h} and breaks angular symmetry, giving rise to conical intersections with an elliptical shape. As a result, nodes in the eigenstates at the conical intersection typically move off the conical intersection. This has been proven here using perturbation theory near Hougen's accidental Born-Oppenheimer case and demonstrated numerically for all other elliptical cases examined, including a nonadiabatic Hamiltonian with global elliptical symmetry.

When pseudo-rotation angular momentum symmetry is destroyed, no good quantum numbers beyond the discrete reflection symmetry eigenvalue remain. However, the integer electronic index (η) that characterizes the electronic circulation around a closed path is useful as a quantum number because it is locally stable with respect to perturbations. Oppositely-signed nodes can be created or annihilated in pairs such that η is conserved. Creation or annihilation typically occurs through a tangential node with an electronic index of 0. The vibrational amplitude surrounding a tangential node grows quadratically in the tangential direction and linearly in the perpendicular direction. For circular conical intersections, the higher order eigenfunction nodes occur at the origin with n nodal lines in each electronic state converging at the conical intersection to make an n^{th} order node. For elliptical conical intersections, these

nodal lines diverge to make n different first order nodes, all with an electronic index of the same sign as each other and as the original n^{th} order node, maintaining the electronic index η. The formation of adiabatic nodal curves appears to involve expansion and coalescence of conical nodes, which can make the electronic index difficult to evaluate as it ultimately becomes ill-defined in the adiabatic limit. Although the electronic index is stable with respect to small perturbations, it is not globally conserved.

None of these nodes found here occur at the conical intersection, so all eigenfunctions can have probability amplitude at the conical intersection as long as the conical intersection is energetically accessible. Depending on the degenerate eigenstate selected, the conical nodes are located at different coordinates, so they are accidental in nature and disappear for complex-valued linear combinations of degenerate eigenstates. Conical nodes were observed for all sets of real-valued eigenstates here. While accidental nodes shifted off the conical intersection may be experimentally difficult to observe, the conclusion that all eigenstates have amplitude at the conical intersection is experimentally testable.

References

1. Teller, E., *Internal Conversion in Polyatomic Molecules.* Israel Journal of Chemistry, 1969. **7**: p. 227-235.

2. Koppel, H., W. Domcke, and L.S. Cederbaum, *Multimode Molecular-Dynamics Beyond the Born-Oppenheimer Approximation.* Advances in Chemical Physics, 1984. **57**: p. 59-246.

3. Zwanziger, J.W. and E.R. Grant, *Topological phase in molecular bound states: Application to the Exe system.* J. Chem. Phys., 1987. **87**(5): p. 2954-2964.

4. Klessinger, M. and J. Michl, *Excited States and Photochemistry of Organic Molecules*. 1995, New York: VCH Publishers.

5. Yarkony, D.R., *Diabolical conical intersections.* Reviews of Modern Physics, 1996. **68**: p. 985-1013.

6. Robb, M.A. and M. Olivucci, *Photochemical processes: potential energy surface topology and rationalization using VB arguments.* J. Photochem. Photobiol. A, 2001. **144**: p. 237-243.

7. Truhlar, D.G. and C.A. Mead, *Relative likelihood of encountering conical intersections and avoided crossings on the potential energy surfaces of polyatomic molecules.* Physical Review A, 2003. **68**(3): p. 032501.

8. Coe, J.D. and T.J. Martinez, *Competitive Decay at Two- and Three-State Conical Intersections in Excited-State Intramolecular Proton Transfer.* J. Am. Chem. Soc., 2005. **127**(13): p. 4560-4561.

9. Matsika, S. and P. Krause, *Nonadiabatic Events and Conical Intersections.* Annual Review of Physical Chemistry, 2011. **62**: p. 621-643.

10. Jonas, D.M., *Vibrational and Nonadiabatic Coherence in 2D Electronic Spectroscopy, the Jahn-Teller Effect and Energy Transfer.* Annual Review of Physical Chemistry, 2018. **69**: p. 327-352.

11. Ryabinkin, I., L. Joubert-Doriol, and A.F. Izmaylov, *When do we need to account for the geometric phase in excited state dynamics?* J. Chem. Phys., 2014. **140**(21): p. 214116.

12. Meek, G.A. and B.G. Levine, *Wave function continuity and the diagonal Born-Oppenheimer correction at conical intersections.* J. Chem. Phys., 2016. **144**(18): p. 184109.

13. Longuet-Higgins, H.C., et al., *Studies of the Jahn-Teller effect II. The dynamical problem.* Proc. R. Soc. Lond. A, 1958. **244**(1236): p. 1-16.

14. Applegate, B.E., T.A. Barckholtz, and T.A. Miller, *Explorations of Conical Intersections and Their Ramifications for Chemistry Through the Jahn-Teller Effect.* Chemical Society Reviews, 2003. **32**: p. 38-49.

15. Jahn, H.A. and E. Teller, *Stability of Polyatomic Molecules in Degenerate Electronic States. I. Orbital Degeneracy.* Proceedings of the Royal Society of London. Series A, Mathematical and Physical Sciences (1934-1990), 1937. **161**(905): p. 220-235.

16. McCusker, J., *Femtosecond absorption spectroscopy of transition metal charge-transfer complexes.* Accounts of Chemical Research, 2003. **36**: p. 876-887.

17. Farrow, D.A., et al., *Polarized Pump-Probe Measurements of Electronic Motion via a Conical Intersection.* J. Chem. Phys., 2008. **128**(7): p. 144510.

18. Hougen, J.T., *Vibronic Interactions in Molecules with a Fourfold Symmetry Axis.* Journal of Molecular Spectroscopy, 1964. **13**: p. 149-167.

19. Gouterman, M., *Electronic Spectra*, in *The Porphyrins*, D. Dolphin, Editor. 1978, Academic Press: New York. p. 1-156.

20. Hunter, G., *Conditional Probability Amplitudes in Wave Mechanics.* International Journal of Quantum Chemistry, 1975. **9**(2): p. 237-242.

21. Abedi, A., N.T. Maitra, and E.K.U. Gross, *Exact Factorization of the Time-Dependent Electron-Nuclear Wave Function.* Physical Review Letters, 2010. **105**(12): p. 123002.

22. Cederbaum, L.S., *The exact molecular wavefunction as a product of an electronic and a nuclear wavefunction.* Journal of Chemical Physics, 2013. **138**(22): p. 224110.

23. Peters, W.K., V. Tiwari, and D.M. Jonas, *Nodeless vibrational amplitudes and quantum nonadiabatic dynamics in the nested funnel for a pseudo Jahn-Teller molecule or homodimer.* J. Chem. Phys., 2017. **147**(19): p. 194306.

24. Foster, P.W., W.K. Peters, and D.M. Jonas, *Nonadiabatic eigenfunctions can have conical nodes.* Chem. Phys. Lett., 2017. **683**(September 1): p. 268-275.

25. Foster, P.W. and D.M. Jonas, *Nonadiabatic Eigenfunctions Can Have Amplitude, Signed Conical Nodes, or Signed Higher Order Nodes at a Conical Intersection with Circular Symmetry.* J. Phys. Chem. A, 2017. **121**(39): p. 7401-7413.

26. Schmidt, L.P.H., et al., *Spatial Imaging of the H_2^+ Vibrational Wave Function at the Quantum Limit.* Phys. Rev. Lett., 2012. **108**(7): p. 073202.

27. Fechner, P.C. and H. Helm, *Imaging of spatial many-body wave functions via linear momentum measurements.* Phys. Chem. Chem. Phys., 2014. **16**(2): p. 453-457.

28. Czub, J. and L. Wolniewicz, *On the Non-Adiabatic Potentials in Diatomic-Molecules.* Molecular Physics, 1978. **36**(5): p. 1301-1308.

29. Hunter, G., *Nodeless Wave-Functions and Spiky Potentials.* International Journal of Quantum Chemistry, 1981. **19**(5): p. 755-761.

30. Gidopoulos, N.I. and E.K.U. Gross, *Electronic non-adiabatic states: towards a density functional theory beyond the Born-Oppenheimer approximation.* Philosophical Transactions of the Royal Society a-Mathematical Physical and Engineering Sciences, 2014. **372**(2011): p. 20130059.

31. Ryabinkin, I. and A.F. Izmaylov, *Geometric Phase Effects in Dynamics Near Conical Intersections: Symmetry Breaking and Spatial Localization.* Phys. Rev. Lett., 2013. **111**(22): p. 220406.

32. Xie, C., et al., *Constructive and Destructive Interference in Nonadiabatic Tunneling via Conical Intersections.* Journal of Chemical Theory and Computation, 2017. **13**(5): p. 1902-1910.

33. Xie, C., D.R. Yarkony, and H. Guo, *Nonadiabatic tunneling via conical intersections and the role of the geometric phase.* Phys. Rev. A, 2017. **95**(2): p. 022104.

34. Herzberg, G.H., *Electronic Spectra of Polyatomic Molecules*. Molecular Spectra and Molecular Structure. Vol. III. 1991, Malabar, FL: Krieger.

35. Shelnutt, J.A., et al., *Nonplanar porphyrins and their significance in proteins.* Chem. Soc. Rev., 1998. **27**: p. 31-41.

36. Farrow, D.A., et al., *The polarization anisotropy of vibrational quantum beats in resonant pump-probe experiments: Diagrammatic calculations for square symmetric molecules.* Journal of Chemical Physics, 2008. **129**(17): p. 174509.

37. Kitney-Hayes, K.A., et al., *Two-Dimensional Fourier Transform Electronic Spectroscopy at a Conical Intersection.* J. Chem. Phys., 2014. **140**(12): p. 124312

38. Marsden, J.E. and A.J. Tromba, *Vector Calculus*. 1981, San Francisco: W. H. Freeman.

39. Papousek, D. and M.R. Aliev, *Molecular Vibrational-Rotational Spectra*. 1982, New York: Elsevier Scientific.

40. Goldstein, H., *Classical Mechanics*. 2nd ed. 1980, Reading, MA: Addison-Wesley.

41. Yarkony, D.R., *Conical intersections: The new conventional wisdom.* Journal of Physical Chemistry A, 2001. **105**: p. 6277-6293.

42. Smith, E.R., D.A. Farrow, and D.M. Jonas, *Response functions for dimers and square symmetric molecules in four-wave-mixing experiments with polarized light.* J. Chem. Phys., 2005. **123**(4): p. 044102.

43. Smith, E.R., D.A. Farrow, and D.M. Jonas, *Publisher's Note: "Response functions for dimers and square symmetric molecules in four-wave-mixing experiments with polarized light" [J. Chem. Phys. **123,** 044102 (2005)].* J. Chem. Phys., 2005. **123**: p. 179902.

44. Smith, E.R., D.A. Farrow, and D.M. Jonas, *Erratum: "Response functions for dimers and square symmetric molecules in four-wave-mixing experiments with polarized light" [J. Chem. Phys. **123,** 044102 (2005)].* J. Chem. Phys., 2008. **128**: p. 109902.

45. Sunder, S. and H.J. Bernstein, *The vibrational spectra of the metalloporphyrins: A normal coordinate analysis of the planar vibrations in the Cu-chelates of porphin, porphin-d_4 (meso), 1:3:5:7-tetramethyl porphin and 1:2:3:4:5:6:7:8-octamethyl porphin.* J. Raman Spectrosc., 1976. **5**(4): p. 351-371.

46. Moffitt, W. and A.D. Liehr, *Configurational Instability of Degenerate Electronic States.* Phys. Rev., 1957. **106**(4): p. 1195-1200.

47. Born, M. and K. Huang, *Dynamical Theory of Crystal Lattices*. 1962, Oxford: Clarendon Press.

48. Longuet-Higgins, H.C., *The intersection of potential energy surfaces in polyatomic molecules.* Proc. R. Soc. Lond. A, 1975. **344**(1637): p. 147-156.

49. Mead, C.A. and D.G. Truhlar, *On the determination of Born–Oppenheimer nuclear motion wave functions including complications due to conical intersections and identical nuclei.* J. Chem. Phys., 1979. **70**(5): p. 2284-2296.

50. Bracewell, R.N., *The Fourier transform and its applications*. 3rd ed. McGraw-Hill series in electrical and computer engineering Circuits and systems. 2000, Boston: McGraw Hill. xx, 616 p.

51. Longuet-Higgins, H.C., *Some recent developments in the theory of molecular energy levels*, in *Advances in Spectroscopy*, H. Thompson, Editor. 1961, Interscience Publishers Inc: New York. p. 429-472.

52. Herzberg, G. and H.C. Longuet-Higgins, *Intersection of Potential Energy Surfaces in Polyatomic Molecules.* Disc. Far. Soc., 1963. **35**: p. 77-82.

53. Berry, M.V., *Quantal phase factors accompanying adiabatic changes.* Proc. R. Soc. Lond. A, 1984. **392**(1802): p. 45-57.

54. Bunker, P.R., *Molecular Symmetry and Spectroscopy*. 1979, Orlando: Academic Press, Inc.

55. Landau, L.D. and E.M. Lifschitz, *Quantum Mechanics*. 3rd ed. 1977, New York: Pergamon Press.

56. Thompson, T.C., D.G. Truhlar, and C.A. Mead, *On the form of the adiabatic and diabatic representation and the validity of the adiabatic approximation for X_3 Jahn–Teller systems.* J. Chem. Phys., 1985. **82**(5): p. 2392-2407.

57. Parlett, B.N., *The Symmetric Eigenvalue Problem*. 1980, Englewood Cliffs, NJ: Prentice-Hall.

58. Judd, B.R., *Exact solutions to a class of Jahn-Teller systems.* J. Phys. C: Solid State Phys., 1979. **12**: p. 1685-1692.

59. Cohen-Tannoudji, C., B. Diu, and F. Lalöe, *Quantum Mechanics*. Vol. 2. 1977, Paris: Wiley-Interscience. 1284-1321 and 1339-1342.

60. Courant, R. and D. Hilbert, *Methods of Mathematical Physics*. First English ed. Vol. I. 1953: Wiley-Interscience. 560.

61. Yarkony, D.R., *Nuclear dynamics near conical intersections in the adiabatic representation: I. The effects of local topography on interstate transitions.* Journal of Chemical Physics, 2001. **114**(6): p. 2601-2613.

62. Lee, J., et al., *Orbiting Orbitals: Visualization of Vibronic Motion at a Conical Intersection.* J. Phys. Chem. A, 2013. **117**(46): p. 11655-11664.

63. Cardinal, G., et al., *Charge-transfer Interactions in the Square-planar Chalcogen Cations, M_4^{2+}: Preparation and Crystal-Structures of the Compounds $(Se_4^{2+})(Sb_2F_4^{2+})(Sb_2F_5^{+})(SbF_6^{-})_5$,$(Se_4^{2+})(AlCl_4^{-})_2$, and $(Te_4^{2+})(SbF_6^{-})_2$.* Journal of the Chemical Society-Dalton Transactions, 1982(4): p. 765-779.

64. Wong, M.W., *Quantum-Chemical Calculations of Sulfur-Rich Compounds.* Top. Curr. Chem., 2003. **231**: p. 1-31.

65. Elliott, B.M. and A.I. Boldyrev, *Ab Initio Probing of the Aromatic Oxygen Cluster O_4^{2+}.* J. Phys. Chem. A, 2005. **109**(1): p. 236-239.

66. Corbett, J.D., *Polyatomic Zintl Anions of the Post-Transition Elements.* Chemical Reviews, 1985. **85**(5): p. 383-397.

67. Schulz, M., et al., *Four-particle Dalitz plots to visualize atomic break-up processes.* Journal of Physics B-Atomic Molecular and Optical Physics, 2007. **40**(15): p. 3091-3099.

68. Ciappina, M.F., et al., *Double ionization of helium by ion impact analyzed using four-body Dalitz plots.* Physical Review A, 2008. **77**(6): p. 12.

69. Mead, C.A., *Electronic Hamiltonian, wave functions, and energies, and derivative coupling between Born-Oppenheimer states in the vicinity of a conical intersection.* J. Chem. Phys., 1983. **78**(2): p. 807-814.

70. Varandas, A.J.C. and Z.R. Xu, *On the behavior of single surface nuclear wavefunctions in the vicinity of the conical intersection for an X_3 system.* Chem. Phys. Lett., 2000. **316**: p. 248-256.

CHAPTER 5

NONADIABATIC EIGENFUNCTIONS CAN HAVE CONICAL NODES IN THE TUNNELING REGION

Conical nodes are observed in nonadiabatic eigenfunctions of different Hamiltonians in the tunneling region. The circularly symmetric Jahn-Teller conical intersection is analyzed using a basis set of adiabatic electronic eigenfunctions and taking advantage of the separability of the projections of the nonadiabatic eigenfunctions onto the adiabatic states. Radial nodes in the adiabatic projections give rise to conical nodes in the exact nonadiabatic states, even in the tunneling region. These tunneling region nodes can also be found in a coupled dimer that does not have a conical intersection.

5.1. Introduction

In a classical understanding of molecular vibrations, the adiabatic electronic potential energy for a given electronic state is a function of nuclear coordinates. The total energy of a particular eigenfunction of the Hamiltonian is fixed and that energy can be potential energy or kinetic energy. Classically, molecules cannot reach points in vibrational space where potential energy $V(q)$ is greater than total eigenfunction energy E because the kinetic energy would be negative.

Quantum mechanics reveals that the situation is more complicated. In 1927, Hund studied chiral molecules racemizing through a one-dimensional potential barrier and discovered that probability amplitude could bleed through a barrier with $V(q) > E$ [1] into what became known

as the tunneling region. Following Hund, Oppenheimer studied the tunneling ionization of hydrogen atoms in an electric field [2] and Gamow [3, 4] and Gurney and Condon [5, 6] used tunneling to explain radioactive decay. Each of these studies looked at tunneling along a one-dimensional coordinate.

In each of the systems studied, there are classically allowed regions where $V(q) < E$ and classically forbidden regions where $V(q) > E$. The time-independent Schrödinger Equation in one Cartesian coordinate q can be written

$$\frac{d^2\psi(q)}{dq^2} = \frac{2m}{\hbar}[V(q) - E]\psi(q). \tag{5.1}$$

Equation (5.1) requires that in the allowed region the second derivative of the eigenfunction must be opposite in sign from the eigenfunction itself and in the forbidden region the signs must agree [7]. At the classical turning point between these regions, where $V(q) = E$, the eigenfunction can have (see below) a point of inflection where it is nonzero and its second derivative changes sign. Finally, there is the possibility that the eigenfunction and its second derivative are both zero at the same point, yet the first derivative is nonzero there; [7] such points are nodes.

Additional information about one-dimensional eigenfunctions comes from the boundary conditions, which require that eigenfunctions have continuous derivatives and that bound eigenfunctions ultimately decay to zero. An eigenfunction in a forbidden region without an allowed region beyond it cannot slope away from zero; if it did, decay to zero would require, at some point, a second derivative opposite in sign to the eigenfunction, which the Schrödinger Equation does not permit within a forbidden region. As a corollary, eigenfunctions must have a monotonic decay toward zero in any forbidden region that extends forever. This corollary

prohibits eigenfunction nodes within any unbounded forbidden region and at its classical turning point, where the eigenfunction *must have* (compare above) nonzero amplitude at its point of inflection. This corollary does not apply to forbidden regions separating two allowed regions, in which eigenfunctions can have a positive local minimum, a negative local maximum, or a node in the forbidden region (for the tunneling inversion of ammonia, these occur at the potential maximum – see ref. [8]). A one-dimensional eigenfunction in an unbounded forbidden region has a second derivative with the same sign as the eigenfunction and monotonically decays towards zero away from the allowed region.

This is not necessarily the case in multiple dimensions because the sign of the eigenfunction can agree with the sign of the Laplacian without the signs matching for the eigenfunction along any particular direction. [9, 10] Separable systems such as the hydrogen atom exhibit angular nodal planes that extend into the forbidden region parallel to lines of steepest ascent into the tunneling region. Also, because the radial kinetic energy is not just a second derivative, the radial eigenfunctions for the hydrogen atom do not obey the second derivative rules found above, but they still monotonically decay with radius in the forbidden region. Regions that are classically allowed based on total energy yet inaccessible because of conserved momenta give rise to “mixed tunneling”. [11] Some high dimensional aspects can be described in terms of friction, which impedes both allowed motion and tunneling. [12] In the forbidden region, The JWKB approximation predicts that eigenfunctions decay monotonically along the direction of steepest ascent, [9] so that there are no nodal surfaces perpendicular to the direction of steepest ascent into the tunneling region.

The phrase nonadiabatic tunneling is used in a great many papers to describe phenomena in which the tunneling barrier is either changing with time [13-15] or as a function of

environmental parameters or vibrational coordinates [16-18]. This is closely related to the treatment in ref. [12]. Closer to the meaning here, Zhu and Nakamura have treated the one-dimensional case in which the tunneling barrier on the lower adiabatic electronic state is close enough to the upper adiabatic electronic state that it influences the tunneling process [19]. Here, the dynamics also involve two electronic states but also depend on two vibrational coordinates. In recent studies [20-23], the effect of the adiabatic sign change around the conical intersection was of interest, and eigenfunctions were used to visualize the interference between tunneling paths through a conical intersection. The figures in those studies show monotonic eigenfunction decay for tunneling into the conical intersection. This chapter investigates tunneling behavior into the outer potential well at large radius which exhibits qualitatively new and different phenomena.

In a study of the eigenstates for a Hamiltonian chosen to model energy transfer in a molecular dimer [24], conical nodes were observed and it was suggested in the discussion surrounding Figure 5 that there might be "two conical nodes moving in from infinity" with the lower panel of Figure 5 showing a nonadiabatic eigenfunction where the nodal lines of the projections approach one another outside the region plotted. The intersection of the nodal lines would create a conical node in the nonadiabatic eigenfunction and, although not noted in the paper, the specified parameters and Equation (3) of ref. [24] can be used to calculate that such nodes exist and are in the tunneling region. Furthermore it can be seen by comparison between Figures (2) and (5) that the distance of these nodes from the origin appears to vary with the difference between ω_1 and ω_2, suggesting that the nodes might exist at larger and larger distances from the origin as the two frequencies approach each other before ultimately disappearing for $\omega_1 = \omega_2$, in which case the nodal lines become parallel.

Possible nodes in the tunneling region were also shown in ref. [25], which studied the eigenstates of Jahn-Teller Hamiltonians with D_{4h} and elliptical symmetry, where it was suggested that conical nodes might move in from large radius. This was pictured in Figure 9 and the shapes of the nodes were pictured in Figure S9 of the Supplementary Materials. Although not noted in the paper, the specified parameters and Equation (4) of ref. [25] can be used to calculate that these nodes are in the tunneling region. It further appears that the distance from nodes to the origin is tunable, as in ref. [24], because it decreases with increasing Jahn-Teller displacement d. This suggests that at small d these nodes, and perhaps others, could exist further into the tunneling region.

These two intriguing observations motivated a study of tunneling in a separable nonadiabatic system, where the results can be most clearly contrasted with adiabatic tunneling on a single potential surface. For a single potential surface, JWKB theory unambiguously predicts that eigenfunctions monotonically decay along the separable coordinate of steepest ascent in the tunneling region [26]. The present study explores separable eigenfunctions of the Jahn-Teller Hamiltonian with circular symmetry, which has a conical intersection at the origin. Prior work has studied nonadiabatic tunneling through and around a conical intersection at the origin; [20-23] this study focuses on nonadiabatic tunneling into circularly symmetric barriers that uniformly increase in height with increasing radius. Here, a colored exact factorization reveals conical nodes far into the tunneling region, and separable projections of numerically exact nonadiabatic eigenstates onto adiabatic electronic eigenstates reveal a systematic origin that breaks the JWKB rules for separable adiabatic tunneling.

The exact nonadiabatic eigenfunctions of a circularly-symmetric Jahn-Teller Hamiltonian (Eq. 3.4) were calculated accurately over a range extending into the tunneling regime at large

radius and many eigenfunctions had nodes beyond the classical turning point. To test their conical nature, the nonadiabatic eigenfunctions were projected onto each of their component diabatic states in a method similar to the approach in ref. [27]. In the left panels of Figure 5.1, the diabatic projections are shown for the second lowest energy $j = 3/2$ nonadiabatic eigenfunction.

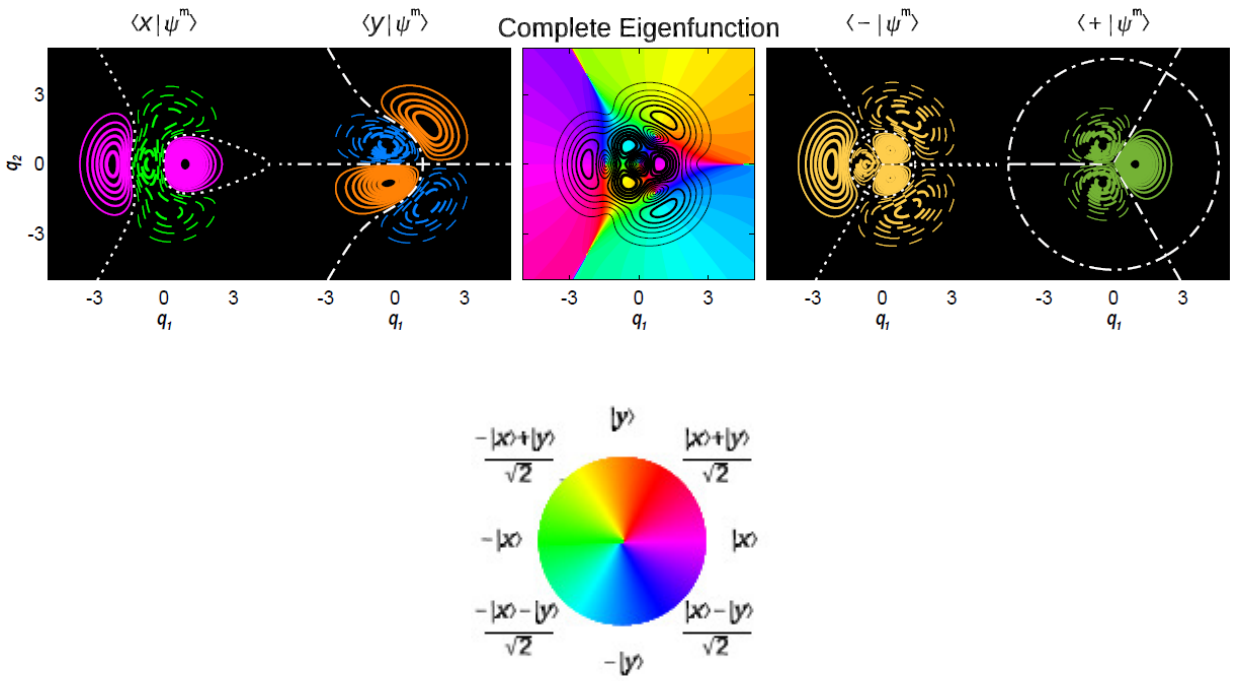

Figure 5.1: Three visualizations of the ($p=1$, $|j|=3/2$, $\sigma_v=+1$) nonadiabatic eigenfunction of the circularly symmetric Jahn-Teller Hamiltonian with $\omega=200$ cm^{-1} and $(D\omega)=25$ cm^{-1}. p is the adiabatic radial quantum number, j is the pseudo-rotation quantum number and σ_v is a reflection operator. In the center panel, the complete nonadiabatic eigenfunction is shown using a colored exact factorization. Contours represent probability amplitude, with contour intervals at 10% of the maximum probability amplitude; higher contours are thicker than lower contours. The color represents electronic character using the color wheel on the bottom of the figure. Outside the lowest contour, three nodes can be seen, each at a radius of ~4.55, with angles of $\pi/3$, π and $5\pi/3$. The left two panels show the projections of the nonadiabatic eigenfunction onto diabatic electronic states $|x\rangle$ and $|y\rangle$. On both projections, solid contours represent positive amplitude and dashed contours represent negative amplitude with contour intervals at 10% of the maximum probability amplitude in the center panel. Nodal curves are represented by white dotted curves on $|x\rangle$ and white dot-dashed curves on $|y\rangle$. The right two panels show the projections of the nonadiabatic eigenfunction onto adiabatic electronic states $|-\rangle$ and $|+\rangle$. As in the diabatic projections, contours represent probability amplitude, with contour intervals at 10% of the maximum probability amplitude in the center panel and with higher contours being thicker than lower contours. Solid contours represent positive amplitude and dashed contours represent negative amplitude. Nodal curves are represented by white dotted curves on $|-\rangle$ and white dot-dashed curves on $|+\rangle$. The rightmost panel shows a radial node in the projection onto the upper adiabatic state near $\rho=4.55$. This is in the tunneling region as the classical turning point for the upper adiabatic state is $\rho\sim 2.01$ and the classical turning point for the lower adiabatic state is $\rho\sim 3.01$.

Conical nodes occur in the exact nonadiabatic eigenfunctions where nodal curves in the projections onto diabatic states intersect one another [24]. A careful observation of Figure 5.1 shows three such nodes, each at a radius of 4.55 and angles from the x-axis of $\frac{\pi}{3}$, π and $\frac{5\pi}{3}$. The nodal curves in the diabatic projections do not have an intuitive pattern. One common definition [16, 19] of the tunneling region (if it can be sensibly defined for a nonadiabatic problem) uses the most permissive adiabatic potential energy surface barrier. This suggests that examination of the adiabatic projections might be informative.

When the nonadiabatic eigenfunctions are projected onto adiabatic electronic eigenfunctions, they display a circular symmetry. Nodal curves in the adiabatic electronic projections are either radial nodes tracing concentric circles with the conical intersection as their center or angular nodes radiating from the origin at the conical intersection to infinite radius at intervals of $\frac{\pi}{j}$ radians where j is the half-odd integer pseudo-rotation quantum number. These nodal curves are a consequence of the separability of the adiabatic projections discovered by Longuet-Higgins et. al. in 1958 [28].

5.2 Theory

The conserved pseudo-rotation quantum number can be used to show that the adiabatic projections of the exact nonadiabatic eigenfunctions are separable in polar coordinates [28]. Polar coordinates here are defined as the radius $\rho = \sqrt{q_1^2 + q_2^2}$ and the polar angle $\phi = \text{atan2}(q_2, q_1)$ where $\text{atan2}(y, x)$ extends $\arctan(y/x)$ over a 2π range. The real-valued adiabatic electronic eigenfunctions are defined as in Equation 4.6 [25] of Chapter 4 as

$$\begin{aligned}\left|-;\phi\right\rangle &= \mathrm{ssqw}(\phi/2)\{\sin(\phi/2)\left|x\right\rangle - \cos(\phi/2)\left|y\right\rangle\}\\ \left|+;\phi\right\rangle &= \mathrm{csqw}(\phi/2)\{\cos(\phi/2)\left|x\right\rangle + \sin(\phi/2)\left|y\right\rangle\}\end{aligned} \tag{5.2}$$

where the sinusoidal square wave $\mathrm{ssqw}(\phi/2)$ and the cosinusoidal square wave $\mathrm{csqw}(\phi/2)$ are defined as in Equation 4.6 [25]. These adiabatic electronic eigenfunctions are transformed into each other by $\phi \to \phi + \pi$.

Each exact nonadiabatic eigenfunction may be written as

$$\left\langle \rho,\phi \middle| \psi^m_{exact} \right\rangle = \psi^m_-(\rho,\phi)\left|-;\phi\right\rangle + \psi^m_+(\rho,\phi)\left|+;\phi\right\rangle \tag{5.3}$$

where m designates the nonadiabatic eigenfunction and $\psi^m_-(\rho,\phi)$ and $\psi^m_+(\rho,\phi)$ are the projections of the exact nonadiabatic eigenfunction ψ^m_{exact} onto adiabatic states.

$$\begin{aligned}\psi^m_-(\rho,\phi) &= \left\langle -;\phi \middle| \left\langle \rho,\phi \middle| \psi^m_{exact} \right\rangle\right.\\ \psi^m_+(\rho,\phi) &= \left\langle +;\phi \middle| \left\langle \rho,\phi \middle| \psi^m_{exact} \right\rangle\right..\end{aligned} \tag{5.4}$$

The continuity of $\psi^m_-(\rho,\phi)\left|-;\phi\right\rangle$ with $\psi^m_+(\rho,\phi)\left|+;\phi+\pi\right\rangle$ requires, since $\left|-;\phi\right\rangle = \left|+;\phi+\pi\right\rangle$, that $\psi^m_-(\rho,\phi)$ is a continuation of $\psi^m_+(\rho,\phi+\pi)$.

For the nonadiabatic eigenfunction with $\sigma_v = +1$, the real-valued pseudo-rotation factors are

$$\mathrm{ssqw}(\phi/2)\sin(|j|\phi) \qquad \text{on } \left|-;\phi\right\rangle \tag{5.5}$$

and

$$\mathrm{csqw}(\phi/2)\cos(|j|\phi) \qquad \text{on } \left|+;\phi\right\rangle \tag{5.6}$$

where j is the half-odd integer pseudo-rotation quantum number. These factors are not eigenfunctions because they do not have continuous derivatives and do not form an orthonormal basis over the vibrational coordinate $0 \le \phi < 2\pi$ (Recent papers have discussed how nonadiabatic eigenfunctions have discontinuities in their projections onto adiabatic electronic states at the origin [29, 30]). As with the adiabatic electronic eigenfunctions, the pseudo-rotation factors are interchanged by the transformation $\phi \to \phi + \pi$.

Anticipating their continuity through the conical intersection, the nonadiabatic eigenfunctions with $\sigma_v = +1$ are written in terms of the following two separable functions of the vibrational coordinates:

$$\begin{aligned} \psi_-^m(\rho,\phi) &= [\theta(\rho)]^{1/2} \chi_j^m(\rho)\mathrm{ssqw}(\phi/2)\sin(j\phi) \\ \psi_+^m(\rho,\phi) &= [\theta(\rho)]^{1/2} \chi_j^m(-\rho)\mathrm{csqw}(\phi/2)\cos(j\phi) \end{aligned} \tag{5.7}$$

where $\theta(\rho)$ is the Heaviside unit step function defined as

$$\theta(\rho) = \begin{cases} 0 & \text{for } \rho < 0 \\ 1/2 & \text{for } \rho = 0 \\ 1 & \text{for } \rho > 0. \end{cases}, \tag{5.8}$$

The polar coordinate ρ is nonnegative, so we define $R = \rho$ for positive R and $R = -\rho$ for negative R such that the radial factor $\chi_j^m(R)$ is a continuous real-valued function with continuous derivatives over the domain $(-\infty, \infty)$. This differentiability follows from the quantum mechanical requirement that the overall wavefunction be differentiable. Figure 5.2 illustrates this continuity in the radial function when crossing from the lower state to the upper state at the conical intersection.

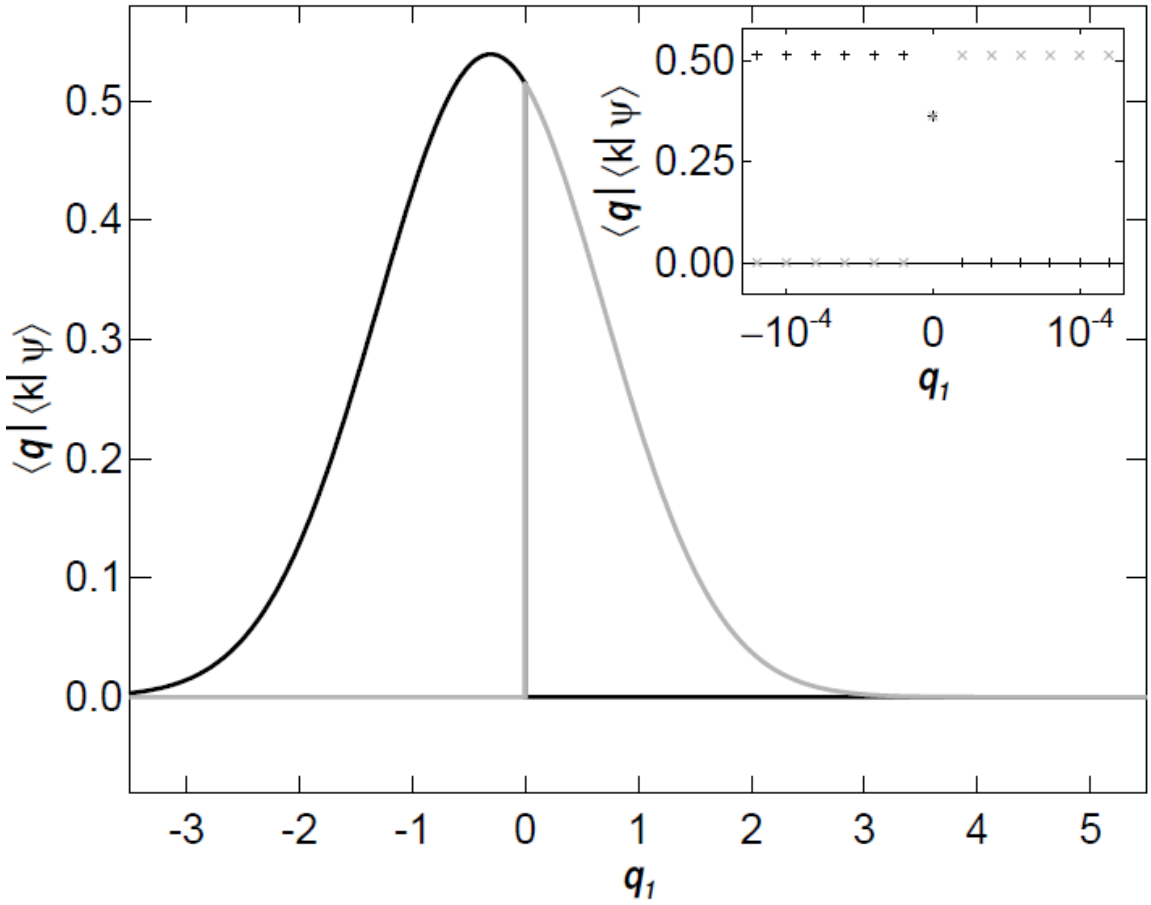

Figure 5.2: The cross-section along $q_2 = 0$ of the probability amplitude for the projections of the lowest energy eigenstate of the $(D\omega)/\omega = 0.05$ Jahn-Teller Hamiltonian onto the upper and lower adiabatic states. The black curve is the projection onto the lower adiabatic state and the gray curve is the projection onto the upper adiabatic state, with both projections experiencing a point discontinuity at $q_1 = 0$. At upper right, a closer view is shown with black $+$ signs showing the projection onto the lower adiabatic state and gray $\times$ signs showing the projections onto the upper adiabatic state. Each point at the origin is $1/\sqrt{2}$ times the total probability amplitude at the conical intersection. Looking at the function in black on the left and the function in gray on the right, the continuity of the radial function $\chi_j^m(R)$ can be seen with $q_1 = -R$.

Based on Eq. (5.7), the nonadiabatic eigenfunction nodes in the tunneling region in Fig. 5.1 indicate a node in the radial factor $\chi_j^m(R)$ at large negative R that gives rise to the radial node in the projection onto the upper adiabatic electronic state. But which eigenfunctions will have nodes in $\chi_j^m(R)$? How are nodes affected by changing $(D\omega)/\omega$? Can they be created or annihilated? What impact do these nodes have on the electronic index η? How are point conical nodes related to the nodal curves of the adiabatic limit? Are other rules about eigenfunction behavior broken in nonadiabatic systems? Clearly these nodes warrant further study.

5.3 Calculations

The nonadiabatic eigenvalues have been checked in Chapters 2 – 4 [24, 25, 27] for convergence and accuracy with regard to previously published results by Longuet-Higgins [28], Judd [31], and Thompson, Truhlar, and Mead [32]. However, these convergence and accuracy checks on the eigenvalues do not directly establish that the eigenvectors are converged or accurate or that the coordinate representation of the eigenfunctions is correctly calculated from the eigenvectors in this basis set. All amplitudes are based on square-normalized nonadiabatic eigenfunctions and radial amplitudes are calculated from them using Eq. (5.3) - (5.7). One check on the accuracy of the eigenvectors was obtained because eigenstates of σ_v have a systematic pattern of zeros in their coefficients; [33] all coefficients that should be zero by symmetry have magnitudes of less than 2×10^{-14}.

To confirm the precision of the coordinate representation of the nonadiabatic eigenfunctions, the twelve lowest two-dimensional eigenfunctions are plotted on a discrete 2D grid with 0.01 spacing over the domain [-9,9] for each coordinate. Using a basis of

25 normalized harmonic oscillator eigenfunctions for each coordinate (1250 total basis states), the normalized eigenfunctions are calculated to be converged at all grid points to within 10^{-14} when compared with the results of a calculation with 35 normalized harmonic oscillator eigenfunctions for each coordinate (2450 total basis states). The eigenfunctions are orthogonal to within 4.8×10^{-14} and normalized to within 2.2×10^{-12}.

Beyond convergence, it is necessary to check that the coordinate representation of the eigenfunctions is accurate. As an accuracy check, the eigenfunctions for $|x, v_1 = 0, v_2 = 0\rangle$, $|y, v_1 = 0, v_2 = 0\rangle$, $|x, v_1 = 1, v_2 = 0\rangle$, and $|y, v_1 = 0, v_2 = 1\rangle$ were calculated for Hougen's accidental Born-Oppenheimer case [34] with $\omega_1 = 200$ cm^{-1}, $(D\omega)_1 = 625$ cm^{-1}, $\omega_2 = 217$ cm^{-1} and $(D\omega)_2 = 0$ cm^{-1}. This Hamiltonian has two-dimensional harmonic oscillators on electronic states $|x\rangle$ and $|y\rangle$ that are displaced by $\pm d_1 = \sqrt{2(D\omega)/\omega} = 2.5$ along q_1 and undisplaced along q_2 and, as such, can be solved analytically. Numerical calculation using the same program used to calculate the Jahn-Teller eigenfunctions served as a check on the accuracy of the coordinate representation of the eigenfunctions. A comparison between the analytical and numerical solutions of this displaced oscillator reveals that the four lowest energy eigenfunctions are accurate to within 1.1×10^{-14} at every point (grid spacing of 0.01) within a $q_1\times q_2$ domain of $[-8,8]\times[-8,8]$. This level of convergence and accuracy allows the investigation of nonadiabatic eigenfunction features at the low amplitudes that arise deep in the tunneling region.

5.4. Results

The lowest energy eigenfunction of the circularly symmetric Jahn-Teller Hamiltonian for which we calculate accidental conical nodes in the tunneling region is $(v,|j|)=(1,1/2)$. Figure 5.3 shows the adiabatic potential energy surfaces and the projection of this eigenfunction onto the upper and lower adiabatic states for $\omega=200$ cm^{-1} and $(D\omega)=100$ cm^{-1}. As in Figure 5.2, the projections may be regarded as a single graph of $\chi_j^m(R)$. In the top panel, most of the probability amplitude resides within the classical turning points for the lower adiabatic state and there is one radial node within the classically allowed region for both adiabatic states (as expected from the vibrational quantum number). The amplitude around the transition into the tunneling region on the left (lower adiabatic state) looks more or less like normal adiabatic tunneling. In contrast, the amplitude around the transition into the tunneling region on the right (upper adiabatic state) looks abnormal because it is nonzero at a point of inflection in a region that is classically allowed for both adiabatic potential energy surfaces. However, this is not necessarily a nonadiabatic effect: for example, the 1s radial eigenfunction of the hydrogen atom is an exponential decay.

To investigate this further, the lower panel shows the amplitudes for $-2.5\times10^{-4}\le\psi_+^m(\rho,\phi)\le5\times10^{-4}$. As can be clearly seen, at increasing radius, the upper adiabatic projection (in grey) crosses through zero near $\rho=2.88$ (where it is well converged for $n=25$); beyond the node, it reaches a minimum of -1.50×10^{-4} around $\rho=3.18$ before turning and monotonically increasing toward zero. When this calculation is repeated with $n=35$ instead of $n=25$, the number of basis states nearly doubles from 1250 to 2450 and the function is converged at every point to within 10^{-15}. The radial node is clearly not an artifact because the extremum beyond it is converged to ten digits.

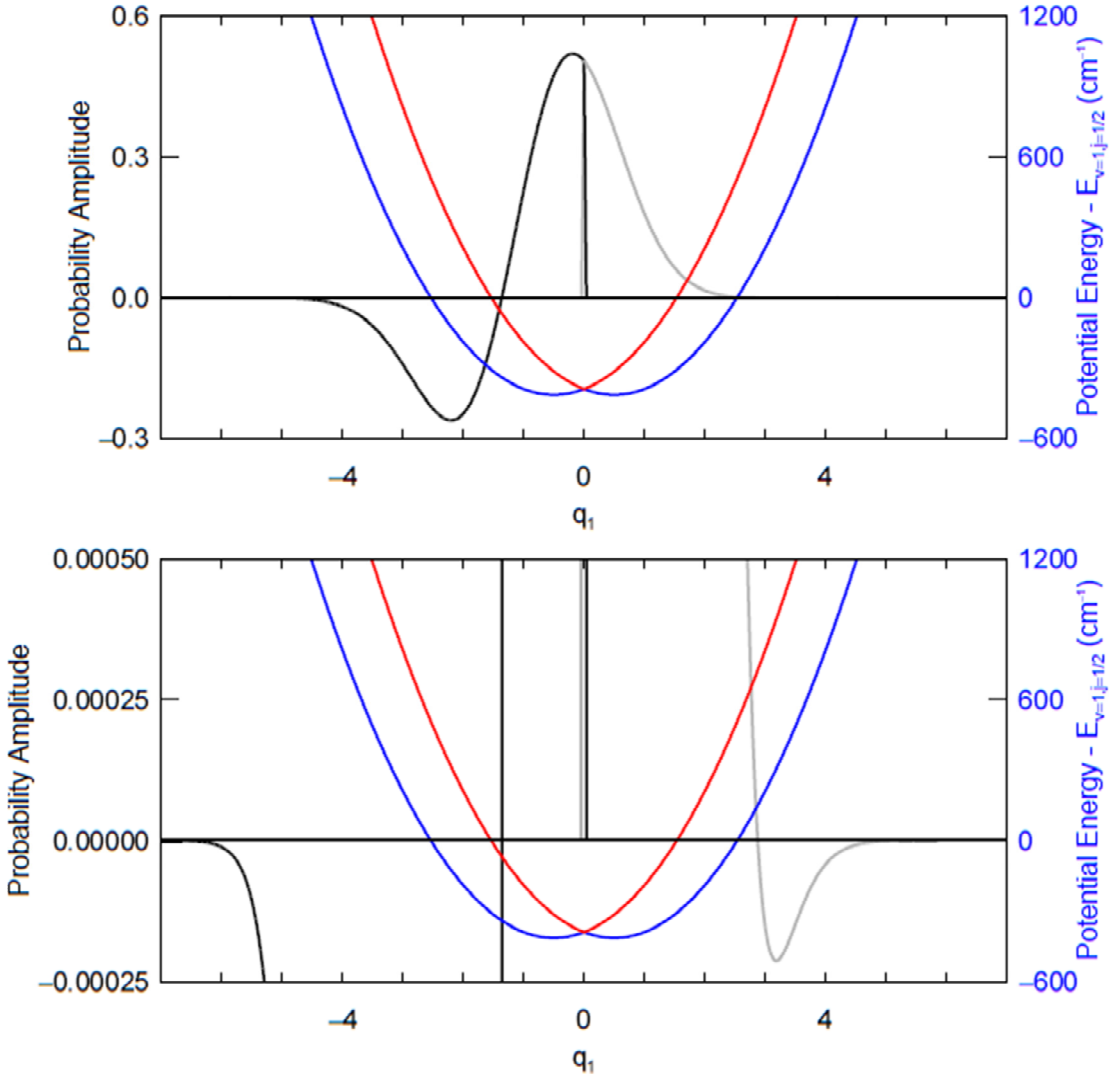

Figure 5.3: Top) A cross-section along q_1 at $q_2 = 0$ of the projections of the $(v,|j|) = (1,1/2)$ eigenstate of the circularly-symmetric Jahn-Teller Hamiltonian with $\omega = 200$ cm^{-1} and $(D\omega) = 100$ cm^{-1}. Projections onto the lower adiabatic electronic state are shown in black and projections onto the upper adiabatic electronic state are shown in grey with amplitude shown using the axis at left. As in Figure 5.2, the black and grey projections show the continuity of the radial function $\chi_j^m(R)$ with $q_1 = -R$. The eigenstate energy (represented by the baseline at 0) and the potential energy surfaces relative to the total energy of the $(1,1/2)$ eigenstate are shown using the energy axis at right. The potential energy curve of the lower adiabatic state is shown in blue and the potential energy curve of the upper adiabatic state is shown in red. Bottom) A version of the top panel in which the amplitude axis has been magnified to reveal a radial node near $q_1 = 2.88$ and the extremum beyond it near $q_1 = 3.18$. The scale on the potential energy axis remains the same.

Figure 5.3 shows that this radial node in $\chi_j^m(R)$ lies beyond the intersection of the nonadiabatic eigenstate energy with both potential energy curves. This unambiguously demonstrates a radial node in $\chi_j^m(R)$ in the tunneling region. Such a radial node is perpendicular to the direction of steepest ascent into the tunneling region, which would be forbidden for separable adiabatic tunneling. This is qualitatively similar to the radial node in the rightmost panel of Figure 5.1. As shown there, the intersection of a radial node with an angular node generates an accidental conical node in the complete nonadiabatic eigenfunction. This conical node will lie in the tunneling region if the radial node lies in a region where $E < V(q)$ for all coupled potential energy surfaces $V(q)$.

For smaller values of $(D\omega)/\omega$, the node occurs at larger radius, further into the tunneling region. For instance, this same $(v,|j|) = (1,1/2)$ eigenfunction of the circularly symmetric Jahn-Teller Hamiltonian with $(D\omega) = 50$ cm^{-1} has a node at $\rho = 4.12$. For $(1,1/2)$, all points with $\rho > 2.74$ are in the tunneling region for both adiabatic states. The projection of this eigenstate onto the upper adiabatic electronic state reaches a minimum of -2.13×10^{-4} in the normalized two-dimensional eigenfunction at $\rho = 4.33$ before turning and monotonically increasing toward zero. This calculation, like the calculation in Figure 5.3, is converged at every point to within 10^{-15}.

For the six lowest energy $\sigma_v = +1$ eigenstates, the nonadiabatic eigenfunctions and their projections onto adiabatic states for $(D\omega)/\omega = 0.2$ can be seen in Figure 5.4. The left column shows the colored factorization of the exact nonadiabatic eigenfunctions and the right two columns show the projections of the nonadiabatic eigenfunction onto adiabatic electronic states.

The adiabatic vibrational projection contours are shown in the same way as in Figure 5.1. However, adiabatic electronic projections are shown here using a method that differs from how nonadiabatic electronic character is shown in the colored exact factorization. Here color represents the conditional probability for each adiabatic electronic state at a given set of vibrational coordinates q_1 and q_2. These conditional probabilities are defined by

$$P^m(-;q_1,q_2)=\frac{\left|\psi_-^m(q_1,q_2)\right|^2}{\left|\psi_-^m(q_1,q_2)\right|^2+\left|\psi_+^m(q_1,q_2)\right|^2}$$
$$P^m(+;q_1,q_2)=\frac{\left|\psi_+^m(q_1,q_2)\right|^2}{\left|\psi_-^m(q_1,q_2)\right|^2+\left|\psi_+^m(q_1,q_2)\right|^2}. \tag{5.9}$$

The color ranges from tan for $P^m(-;q_1,q_2)=1$ to olive for $P^m(+;q_1,q_2)=1$. For each eigenstate, this coloration is necessarily the same function of vibrational coordinates for the projection onto either adiabatic electronic state.

Olive areas in the adiabatic projections in Figure 5.4 illuminate regions where most amplitude comes from the upper adiabatic state. Tan areas illuminate regions where most amplitude comes from the lower state. Olive regions generally surround the nodal curves in the middle row, where the projection of the eigenstate onto the lower adiabatic state is zero.

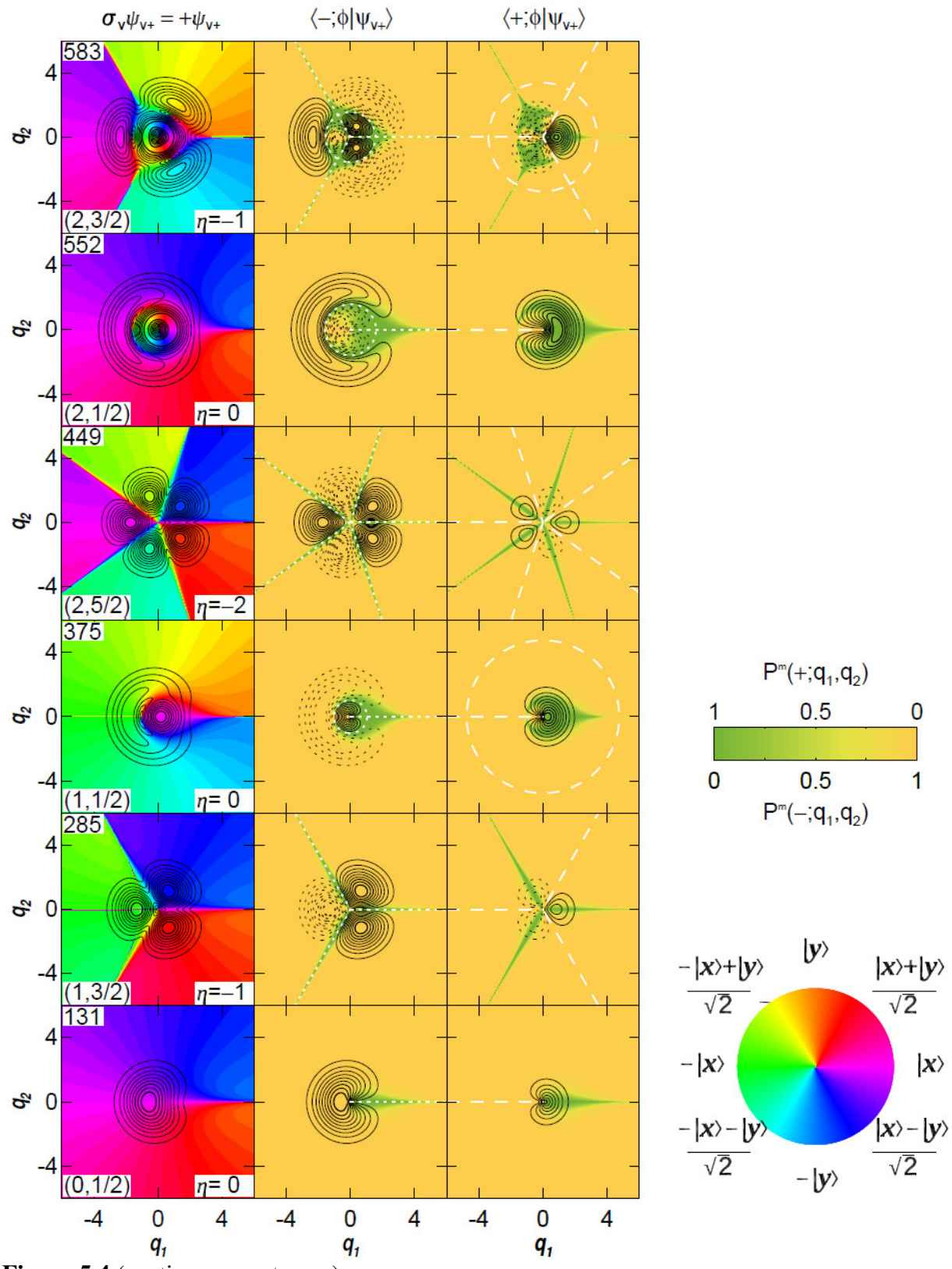

Figure 5.4 (caption on next page)

Figure 5.4 (on previous page)**:** The left column shows the six lowest energy $\sigma_v = +1$ eigenstates for the circularly symmetric Jahn-Teller Hamiltonian with $\omega = 200$ cm^{-1} and $(D\omega)/\omega = 0.2$. The contours represent probability amplitude in 10 % intervals, with thicker contour lines for higher amplitudes. Color represents nonadiabatic electronic character $\Theta_m(q_1, q_2)$ in terms of the diabatic basis states according to the color wheel at the bottom right. The energy of the eigenstate (in cm^{-1}) is labelled in the upper left corner, the vibrational and pseudo-rotation quantum numbers are labelled at bottom left, and the electronic index around the perimeter of the figure is labelled at bottom right. The middle (right) column shows the projection of the eigenstate at left onto the lower (upper) adiabatic electronic state. Contours represent 10 % intervals of the maximum total probability amplitude of the eigenstate, with solid contours representing positive amplitude and dashed contours representing negative amplitude. In the middle and right columns, colors indicate the conditional probabilities for the adiabatic electronic states (represented by the color bar at the right on the top). Nodal curves in the projections are shown in the middle (right) column as dotted (dashed) white lines where the projection onto the lower (upper) adiabatic state is zero.

The left column of Fig. 5.4 may be compared to the leftmost column of Fig 3.2 (Figure 2 of ref. [27]) and the rightmost column of Fig 4.2 (Figure 2 of ref. [25]), both of which show eigenstates that correlate to those shown here as $(D\omega)$ is varied. The eigenfunctions plotted here are for a larger stabilization energy, so that the small Jahn-Teller stabilization energy vibrational quantum number v is no longer good except as a correlation label (see Figure 1.5 of Ch. 1 or Fig. S1E of ref. [35]). Further, the eigenfunctions are shown over an expanded range in Fig. 5.4. In Fig 5.4, the $(v=2,|j|=5/2)$ eigenfunction is plotted with the opposite arbitrary overall sign compared to Fig. 3.2 and Fig 4.2 and the $(v=1,|j|=3/2)$ eigenfunction is plotted with the opposite arbitrary overall sign compared with Fig. 4.2. The signs in Fig. 5.4 were chosen to agree with the signs chosen in the perturbation theory equation below.

In Figure 5.4, the projections of the nonadiabatic eigenfunctions onto adiabatic electronic states have radial and angular nodes as anticipated by the separability of the adiabatic projections into radial and angular portions. Further, the angular factors strictly depend on the pseudo-rotation quantum number with the projections onto the lower adiabatic state having an angular factor of $\mathrm{ssqw}(\phi/2)\sin(j\phi)$ and the projections onto the upper adiabatic state having an angular factor of $\mathrm{csqw}(\phi/2)\cos(j\phi)$. Three eigenfunctions in Figure 5.4 have nodes in the radial factor $\chi_j^m(R)$. Radial nodes are visible in the projection onto the lower adiabatic state for the 375 cm^{-1}, 552 cm^{-1} and 583 cm^{-1} eigenstates. Radial nodes are visible in the projection onto the upper adiabatic state for the 375 cm^{-1} and 583 cm^{-1} eigenstates.

The $(v,|j|)=(1,1/2)$ eigenfunction has the same quantum numbers as the eigenfunction for which $\chi_j^m(R)$ was shown in Figure 5.3. Like that eigenfunction, it has one radial node in the

allowed region and one radial node deep in the tunneling region. Each radial node gives rise to an accidental conical node in the exact nonadiabatic eigenfunction. Compared to Chapters 3 [27] and 4 [25], the nonadiabatic eigenfunctions here reveal previously undetected conical nodes in the tunneling region. As a result, the electronic index η around the perimeter shown here differs from that reported for this eigenfunction in Chapter 3 [27] and Chapter 4 [25]. Likewise for the Hamiltonian parameters in ref. [27], the outermost conical nodes in the $(v,|j|)=(2,3/2)$ eigenstate lay beyond the coordinate range plotted there and did not contribute to the electronic index reported there. Around the perimeter shown in Figure 5.4, the net electronic index for each eigenfunction is equal to the electronic index around the conical intersection at the origin, where eigenfunctions may have no node (for $|j|=1/2$) or an essential node with index $-(|j|-1/2)$.

The radial behavior of eigenfunctions varies with $(D\omega)/\omega$ [28, 32]. Figure 5.5 shows this variation for the $|j|=1/2$ eigenfunction that appears in the fourth row from the top of Figure 5.4. Figure 5.5 plots the nonadiabatic eigenfunction and its adiabatic projections for each of six different values of $(D\omega)/\omega$. The $(D\omega)/\omega=0.05$ eigenfunction was shown in Fig 3.2 (Figure 2 of ref. [27]), but is plotted over an expanded coordinate range here. As can be seen in the top two rows, for large $(D\omega)/\omega$, radial nodes on both adiabatic projections appear near the same radius. These nonadiabatic eigenfunctions almost have the radial node at $\rho=d$ expected in the adiabatic limit. The top four rows have radial nodes in both projections, though the nodes are progressively further apart in the lower rows. The radial node in the projection onto the lower adiabatic electronic state decreases in radius with decreasing $(D\omega)/\omega$ while the radial node in the projection onto the upper adiabatic electronic state increases in radius with decreasing

$(D\omega)/\omega$. The node on the upper adiabatic surface moves into the tunneling region as $(D\omega)/\omega$ decreases, apparently moving beyond the maximum radius shown for the lowest two panels.

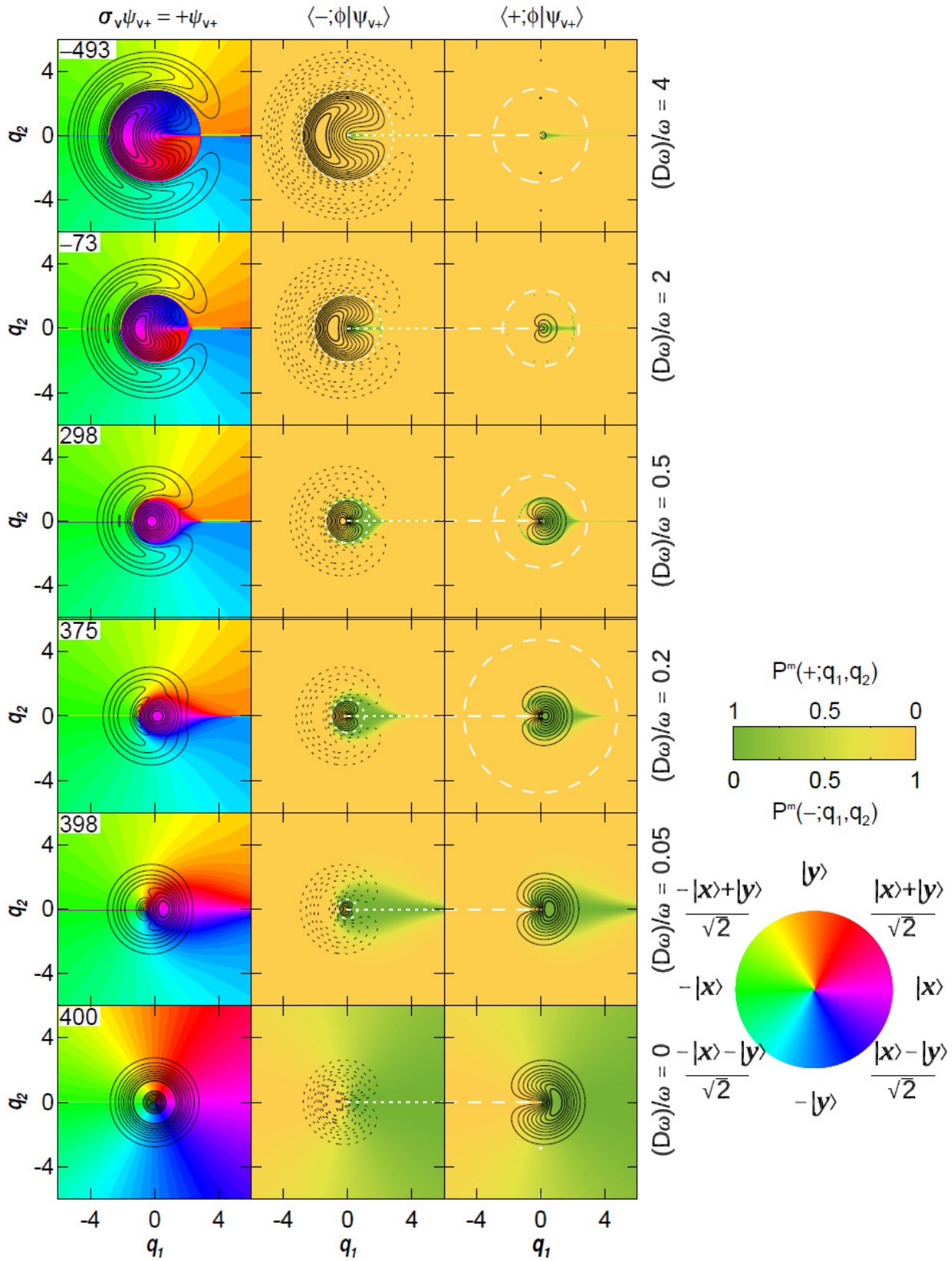

Figure 5.5 (caption on next page)

Figure 5.5 (on previous page)**:** The left column shows a colored factorization of the $\sigma_v = +1$ eigenstate with low stabilization energy quantum numbers $(v = 1, |j| = 1/2)$ for a circularly symmetric Jahn-Teller Hamiltonian with $\omega = 200$ cm^{-1} and $(D\omega)/\omega$ as shown to the right of each row. This eigenstate becomes the $(p = 1, |j| = 1/2)$ eigenstate with one radial node in the adiabatic limit. The contours here represent probability amplitude in 10 % intervals and the contour lines get thicker for higher contours. In the left column, color represents nonadiabatic electronic character $\Theta_m(q_1, q_2)$ according to the color wheel at the bottom right. The middle (right) column shows the projection of the eigenstate at left onto the lower (upper) adiabatic potential. Contours represent 10 % intervals of the maximum total probability amplitude of the eigenstate with solid contours representing positive amplitude and dashed contours representing negative amplitude. In the right two columns, colors indicate the adiabatic conditional probabilities represented by the horizontal color bar. Radial nodes in the projections are shown as dotted white lines in the middle column for nodes in the projection onto the lower adiabatic electronic state and dashed white lines in the right column for nodes in the projection onto the upper adiabatic electronic state.

First order perturbation theory can be used to locate radial nodes at very small d. In the limit of zero Jahn-Teller displacement d, we can analytically describe the wavefunctions as the system becomes "accidentally" adiabatic and separable at $d = 0$. Each adiabatic vibrational eigenfunction becomes a product of harmonic oscillator eigenfunctions with the familiar dependences on the vibrational coordinate, such as

$$\begin{aligned}
\phi_0(q) &= (\frac{1}{\pi})^{1/4} e^{-q^2/2} \\
\phi_1(q) &= (\frac{1}{\pi})^{1/4} \sqrt{2} q e^{-q^2/2} \\
\phi_2(q) &= (\frac{1}{\pi})^{1/4} \frac{1}{\sqrt{2}} (2q^2 - 1) e^{-q^2/2}
\end{aligned} \tag{5.10}$$

In this highly degenerate limit where energy depends only on v, the exact vibrational-electronic states with $\sigma_v = +1$ may also be taken as linear combinations with definite absolute values of the pseudo-rotation quantum number.

$$\begin{aligned}
&\left| v = 0, \left| j \right| = 1/2, \sigma_v = +1 \right\rangle^{(0)} = \left| v_1 = 0, v_2 = 0, x \right\rangle \\
&\left| v = 1, \left| j \right| = 1/2, \sigma_v = +1 \right\rangle^{(0)} = \frac{1}{\sqrt{2}} (\left| v_1 = 1, v_2 = 0, x \right\rangle + \left| v_1 = 0, v_2 = 1, y \right\rangle) \\
&\left| v = 1, \left| j \right| = 3/2, \sigma_v = +1 \right\rangle^{(0)} = \frac{1}{\sqrt{2}} (\left| v_1 = 1, v_2 = 0, x \right\rangle - \left| v_1 = 0, v_2 = 1, y \right\rangle) \\
&\left| v = 2, \left| j \right| = 1/2, \sigma_v = +1 \right\rangle^{(0)} = \frac{1}{\sqrt{2}} (\left| v_1 = 2, v_2 = 0, x \right\rangle + \left| v_1 = 0, v_2 = 2, x \right\rangle) \\
&\left| v = 2, \left| j \right| = 3/2, \sigma_v = +1 \right\rangle^{(0)} = \frac{1}{2} \left| v_1 = 2, v_2 = 0, x \right\rangle + \frac{1}{\sqrt{2}} \left| v_1 = 1, v_2 = 1, y \right\rangle - \frac{1}{2} \left| v_1 = 0, v_2 = 2, x \right\rangle \\
&\left| v = 2, \left| j \right| = 5/2, \sigma_v = +1 \right\rangle^{(0)} = \frac{1}{2} \left| v_1 = 2, v_2 = 0, x \right\rangle - \frac{1}{\sqrt{2}} \left| v_1 = 1, v_2 = 1, y \right\rangle - \frac{1}{2} \left| v_1 = 0, v_2 = 2, x \right\rangle
\end{aligned}$$

(5.11)

Except for $\left|v=2,\left|j\right|=5/2,\sigma_v=+1\right\rangle^{(0)}$, the arbitrary overall sign for each of these vibrational-electronic states agrees with the signs chosen in Chapter 4. For small d, these can be used to calculate approximate eigenfunctions of the Jahn-Teller Hamiltonian from first-order perturbation theory, such as

$$\begin{aligned}\left|v=1,\left|j\right|=1/2,\sigma_v=+1\right\rangle^{(1)} = &\left|v=1,\left|j\right|=1/2,\sigma_v=+1\right\rangle^{(0)} \\ &+d\left|v=0,\left|j\right|=1/2,\sigma_v=+1\right\rangle^{(0)} \\ &-d\left|v=2,\left|j\right|=1/2,\sigma_v=+1\right\rangle^{(0)}\end{aligned} \tag{5.12}$$

which is used to predict the low-displacement perturbation theory result for the location of the radial node in Figure 5.6.

These predict a node in the projection onto the lower surface at $(q_1,q_2)=(-2d,0)$ [equivalently $R=2d$] near the origin (solid blue line in Figure 5.6) and a node on the projection onto the upper surface at $(q_1,q_2)=(\frac{1}{d},0)$ at large radius [equivalently $R=-\frac{1}{d}$]. The result for the small radius node on the lower adiabatic surface is proportional to d and thus a valid result of first order perturbation theory that becomes increasingly accurate in the limit of small d. The large radius node is not proportional to d and therefore is not a valid result of first order perturbation theory; first order perturbation theory cannot legitimately be used to conclude that a large radius node exists (it predicts a non-existent large radius node for the analytically solvable displaced harmonic oscillator). The small radius node occurs at $\rho=0.595$ for $d=0.316$, $\rho=0.390$ for $d=0.200$, and $\rho=0.199$ for $d=0.100$, demonstrating the increasing accuracy of first order perturbation theory at small d.

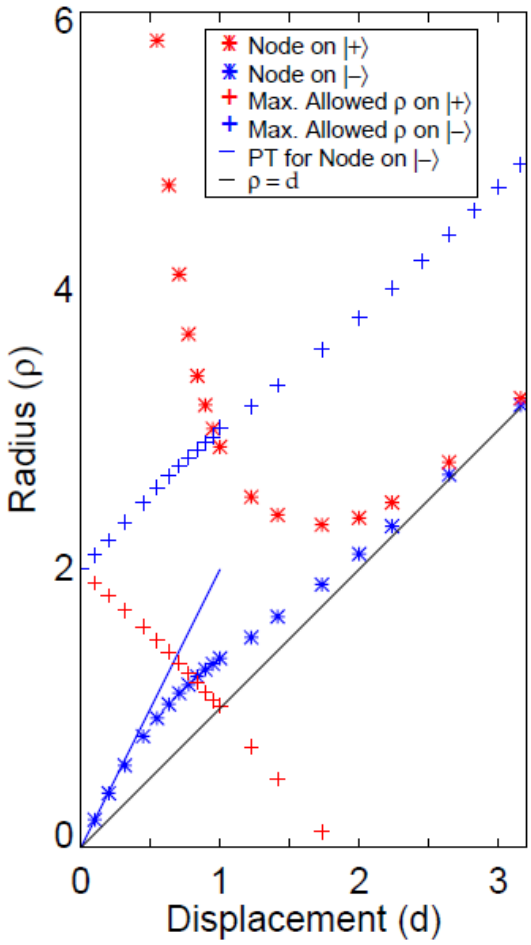

Figure 5.6: This plot shows the radii of the nodal curves in the adiabatic projections of the $(v,|j|)=(1,1/2)$ eigenstate of a circularly symmetric Jahn-Teller Hamiltonian as a function of the Jahn-Teller displacement. The radii of the nodes in the projection onto the lower adiabatic state are shown with blue asterisks and radii of the nodes in the projections onto the upper adiabatic state are shown with red asterisks. The black solid line marks a radius equal to the Jahn-Teller displacement. For small displacements, the solid blue line represents the radius of the node on the lower adiabatic state that is predicted by first order perturbation theory ($\rho = 2d$). All points above the red crosses are in the tunneling region for the upper adiabatic state and all points above the blue crosses are in the tunneling region for the lower adiabatic state as well. The large radius nodes for $d < 0.9$ are in the tunneling region with respect to both adiabatic potentials and thus in the nonadiabatic tunneling region.

The variation of the radii of the nodes in the projections can be seen in Figure 5.6. For large $(D\omega)/\omega$, both radial nodes in the projections converge to $\rho = d$. The radial node on the

upper state is always at a larger radius than the radial node on the lower state. For small $(D\omega)/\omega$, the radius of the node on the lower adiabatic projection goes to zero such that it becomes a point node for $(D\omega)/\omega = 0$. This conical node in an adiabatic eigenfunction is predicted by Eqs. (5.11) and (5.12), which also show that it can be removed by taking linear combinations of the degenerate $\left|v=1,\left|j\right|=1/2,\sigma_v=+1\right\rangle$ and $\left|v=1,\left|j\right|=3/2,\sigma_v=+1\right\rangle$ eigenfunctions. A similar adiabatic limiting accident is shown in Fig 4.2 (Fig. 2 of ref. [25]).

The radius of the node on the upper adiabatic projection appears to diverge in this limit, in qualitative (but not quantitative) agreement with the (invalid) prediction of first order perturbation theory. Since a single nodal curve cannot disappear and the analytic solution in Eq. (5.11) shows there is no node at finite radius when both couplings are zero, the radius of this node goes to infinity in the limit of small $(D\omega)/\omega$.

Over the entire range of $(D\omega)/\omega$ investigated, eigenfunctions correlating to an adiabatic vibrational quantum number of $p=0$ do not have any observed nodes apart from their nodes at the conical intersection for $\left|j\right|>1/2$. This is expected based on the analysis of ref. [32] and the discussion in Chapter 4 (Supplemental Material for ref. [25]). An example of this can be seen in the $(v,\left|j\right|)=(1,3/2)$ eigenfunction pictured in Figure 5.7. The calculation for $(D\omega)/\omega=0.05$ in Fig. 5.7 replicates that in Figure 3.2 over a wider range. Because the pseudo-rotation quantum number is $\left|j\right|=3/2$, these eigenfunctions all have a first-order conical node at the origin [27], but need not have nodes elsewhere because they have no radial nodes in the adiabatic limit and indeed no nodes are observed.

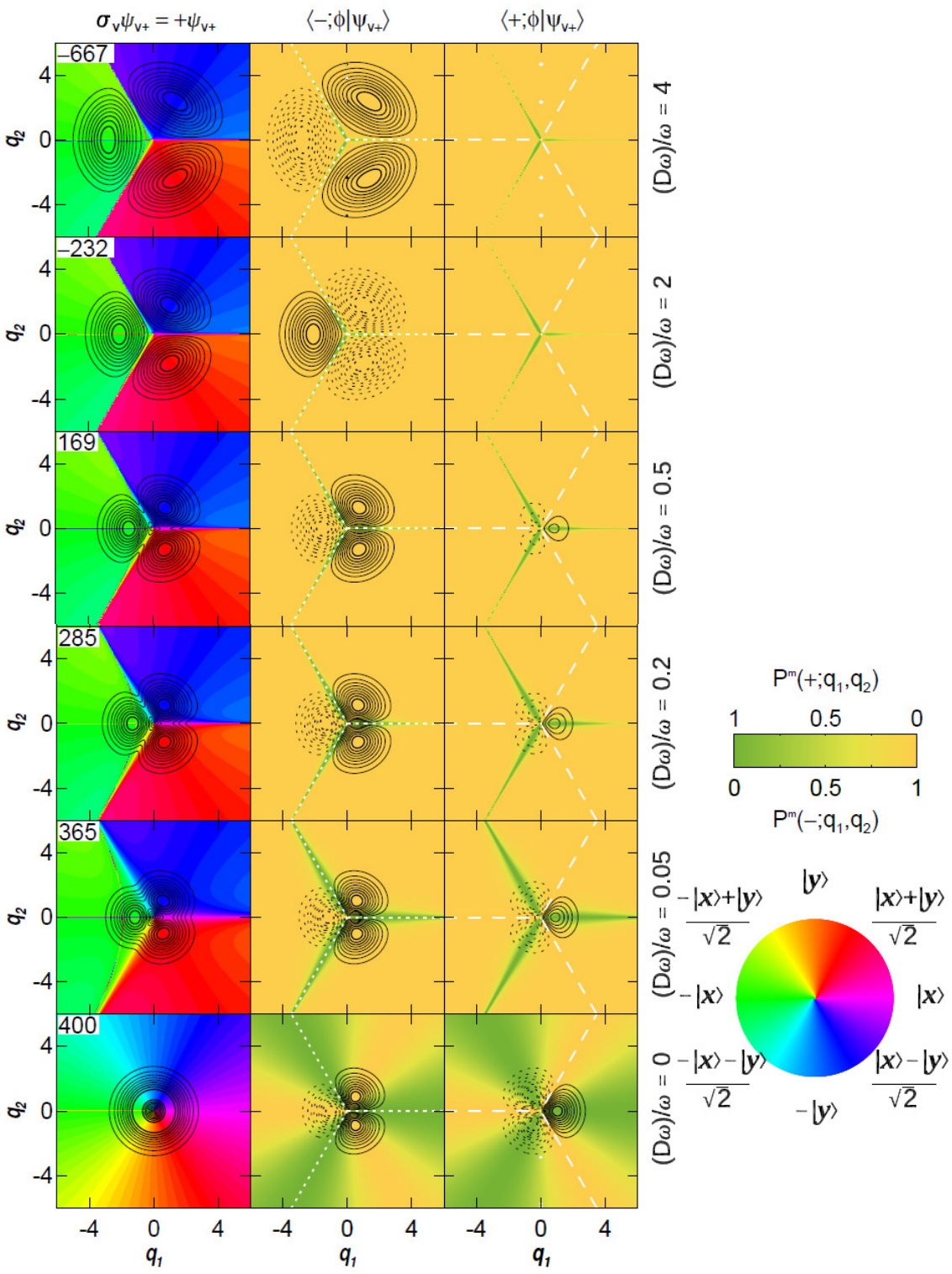

Figure 5.7 (caption on next page)

Figure 5.7 (on previous page)**:** The left column shows a colored factorization of the $\sigma_v = +1$ eigenstate with low stabilization energy quantum numbers $(v = 1, |j| = 3/2)$ for a circularly symmetric Jahn-Teller Hamiltonian with $\omega = 200$ cm^{-1} and $(D\omega)/\omega$ as shown to the right of each row. This eigenstate becomes the $(p = 0, |j| = 3/2)$ eigenstate with no radial nodes in the adiabatic limit. The contours here represent probability amplitude in 10 % intervals and the contour lines get thicker for higher contours. In the left column, color represents nonadiabatic electronic character $\Theta_m(q_1, q_2)$ according to the color wheel at the bottom right. The middle (right) column shows the projection of the eigenstate at left onto the lower (upper) adiabatic potential. Contours represent 10 % intervals of the maximum total probability amplitude of the eigenstate with solid contours representing positive amplitude and dashed contours representing negative amplitude. In the right two columns, colors indicate the adiabatic conditional probabilities represented by the horizontal color bar. Angular nodes in the projections are shown as dotted white lines in the middle column for nodes in the projection onto the lower adiabatic electronic state and dashed white lines in the right column for nodes in the projection onto the upper adiabatic electronic state.

Because the angular dependence of each projection is independent of its radial behavior, higher $|j| = 3/2$ states will have the same angular nodal structures as the $(1,3/2)$ state, but they will have accidental conical nodes because each adiabatic electronic state projection has radial nodes. Figure 5.8 shows $(v,|j|) = (2,3/2)$ eigenfunctions as $(D\omega)/\omega$ is varied. The calculation for $(D\omega)/\omega = 0.05$ replicates that in Figure 3.2 over a wider coordinate range. The $(2,3/2)$ state has 1 adiabatic radial node, so each projection onto one adiabatic electronic state has 1 radial node crossed by three angular half nodes on the other adiabatic electronic state to make 3 conical nodes each. The two sets of $2|j| = 3$ accidental conical nodes have opposite electronic indices (all 3 on the lower adiabatic surface have an index of $+1$ and all 3 on the upper adiabatic surface have an index of -1). The net electronic index from these accidental nodes is zero for $(D\omega)/\omega = 0.2$ and up in Figure 5.8. For $(D\omega)/\omega = 0.05$ in Figure 5.8, the 3 nodes on the upper adiabatic surface with an electronic index of -1 have apparently moved beyond the range shown so that the electronic index around the perimeter is $+2$. The radial nodal behavior can be compared with the eigenfunctions with low stabilization energy quantum numbers $(v = 1,|j| = 1/2)$ and adiabatic limit quantum numbers $(p = 1,|j| = 1/2)$ in Figure 5.5 which also have 1 radial node in the adiabatic limit. The key difference is that, in the adiabatic limit at $d = 0$, the $(2,3/2)$ eigenfunction has an accidental second order node with an index of $+2$ at the origin [which can be removed by taking linear combinations of the degenerate eigenfunctions in Eq. (5.11)]. As d increases, it not only spawns a radial node on the lower adiabatic state (as in Fig 5.5), but also leaves an essential nonadiabatic conical node (with index -1) behind at the origin.

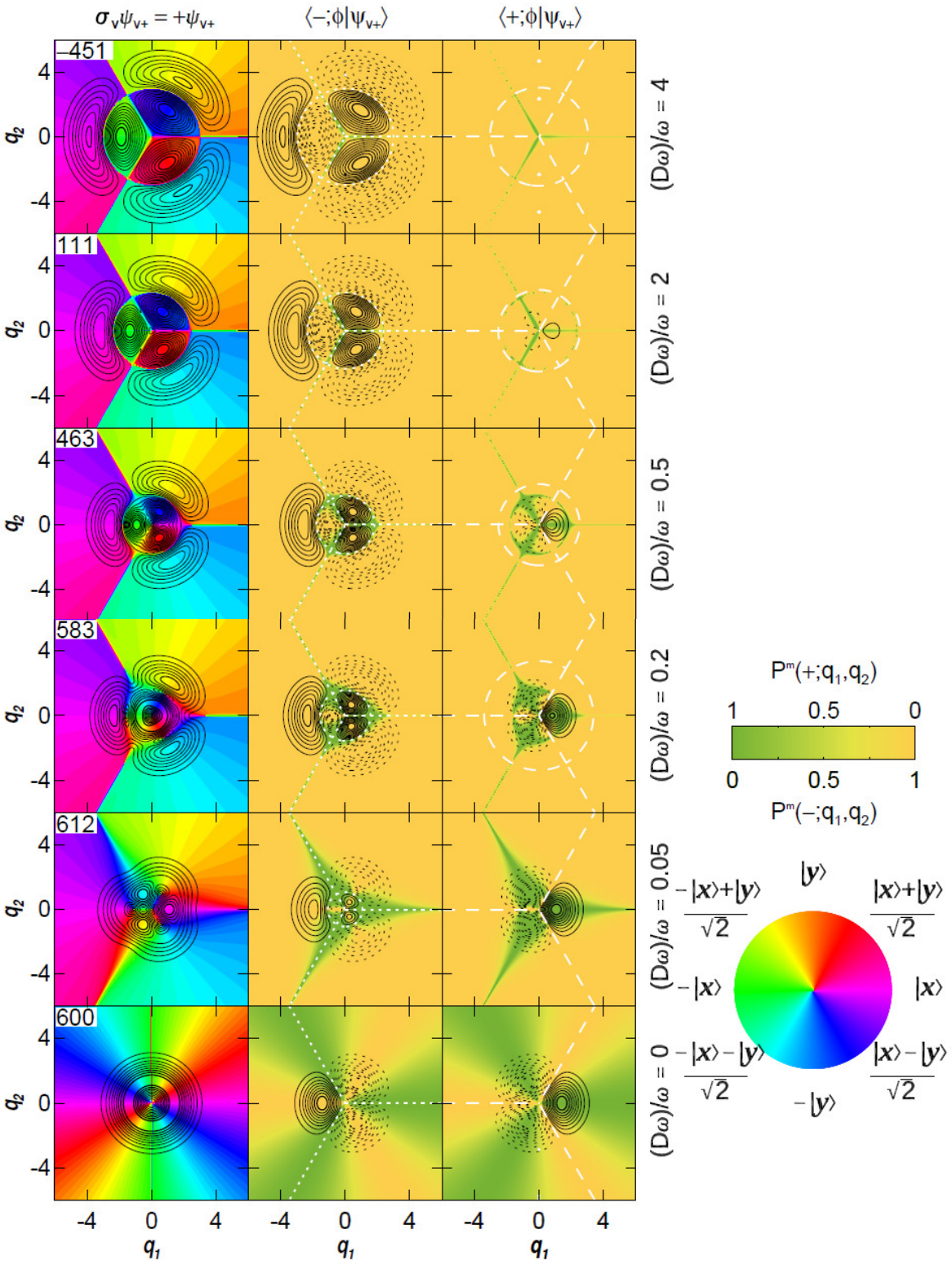

Figure 5.8 (caption on next page)

Figure 5.8 (on previous page)**:** The left column shows a colored factorization of the $\sigma_v = +1$ eigenstate with low stabilization energy quantum numbers $(v = 2, |j| = 3/2)$ for a circularly symmetric Jahn-Teller Hamiltonian with $\omega = 200$ cm^{-1} and $(D\omega)/\omega$ as shown to the right of each row. This eigenstate becomes the $(p = 1, |j| = 3/2)$ eigenstate with one radial node in the adiabatic limit. The contours here represent probability amplitude in 10 % intervals and the contour lines get thicker for higher contours. In the left column, color represents nonadiabatic electronic character $\Theta_m(q_1, q_2)$ according to the color wheel at the bottom right. The middle (right) column shows the projection of the eigenstate at left onto the lower (upper) adiabatic potential. Contours represent 10 % intervals of the maximum total probability amplitude of the eigenstate with solid contours representing positive amplitude and dashed contours representing negative amplitude. In the right two columns, colors indicate the adiabatic conditional probabilities represented by the horizontal color bar. Radial and angular nodes in the projections are shown as dotted white lines in the middle column for nodes in the projection onto the lower adiabatic electronic state and dashed white lines in the right column for nodes in the projection onto the upper adiabatic electronic state.

Figures 5.5 and 5.8 show $p=1$ eigenfunctions with 1 radial node each in the adiabatic limit; the number of radial nodes in each projection of the eigenfunction onto adiabatic electronic states is the adiabatic vibrational quantum number p. Compared to these functions, an eigenfunction with the same pseudo-rotation quantum number and $p=2$ has twice as many intersections between angular and radial nodes in the projections onto adiabatic electronic states and thus has twice as many accidental nodes in the exact nonadiabatic eigenfunction. This can be seen by comparing the $(p=2,|j|=1/2)$ eigenfunctions shown in Figure 5.9 to the $(p=1,|j|=1/2)$ eigenfunctions in Figure 5.5. In Fig. 5.9, the eigenfunction for $(D\omega)/\omega=0.05$ replicates that in Figure 3.2 over a wider coordinate range.

Figure 5.9 hints that nodes that appear for changing stabilization energy need not come from the origin or from very large radius. This eigenfunction has a real radial node for zero stabilization energy (which is an accidental adiabatic case). As stabilization energy increases, the radial nodes on the projections separate as the radial node on the projection onto the lower adiabatic electronic state increases in radius while the radial node on the projection onto the upper adiabatic electronic state decreases in radius until it moves through the origin to the lower adiabatic state near $(D\omega)/\omega=0.2$. This can be conceptualized as a pair of nodes in $\chi_j^m(R)$ moving toward positive R as d increases so that the eigenstate with two radial nodes becomes localized on the lower adiabatic electronic state.

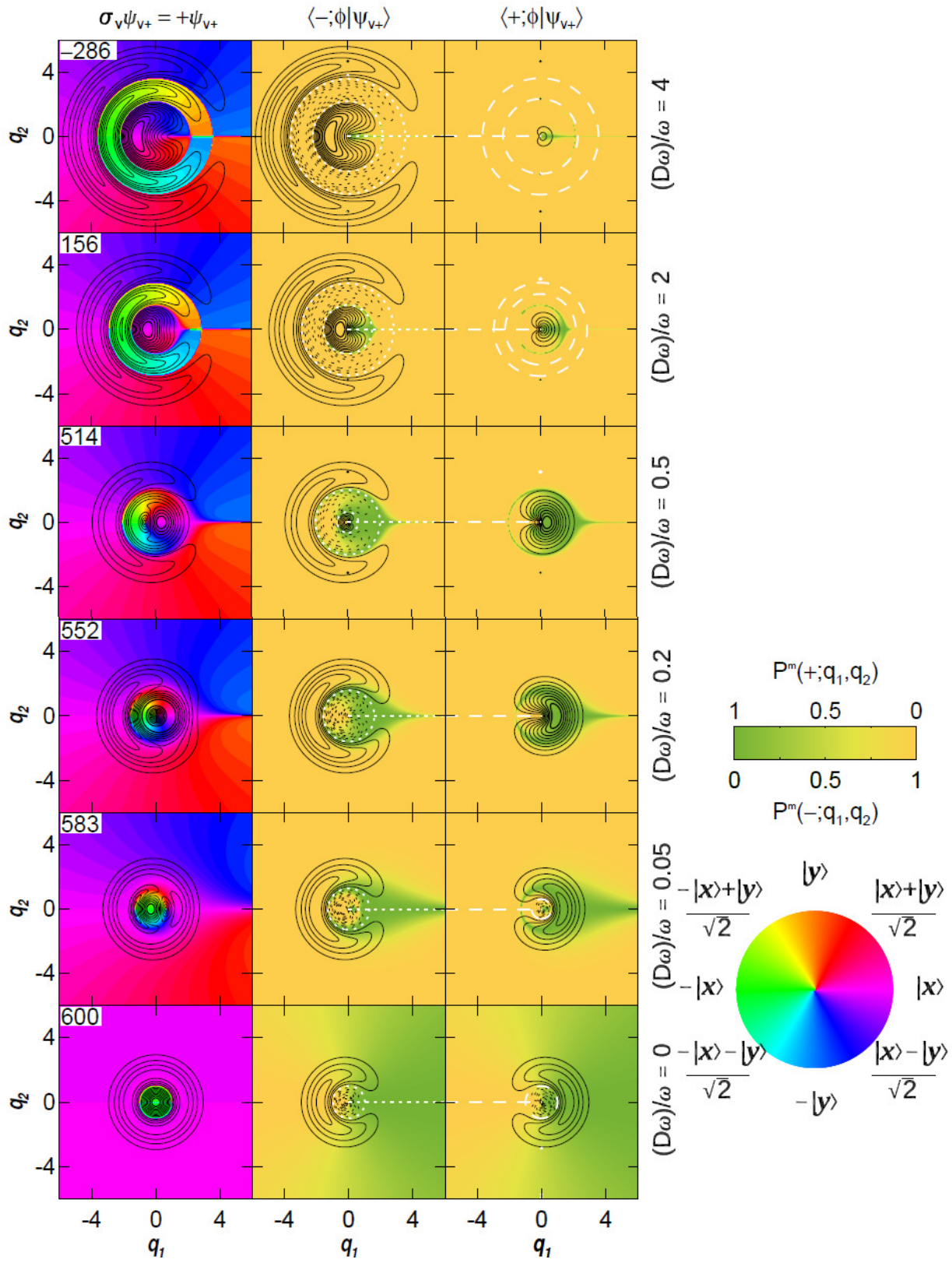

Figure 5.9 (caption on next page)

Figure 5.9 (on previous page)**:** The left column shows a colored factorization of the $\sigma_v = +1$ eigenstate with low stabilization energy quantum numbers $(v = 2, |j| = 1/2)$ for a circularly symmetric Jahn-Teller Hamiltonian with $\omega = 200$ cm^{-1} and $(D\omega)/\omega$ as shown to the right of each row. This eigenstate becomes the $(p = 2, |j| = 1/2)$ eigenstate with two radial nodes in the adiabatic limit. The contours here represent probability amplitude in 10 % intervals and the contour lines get thicker for higher contours. In the left column, color represents nonadiabatic electronic character $\Theta_m(q_1, q_2)$ according to the color wheel at bottom right. The middle (right) column shows the projection of the eigenstate at left onto the lower (upper) adiabatic potential. Contours represent 10 % intervals of the maximum total probability amplitude of the eigenstate with solid contours representing positive amplitude and dashed contours representing negative amplitude. In the right two columns, colors indicate the adiabatic conditional probabilities represented by the horizontal color bar. Radial and angular nodes in the projections are shown as dotted white lines in the middle column for nodes in the projection onto the lower adiabatic electronic state and dashed white lines in the right column for nodes in the projection onto the upper adiabatic electronic state.

Between $(D\omega)/\omega = 0.5$ and 2, two nodes appear at finite radius in the projection onto the upper adiabatic electronic state in Figure 5.9. Figure 5.10 shows that these come from a minimum in the $\chi_j^m(R)$ function that crosses through zero to create two new radial nodes in the adiabatic projections. The radial slopes at these new radial nodes are oppositely signed, so that the conical nodes they create have oppositely signed electronic indices and do not affect the electronic index of the eigenfunction around the perimeter, which remains zero throughout.

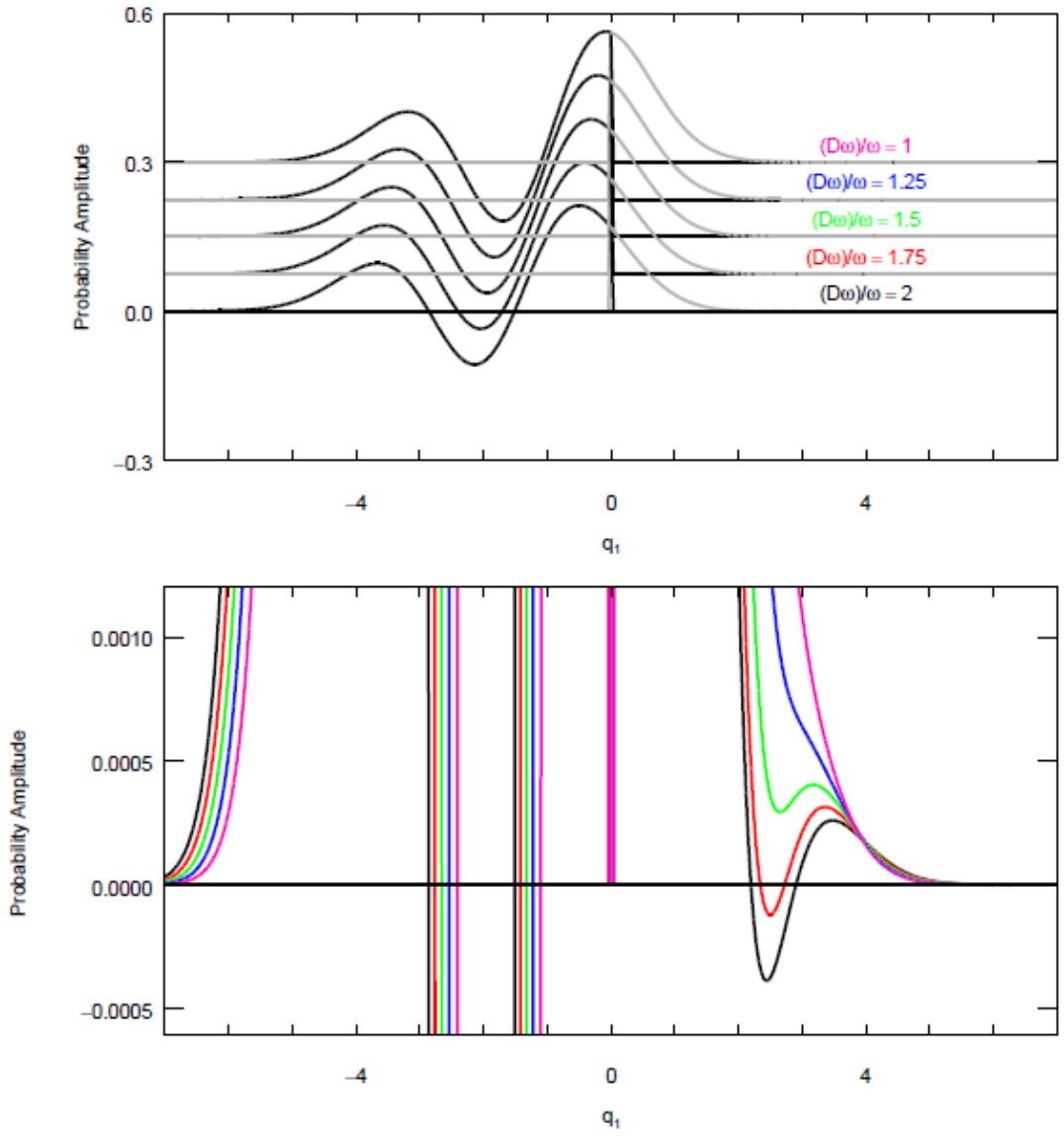

Figure 5.10: The radial function $\chi_j^m(R)$ for the eigenfunction $(v,|j|)=(2,1/2)$ is shown for five values of $(D\omega)/\omega$ from 1 to 2 where $q_1=-R$. At the top, the five radial functions are plotted with a vertical offset from one another. For each value of $(D\omega)/\omega$, the projection onto the upper adiabatic electronic state is gray and the projection onto the lower adiabatic electronic state is black. The values of $(D\omega)/\omega$ are labelled at right. On the bottom, the same projections are plotted over a smaller probability amplitude range to show the creation of two radial nodes. The projections onto either state for $(D\omega)/\omega=1,\ 1.25,\ 1.5,\ 1.75$ and 2 are plotted using fuchsia, blue, green, red, and black respectively.

For negative q_1, Figure 5.10 shows the projections onto the lower adiabatic state where there are two nodes for each value of $(D\omega)/\omega$. These eigenfunctions $\chi_j^m(R)$ resemble the $v=2$ eigenstate of a harmonic oscillator for which the equilibrium is shifted to the left. With increasing $(D\omega)/\omega$ both nodes move toward larger R (more negative q_1). These results are in keeping with the adiabatic limit, in which two radial nodes increase in radius with the Jahn-Teller displacement.

For positive q_1, the lower panel of Figure 5.10 shows results that appear abnormal from the adiabatic prospective. With increasing $(D\omega)/\omega$, a shoulder develops and becomes a local minimum near $(D\omega)/\omega = 1.5$. As discussed in Section 5.1, one-dimensional eigenfunctions along one Cartestian coordinate cannot have positive local minima, yet such positive minima are evident in $\chi_j^m(R)$. This minimum continues to develop and crosses the axis to create a pair of radial nodes. As in Fig 4.7 and C.5 (Fig. 7 and S7 in ref. [25]), this creation of two oppositely signed conical nodes proceeds through a zeroth-order tangential node. The pair of nodes, once formed, separate from one another.

In Figure 5.5, comparing the radial nodes in the projections onto the upper adiabatic electronic state for increasing values of $(D\omega)/\omega$ shows that nodes move in from the large radius classically forbidden region. In Figure 5.10, as $(D\omega)/\omega$ increases, a pair of nodes appears in $\chi_j^m(R)$ in a region that would be classically allowed for the lower adiabatic state, but is classically forbidden on the upper adiabatic state, which is where the nodes appear. In this study, node creation has not been observed in regions where both surfaces are classically forbidden.

5.5 Discussion

For large Jahn-Teller stabilization energies, the number of observed conical nodes in eigenfunctions for the circularly symmetric Jahn-Teller Hamiltonian can be understood. In the $(p,|j|)$ adiabatic eigenfunction, p radial nodes were observed in the projection onto each adiabatic electronic state. The formation of a nodal curve in an adiabatic vibrational-electronic state necessarily requires that either the amplitude in one of the adiabatic projections becomes zero or the nodal curves in both adiabatic projections coalesce. Czub and Wolniewicz argued that it was unlikely that the nodes on different surfaces would coincide [36]. Remarkably, as shown in Figures 5.5, 5.6, 5.8 and 5.9, the radial nodes observed here on the upper and lower state appear to be approaching coincidence toward the adiabatic limit.

Each of these radial nodes in the projections intersects $2|j|$ angular nodes on the other projection of the same nonadiabatic eigenstate. All nodes within each set of $2|j|$ accidental conical nodes have the same electronic index, but the two sets have nodes with equal and opposite electronic indices, so that the sum of electronic indices over all $4|j|$ accidental conical nodes at nearly the same radius vanishes. Thus, at large $(D\omega)/\omega$, the sum of the electronic indices over the $4p|j|$ accidental conical nodes is zero. The electronic index for paths around the perimeter of the figures shown here is equal to the electronic index of the essential node at the origin when the adiabatic vibrational quantum number p is good.

These radial nodes can switch adiabatic state or annihilate (as seen in Figure 5.9) for smaller values of $(D\omega)/\omega$. This suggests the conjecture that, for any nonzero Jahn-Teller stabilization energy, the electronic index of any eigenfunction around a path that encircles all

nodes at finite radius is the index of its essential node, which is determined by the pseudo-rotation quantum number j, because the indices of all accidental nodes will cancel. Even with the extended coordinate range of the calculations presented here, this conjecture relies on extrapolation from larger Jahn-Teller stabilization energies to infer large radius conical nodes at small Jahn-Teller stabilization energies. For the small Jahn-Teller stabilization energies studied in Chapter 3 [27], the large radius conical nodes lie beyond the radius calculated here. The large radius nodes found in this chapter would occur in numerically zero parts of the eigenfunction when the small Jahn-Teller stabilization energy vibrational quantum number v is good.

When nodes cross from one adiabatic state to the other they preserve their index and when nodes are created or annihilated they do this through the cancellation of oppositely signed pairs. As such, it is possible the conjecture that the electronic index of any eigenfunction around a path that encircles all nodes at finite radius is the index of its essential node at the origin may hold for all nonzero Jahn-Teller stabilization energies $(D\omega)/\omega$.

In one case, $(v=1,|j|=1/2)$, it has been argued that a conical node moves toward an infinite radius as the Jahn-Teller stabilization energy tends to zero. For the lower symmetry D_{4h} Jahn-Teller Hamiltonian it was shown in Chapter 4 [25] that a low symmetry path in which one Jahn-Teller stabilization energy is adjusted from $d_2 = d_1$ to $d_2 = -d_1$ connects the $(v=1,|j|=1/2)$ eigenfunction to the $(v=1,|j|=3/2)$ eigenfunction through the accidental adiabatic case when $d_2 = 0$. Conceivably, there could be a conical node at infinity for $(v=1,|j|=3/2)$. The possibility of conical nodes existing or being created at infinity requires further exploration. It suggests caution in extrapolating to a “large radius” electronic index for

any Jahn-Teller stabilization energy because there might be further unobserved nodes at larger radii that may or may not occur in oppositely signed pairs.

Previous chapters [24, 25] have displayed conical nodes that are demonstrated here to lie in the tunneling region. Beyond the circularly symmetric conical intersection discussed in this chapter, these nodes occur in the tunneling region for a lower symmetry conical intersection (Chapter 4) and for a nonadiabatic dimer Hamiltonian without a conical intersection (Chapter 2). This suggests that nonadiabatic dynamics could give rise to nodes in the forbidden region for many systems.

This chapter has established that accidental nonadiabatic conical nodes can occur in the tunneling region. The calculations (e.g. Figure 5.3 and 5.10) have focused on radial nodes deep in the tunneling region, where eigenfunction amplitude is very small, but tunneling is unambiguously established. However, Figures 5.5, 5.6 and 5.8 show that these nodes move into the classically allowed region as the Jahn-Teller displacement increases. This implies that the resulting nonadiabatic conical nodes will occur in tunneling regions with appreciable amplitude. It is in these cases that nonadiabatic nodes might be expected to have the greatest impact on tunneling rates through barriers.

5.6. Conclusion

Conical nodes can exist at classically allowed and classically forbidden points in vibrational space. In Chapter 2 on vibronically resonant antennas [24] and in Chapter 4 on conical intersections with elliptical symmetry [25], conical nodes were found in what is shown here to be the tunneling region. The existence of conical nodes in tunneling region is confirmed

by investigation into circularly-symmetric conical intersections where we can calculate nodal lines in the adiabatic projections that are perpendicular to the direction of steepest ascent. The radii of these radial nodal lines are tunable by $(D\omega)/\omega$. The angles at which they occur are a function of the symmetry operator (e.g. σ_v, σ_d) used to uniquely define the eigenfunction for a given pair of degenerate states. As such, combining these two observations, conical nodes for the circularly symmetric Jahn-Teller Hamiltonian can be tuned to occur at any radius and a linear combination of degenerate states can be chosen to create a conical node at any point in vibrational coordinate space, regardless of the potential energy at that point.

Conical nodes in the barely forbidden region occur when the dynamics are neither diabatic (good vibrational quantum number v) nor adiabatic (good vibrational quantum number p), but nonadiabatic. Deeply nonadiabatic tunneling phenomena are unlikely to have the normally assumed monotonic decay with tunneling depth. As demonstrated here, all of the rules for one-dimensional Cartesian eigenfunction tunneling behavior are broken in this regime of electronically nonadiabatic vibrational tunneling.

References

1. Hund, F.Z., *Zur Deutung der Molekelspektren. I.* Z. Phys., 1927. **40**: p. 742.

2. Oppenheimer, J.R., *Three Notes on the Quantum Theory of Aperiodic Effects.* Phys. Rev., 1928. **31**: p. 66 - 81.

3. Gamow, G., *Zur Quantentheorie des Atomkernes.* Z. Phys., 1928. **51**(3-4): p. 204-212.

4. Gamow, G., *The Quantum Theory of Nuclear Disintegration.* Nature, 1928. **122**: p. 805-806.

5. Gurney, R.W. and E.U. Condon, *Quantum Mechanics and Radioactive Disintegration.* Nature, 1928. **122**: p. 439-440.

6. Gurney, R.W. and E.U. Condon, *Quantum Mechanics and Radioactive Disintegration.* Phys. Rev., 1929. **33**: p. 127.

7. Feynman, R.P., *The Feynman Lectures on Physics*. 1918-1988, Reading, Mass.: Addison-Wesley Pub. Co.

8. Townes, C.H. and A.L. Schawlow, *Microwave Spectroscopy*. 2012, New York: McGraw-Hill Book Company.

9. Kapur, P.L. and R. Peierls, *Penetration into Potential Barriers in Several Dimensions.* Proc. R. Soc. Lond. A, 1937. **163**: p. 606-610.

10. Peierls, R., *More Surprises in Theoretical Physics*. Princeton Series in Physics, ed. P.W. Anderson, A.S. Wightman, and S.B. Tremain. 1991, Princeton, NJ: Princeton University Press.

11. Takada, S. and H. Nakamura, *Wentzel–Kramers–Brillouin theory of multidimensional tunneling: General theory for energy splitting.* J. Chem. Phys., 1994. **100**(1): p. 98-113.

12. Caldeira, A.O. and A.J. Leggett, *Quantum Tunneling in a Dissipative System.* Ann. Phys., 1983. **149**: p. 374-456.

13. Barth, I. and O. Smirnova, *Nonadiabatic tunneling in circularly polarized laser fields: Physical picture and calculations.* Phys. Rev. A, 2011. **84**: p. 063415(5).

14. Yudin, G.L., *Physics of correlated double ionization of atoms in intense laser fields: Quasistatic tunneling limit.* Phys. Rev. A, 2001. **63**(3).

15. Eckle, P., et al., *Attosecond Ionization and Tunneling Delay Time Measurements in Helium.* Science, 2008. **322**(5907): p. 1525-1529.

16. Nakamura, H., *Semiclassical treatment of nonadiabatic transitions: Multilevel curve crossing and nonadiabatic tunneling problems.* J. Chem. Phys., 1987. **87**(7): p. 4031-4041.

17. Takigawa, N., K. Hagino, and M. Abe, *Dynamical norm method for nonadiabatic tunneling macroscopic quantum tunneling.* Phys. Rev. C, 1995. **51**(1): p. 187-197.

18. Kiefer, P.M. and J.T. Hynes, *Kinetic Isotope Effects for Nonadiabatic Proton Transfer Reactions in a Polar Environment. 1. Interpretation of Tunneling Kinetic Isotopic Effects.* J. Phys. Chem. A, 2004. **108**(52): p. 11793-11808.

19. Zhu, C. and H. Nakamura, *Theory of nonadiabatic transition for general two-state curve crossing problems. I. Nonadiabatic tunneling case.* J. Chem. Phys., 1994. **101**(12): p. 10630-10647.

20. Ryabinkin, I.G., L. Joubert-Doriol, and A.F. Izmaylov, *Geometric Phase Effects in Nonadiabatic Dynamics near Conical Intersections.* Acc. Chem. Res., 2017. **50**(7): p. 1785-1793.

21. Xie, C., et al., *Constructive and Destructive Interference in Nonadiabatic Tunneling via Conical Intersections.* J. Chem. Theory Comput., 2017. **13**(5): p. 1902-1910.

22. Xie, C., et al., *Up to a Sign. The Insidious Effects of Energetically Inaccessible Conical Intersections on Unimolecular Reactions.* Acc. Chem. Res., 2019. **52**(2): p. 501-509.

23. Xie, C., D.R. Yarkony, and H. Guo, *Nonadiabatic tunneling via conical intersections and the role of the geometric phase.* Phys. Rev. A, 2017. **95**.

24. Foster, P.W., W.K. Peters, and D.M. Jonas, *Nonadiabatic Eigenfunctions Can Have Conical Nodes.* Chem. Phys. Lett., 2017. **683**: p. 268-275.

25. Foster, P.W. and D.M. Jonas, *Nonadiabatic conical nodes are near but not at an elliptical conical intersection.* Chem. Phys., 2019. **520**: p. 108-121.

26. Kemble, E.C., *A Contribution to the Theory of the B.W.K. Method.* Phys. Rev., 1935. **48**: p. 549.

27. Foster, P.W. and D.M. Jonas, *Nonadiabatic Eigenfunctions Can Have Amplitude, Signed Conical Nodes, or Signed Higher Order Nodes at Conical Intersection with Circular Symmetry.* J. Phys. Chem. A., 2017. **121**(39): p. 7401-7413.

28. Longuet-Higgins, H.C., et al., *Studies of the Jahn-Teller Effect II. The Dynamical Problem.* Proc. R. Soc. Lond. A, 1958. **244**(1236): p. 1-16.

29. Yarkony, D.R., et al., *Diabatic and adiabatic representations: Electronic structure caveats.* Comput. Theor. Chem., 2019. **1152**: p. 41-52.

30. Fedorov, D.A. and B.G. Levine, *A discontinuous basis enables numerically exact solution of the Schrödinger equation around conical intersections in the adiabatic representation.* J. Chem. Phys., 2019. **150**.

31. Judd, B.R., *Exact Solutions to a Class of Jahn-Teller Systems.* J. Phys. C: Solid State Phys., 1979. **12**: p. 1685-1692.

32. Thompson, T.C., D.G. Truhlar, and C.A. Mead, *On the form of the adiabatic and diabatic representation and the validity of the adiabatic approximation for X3 Jahn-Teller systems.* 82, 1985. **5**(2392-2407).

33. Kitney-Hayes, K.A., et al., *Two-Dimensional Fourier Transform Electronic Spectroscopy at a Conical Intersection.* J. Chem. Phys., 2014. **140**: p. 124312

34. Hougen, J.T., *Vibronic Interactions in Molecules with a Fourfold Symmetry Axis.* J. Mol. Spectrosc., 1964. **13**: p. 149-167.

35. Foster, P.W. and D.M. Jonas, *Correction to "Nonadiabatic Eigenfunctions Can Have Amplitude, Signed Conical Nodes, or Signed Higher Order Nodes at a Conical Intersection with Circular Symmetry".* J. Phys. Chem. A, 2019. **123**: p. 1273.

36. Czub, J. and L. Wolniewicz, *On the Non-Adiabatic Potentials in Diatomic-Molecules.* Mol. Phys., 1978. **36**(5): p. 1301-1308.

BIBLIOGRAPHY

Abedi, A., N.T. Maitra, and E.K.U. Gross, *Exact Factorization of the Time-Dependent Electron-Nuclear Wave Function.* Phys. Rev. Lett., 2010. **105**: p. 123002.

Abedi, A., N.T. Maitra, and E.K.U. Gross, *Correlated electron-nuclear dynamics: Exact factorization of the molecular wavefunction.* Journal of Chemical Physics, 2012. **137**(22): p. 22A530.

Applegate, B.E., T.A. Barckholtz, and T.A. Miller, *Explorations of Conical Intersections and Their Ramifications for Chemistry Through the Jahn-Teller Effect.* Chemical Society Reviews, 2003. **32**: p. 38-49.

Arnold, V.I., *Mathematical Methods of Classical Mechanics*. 1st ed. 1978, New York: Springer.

Atchity, G.J., S.S. Xantheas, and K. Ruedenberg, *Potential energy surfaces near intersections.* Journal of Chemical Physics, 1991. **95**(3): p. 1862-1876.

Atkins, P.W. and R.S. Friedman, *Molecular Quantum Mechanics*. 3rd ed. 1997, New York: Oxford University Press.

Barth, I. and O. Smirnova, *Nonadiabatic tunneling in circularly polarized laser fields: Physical picture and calculations.* Phys. Rev. A, 2011. **84**: p. 063415(5).

Ben-Nun, M., et al., *The role of intersection topography in bond selectivity of cis-trans photoisomerization.* Proceedings of the National Academy of Sciences of the United States of America, 2002. **99**(4): p. 1769-1773.

Bernardi, F., M. Olivucci, and M.A. Robb, *Potential Energy Surface Crossings in Organic Photochemistry.* Chem. Soc. Rev., 1996. **25**(5): p. 321-328.

Berry, M.V., *Quantal Phase Factors Accompanying Adiabatic Changes.* Proc. R. Soc. Lond. A, 1984. **392**: p. 45-57.

Born, M. and R. Oppenheimer, *Zur Quantentheorie Der Molekeln.* Ann. Phys. (Berlin), 1927. **389**(20): p. 457-470.

Born, M. and K. Huang, *Dynamical Theory of Crystal Lattices*. 1962, Oxford: Clarendon Press.

Bracewell, R.N., *The Fourier transform and its applications*. 3rd ed. McGraw-Hill series in electrical and computer engineering Circuits and systems. 2000, Boston: McGraw Hill. xx, 616 p.

Bunker, P.R., *The Effect of the Breakdown of the Born-Oppenheimer Approximation on the Determination of Be and we for a Diatomic Molecule.* J. Mol. Spectrosc., 1970. **35**: p. 306-313.

Bunker, P.R., *Errata of "The Effect of the Breakdown of the Born-Oppenheimer Approximation on the Determination of Be and we for a Diatomic Molecule"*. J. Mol. Spectrosc., 1971. **38**(1): p. 197.

Bunker, P.R., *Molecular Symmetry and Spectroscopy*. 1979, Orlando: Academic Press, Inc.

Caldeira, A.O. and A.J. Leggett, *Quantum Tunneling in a Dissipative System.* Ann. Phys., 1983. **149**: p. 374-456.

Cardinal, G., et al., *Charge-transfer Interactions in the Square-planar Chalcogen Cations, M_4^{2+} : Preparation and Crystal-Structures of the Compounds $(Se_4^{2+})(Sb_2F_4^{2+})(Sb_2F_5^{+})(SbF_6^{-})_5$,$(Se_4^{2+})(AlCl_4^{-})_2$, and $(Te_4^{2+})(SbF_6^{-})_2$.* Journal of the Chemical Society-Dalton Transactions, 1982(4): p. 765-779.

Cederbaum, L.S., *The exact molecular wavefunction as a product of an electronic and a nuclear wavefunction.* J. Chem. Phys., 2013. **138**(22).

Chiang, Y.-C., et al., *The exact wavefunction factorization of a vibronic coupling system.* Journal of Chemical Physics, 2014. **140**(5): p. 054104.

Child, M.S. and H.C. Longuet-Higgins, *Studies of the Jahn-Teller effect III. The rotational and vibrational spectra of symmetric top molecules in electronically degenerate states.* Philosophical Transactions of the Royal Society A, 1961. **254**(1041): p. 259-294.

Child, M.S., *Studies of the Jahn-Teller effect IV. The vibrational spectra of spin-degenerate molecules.* Philosophical Transactions of the Royal Society A, 1962. **255**(1050): p. 31-53.

Child, M.S., *Anomalous spectrocopic properties accompanying a weak dynamic Jahn-Teller effect.* Journal of Molecular Spectroscopy, 1963. **10**: p. 357-365.

Ciappina, M.F., et al., *Double ionization of helium by ion impact analyzed using four-body Dalitz plots.* Physical Review A, 2008. **77**(6): p. 12.

Clinton, W.L. and B. Rice, *Reformulation of the Jahn-Teller Theorem.* J. Chem. Phys., 1959. **30**(2): p. 542-546.

Coe, J.D. and T.J. Martinez, *Competitive Decay at Two- and Three-State Conical Intersections in Excited-State Intramolecular Proton Transfer.* J. Am. Chem. Soc., 2005. **127**(13): p. 4560-4561.

Cohen-Tannoudji, C., B. Diu, and F. Lalöe, *Quantum Mechanics*. Vol. 2. 1977, Paris: Wiley-Interscience. 1284-1321 and 1339-1342.

Corbett, J.D., *Polyatomic Zintl Anions of the Post-Transition Elements.* Chemical Reviews, 1985. **85**(5): p. 383-397.

Corrales, M.E., et al., *Structural dynamics effects on the ultrafast chemical bond cleavage of a photodissociation reaction.* Phys. Chem. Chem. Phys., 2014. **16**(19): p. 8812-8818.

Courant, R. and D. Hilbert, *Methods of Mathematical Physics*. First English ed. Vol. I. 1953: Wiley-Interscience. 560.

Czub, J. and L. Wolniewicz, *On the Non-Adiabatic Potentials in Diatomic-Molecules.* Mol. Phys., 1978. **36**(5): p. 1301-1308.

DiLauro, C. and I.M. Mills, *Coriolis Interactions about X-Y axes in Symmetric Tops.* J. Mol. Spectrosc., 1966. **21**(1-4): p. 386-413.

do Carmo, M.P., *Differential Geometry of Curves and Surfaces*. 1976, Englewood Cliffs, NJ: Prentice-Hall.

Dunham, J.L., *The Wentzel-Brillouin-Kramers Method os Solving the Wave Equation.* Phys. Rev., 1932. **41**: p. 713.

Eckle, P., et al., *Attosecond Ionization and Tunneling Delay Time Measurements in Helium.* Science, 2008. **322**(5907): p. 1525-1529.

Eich, F.G. and F. Agostini, *The adiabatic limit of the exact factorization of the electron-nuclear wave function.* J. Chem. Phys., 2016. **145**(5): p. 054110.

Elliott, B.M. and A.I. Boldyrev, *Ab Initio Probing of the Aromatic Oxygen Cluster O_4^{2+}*. J. Phys. Chem. A, 2005. **109**(1): p. 236-239.

Englman, R., *The Jahn-Teller Effect in Molecules and Crystals*. 1972, London: Wiley-Interscience.

Farrow, D.A., et al., *Polarized Pump-Probe Measurements of Electronic Motion via a Conical Intersection.* J. Chem. Phys., 2008. **128**(7): p. 144510.

Farrow, D.A., et al., *The polarization anisotropy of vibrational quantum beats in resonant pump-probe experiments: Diagrammatic calculations for square symmetric molecules.* Journal of Chemical Physics, 2008. **129**(17): p. 174509.

Fechner, P.C. and H. Helm, *Imaging of spatial many-body wave functions via linear momentum measurements.* Phys. Chem. Chem. Phys., 2014. **16**(2): p. 453-457.

Fedorov, D.A. and B.G. Levine, *A discontinuous basis enables numerically exact solution of the Schrödinger equation around conical intersections in the adiabatic representation.* J. Chem. Phys., 2019. **150**: p. 054102.

Feynman, R.P., *The Feynman Lectures on Physics*. 1918-1988, Reading, Mass.: Addison-Wesley Pub. Co.

Field, R.W. and H. Lefebvre-Brion, *The Spectra and Dynamics of Diatomic Molecules*. 2004: Elsevier Academic Press.

Förster, T., *Delocalized excitation and excitation transfer*, in *Modern Quantum Chemistry*, O. Sinanoglu, Editor. 1965, Academic Press, Inc.: New York. p. 93-137.

Foster, P.W., W.K. Peters, and D.M. Jonas, *Nonadiabatic Eigenfunctions Can Have Conical Nodes.* Chem. Phys. Lett., 2017. **683**: p. 268-275.

Foster, P.W. and D.M. Jonas, *Nonadiabatic Eigenfunctions Can Have Amplitude, Signed Conical Nodes, or Signed Higher Order Nodes at Conical Intersection with Circular Symmetry.* J. Phys. Chem. A., 2017. **121**(39): p. 7401-7413.

Foster, P.W. and D.M. Jonas, *Nonadiabatic conical nodes are near but not at an elliptical conical intersection.* Chem. Phys., 2019. **520**: p. 108-121.

Foster, P.W. and D.M. Jonas, *Correction to "Nonadiabatic Eigenfunctions Can Have Amplitude, Signed Conical Nodes, or Signed Higher Order Nodes at a Conical Intersection with Circular Symmetry".* J. Phys. Chem. A, 2019. **123**: p. 1273.

Friesner, R. and R. Silbey, *Exciton-phonon coupling in a dimer: An analytical approximation for eigenvalues and eigenvectors.* J. Chem. Phys., 1981. **74**(2): p. 1166-1174.

Fulton, R.L. and M. Gouterman, *Vibronic Coupling. I. Mathematical Treatment for 2 Electronic States.* Journal of Chemical Physics, 1961. **35**(3): p. 1059-1071.

Fulton, R.L. and M. Gouterman, *Vibronic Coupling. II. Spectra of Dimers.* Journal of Chemical Physics, 1964. **41**(8): p. 2280-2286.

Gamow, G., *Zur Quantentheorie des Atomkernes.* Z. Phys., 1928. **51**(3-4): p. 204-212.

Gamow, G., *The Quantum Theory of Nuclear Disintegration.* Nature, 1928. **122**: p. 805-806.

Gidopoulos, N.I. and E.K.U. Gross, *Electronic non-adiabatic states: towards a density functional theory beyond the Born-Oppenheimer approximation.* Phil. Trans. R. Soc. A, 2014. **372**(2011): p. 20130059.

Goldstein, H., *Classical Mechanics*. 2nd ed. 1980, Reading, MA: Addison-Wesley.

Gouterman, M., *Electronic Spectra*, in *The Porphyrins*, D. Dolphin, Editor. 1978, Academic Press: New York. p. 1-156.

Gurney, R.W. and E.U. Condon, *Quantum Mechanics and Radioactive Disintegration.* Nature, 1928. **122**: p. 439-440.

Gurney, R.W. and E.U. Condon, *Quantum Mechanics and Radioactive Disintegration.* Phys. Rev., 1929. **33**: p. 127.

Gutzwiler, M.C., *Chaos in Classical and Quantum Mechanics*. 1991, New York: Springer.

Hagelberg, F., *Electron Dynamics in Molecular Interactions*. 2014, London: Imperial College Press.

Herzberg, G. and H.C. Longuet-Higgins, *Intersection of Potential Energy Surfaces in Polyatomic Molecules.* Disc. Far. Soc., 1963. **35**: p. 77-82.

Herzberg, G.H., *Infrared and Raman Spectra of Polyatomic Molecules*. Molecular Spectra and Molecular Structure. Vol. II. 1991, Malabar, FL: Krieger.

Herzberg, G.H., *Electronic Spectra of Polyatomic Molecules*. Molecular Spectra and Molecular Structure. Vol. III. 1991, Malabar, FL: Krieger.

Hougen, J.T., *Vibronic Interactions in Molecules with a Fourfold Symmetry Axis.* Journal of Molecular Spectroscopy, 1964. **13**: p. 149-167.

Hougen, J.T., *The Calculation of Rotational Energy Levels and Rotational Line Intensities in Diatomic Molecules (National Bureau of Standards Monograph 115).* 1970, Washington, DC: US Government Printing Office. (52 pages).

Hund, F.Z., *Zur Deutung der Molekelspektren. I.* Z. Phys., 1927. **40**: p. 742.

Hunter, G., *Conditional Probability Amplitudes in Wave Mechanics.* Int. J. Quantum Chem., 1975. **9**(2): p. 237-242.

Hunter, G., *Nodeless Wave-Functions and Spiky Potentials.* Int. J. Quantum Chem., 1981. **19**(5): p. 755-761.

Jahn, H.A. and E. Teller, *Stability of Polyatomic Molecules in Degenerate Electronic States. I. Orbital Degeneracy.* Proc. R. Soc. of Lond. A, 1937. **161**(905): p. 220.

Jecko, T., B.T. Sutcliffe, and R.G. Woolley, *On factorization of molecular wavefunctions.* J. Phys. A: Math. Theor., 2015. **48**: p. 445201.

Jonas, D.M., *Vibrational and Nonadiabatic Coherence in 2D Electronic Spectroscopy, the Jahn-Teller Effect and Energy Transfer.* Annual Review of Physical Chemistry, 2018. **69**: p. 327-352.

Judd, B.R., *Exact Solutions to a Class of Jahn-Teller Systems.* J. Phys. C: Solid State Phys., 1979. **12**: p. 1685-1692.

Kapur, P.L. and R. Peierls, *Penetration into Potential Barriers in Several Dimensions.* Proc. R. Soc. Lond. A, 1937. **163**: p. 606-610.

Kemble, E.C., *A Contribution to the Theory of the B.W.K. Method.* Phys. Rev., 1935. **48**: p. 549.

Kiefer, P.M. and J.T. Hynes, *Kinetic Isotope Effects for Nonadiabatic Proton Transfer Reactions in a Polar Environment. 1. Interpretation of Tunneling Kinetic Isotopic Effects.* J. Phys. Chem. A, 2004. **108**(52): p. 11793-11808.

Kitney-Hayes, K.A., et al., *Two-Dimensional Fourier Transform Electronic Spectroscopy at a Conical Intersection.* J. Chem. Phys., 2014. **140**: p. 124312

Klessinger, M. and J. Michl, *Excited States and Photochemistry of Organic Molecules*. 1995, New York: VCH Publishers.

Koppel, H., W. Domcke, and L.S. Cederbaum, *Multimode Molecular-Dynamics Beyond the Born-Oppenheimer Approximation.* Advances in Chemical Physics, 1984. **57**: p. 59-246.

Kupper, J., et al., *X-Ray Diffraction from Isolated and Strongly Aligned Gas-Phase Molecules with a Free-Electron Laser.* Phys. Rev. Lett., 2014. **112**(8): p. 083002.

Landau, L.D., *Zur Theorie der Energieubertragung. II.* Physikalische Zeitschrift der Sowjetunion, 1932. **2**: p. 46-51.

Landau, L.D. and E.M. Lifschitz, *Mechanics*. 3rd ed. 1976, New York: Pergamon Press.

Landau, L.D. and E.M. Lifschitz, *Quantum Mechanics*. 3rd ed. ed. 1977, New York: Pergamon Press.

Lee, J., et al., *Orbiting Orbitals: Visualization of Vibronic Motion at a Conical Intersection.* J. Phys. Chem. A, 2013. **117**(46): p. 11655-11664.

Lefebvre, R., *Perturbations in vibrational diatomic spectra: Factorization of the molecular wave function.* Journal of Chemical Physics, 2015. **142**(7): p. 074106.

Levine, B.G. and T.J. Martinez, *Isomerization Through Conical Intersections.* Annu. Rev. Phys. Chem., 2007. **58**: p. 613-634.

Longuet-Higgins, H.C., et al., *Studies of the Jahn-Teller Effect II. The Dynamical Problem.* Proc. R. Soc. Lond. A, 1958. **244**(1236): p. 1-16.

Longuet-Higgins, H.C., *The Geometric Phase Effect.* Adv. Spectrosc., 1961. **2**: p. 429.

Longuet-Higgins, H.C., *Some recent developments in the theory of molecular energy levels*, in *Advances in Spectroscopy*, H. Thompson, Editor. 1961, Interscience Publishers Inc: New York. p. 429-472.

Longuet-Higgins, H.C., *The intersection of potential energy surfaces in polyatomic molecules.* Proc. R. Soc. Lond. A, 1975. **344**: p. 147-156.

Marcus, R.A., *Electron Transfer Reactions in Chemistry: Theory and Experiment (Nobel Lecture).* Angewandte Chemie, 1993. **32**(8): p. 1111-1121.

Marsden, J.E. and A.J. Tromba, *Vector Calculus*. 1981, San Francisco: W. H. Freeman.

Matsika, S. and D.R. Yarkony, *Intersecting Conical Intersection Seams: Their Location, Representation, and Effect on Local Topography.* J. Phys. Chem. A., 2002. **106**(11): p. 2580-2591.

Matsika, S. and P. Krause, *Nonadiabatic Events and Conical Intersections.* Annual Review of Physical Chemistry, 2011. **62**: p. 621-643.

McCusker, J., *Femtosecond absorption spectroscopy of transition metal charge-transfer complexes.* Accounts of Chemical Research, 2003. **36**: p. 876-887.

McQuarrie, D.A., *Quantum Chemistry*. 2008, Sausalito, CA: University Science Books.

Mead, C.A. and D.G. Truhlar, *On the Determination of Born–Oppenheimer Nuclear Motion Wave Functions Including Complications Due to Conical Intersections and Identical Nuclei.* J. Chem. Phys., 1979. **70**(5): p. 2284-2296.

Mead, C.A. and D.G. Truhlar, *Conditions for the definition of a strictly diabatic electronic basis for molecular systems.* J. Chem. Phys., 1982. **77**(12): p. 6090-6096.

Mead, C.A., *Electronic Hamiltonian, wave functions, and energies, and derivative coupling between Born-Oppenheimer states in the vicinity of a conical intersection.* J. Chem. Phys., 1983. **78**(2): p. 807-814.

Meek, G.A. and B.G. Levine, *Wave Function Continuity and the Diagonal Born-Oppenheimer Correction at Conical Intersections.* J. Chem. Phys., 2016. **144**(18): p. 184109.

Michl, J., *Photochemical Reactions of Large Molecules. I. A Simple Physical Model of Photochemical Reactivity.* Mol. Photochem., 1972. **4**: p. 243-257.

Moffitt, W. and A.D. Liehr, *Configurational Instability of Degenerate Electronic States.* Phys. Rev., 1957. **106**(4): p. 1195-1200.

Nakamura, H., *Semiclassical treatment of nonadiabatic transitions: Multilevel curve crossing and nonadiabatic tunneling problems.* J. Chem. Phys., 1987. **87**(7): p. 4031-4041.

Oka, T., *Vibration—Rotation Interaction in Symmetric-Top Molecules and the Splitting between A_1 and A_2 Levels.* J. Chem. Phys., 1967. **47**(12): p. 5410-5426.

Oppenheimer, J.R., *Three Notes on the Quantum Theory of Aperiodic Effects.* Phys. Rev., 1928. **31**: p. 66 - 81.

Papousek, D. and M.R. Aliev, *Molecular Vibrational-Rotational Spectra*. 1982, New York: Elsevier Scientific.

Parlett, B.N., *The Symmetric Eigenvalue Problem*. 1980, Englewood Cliffs, NJ: Prentice-Hall.

Peierls, R., *More Surprises in Theoretical Physics*. Princeton Series in Physics, ed. P.W. Anderson, A.S. Wightman, and S.B. Tremain. 1991, Princeton, NJ: Princeton University Press.

Peters, W.K., *Carrier Dynamics in Nanocrystalline Lead Salts and Non-Adiabatic Dynamics in Near-Degenerate States of Molecules*, in *Chemistry*. 2013, University of Colorado: Boulder.

Peters, W.K., V. Tiwari, and D.M. Jonas, *Nodeless vibrational amplitudes and quantum nonadiabatic dynamics in the nested funnel for a pseudo Jahn-Teller molecule or homodimer.* J. Chem. Phys., 2017. **147**(19): p. 194306.

Renner, R., *Zur Theorie der Wechselwirkung zwischen Elektronen- und Kernbewegung bei dreiatomigen, stabförmigen Molekülen.* Z. Phys., 1934. **92**(3-4): p. 172-193.

Robb, M.A. and M. Olivucci, *Photochemical processes: potential energy surface topology and rationalization using VB arguments.* J. Photochem. Photobiol. A, 2001. **144**(2-3): p. 237-243.

Ryabinkin, I. and A.F. Izmaylov, *Geometric Phase Effects in Dynamics Near Conical Intersections: Symmetry Breaking and Spatial Localization.* Phys. Rev. Lett., 2013. **111**(22): p. 220406.

Ryabinkin, I., L. Joubert-Doriol, and A.F. Izmaylov, *When do we need to account for the gemoetric phase in excited state dynamics?* J. Chem. Phys., 2014. **140**(21): p. 214116.

Ryabinkin, I.G., L. Joubert-Doriol, and A.F. Izmaylov, *Geometric Phase Effects in Nonadiabatic Dynamics near Conical Intersections.* Acc. Chem. Res., 2017. **50**(7): p. 1785-1793.

Schmidt, L.P.H., et al., *Spatial Imaging of the H_2^+ Vibrational Wave Function at the Quantum Limit.* Phys. Rev. Lett., 2012. **108**(7): p. 073202.

Schulz, M., et al., *Four-particle Dalitz plots to visualize atomic break-up processes.* Journal of Physics B-Atomic Molecular and Optical Physics, 2007. **40**(15): p. 3091-3099.

Shelnutt, J.A., et al., *Nonplanar porphyrins and their significance in proteins.* Chem. Soc. Rev., 1998. **27**: p. 31-41.

Simon, B., *Holonomy, the Quantum Adiabatic Theorem, and Berry's Phase.* Phys. Rev. Lett., 1983. **51**(24): p. 2167-2170.

Smith, E.R., D.A. Farrow, and D.M. Jonas, *Response functions for dimers and square symmetric molecules in four-wave-mixing experiments with polarized light.* J. Chem. Phys., 2005. **123**(4): p. 044102.

Smith, E.R., D.A. Farrow, and D.M. Jonas, *Publisher's Note: "Response functions for dimers and square symmetric molecules in four-wave-mixing experiments with polarized light" [J. Chem. Phys. **123,** 044102 (2005)].* J. Chem. Phys., 2005. **123**: p. 179902.

Smith, E.R., D.A. Farrow, and D.M. Jonas, *Erratum: "Response functions for dimers and square symmetric molecules in four-wave-mixing experiments with polarized light" [J. Chem. Phys. **123,** 044102 (2005)].* J. Chem. Phys., 2008. **128**: p. 109902.

Strickler, S.J., *Spectroscopic Effects of a Breakdown of the Born-Oppenheimer Approximation.* J. Phys. Chem., 1976. **80**(20): p. 2149-2154.

Sunder, S. and H.J. Bernstein, *The vibrational spectra of the metalloporphyrins: A normal coordinate analysis of the planar vibrations in the Cu-chelates of porphin, porphin-d_4 (meso), 1:3:5:7-tetramethyl porphin and 1:2:3:4:5:6:7:8-octamethyl porphin.* J. Raman Spectrosc., 1976. **5**(4): p. 351-371.

Takada, S. and H. Nakamura, *Wentzel–Kramers–Brillouin theory of multidimensional tunneling: General theory for energy splitting.* J. Chem. Phys., 1994. **100**(1): p. 98-113.

Takigawa, N., K. Hagino, and M. Abe, *Dynamical norm method for nonadiabatic tunneling macroscopic quantum tunneling.* Phys. Rev. C, 1995. **51**(1): p. 187-197.

Teller, E., *Internal Conversion in Polyatomic Molecules.* Israel Journal of Chemistry, 1969. **7**(2): p. 227-235.

Thompson, T.C., D.G. Truhlar, and C.A. Mead, *On the form of the adiabatic and diabatic representation and the validity of the adiabatic approximation for X3 Jahn-Teller systems.* 82, 1985. **5**: p. 2392-2407.

Thorson, W. and W. Moffitt, *Some Calculations on the Jahn-Teller Effect in Octahedral Systems.* Phys. Rev., 1968. **168**(2): p. 362-369.

Tiwari, V., W.K. Peters, and D.M. Jonas, *Electronic resonance with anticorrelated pigment vibrations drives photosynthetic energy transfer outside the adiabatic framework.* Proc. Natl. Acad. Sci. USA, 2013. **110**(4): p. 1203-1208.

Townes, C.H. and A.L. Schawlow, *Microwave Spectroscopy*. 2012, New York: McGraw-Hill Book Company.

Truhlar, D.G. and C.A. Mead, *Relative likelihood of encountering conical intersections and avoided intersections on the potential energy surfaces of polyatomic molecules.* Phys. Rev. A, 2003. **68**(3): p. 032501.

Tully, J.C., *Nonadiabatic Processes in Molecular Collisions*, in *Dynamics of Molecular Collisions Part B*, W.H. Miller, Editor. 1976, Plenum Press: New York. p. 217-267.

Vager, Z., R. Naaman, and E.P. Kanter, *Coulomb Explosion Imaging of Small Molecules.* Science, 1989. **244**(4903): p. 426-431.

Varandas, A.J.C. and Z.R. Xu, *On the behavior of single surface nuclear wavefunctions in the vicinity of the conical intersection for an X_3 system.* Chem. Phys. Lett., 2000. **316**: p. 248-256.

Visual Numerics IMSL numerical libraries. Rogue Wave Software: Boulder, CO.

von Neumann, J. and E. Wigner, *Uber Das Verhalten Von Eigenwerten Bei Adiabatischen Prozessen.* Physik. Z., 1929. **30**(15): p. 467-470.

Witkowski, A. and W. Moffitt, *Electronic Spectra of Dimers: Derivation of the Fundamental Vibronic Equation.* Journal of Chemical Physics, 1960. **33**(3): p. 872-875.

Wong, M.W., *Quantum-Chemical Calculations of Sulfur-Rich Compounds.* Top. Curr. Chem., 2003. **231**: p. 1-31.

Worth, G.A. and L.S. Cederbaum, *Beyond Born-Oppenheimer: Molecular Dynamics Through a Conical Intersection.* Annual Review of Physical Chemistry, 2004. **55**: p. 127-58.

Xie, C., et al., *Nonadiabatic Tunneling in Photodissociation of Phenol.* J. Am. Chem. Soc., 2016. **138**(25): p. 7828-7831.

Xie, C., et al., *Constructive and Destructive Interference in Nonadiabatic Tunneling via Conical Intersections.* J. Chem. Theory Comput., 2017. **13**(5): p. 1902-1910.

Xie, C., D.R. Yarkony, and H. Guo, *Nonadiabatic tunneling via conical intersections and the role of the geometric phase.* Phys. Rev. A, 2017. **95**: p. 022104.

Xie, C., et al., *Up to a Sign. The Insidious Effects of Energetically Inaccessible Conical Intersections on Unimolecular Reactions.* Acc. Chem. Res., 2019. **52**(2): p. 501-509.

Yarkony, D.R., *Diabolical conical intersections.* Reviews of Modern Physics, 1996. **68**(4): p. 985-1013.

Yarkony, D.R., *Nuclear Dynamics near Conical Intersections in the Adiabatic Representation: I. The Effects of Local Topography on Interstate Transitions.* J. Chem. Phys., 2001. **114**(6): p. 2601-2613.

Yarkony, D.R., *Conical intersections: The new conventional wisdom.* Journal of Physical Chemistry A, 2001. **105**(26): p. 6277-6293.

Yarkony, D.R., *Nonadiabatic Quantum Chemistry—Past, Present, and Future.* Chem. Rev., 2012. **112**(1): p. 481-498.

Yarkony, D.R., et al., *Diabatic and adiabatic representations: Electronic structure caveats.* Comput. Theor. Chem., 2019. **1152**: p. 41-52.

Yudin, G.L., *Physics of correlated double ionization of atoms in intense laser fields: Quasistatic tunneling limit.* Phys. Rev. A, 2001. **63**(3).

Zener, C., *Non-Adiabatic Crossing of Energy Levels.* Proc. R. Soc. Lond. A, 1932. **137**(6): p. 696-702.

Zhu, C. and H. Nakamura, *Theory of nonadiabatic transition for general two-state curve crossing problems. I. Nonadiabatic tunneling case.* J. Chem. Phys., 1994. **101**(12): p. 10630-10647.

Zimmerman, H.E., *MO Following: the Molecular Orbital Counterpart of Electron Pushing.* Accounts of Chemical Research, 1972. **5**(12): p. 393-401.

Zwanziger, J.W. and E.R. Grant, *Topological phase in molecular bound states: Application to the Exe system.* J. Chem. Phys., 1987. **87**(5): p. 2954-2964.

APPENDIX A

Label	Circular Quantum Numbers		Judd's Quantum Numbers		k^2 (Judd) or d^2 (here)	Jahn-Teller Stabilization Energy ($D\omega$) for ω = 200 cm^{-1}	Analytical Eigenvalue (cm^{-1})	Numerical Eigenvalues (cm^{-1})		Errors (10^{-12} cm^{-1})	
	v	j	v	m							
y	1	3/2	1	1	5/8	62.500000000000	237.500000000000	237.499999999994	237.499999999999	−6	−1
z	2	5/2	1	2	21/8	262.500000000000	37.5000000000000	37.5000000000007	37.5000000000018	0.7	1.8
w	2	3/2	2	1	$(27/32) + ((1009)^{1/2}/32)$	183.639876089179	316.360123910821	316.360123910819	316.360123910825	−2	4
x	3	5/2	2	2	$(75/32) + ((4113)^{1/2}/32)$	434.789609310300	65.2103906897004	65.2103906897046	65.2103906897078	4.2	7.4
u	2	5/2	2	2	$(75/32) - ((4113)^{1/2}/32)$	33.9603906897004	466.039609310300	466.039609310297	466.039609310298	−3	−2
v	3	7/2	2	3	$(147/32) - ((9729)^{1/2}/32)$	151.138458322995	348.861541677005	348.861541676996	348.861541676997	−9	−8
t	3	3/2	3	1	$(19/16) + p + [269/(256p)]$ where $p = [(4867 + (4222580)^{1/2})/4096)^{1/3}$	326.079876508688	373.920123491312	373.920123491315	373.920123491316	3	4
s	4	5/2	3	2	$(74941/5184)^{1/2}\cos(\chi) + (347/144)$ where $\cos(3\chi) = 17105435/(74941)^{3/2}$	613.982855981044	86.0171440189559	86.0171440189474	86.0171440189597	−8.5	3.8
r	5	7/2	3	3	$(167149/5184)^{1/2}\cos(\xi) + (611/144)$ where $\cos(3\xi) = 48524723/(167149)^{3/2}$	972.994449879604	−272.994449879604	−272.994449879601	−272.994449879599	−3	−5

Table A.1 (caption on next page)

Table A.1 (on previous page)**:** For circular conical intersections with special ratios of the Jahn-Teller stabilization energy to vibrational frequency, Judd obtained an analytic expression for some isolated eigenvalues [1]. Judd used an angular quantum number $m = |j| - 1/2$ and a baseline quantum number v that does not have a simple relation to the eigenfunction. Eq. (10) of Judd's paper gives some isolated analytic energy eigenvalues as $E(v) = \omega(v + 1/2) - (D\omega)$, where v is Judd's baseline quantum number. Table 1 of ref. [2] compares the numerical eigenvalues obtained here by truncated Hamiltonian diagonalization with all nine analytic eigenvalues in Table 2 of ref. [1] for the $E \otimes e$ Jahn-Teller system. The states Judd labeled '*x*' and '*u*' are separately correlated with their stabilization energies based on Figure 2 of Judd's paper. Comparing their coordinates in Table 2 and Figure 2 of Judd's paper, it is clear that the states labeled '*r*' and '*s*' have been qualitatively mis-positioned in Judd's Figure 2, where they should lie at the lower right range of the plot (large stabilization energy, small energy) instead of the upper left (small stabilization energy, large energy). As a result, the small stabilization energy circular quantum number assignments suggested by Judd's Figure 2 are incorrect ['*r*' ≠ (*v*=3,|*j*|=7/2) and '*s*' ≠ (*v*=3,|*j*|=5/2)], and the assignments for these two states are based on Fig. 1.7. All other quantum number assignments are based on following the eigenvalue curves in Judd's Figure 2 back to small stabilization energies, where perturbation theory Eq. (7) of ref. [3] connects the energy to the quantum numbers. In Table 1 of ref. [2], the ratio $(D\omega)/\omega$ of Jahn-Teller stabilization energy to vibrational frequency ranges from ~1/6 to ~5 and the quantum numbers go as high as $(v = 5, |j| = 7/2)$. For the vibrational frequency of $\omega = 200$ cm^{-1} used in Table 1 of ref. [2], the eigenvalues are typically a few hundred cm^{-1} and all errors are less than 10^{-11} cm^{-1}. Errors typically occur only in the 15th digit, as measured either by discrepancies with Judd's analytic results or by departures from numerical degeneracy.

References

1. Judd, B.R., *Exact Solutions to a Class of Jahn-Teller Systems.* J. Phys. C: Solid State Phys., 1979. **12**: p. 1685-1692.

2. Foster, P.W. and D.M. Jonas, *Nonadiabatic conical nodes are near but not at an elliptical conical intersection.* Chem. Phys., 2019. **520**: p. 108-121.

3. Foster, P.W., W.K. Peters, and D.M. Jonas, *Nonadiabatic Eigenfunctions Can Have Conical Nodes.* Chem. Phys. Lett., 2017. **683**: p. 268-275.

APPENDIX B: Chapter 3 Supporting Information

The nonadiabatic eigenvalues are precisely calculated. For all systems in Table 1.1 (shown in Chapter 1), increasing the number of harmonic oscillator basis states for each vibration from 25 to 37 (from a total of 1250 to a total of 2738 basis states) indicates that the 30 lowest energy eigenstates are all converged to within $7 * 10^{-12}\ cm^{-1}$. Using 25 harmonic oscillator basis states for each vibration, the 30 lowest energy eigenstates have degenerate states with a maximum difference in energy of $7 * 10^{-12}\ cm^{-1}$ and replicate second-order perturbation theory for $(D\omega) = 0.01\ cm^{-1}$ with maximum deviations only on the order of $10^{-5}\ cm^{-1}$. As $(D\omega)$ increases, results increasingly differ from second-order perturbation theory. For larger stabilization energies, the eigenvalues agree with those reported by Longuet-Higgins et al. for $j = 1/2$ and $j = 3/2$. The energies reported there are E/ω with $k^2 = 0.25$ corresponding to $(D\omega) = 25\ cm^{-1}$ and $k^2 = 1$ corresponding to $(D\omega) = 100\ cm^{-1}$. Expanding beyond Table 1.1 to the full set of the 10 lowest eigenvalues reported by Longuet-Higgins et al. for $j = 1/2$ and $j = 3/2$ reveals 3 eigenvalues with roundoff errors of one in the last digit reported by Longuet-Higgins et al. – these are evidently caused by small numerical errors in the first digit not reported there.

In Table 1.1, it is important to note that that the last two columns do not appear in an energetic ordering as do the other columns. This is because the energetic ordering of the eigenstates according to quantum number that holds for Jahn-Teller stabilization energies $(D\omega)$ up to 25 cm^{-1} changes for $(D\omega) = 100$ cm^{-1} and $(D\omega) = 200$ cm^{-1}. Some of the avoided crossings involved can be seen in Figures 8(a) [$(j = 1/2)$], 8(b) [$(j = 5/2)$] and 8(c) [$(j = 9/2)$] of ref. [1]. They are part of a transition [2] from a small $(D\omega)/\omega$ regime in which the energy level

pattern is derived from the circular harmonic oscillator [3-5] to a large $(D\omega)/\omega$ regime in which the lowest states are on the lower adiabatic state [1, 5]. The half-odd integer pseudo-rotation quantum number j remains valid throughout, but the most natural vibrational quantum number v is different in these two limits. Since the adiabatic large $(D\omega)/\omega$ limit is not reached here, v will be labelled here by correlation to the circular 2D harmonic oscillator energy levels at small $(D\omega)/\omega$. In other words, for each j, the vibrational quantum number starts at $v = (|j| - 1/2)$ for the lowest energy eigenvalue and increases by 1 for each successive energy eigenvalue with that value of j. The assignments of j can be made visually by inspection of the eigenfunction. To assign v, the eigenvalues with a given j are ordered by energy, which works because the non-crossing rule holds for each value of j. As a check on the eigenfunction calculation, the vibrational amplitude for several eigenstates can be squared to graphically reproduce Figures 7 and 9 in ref. [1].

Figures B.1 and B.2 will extend Figure 3.2 to show states were v as defined above is 3 and 4 respectively. Figure B.3 shows the affect the reversing the sign of a displacement (d_1) and how it results in the reflection on the amplitude factor across the q_2 axis for σ_v symmetry states as well as the reversal of the sign of the node and the sign of the index for each node. After that, the quantum number assignments in Table 1.1 will be visually justified with Figure 1.5 showing the energies of all discussed states as a function of Jahn-Teller stabilization energy $(D\omega)$ from 0 cm^{-1} to 200 cm^{-1} where $\omega = 200$ cm^{-1}. Eigenvalues with the same j do not cross, but eigenvalues with different j values do. Similar crossings were discussed by Moffit and Thorson for the $\tau_{2g} \otimes \Gamma_g$ problem [6]. The eigenfunctions for five Jahn-Teller stabilization energies are plotted in Figures B.4 – B.6 to visually show their pseudo-rotation quantum number assignments.

Quantum number assignments for the fifteen lowest energy eigenstates at each displacement are shown in Table B.1. The four eigenfunctions from Table B.1 that are not shown in Figures B.4 – B.6 are shown in Figure B.7.

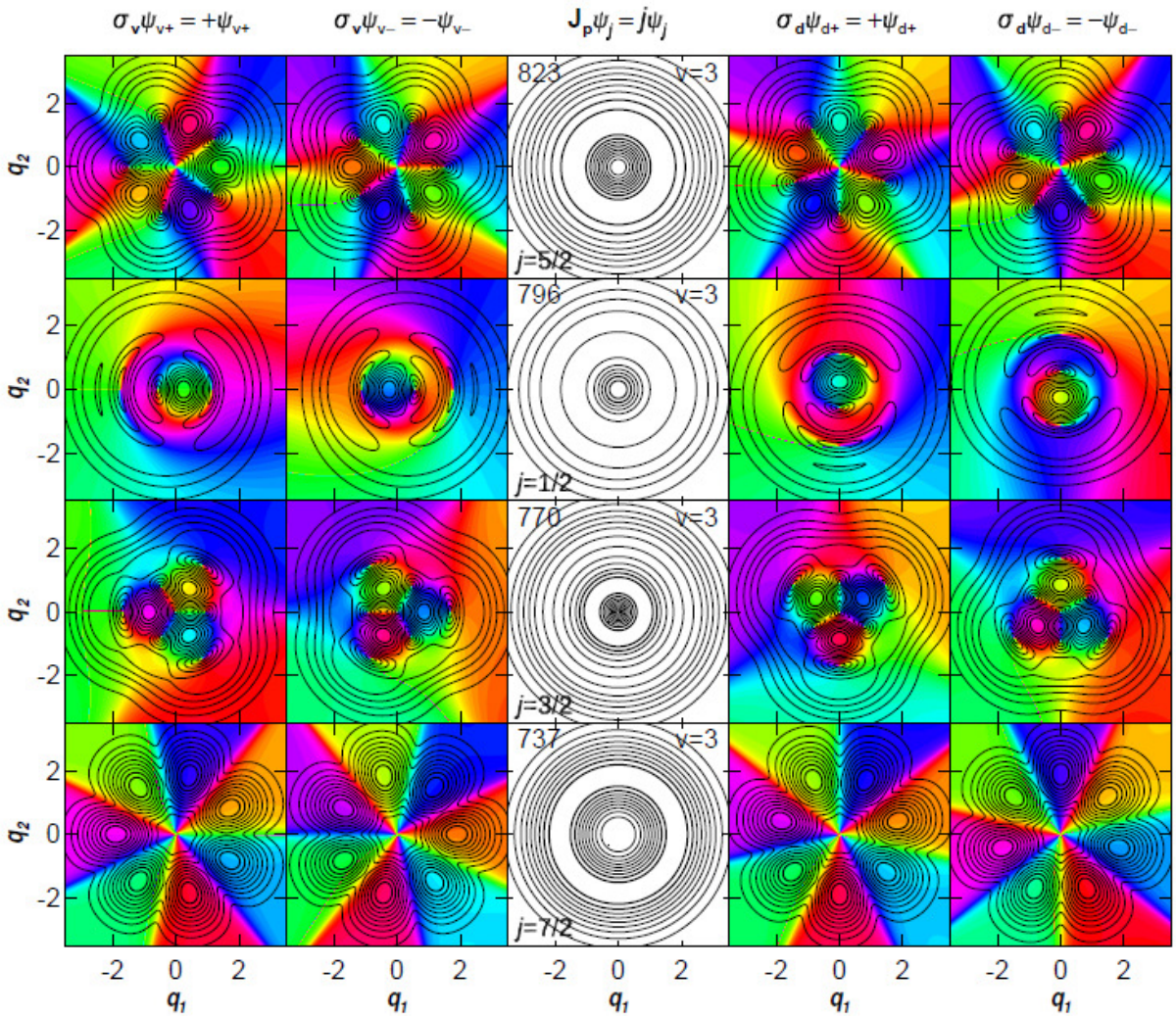

Figure B.1: Three representations of the 8 nonadiabatic eigenstates of the Hamiltonian with vibrational quantum number $v = 3$ as an extension of Figure 3.2. The Jahn-Teller stabilization energy is $(D\omega) = 10\ cm^{-1}$ and the vibrational frequency is $\omega = 200\ cm^{-1}$. The left two columns show real-valued eigenstates of σ_v with eigenvalues of $+1$ and -1, the right two columns show real-valued eigenstates of σ_d, with eigenvalues of $+1$ and -1, and the center column shows the circularly-symmetric amplitude factor for complex-valued eigenstates with signed pseudo-rotation quantum numbers. The labels in each panel of the center column give the energy in cm^{-1} (upper left), the pseudo-rotation quantum number (lower left) and the vibrational quantum number (upper right). The contours represent 10 % intervals of the maximum amplitude factor with higher contour lines being thicker. Color represents nonadiabatic electronic character using the color wheel in Fig. 3.1.

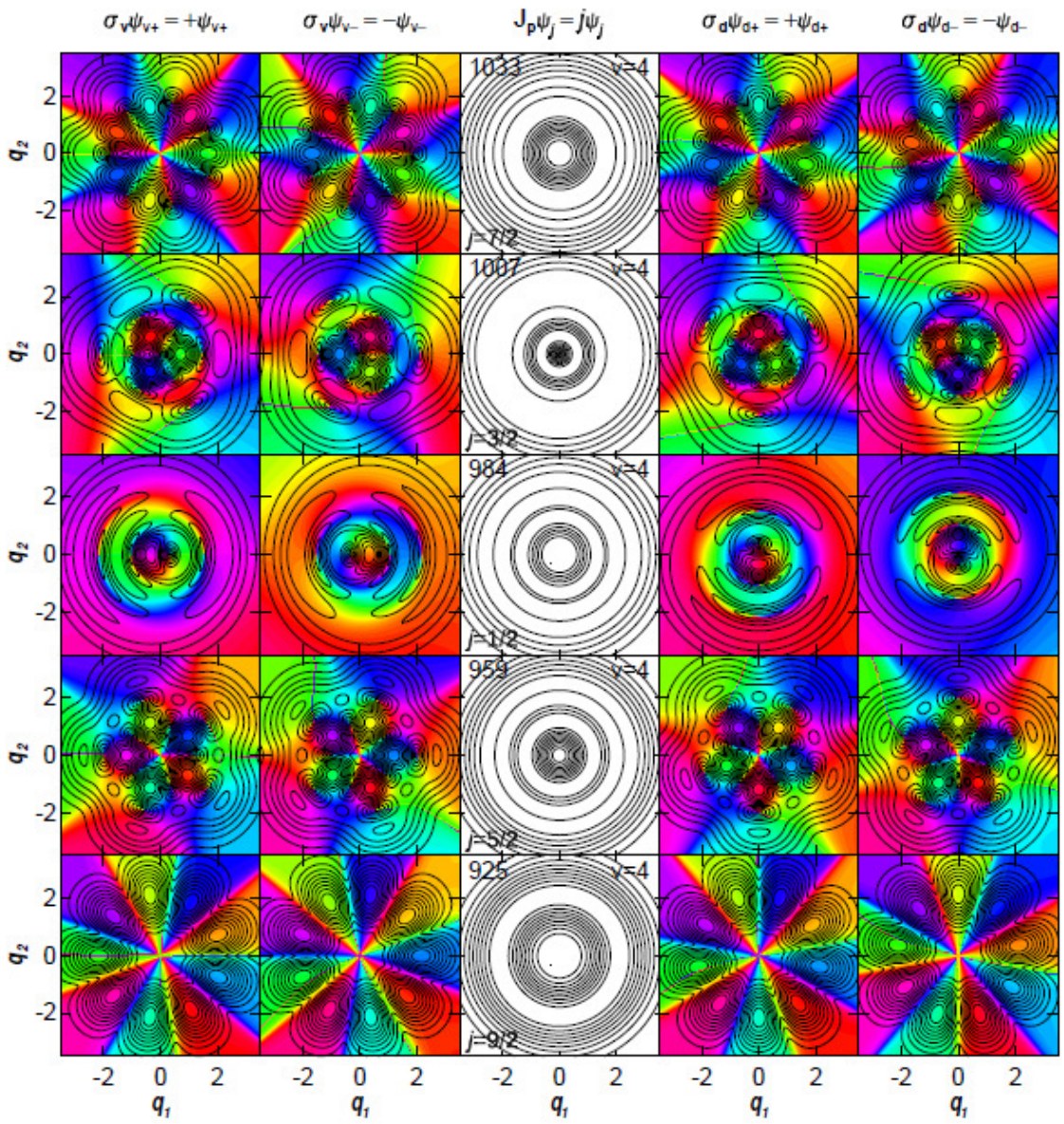

Figure B.2: Three representations of the 10 nonadiabatic eigenstates of the Hamiltonian with vibrational quantum number $v = 4$ as an extension of Figure 3.2. The Jahn-Teller stabilization energy is $(D\omega) = 10\ cm^{-1}$ and the vibrational frequency is $\omega = 200\ cm^{-1}$. The left two columns show real-valued eigenstates of σ_v with eigenvalues of $+1$ and -1, the right two columns show real-valued eigenstates of σ_d, with eigenvalues of $+1$ and -1, and the center column shows the circularly-symmetric amplitude factor for complex-valued eigenstates with signed pseudo-rotation quantum numbers. The labels in each panel of the center column give the energy in cm^{-1} (upper left), the pseudo-rotation quantum number (lower left) and the vibrational quantum number (upper right). The contours represent 10 % intervals of the maximum amplitude factor with higher contour lines being thicker. Color represents nonadiabatic electronic character using the color wheel in Fig. 3.1.

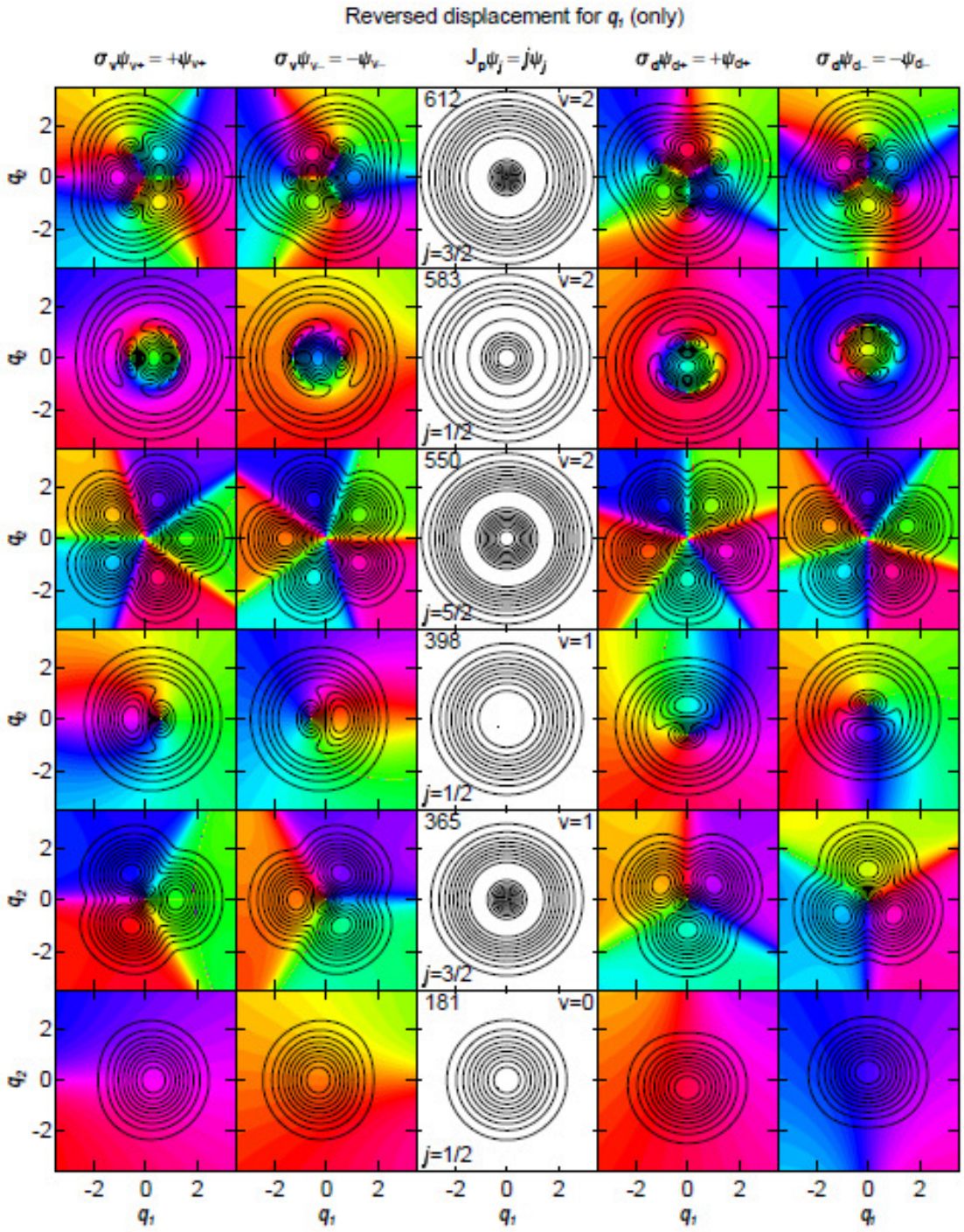

Figure B.3: Eigenstates where the sign of the conical intersection has been reversed as in Fig. 3.6 by reversing the Franck-Condon displacement in q_1 relative to Fig. 3.2 while the displacement in q_2 remains unchanged. As in Fig. 3.2, this figure shows three representations of the lowest 12 nonadiabatic eigenstates of the Hamiltonian with Jahn-Teller stabilization energy $(D\omega) = 10\ cm^{-1}$ and vibrational frequency $\omega = 200\ cm^{-1}$. The left two columns show real-valued eigenstates of σ_v with eigenvalues of $+1$ and -1, the right two columns show real-valued eigenstates of σ_d, with eigenvalues of $+1$ and -1, and the center column shows the circularly-

symmetric amplitude factor for complex-valued eigenstates with signed pseudo-rotation quantum numbers. The labels in each panel of the center column give the energy in cm^{-1} (upper left), the pseudo-rotation quantum number (lower left) and the vibrational quantum number (upper right). The contours represent 10 % intervals of the maximum amplitude factor with higher contour lines being thicker. Color represents nonadiabatic electronic character using the color wheel in Fig. 3.1.

Relative to Fig. 3.2, the amplitude factors in Fig. B.3 are swapped between σ_v eigenstates by the reversal of the displacement along q_1. For example, the $v = 0, |j| = 1/2$ $\sigma_v = +1$ eigenstate has its maximum on the right here (vs. on the left in Fig. 3.2), while the $\sigma_v = -1$ eigenstate has its maximum on the left here(vs. on the right in Fig. 3.2). The reversed q_1 displacement has no effect on the amplitude factors for σ_d eigenstates. The amplitude factors for pseudo-rotation eigenstates in the center column are not affected by reversal of the displacement along q_1.

The sign reversal for one displacement has reversed the sign of the conical intersection in Fig. 3.6. As a consequence, for each eigenstate of σ_v and σ_d, the sense of rotation around the color wheel is reversed in Fig. B.3 relative to the corresponding eigenstate in Fig. 3.2. The electronic index around each node in Fig. B.3 is equal and opposite the corresponding index in Fig. 3.2.

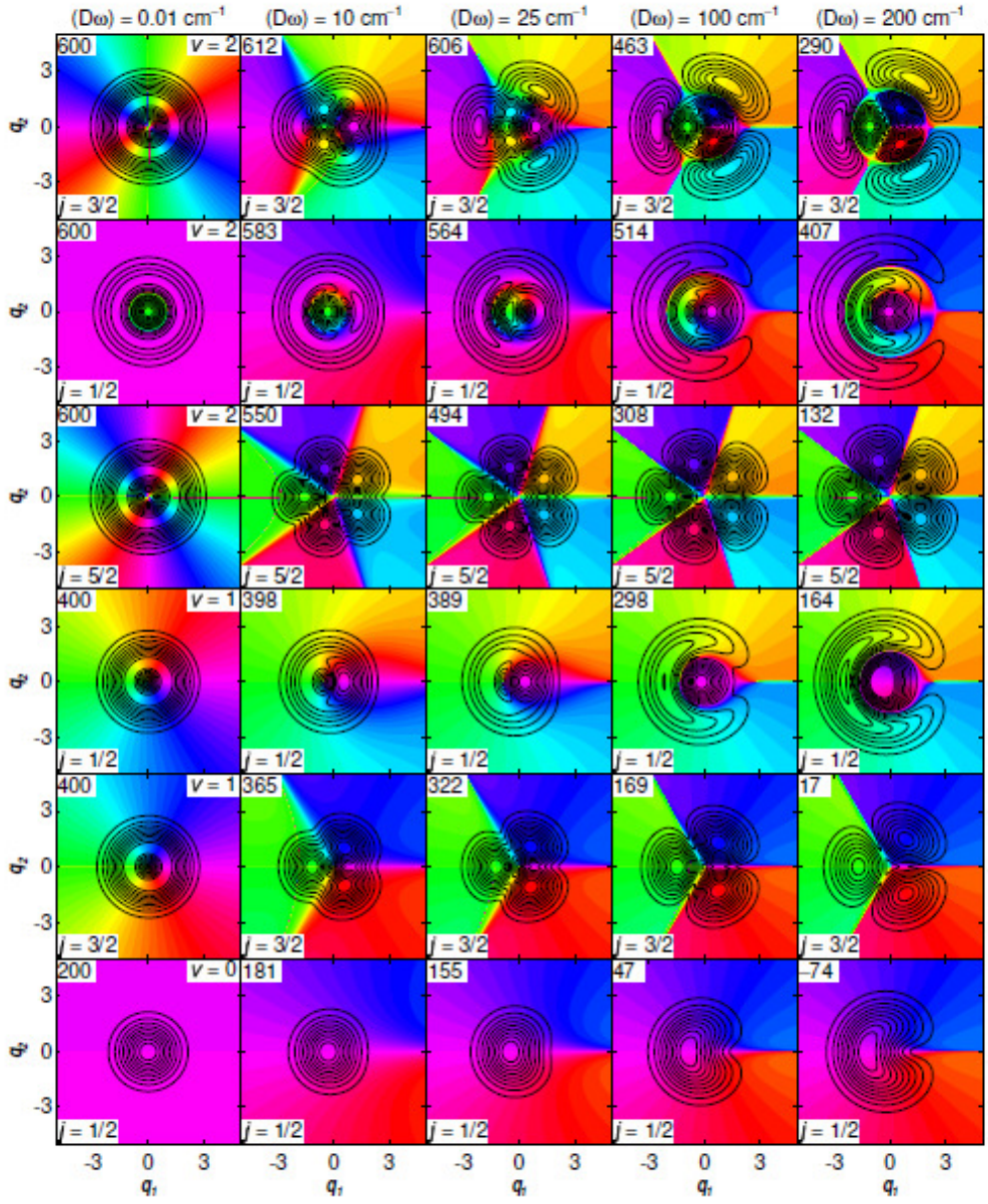

Figure B.4: The $\sigma_v = +1$ eigenfunctions correlating to the six lowest energy eigenvalues for the limit of small displacement. The left column shows $(D\omega) = 0.01$ cm^{-1} with energies (upper left) and quantum numbers (pseudo-rotation at lower left and vibrational at upper right) labelled. The next four columns show the eigenfunctions to which they correlate for $(D\omega) = 10$, 25, 100 and 200 cm^{-1}, also labelled with their energies (upper left) and pseudo-rotation quantum numbers (lower left). For each eigenstate, the contour lines show 10% intervals of its maximum probability amplitude and color shows electronic character from the color wheel in Fig. 3.1. The energetic ordering of states changes with the two highest states shown here crossing each other below $(D\omega) = 100$ cm^{-1} and the two states below them crossing each other below $(D\omega) = 200$ cm^{-1}. For $(D\omega) = 200$ cm^{-1}, the zero point level is energetically below the conical intersection at $E = 0$.

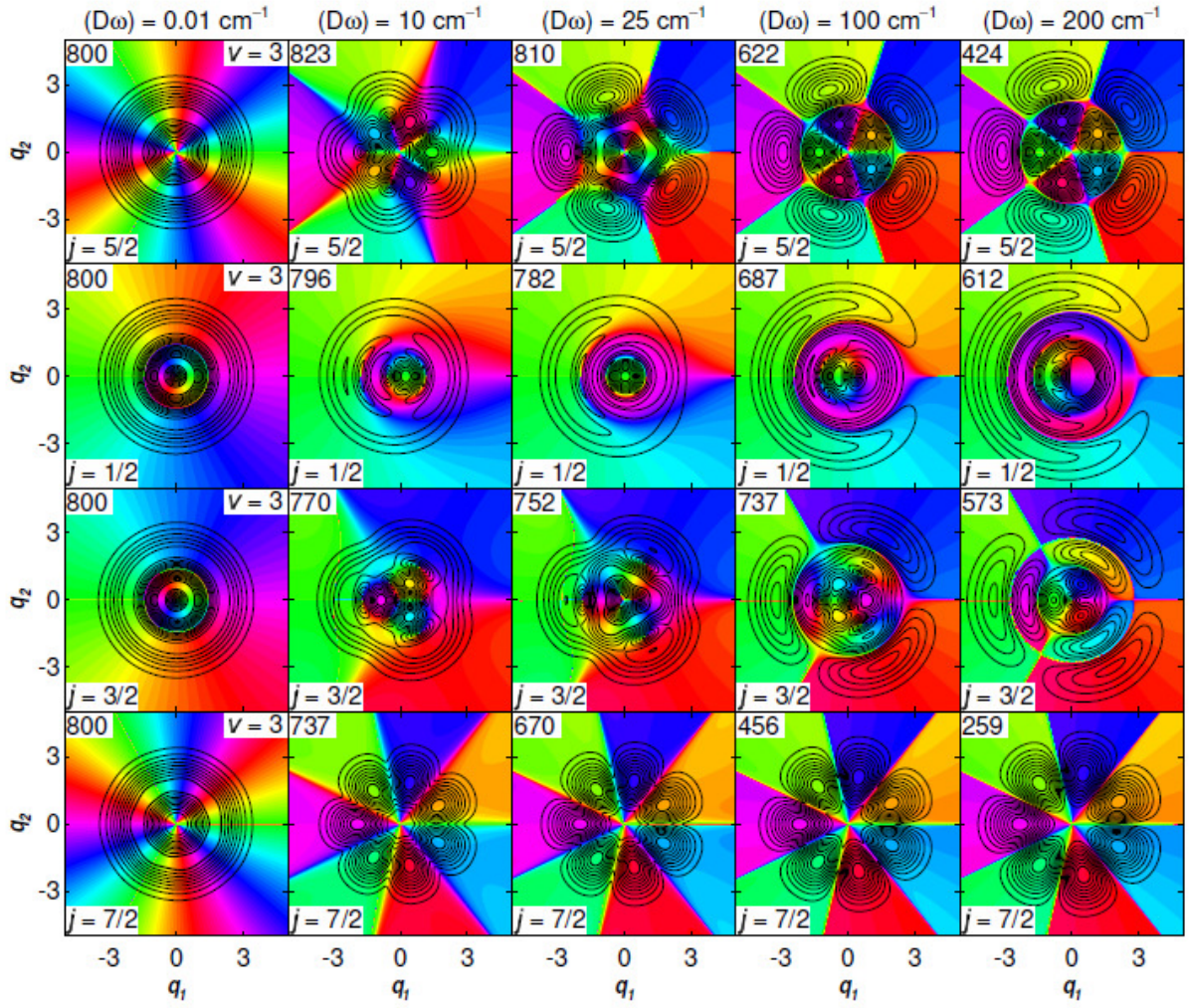

Figure B.5: The seventh to tenth lowest energy eigenstates with $\sigma_v = +1$ for $(D\omega) = 0.01$ cm^{-1} with their energies (upper left) and quantum numbers (pseudo-rotation at lower left and vibrational at upper right) and the eigenstates to which they correlate for $(D\omega) = 10$, 25, 100 and 200 cm^{-1}, also labelled with their energies (upper left) and pseudo-rotation quantum number (lower left). These states are the states shown in Figure B.1, which correlate to low displacement vibrational quantum number $v = 3$. The energetic ordering of states changes with the three highest states shown here crossing each other between $(D\omega) = 25$ cm^{-1} and $(D\omega) = 100$ cm^{-1} and with the two middle states shown here crossing each other again between $(D\omega) = 100$ cm^{-1} and $(D\omega) = 200$ cm^{-1}. For each eigenstate, the contour lines show 10% intervals of its maximum probability amplitude and color shows electronic character from the color wheel in Fig. 3.1.

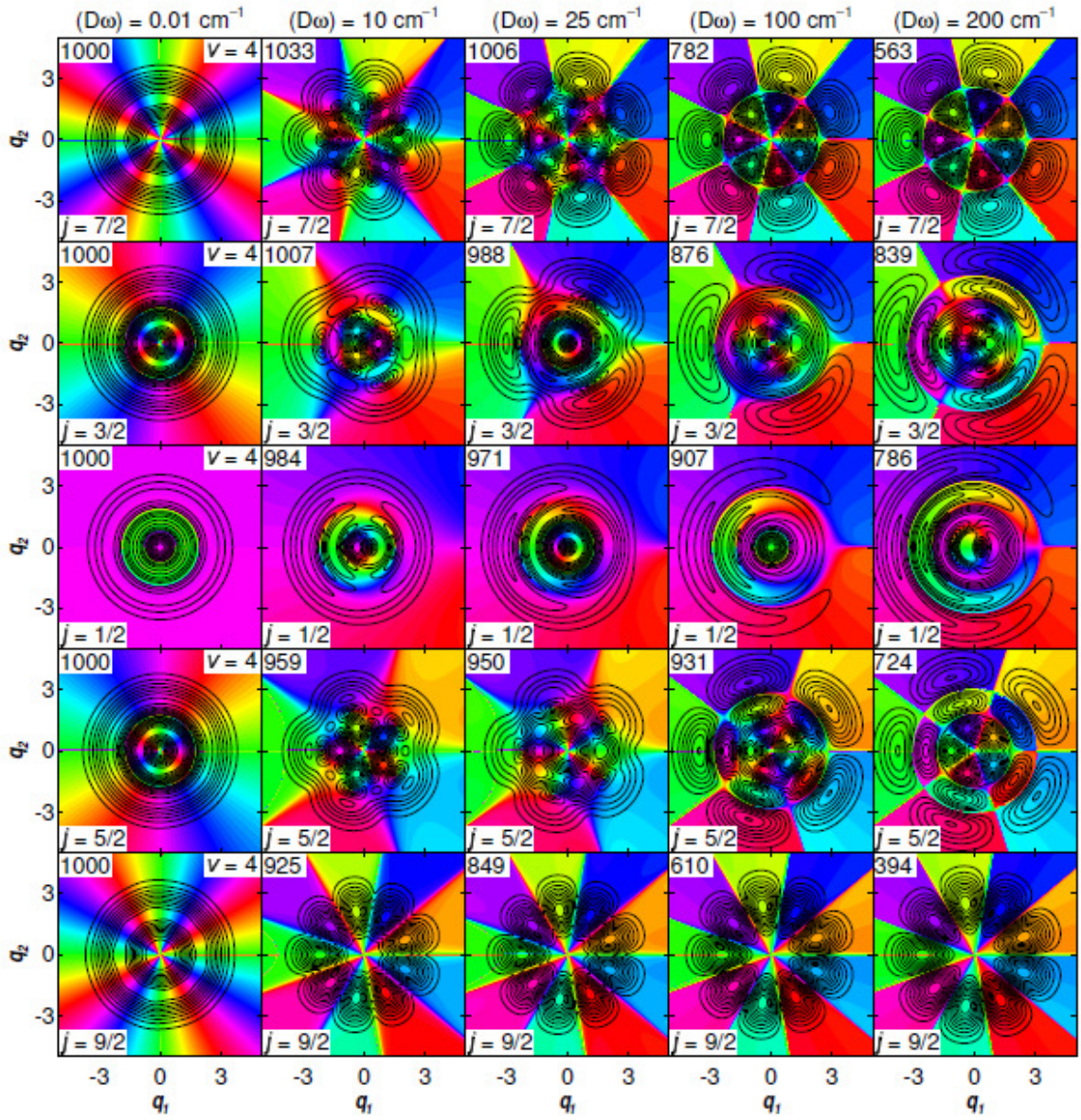

Figure B.6: The eleventh to fifteenth lowest energy eigenstates with $\sigma_v = +1$ for $(D\omega) = 0.01$ cm^{-1} with their energies (upper left) and quantum numbers (pseudo-rotation at lower left and vibrational at upper right) and the eigenstates to which they correlate for $(D\omega) = 10$, 25, 100 and 200 cm^{-1}, also labelled with their energies (upper left) and pseudo-rotation quantum number (lower left). These states are the states shown in Figure B.2, which correlate to low displacement vibrational quantum number $v = 4$. The energetic ordering of states changes with the four highest states shown here inverting their order between $(D\omega) = 25$ cm^{-1} and $(D\omega) = 100$ cm^{-1} and with the three middle states shown here inverting their order again between $(D\omega) = 100$ cm^{-1} and $(D\omega) = 200$ cm^{-1}. For each eigenstate, the contour lines show 10% intervals of its maximum probability amplitude and color shows electronic character from the color wheel in Fig. 3.1.

Energies (in cm^{-1}) of 15 lowest-energy eigenstates with $(D\omega) = 100$ cm^{-1}	Eigenstate Correlation		Energies (in cm^{-1}) of 15 lowest-energy eigenstates with $(D\omega) = 200$ cm^{-1}	Eigenstate Correlation	
	v	j		v	j
46.6061807	0	1/2	-73.7859940	0	1/2
168.7828555	1	3/2	17.2671417	1	3/2
297.5589610	1	1/2	131.6875166	2	5/2
307.9879554	2	5/2	163.7523481	1	1/2
456.2648409	3	7/2	258.7277687	3	7/2
463.0188545	2	3/2	290.3043903	2	3/2
513.8908239	2	1/2	394.0125835	4	9/2
610.4334811	4	9/2	406.9487443	2	1/2
621.8937900	3	5/2	423.5380654	3	5/2
686.9145459	3	1/2	535.2365454	5	11/2
736.6262814	3	3/2	562.8087185	4	7/2
768.8326591	5	11/2	573.1944144	3	3/2
781.8296853	4	7/2	611.7052511	3	1/2
875.6301918	4	3/2	681.0055787	6	13/2
907.1866038	4	1/2	706.8881360	5	9/2

Table B.1: The pseudo-rotation quantum number assignments and small Jahn-Teller displacement vibrational quantum number correlations for the fifteen lowest energy eigenvalues E_m for the nonadiabatic Hamiltonian in Eq. (3.1). The vibrational frequency is $\omega = 200$ cm^{-1} and the Jahn-Teller stabilization energies are $(D\omega) = 100$ cm^{-1} [left three columns] and 200 cm^{-1} [right three columns]. For each eigenvalue listed here, the eigenfunction is pictured in either Figure B.4, B.5, B.6 or B.7.

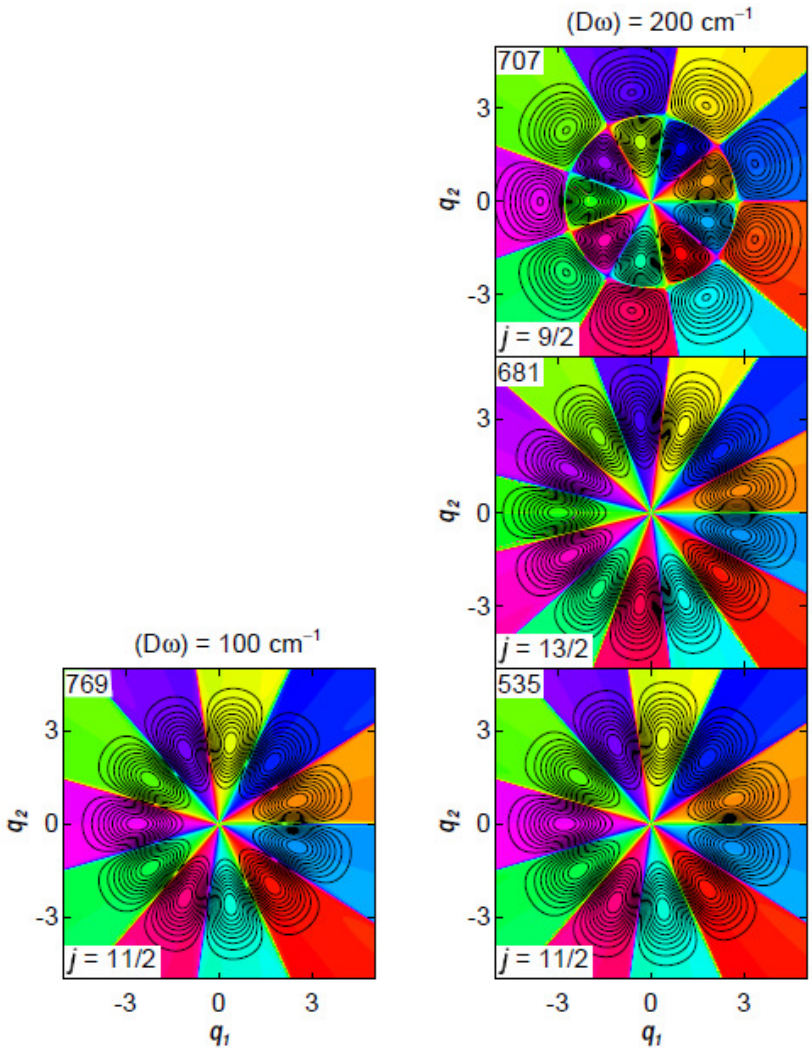

Figure B.7: The four $\sigma_v = +1$ eigenfunctions of Eq. (1) with vibrational frequency $\omega = 200$ cm^{-1} and Jahn-Teller stabilization energies $(D\omega)$ of 100 cm^{-1} or 200 cm^{-1} whose energy eigenvalues are among the fifteen lowest (hence are included in Table B.1), but do not correlate with the fifteen lowest energy eigenvalues in the limit of small displacement (hence are not included in Table 1.1). For each eigenstate, the contour lines show 10% intervals of the maximum probability amplitude and color shows electronic character from the color wheel in Fig. 3.1. Energies (in cm^{-1}) are labelled in the upper left and pseudo-rotation quantum numbers are labelled in the lower left. The eigenfunctions present in Table 1.1 are shown in Figures B.4 – B.6. Based on the energy eigenvalues in Table B.1, the four eigenfunctions pictured here justify the remaining quantum number correlations.

References

1. Thompson, T.C., D.G. Truhlar, and C.A. Mead, *On the form of the adiabatic and diabatic representation and the validity of the adiabatic approximation for X3 Jahn-Teller systems.* 82, 1985. **5**: p. 2392-2407.

2. Foster, P.W. and D.M. Jonas, *Nonadiabatic conical nodes are near but not at an elliptical conical intersection.* Chem. Phys., 2019. **520**: p. 108-121.

3. Foster, P.W. and D.M. Jonas, *Nonadiabatic Eigenfunctions Can Have Amplitude, Signed Conical Nodes, or Signed Higher Order Nodes at Conical Intersection with Circular Symmetry.* J. Phys. Chem. A., 2017. **121**(39): p. 7401-7413.

4. Moffitt, W. and A.D. Liehr, *Configurational Instability of Degenerate Electronic States.* Phys. Rev., 1957. **106**(4): p. 1195-1200.

5. Longuet-Higgins, H.C., et al., *Studies of the Jahn-Teller Effect II. The Dynamical Problem.* Proc. R. Soc. Lond. A, 1958. **244**(1236): p. 1-16.

6. Thorson, W. and W. Moffitt, *Some Calculations on the Jahn-Teller Effect in Octahedral Systems.* Phys. Rev., 1968. **168**(2): p. 362-369.

APPENDIX C: Chapter 4 Supplementary Materials

The circular symmetry Jahn-Teller Hamiltonian has three parameter regimes with simple expressions for the energy eigenvalues [1]. The half-odd integral pseudo-rotation quantum number *j* is rigorously conserved across all three parameter regimes. For small Jahn-Teller displacements, the 2D harmonic oscillator vibrational quantum number is good and the energy levels are well approximated by perturbation theory [1, 2]. The perturbation theory expression involves three quantum numbers: the 2D harmonic oscillator vibrational quantum number v and vibrational angular momentum l plus an electronic angular momentum $\lambda = \pm 1$ that couple to give the pseudo-rotation quantum number $j = l + (\lambda / 2)$. The energy eigenvalues are given by $E = \omega(v+1) - 2(D\omega)[l\lambda + 1]$ [2]. As d increases, all three electronic and vibrational quantum numbers break down through $j-$ conserving avoided crossings [3]. Before a level undergoes its first avoided crossing, the small Jahn-Teller displacement quantum numbers $(v, |j|)$ remain good. For larger displacements, the lower eigenvalues approximate those of a double-valued radial potential $V^d(r) = (1/2)\omega(r-d)^2$ with half-odd integral pseudo-rotation quantum numbers. In this regime, the eigenvalues are $E = \omega(p+1/2) - (D\omega) + \omega j^2/(2d^2)$, where the radial vibrational quantum number *p* is a non-negative integer (Eq. (6.16) of ref. [1] defines *p* differently). Since radial curve crossing between the lower and upper adiabatic potentials is unhindered at the origin in this model, it has diabatic aspects. At very large displacements, the low energy eigenstates become vibrational eigenstates of the lower adiabatic potential (the hat) and the pseudo-rotation term in the energy tends to zero [1]. For any given vibrational eigenstate of the hat, this transition involves a finite number of avoided crossings. After a level's last avoided crossing, its adiabatic quantum numbers $(p, |j|)$ become good. Since the vibronic eigenstates of the upper adiabatic potential (the cone) are embedded among the higher energy vibrational eigenstates of the hat, an endless series of avoided crossings prevents convergence

to adiabatic behavior as the Jahn-Teller displacement increases [3]. Nonetheless, for specific Jahn-Teller displacements, some eigenstates are predominantly on the cone [3].

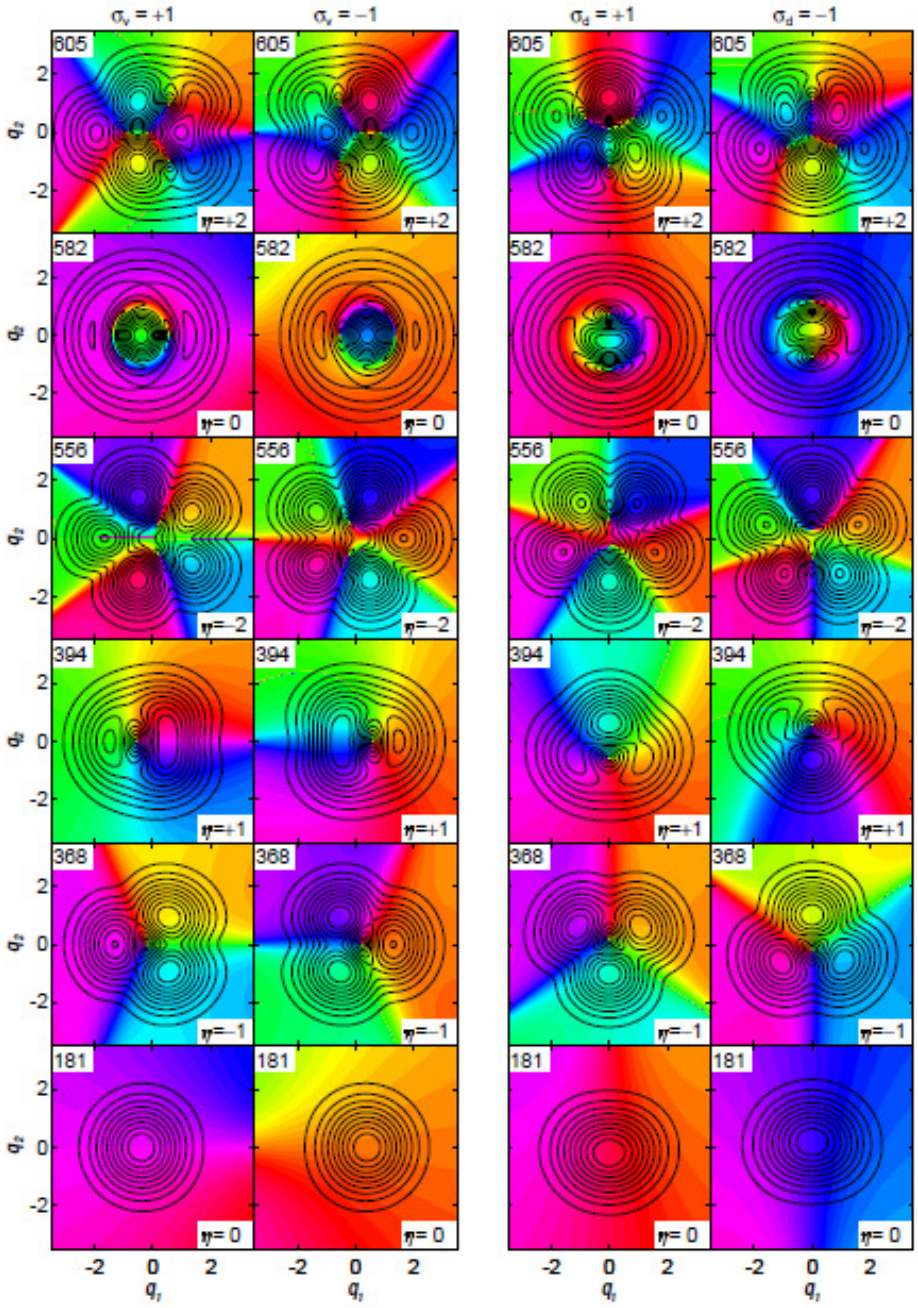

Figure C.1: The four columns each have six panels showing the probability amplitude and electronic character of the six lowest energy eigenstates with a given reflection symmetry for the Jahn-Teller Hamiltonian with vibrational frequencies $\omega_1 = \omega_2 = 200$ cm^{-1} and Jahn-Teller displacements $d_1 = 0.4$ and $d_2 = 0.2$. The left column has $\sigma_v = +1$ symmetry, the second column has $\sigma_v = -1$ symmetry, the third column has $\sigma_d = +1$ symmetry, and the right column has $\sigma_d = -1$ symmetry. In each panel, the contour interval is 10% of the maximum probability amplitude for that state, with thicker contour lines for higher amplitude. The color wheel in Figure 4.1 is used to represent electronic character. In each column, the lowest energy state is on the bottom and energy increases upward. In each panel, the label at upper left gives the eigenstate energy in wavenumbers

and the label at lower right specifies the electronic index η around the perimeter of each panel. η is constant for each row, while the location of the nodes is different between the paired columns.

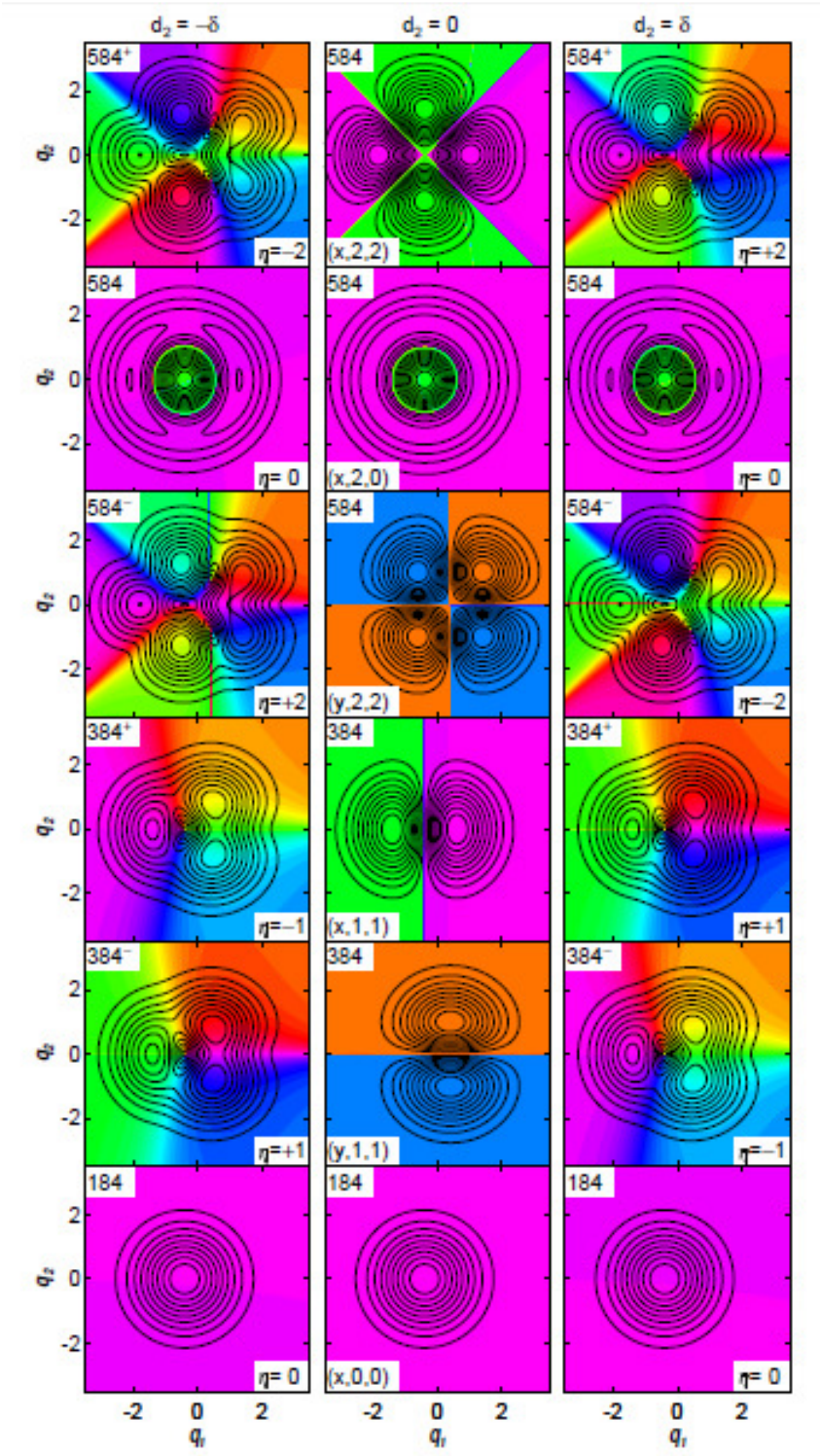

Figure C.2: The three columns each have six panels showing the probability amplitude and electronic character of the six lowest energy eigenstates with $\sigma_v = +1$ for the Jahn-Teller

Hamiltonian with vibrational frequencies $\omega_1 = \omega_2 = 200$ cm^{-1} and Jahn-Teller displacement $d_1 = 0.4$ for the tuning coordinate. The three columns systematically vary the Jahn-Teller displacements d_2 for the coupling coordinate. In each panel, the contour interval is 10% of the maximum probability amplitude for that state, with thicker contour lines for higher amplitude. The color wheel in Figure 4.1 is used to represent electronic character. In each column, the lowest energy state is on the bottom and energy increases upward. In each panel, the label at upper left gives the eigenstate energy in wavenumbers and the label at lower right specifies the electronic index η for large radius circles. The center column shows an accidental Born-Oppenheimer case with adiabatic nodal lines or curves indicated by abrupt color changes. Degenerate $\sigma_v = +1$ states are chosen so each has a definite adiabatic electronic state (x or y), vibrational quantum number v, and absolute value of the vibrational angular momentum $|l|$ about the equilibrium geometry on its adiabatic potential energy surface given at lower left $(x/y, v, |\ell|)$. The left and right columns show perturbations from the accidental Born-Oppenheimer case with $d_2 = -10^{-10}$ on the left and $d_2 = +10^{-10}$ on the right. Energies of the left and right columns agree with each other to 14-digit precision. The energies with a $+$ or – superscript are slightly above or below the energy for the accidental Born-Oppenheimer case, respectively (see Table 1.2 and corresponding perturbation theory). The probability amplitudes of the left and right column also agree to 14-digit precision, though the electronic characters differ significantly, with index η reversing with a change in the sign of d_2. Alternately, this can be viewed as showing that η is conserved while the energetic ordering changes as d_2 varies through the degenerate case.

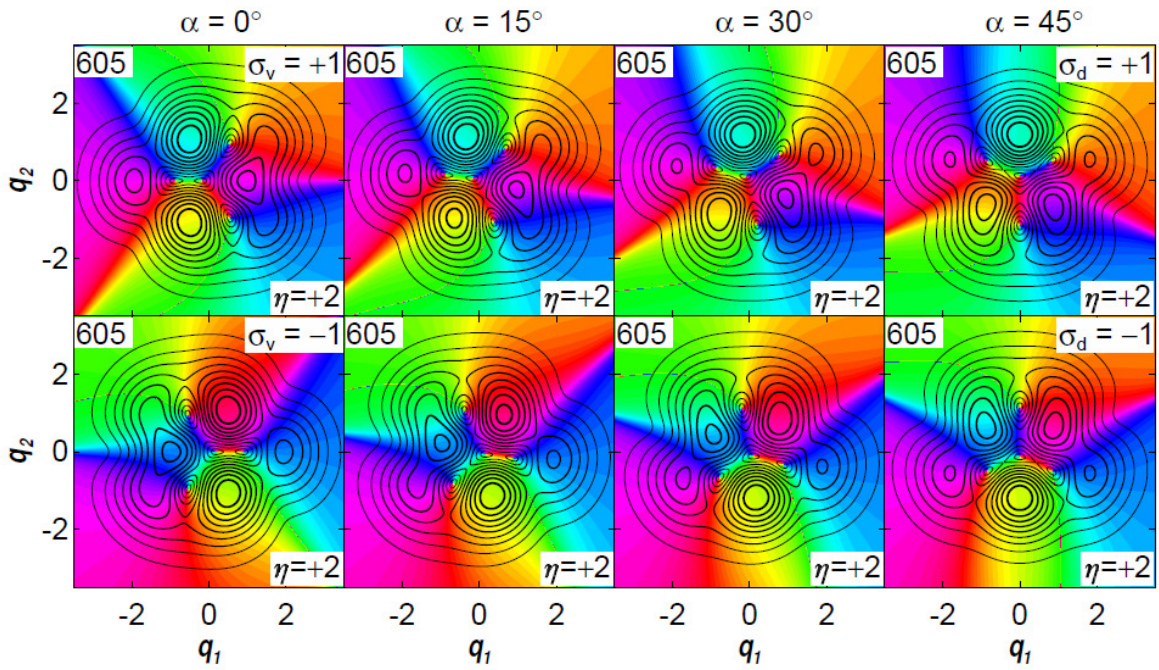

Figure C.3: The four panels show how different orthogonal transformations among a degenerate eigenstate pair affect the probability amplitude and electronic character. Each panel shows the 605 cm^{-1} eigenstate of the Jahn-Teller Hamiltonian with vibrational frequencies $\omega_1 = \omega_2 = 200$ cm^{-1} and Jahn-Teller displacements of $d_1 = 0.4$ and $d_2 = 0.2$. The contour interval is 10% and the color wheel from Fig. 4.1 indicates electronic character. The orthogonal transformation is defined as

$$\begin{bmatrix} |\alpha_+\rangle \\ |\alpha_-\rangle \end{bmatrix} = \begin{bmatrix} \cos(\alpha) & -\sin(\alpha) \\ \sin(\alpha) & \cos(\alpha) \end{bmatrix} \begin{bmatrix} |\sigma_v = +1\rangle \\ |\sigma_v = -1\rangle \end{bmatrix}$$

For $\alpha = \pi/4$, $|\alpha_+\rangle = |\sigma_d = +1\rangle$ and $|\alpha_-\rangle = |\sigma_d = -1\rangle$. The eigenstates in the left panel have σ_v symmetry, while the second panel has the degenerate state pair transformed with $\alpha = 15°$. The third panel has $\alpha = 30°$ and the right panel has $\alpha = 45°$ so that the states exhibit σ_d symmetry. As all nodes are accidental, the location of the nodes is different in each panel, but the electronic index η around the perimeter is conserved.

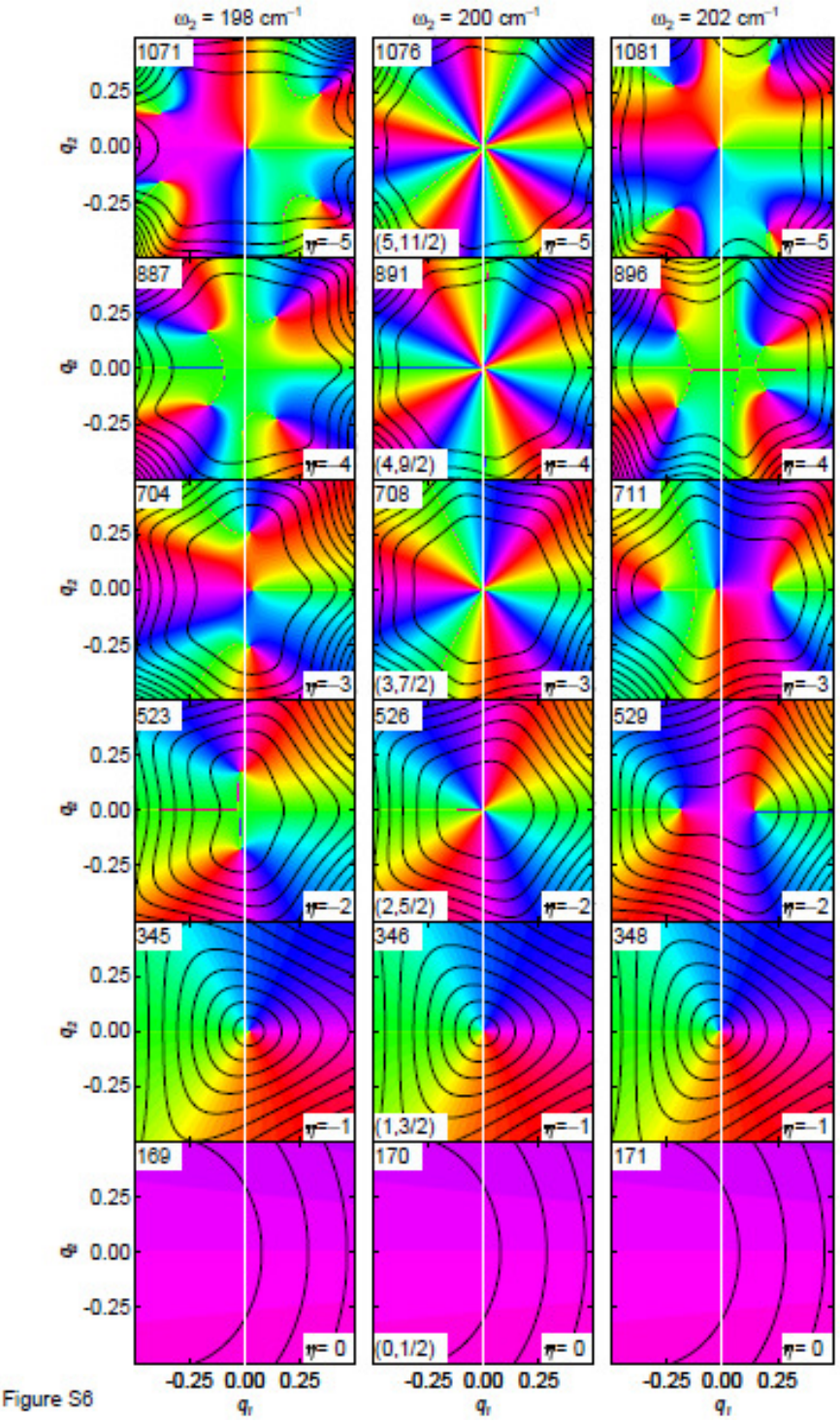

Figure C.4: The probability amplitude and electronic character for six selected eigenstates of the Jahn-Teller Hamiltonian with vibrational frequency $\omega_1 = 200$ cm^{-1} and $d_1 = d_2 = 0.4$. Each column has a different coupling vibration frequency ω_2 given at the top. Energy eigenvalues are given in cm^{-1} at the upper left of each panel. For the bottom two rows, each contour represents 10% of the maximum probability amplitude. For the third row, each contour represents 5% of the maximum

probability amplitude, while each contour for the fourth row represents 2% of the maximum probability amplitude, each contour for the fifth row represents 0.5% of the maximum probability amplitude, and each contour for the top (sixth) row represents 0.1% of the maximum probability amplitude. Thicker contours represent higher amplitude. Color represents electronic character as shown in the color wheel in Fig. 4.1. The eigenfunctions in the center column have circular symmetry and quantum numbers $(v,|j|)$ specified in the lower left of each panel. From bottom to top, they are the lowest energy eigenstate with no node, a first order node, a second order node, a third order node, a fourth order node and a fifth order node, respectively. The columns to the left and right have square-symmetric Jahn-Teller Hamiltonians that generate elliptical conical intersections and have no higher order nodes. In every row, η is conserved for simple closed paths around the perimeter of each panel. A thin white vertical line marking $q_1 = 0$ shows that no node occurs at the origin for the elliptical conical intersections.

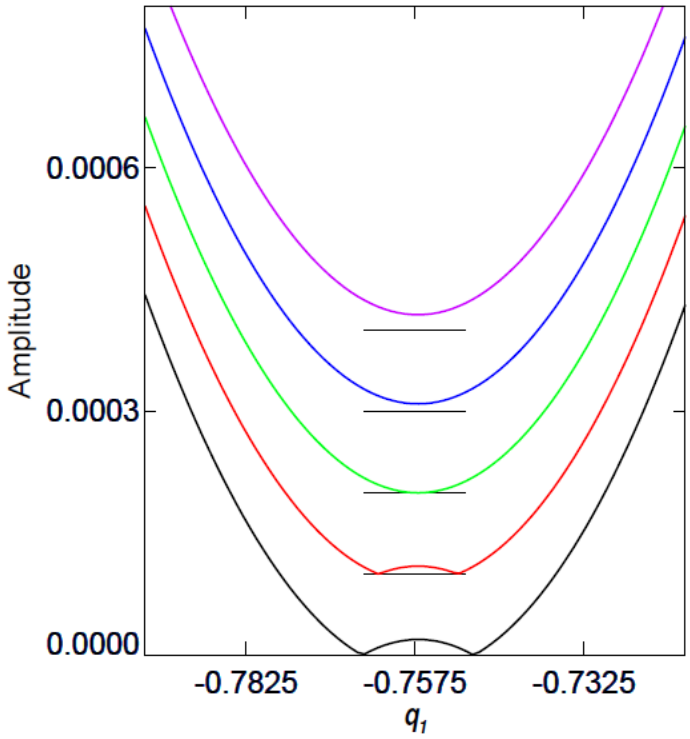

Figure C.5: Cross-sections along $q_2 = 0$ for the tangential node in Fig. 4.7 and 4.8. Relative probability amplitudes as a function of q_1 are offset vertically (by 0.0001) for five different Jahn-Teller Hamiltonians. Each Hamiltonian has a vibrational frequency of $\omega_1 = 200$ cm^{-1} and Jahn-Teller displacements of $d_1 = d_2 = 0.4$; $\omega_2 =$ 230.9005 cm^{-1} for the black line, 230.903 cm^{-1} for the red line, 230.90555 cm^{-1} for the green line, 230.908 cm^{-1} for the blue line and 230.9105 cm^{-1} for the violet line. As two conical nodes with opposite signs approach each other, continuity of the total eigenfunction and its derivative along their line of approach requires that the linear term in a Taylor series for the amplitude vanish in between them. This leaves a quadratic term as the lowest order term in the Taylor series expansion of the amplitude along their line of approach.

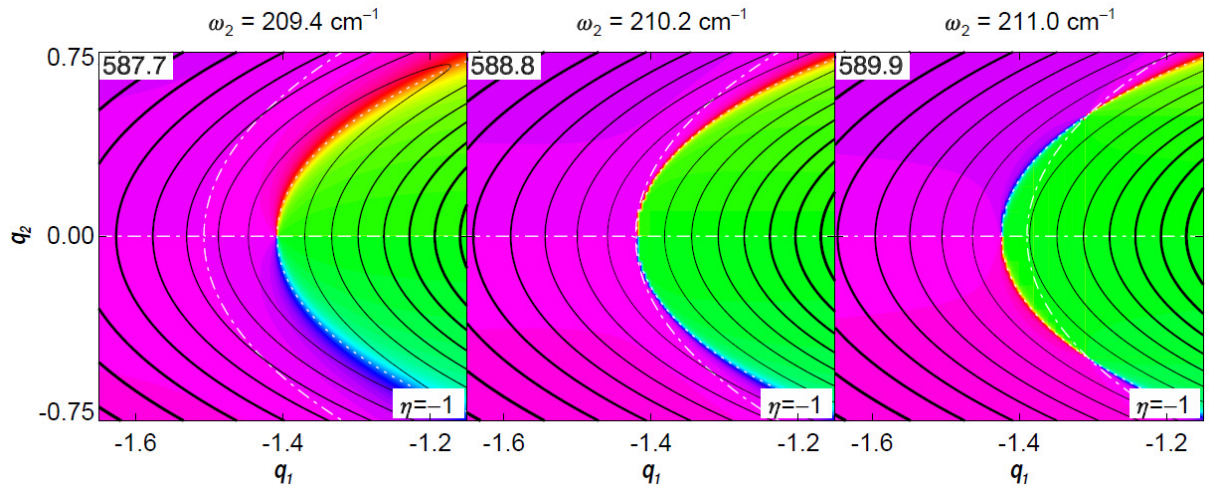

Figure C.6: Close up view of the nonadiabatic eigenfunctions correlated to $(v = 2, |\, j \,| = 1/2)$ for fixed Jahn-Teller Hamiltonian parameters of $\omega_1 = 200$ cm^{-1} and $d_1 = d_2 = 0.4$ as ω_2 (indicated above each panel) increases. The horizontal axis has been stretched by a factor of 3 relative to the vertical axis. The positive vibrational amplitude factor's contour interval is 5%, with thicker contours indicating higher amplitude. The electronic factor is shown using the color wheel from Fig. 4.1. Each panel overlays the nodal curves in the eigenfunction projections onto adiabatic electronic states *x* (dotted white curve) and *y* (dot-dashed white line). In each panel, the eigenstate energy (cm^{-1}) is given at top left and the total electronic index for a simple closed path around the perimeter is given at lower right. Left) One conical node with electronic index -1 occurs where the nodal curve on *x* intersects the horizontal nodal line on *y*. The nodal curve on *y* lies to the left of the nodal curve on *x* and does not intersect it to generate conical nodes. Middle) At $\omega_2 \approx 210.2$ cm^{-1}, the vertices of the nodal curves on *x* and *y* coincide with each other at the horizontal nodal line on *y*. Right) The nodal curves on *x* and *y* now cross each other twice (generating two new conical nodes, each with electronic index of -1), and the nodal curve on *x* still crosses the nodal line on *y*, so there are three conical nodes. Compared to the left panel, the node at $q_2 = 0$ has changed its electronic index from -1 to +1. The electronic index for simple closed paths around all these nodes is the sum of the individual electronic indices and remains -1 throughout.

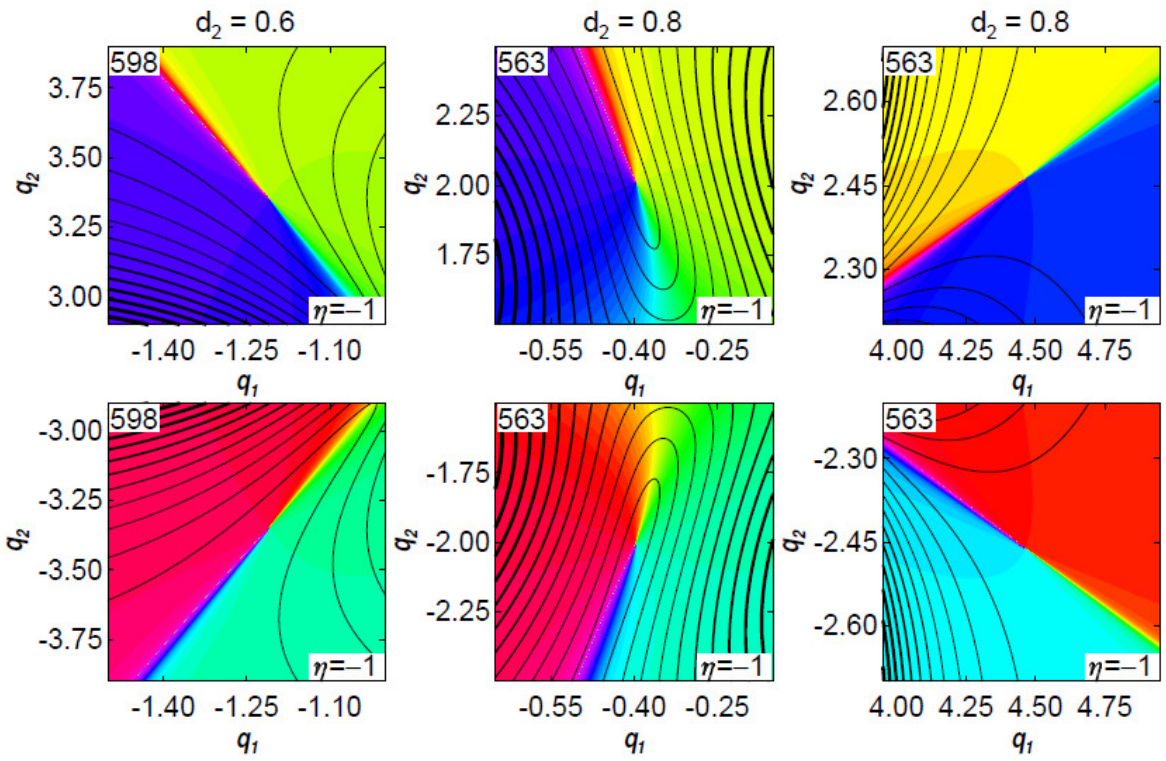

Figure C.7: The six panels show the probability amplitude and electronic character around the conical nodes that are circled in Figure 4.9. The two panels on the left show close-up views of the sixth lowest energy $\sigma_v = +1$ eigenfunction of the Jahn-Teller Hamiltonian when both vibrational frequencies in the Hamiltonian are $\omega_1 = \omega_2 = 200$ cm^{-1}, $d_1 = 0.4$ and $d_2 = 0.6$. The contour interval is 0.5%. The four panels in the center and on the right show close-up views of the sixth lowest energy $\sigma_v = +1$ eigenfunction of the Jahn-Teller Hamiltonian when $\omega_1 = \omega_2 = 200$ cm^{-1}, $d_1 = 0.4$ and $d_2 = 0.8$. The contour interval is 2.5% in the center and 0.025% on the right. All six nodes are shown with uneven aspect ratios to reveal the conical character, which has one highly elongated axis. Due to σ_v symmetry, corresponding nodes in the top row and bottom row have surrounding amplitudes that are reflections of one another and have equal electronic indices.

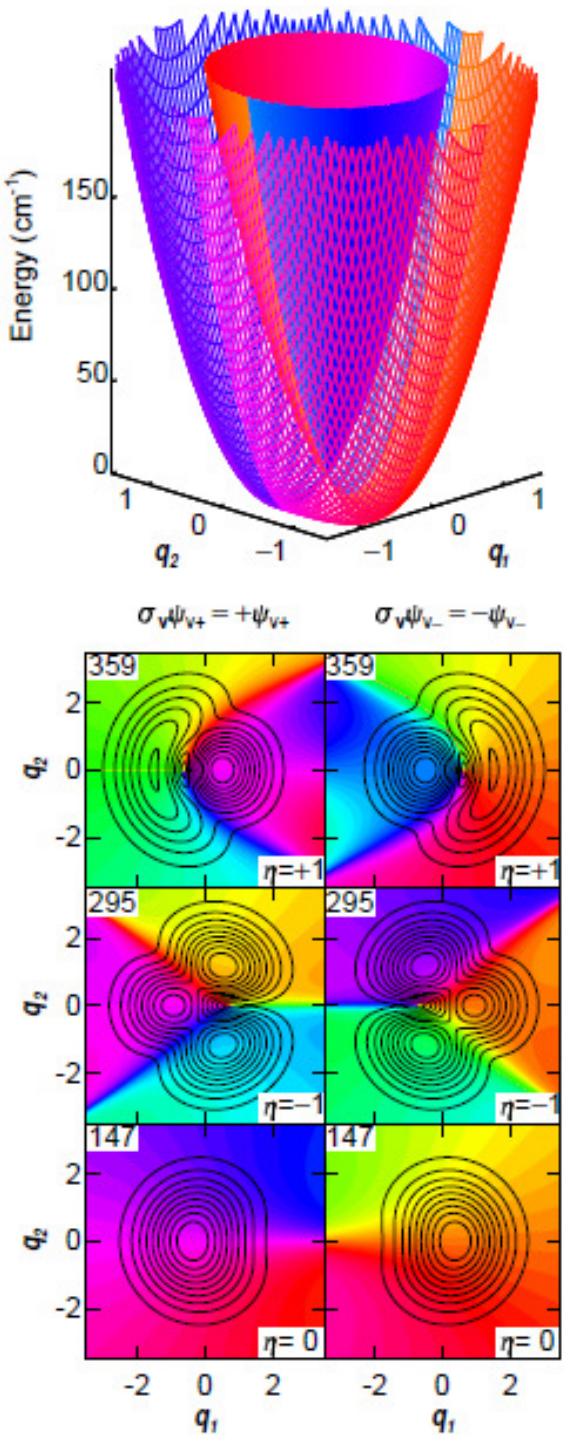

Figure C.8: Top) The adiabatic potential energy surfaces for a doubly degenerate E symmetry electronic state as a function of Jahn-Teller active normal coordinates (q_1, q_2). The Hamiltonian parameters in Eq. (4.1) have unequal vibrational frequencies $\omega_1 = 200$ cm^{-1} and $\omega_2 = 160$ cm^{-1} and unequal displacements $d_1 = 0.4$ and $d_2 = 0.5$ such that $\omega_1 d_1 = \omega_2 d_2$. The unequal frequencies make the Hamiltonian and adiabatic potential surfaces globally non-circular, while the last condition gives the conical intersection local circular symmetry. The lower surface has minima

[front right and back left] at $(0,\pm d_2)$ that are stabilized $(D\omega)_2 = 20$ cm^{-1} below the conical intersection. The two saddle points [front left and back right] at $(\pm d_1, 0)$ are stabilized by $(D\omega)_1 = 16$ cm^{-1}. The color of each potential surface at each coordinate indicates the adiabatic electronic eigenfunction according to the color wheel in Figure 4.1. Bottom) The six lowest energy eigenfunctions (shown as eigenstates of σ_v). Contours show probability amplitude, with each contour representing 10% of the maximum amplitude and thicker lines for higher contours. Electronic character is shown by color, again using the color wheel in Figure 4.1. The asymmetry of these states and the lack of nodes at the conical intersection point (the origin) shows that local circular symmetry is not sufficient to force nodes onto the conical intersection.

146.832358574305
146.832358574306
295.140369817599
295.140369817600
359.209017149936
359.209017149937
449.384364655300
449.384364655301
505.829709426359
505.829709426359
562.967387357872
562.967387357873

Table C.1: Numerical energy eigenvalues (cm^{-1}) for the twelve lowest energy eigenstates of the Jahn-Teller Hamiltonian in Eq. (4.1) with the parameters used to generate the adiabatic potential surfaces and nonadiabatic eigenfunctions in Figure C.8.

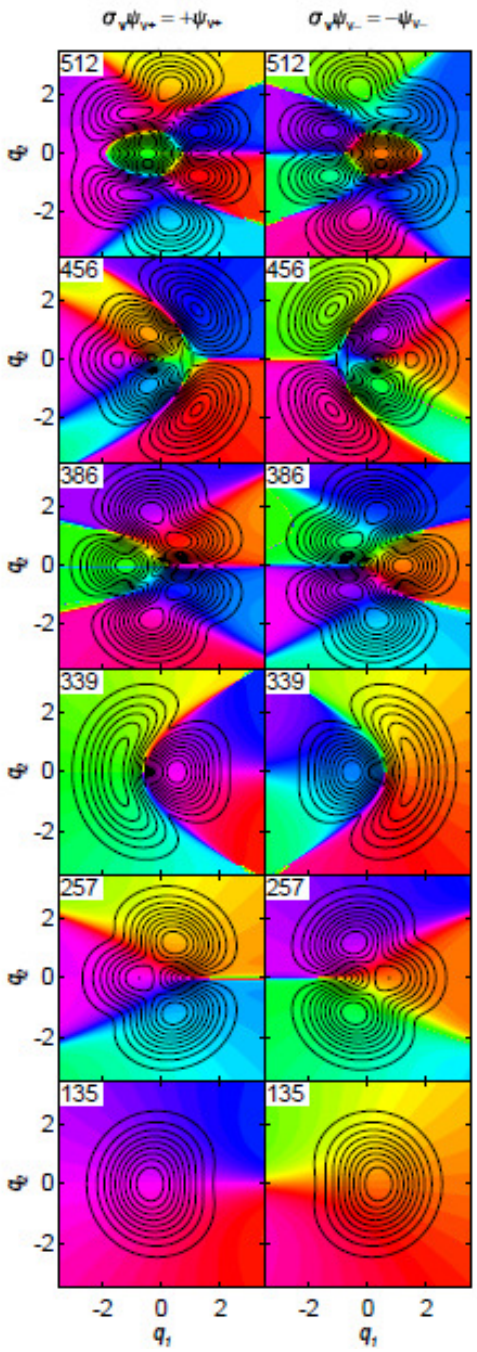

Figure C.9: The twelve lowest energy eigenfunctions are shown for a Hamiltonian with unequal vibrational frequencies ($\omega_1 = 200$ cm^{-1}, $\omega_2 = 128$ cm^{-1}) and unequal Jahn-Teller displacements ($(d_1 = 0.4\,,\ d_2 = 0.5)$ chosen to generate the same Jahn-Teller stabilization energy [$(D\omega)$ = 16 cm^{-1}] for both vibrations. All contours of both adiabatic potential energy surfaces are concentric ellipses with exactly the same eccentricity, $e = \sqrt{1-(\omega_2/\omega_1)} = 0.6$. The kinetic energy operator has the same eccentricity, so these eigenfunctions arise from a purely elliptical nonadiabatic Hamiltonian.

134.500041759584
134.500041759585
256.713166795670
256.713166795673
338.978806048831
338.978806048833
385.600744578583
385.600744578585
456.410107135765
456.410107135766
511.741881836435
511.741881836437

Table C.2: Numerical energy eigenvalues (cm^{-1}) for the twelve lowest energy eigenstates of Jahn-Teller Hamiltonian in Eq. (4.1) with the parameters used to generate the nonadiabatic eigenfunctions in Figure C.9.

References

1. Longuet-Higgins, H.C., et al., *Studies of the Jahn-Teller Effect II. The Dynamical Problem.* Proc. R. Soc. Lond. A, 1958. **244**(1236): p. 1-16.

2. Foster, P.W. and D.M. Jonas, *Nonadiabatic Eigenfunctions Can Have Amplitude, Signed Conical Nodes, or Signed Higher Order Nodes at Conical Intersection with Circular Symmetry.* J. Phys. Chem. A., 2017. **121**(39): p. 7401-7413.

3. Thompson, T.C., D.G. Truhlar, and C.A. Mead, *On the form of the adiabatic and diabatic representation and the validity of the adiabatic approximation for X3 Jahn-Teller systems.* 82, 1985. **5**: p. 2392-2407.

APPENDIX D: Supporting Information for Chapter 5

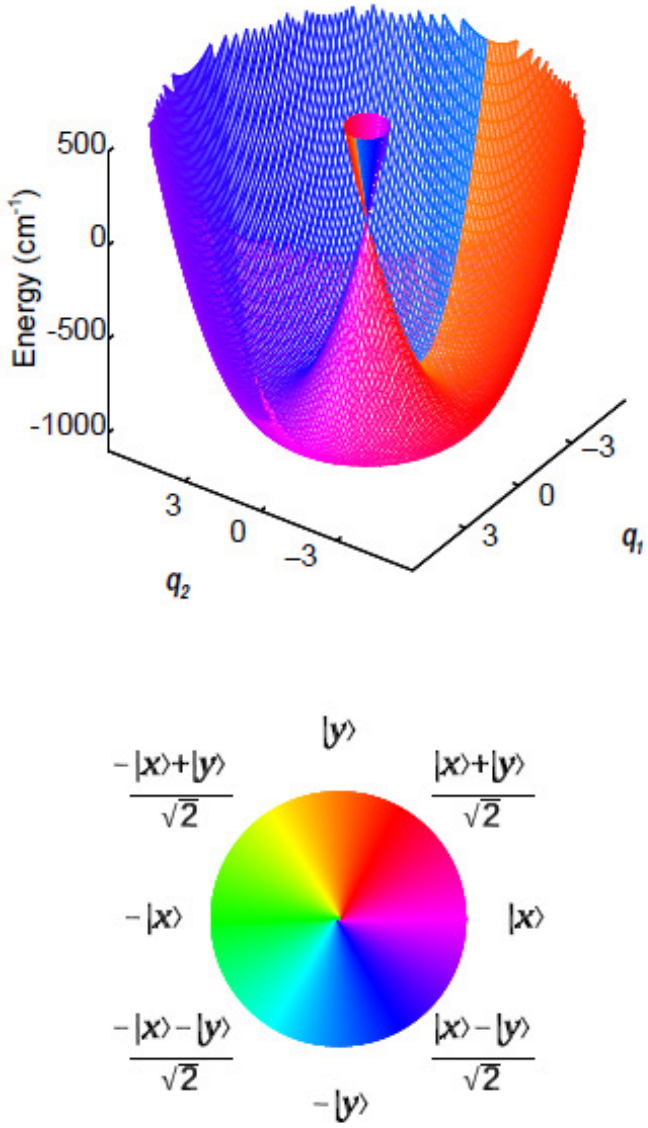

Figure D.1: The adiabatic potential energy surfaces and coordinate dependent electronic character a model Hamiltonian. The vibrational frequency is $\omega = 200$ cm^{-1} and the Jahn-Teller stabilization energy is $(D\omega) = 1000$ cm^{-1}. Color represents adiabatic electronic character $\left|\psi_{elec}(q_1, q_2)\right\rangle$ according to the color wheel at the bottom. The conical intersection at $q_1 = q_2 = 0$ and $E = 0$ is well above below the zero-point energy. The lower adiabatic potential surface descends from the conical intersection to its minimum at $E_{\min} = -(D\omega)$ around the circle $(q_1^2 + q_2^2)^{1/2} = d$. An adiabatic phase discontinuity in electronic character must occur for both the inner (solid) and outer (mesh) surfaces, is arbitrarily placed along $q_2 = 0$, and is visible as an angular color discontinuity from orange $\left|y\right\rangle$ to light blue $-\left|y\right\rangle$. Starting and stopping at the discontinuity, a counterclockwise path around either adiabatic surface rotates halfway around the color wheel in a counterclockwise direction.

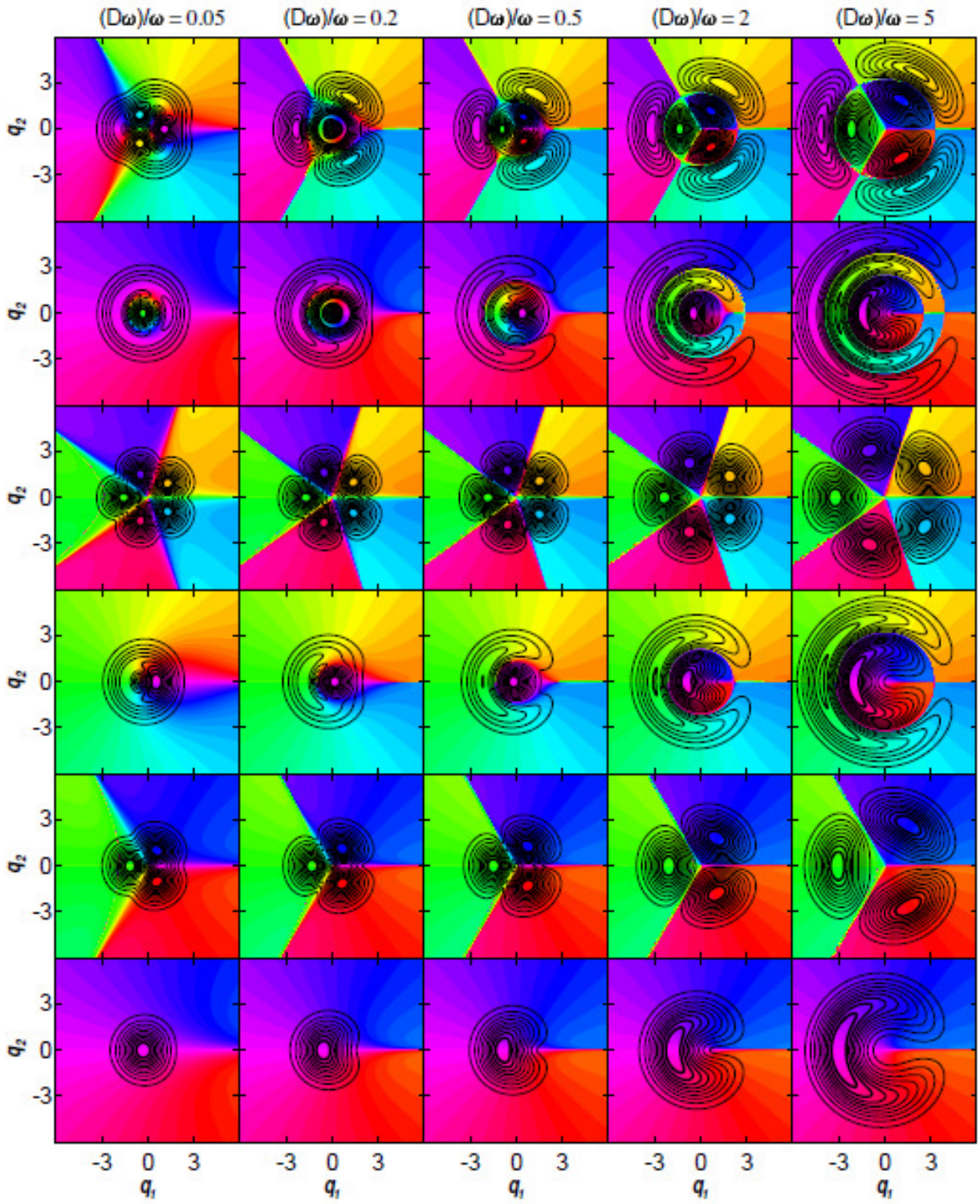

Figure D.2 (caption on next page)

Figure D.2 (on previous page)**:** The left column shows the six lowest energy $\sigma_v = +1$ eigenstates for the circularly symmetric Hamiltonian where $\omega = 200$ cm^{-1} and $(D\omega)/\omega = 0.05$. The contours represent probability amplitude in 10 % intervals where the contour lines get thicker for higher contours. Color represents electronic character with each color representing a value of $\Theta_m(q_1, q_2)$ according to the color wheel in Figure 5.1. The other four columns show the corresponding eigenstates for $(D\omega)/\omega = 0.2$, 0.5, 2, and 5, plotted similarly. Eigenstates can be compared with those in Figure 5.4.